RESEARCH & DEVELOPMENT

Development of Geosynthetic Pavement Interlayer Improvements

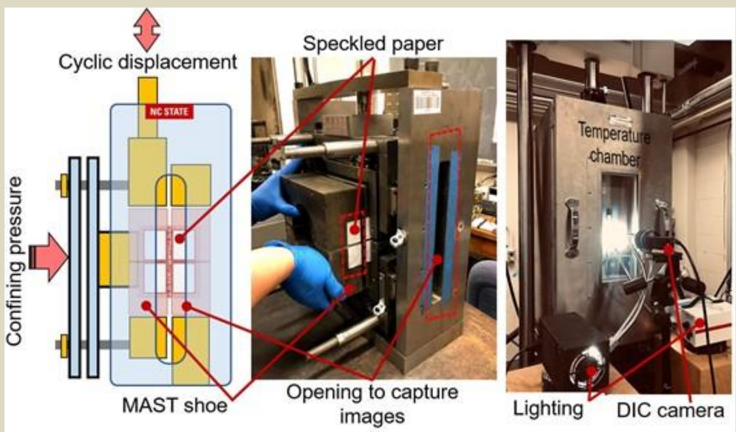

MAST test set-up: (a) schematic diagram, (b) loading MAST shoes into loading jig, and (c) test set-up with DIC system

Y. Richard Kim, Ph.D., P.E., F. ASCE

Nithin Sudarsanan, Ph.D.

Lei Gabriel Xue

Dept. of Civil, Construction, & Environmental Engineering

North Carolina State University

NCDOT Project 2019-19

March 2022

Development of Geosynthetic Pavement Interlayer Improvements

FINAL REPORT

Submitted to:
North Carolina Department of Transportation
Office of Research
(Research Projection No. RP 2019-19)

Submitted by

Y. Richard Kim, Ph.D., P.E., F.ASCE
Jimmy D. Clark Distinguished University Professor
Campus Box 7908
Department of Civil, Construction & Environmental Engineering
North Carolina State University
Raleigh, NC 27695-7908
Tel: 919-515-7758, Fax: 919-515-7908
kim@ncsu.edu

Nithin Sudarsanan, Ph. D.
Postdoctoral Researcher

Lei Gabriel Xue
Graduate Research Assistant

Department of Civil, Construction & Environmental Engineering
North Carolina State University
Raleigh, NC

March 2022

Technical Report Documentation Page

1. Report No. FHWA/NC/2019-19	2. Government Accession No.	3. Recipient's Catalog No.
4. Title and Subtitle Development of Geosynthetic Pavement Interlayer Improvements		5. Report Date March 2022
7. Author(s) Y. Richard Kim, Nithin Sudarsanan, Lei Xue		8. Performing Organization Report No.
9. Performing Organization Name and Address Campus Box 7908, Dept. of Civil, Construction, & Environmental Engrg. NCSU, Raleigh, NC 27695-7908		10. Work Unit No. (TRAIS) 11. Contract or Grant No.
12. Sponsoring Agency Name and Address NC Department of Transportation Research and Analysis Group 1 South Wilmington Street Raleigh, NC 27601		13. Type of Report and Period Covered Final Report August 2018– May 2021 14. Sponsoring Agency Code RP2019-19
15. Supplementary Notes		

16. Abstract

Asphalt overlays often fail prematurely by allowing the propagation of existing cracks over the overlay surface, thereby forming reflective cracks. Among the many available interlayer reinforcement technologies, geosynthetic products are gaining popularity for mitigating reflective cracking. The main goal of this research effort is to ensure that North Carolina Department of Transportation engineers can choose the appropriate geosynthetic pavement interlayer product for a specific application based on performance data. The negative side effect of geosynthetic applications for surface paving is aggravation of the debonding distress. Hence, another objective is to develop a tack coat selection criterion for a specific geosynthetic type that safeguards against debonding failure. The scope of the test plan includes five geosynthetic products designated as paving composite #1 (PC#1), paving composite #2 (PC#2), paving grid (PaG), paving mat (PM), and paving fabric (PF). In this study, geosynthetic-reinforced and unreinforced specimens were tested using four-point notched beam fatigue test equipment together with the digital image correlation (DIC) technique and a Modified Asphalt Shear Tester to measure the specimens' crack resistance capacity and interface shear strength, respectively. The double-layered asphalt concrete specimens were fabricated in gyratory and slab compactors using a hot mix designated as RS9.5C with 40% reclaimed asphalt pavement. The geosynthetic product was sandwiched between the asphalt layers with a tack coat (PG 64-22) applied at the rate recommended by the geosynthetic product's manufacturer. Binder bond strength (BBS) tests were performed on the PG 64-22 binder. The DIC data were analyzed to determine the Von Mises strain, which in turn was used to determine the failure mode of the geosynthetic-reinforced asphalt beams. The DIC contours revealed that the failure mode could be classified into either vertical cracking or debonding and that each of these two failure modes depends on the geosynthetic product type, tack coat application rate, and strain level. Sufficient bond strength is needed to minimize debonding at the interface and is an important factor to mitigate vertical reflective cracking as well.

The three-dimensional pavement analysis program, FlexPAVE™ v. 1.1, and EverStressFE v 1.0 were used to determine the pavement responses. The pavement response analysis for numerous layer modulus and thickness combinations led to a predictive equation for interface tensile strain ($\varepsilon_{t\text{-}overlay}$). The predictive $\varepsilon_{t\text{-}overlay}$ equation is a function of the surface curvature index, base damage index, base curvature index, and overlay thickness. A geosynthetic product selection table was developed based on the expected improvement factor and failure mode that correspond to the field $\varepsilon_{t\text{-}overlay}$. Subsequently, a tack coat criterion for each geosynthetic product was developed based on the maximum shear ratio and BBS relationship. The BBS threshold values for PC#1, PC#2, PaG, PM, and PF are 280 kPa, 860 kPa, 455 kPa, 860 kPa, and 280 kPa, respectively. The results of this research effort are the guidelines developed for geosynthetic interlayer product selection and for tack coat selection. Populating more laboratory and field data is highly encouraged and will help to reinforce and improve the findings from this study and assist in the implementation of the developed guidelines in practice.

17. Keywords			18. Distribution Statement
Geosynthetics, tack coat, reflective cracking, debonding, bond strength, shear strength, digital image correlation (DIC), binder bond strength (BBS), FlexPAVE™, EverStressFE, falling weight deflectometer (FWD), deflection basin parameter, maximum shear ratio (MSR)			
19. Security Classif.	20. Security Classif.	21. No. of Pages: 283	22. Price

DISCLAIMER

ACKNOWLEDGEMENTS

This research was sponsored by the North Carolina Department of Transportation. The Steering and Implementation Committee was comprised of Shihai Zhang, P.E. (Chair); Josh Holland, P.E; Clark Morrison, Ph.D., P.E.; Andrew Wargo, Ph.D., P.E.; Christopher A. Peoples, P.E.; Wiley Jones, P.E.; David Snow; Brad Wall; James B. Phillips, P.E.; Neil Mastin, P.E.; and Mustan Kadibhai, P.E. These advisors have given invaluable direction and support to the North Carolina State University research team throughout the project.

EXECUTIVE SUMMARY

Background

As pavement systems age, distress types such as cracking, rutting, raveling, and polishing the surface aggregate impede the pavement's ability to carry the daily traffic demand safely, comfortably, and effectively. Each year, highway agencies spend billions of dollars on pavement repair and rehabilitation to keep roadways in an acceptable condition for the traveling public. A commonly cited statistic is that 94% of the over 2.27 million miles of roads throughout the United States are surfaced with asphalt materials. Therefore, the maintenance and rehabilitation of these roads consume a significant portion of highway agencies' transportation budgets.

Geosynthetics have been recognized as a cost-effective technology that can enhance pavement performance by providing reinforcement, stress relief, rutting and moisture resistance, good drainage, and minimal reflective cracking (Sudarsanan et al. 2015, 2018b). However, despite their proven effectiveness, geosynthetic products are not widely used in North Carolina due to the lack of proper specifications and product selection guidelines. Currently, the North Carolina Department of Transportation (NCDOT) does not have enough information, testing capability, and performance requirements to evaluate and select geosynthetic pavement interlayer products effectively for its transportation projects.

Objectives

The proposed research aims to develop performance testing methodologies and performance criteria that can be used in performance specifications and product selection guidelines by the NCDOT for geosynthetic products in pavement interlayer applications. The scope of the proposed research includes geosynthetic interlayer products that are placed between asphalt layers.

Materials and Methodology

This study's asphalt concrete (AC) loose mixture is RS9.5C with 40% reclaimed asphalt pavement (RAP). The five types of geosynthetic products investigated in this study are referred to as paving composite #1 (PC#1), paving composite #2 (PC#2), paving mat (PM), paving fabric (PF), and paving grid (PaG). A hot binder of performance grade (PG) 64-22 was used as the tack coat for all five geosynthetic products as well as control specimen (with no geosynthetic interlayer) and was applied at the rates recommended by the respective manufacturers. Table I-1 presents the tack coat rates used for these five geosynthetic products and control specimen.

Table I-1. Tack Coat Rates for Different Geosynthetic Types

Geosynthetic Type	**Control Specimen (no interlayer)**	**Paving Composite #1**	**Paving Composite #2**	**Paving Mat**	**Paving Fabric**	**Paving Grid**
Nomenclature	CS	PC#1	PC#2	PM	PF	PaG
Tack coat type	PG 64-22					
Application rate, gal/yd^2 (L/m^2)	0.03 (0.14)	0.14 (0.63)	0.33 (1.49)	0.12 (0.59)	0.08 (0.36)	0.23 (1.04)

The experimental design includes measuring the interface shear strength (ISS) and crack resistance capacity of geosynthetic-reinforced and unreinforced specimens in terms of the number of cycles to failure (N_f). The AC test specimens are double-layered and either unreinforced (the control specimen, referred to as 'CS' hereafter) or reinforced with one of the five geosynthetic products. The ISS and crack resistance were measured using a Modified Asphalt Shear Tester (MAST) and four-point bending beam fatigue test equipment, respectively. The binder bond strength (BBS) of the PG 64-22 binder was measured using a Pneumatic Adhesion Tension Testing Instrument (PATTI).

Figure I-1 (a), (b), and (c) present schematic illustrations of the MAST, PATTI, and four-point beam fatigue test set-ups, respectively. The MAST is a monotonic shear tester that is used to measure the ISS of a double-layered AC specimen with or without a geosynthetic interlayer (impregnated with asphalt) sandwiched between the layers. Each layer of the MAST test specimens was 38.1-mm (1.5-in.) thick. The MAST tests were carried out at various confining pressures, temperatures, and (monotonic) strain rates, as shown in Table I-2. The PATTI tests were carried out using PG 64-22 binder at six (6) different temperatures; the temperature data were then used to construct BBS mastercurves. Notched beam fatigue tests (NBFTs) were carried out using double-layered AC beam specimens with an 18-mm (0.7-in.) thick bottom layer and 36-mm (1.41-in.) top layer. A 7.5-mm (19/64-in.) deep and 2.5-mm (3/32-in.) wide notch was milled at the bottom of the beam specimens to mimic the existing crack damage. The NBFTs were conducted in controlled-strain mode at a minimum of four different strain levels for each type of geosynthetic-reinforced beam specimen, as shown in Table I-2. All the NBFTs were conducted at 23°C (73°F), which is the nominal average temperature in North Carolina, using the standard load frequency of 10 Hz.

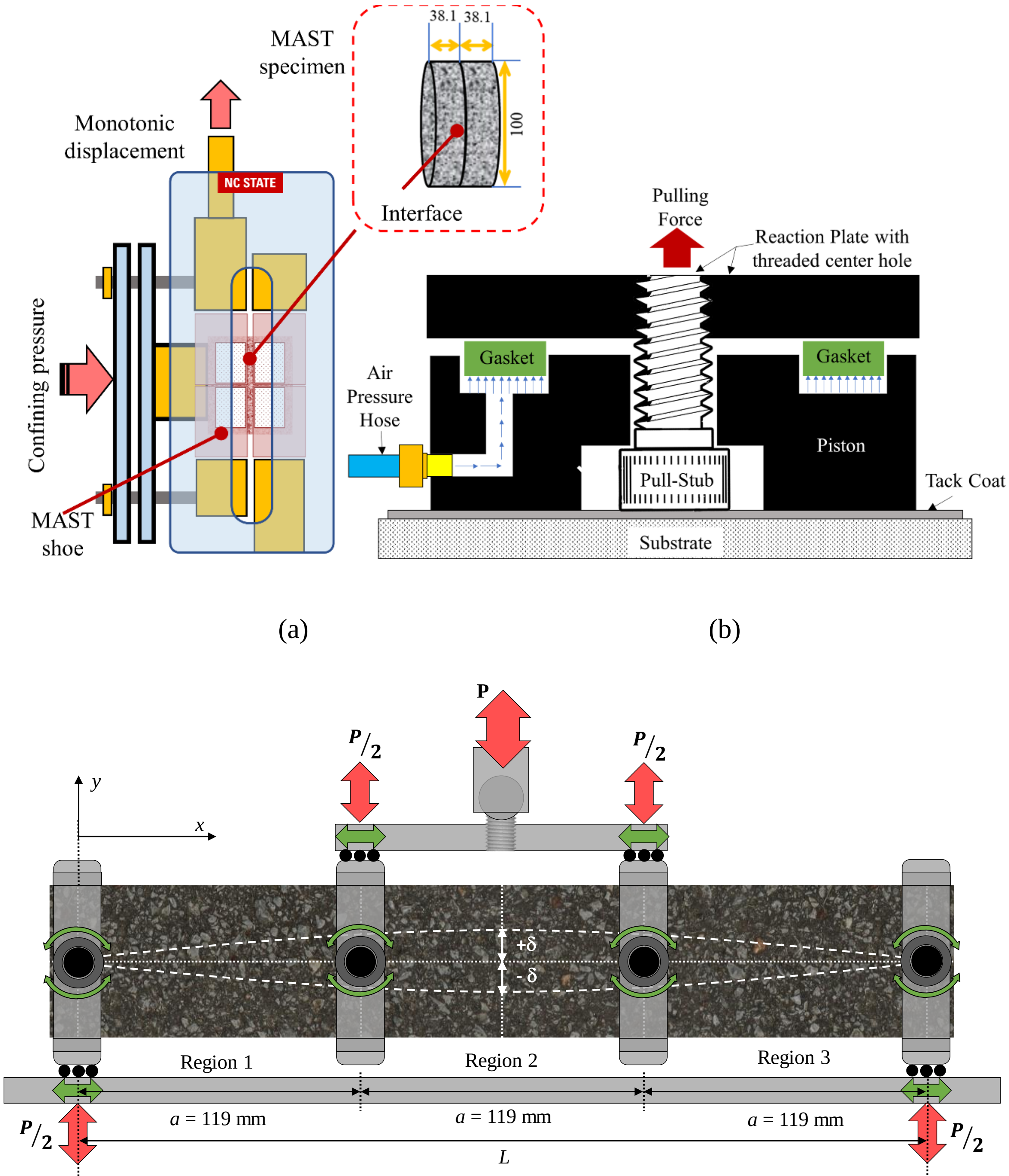

(c)

Figure I-1. Schematic illustrations for (a) MAST test set-up, (b) PATTI test set-up, and (c) four-point bending beam fatigue test set-up.

Table I-2. Test Conditions Used in Study

Test Type	**MAST Test**	**Notched Beam Fatigue Test**
Loading rate	5.08 mm/min (0.2 in./min)	10 Hz
Strain level	N/A*	180, 200, 250, 300, 350, 400 microstrain
Confinement	172 kPa (25 psi), 276 kPa (40 psi), 483 kPa (70 psi)	N/A
Temperature	23°C (73°F), 35°C (95°F), 54°C (129°F)	23°C (73°F)

Note: *Not applicable

The digital image correlation (DIC) technique was used to track and measure the deformations on the surface of the beam specimens, especially at areas around the interlayer and cracks. The DIC technique captures a sequence of images during the test. Vic-2D®, which is commercial two-dimensional (2-D) DIC analysis software developed by Correlated Solutions, Inc., was used to calibrate the scales, analyze the images, and calculate the displacements and strains on the surface of the specimens. The DIC analysis results were used to determine the interfacial debonding and vertical crack propagation throughout the AC beams subjected to the NBFTs.

Pavement response analysis of various test sections was undertaken by running numerical simulations using the three-dimensional finite element software, FlexPAVE™. The section dimensions of the simulated pavements represent those of a thick pavement structure used in North Carolina, as shown in Figure I-2. In an earlier NCDOT project, HWY-2013-04, the North Carolina State University researchers found that a thick pavement structure is more vulnerable to debonding at the AC layer interface than a thinner structure due to the greater shear stress that is induced in a thick pavement. Also, previous analyses of the maximum shear ratio (MSR) indicate that a high temperature, low speed, and heavy axle load constitute the worst field conditions that are conducive to debonding at the AC layer interface (Cho 2016, Kim et al. 2015b). Therefore, the thick pavement simulated in this study was loaded using a dual tire with an axle load of 80 kN (18 kips) at various vehicular speeds of 1.61 km/h (1 mph), 4.82 km/h (3 mph), 8.04 km/h (5 mph), 16 km/h (10 mph), 32.2 km/h (20 mph), and 72.4 km/h (45 mph). The test conditions also assume a vehicle in the braking state with a frictional coefficient of 0.55 at the speed under consideration. The pavement temperature was set at 50°C (122°F).

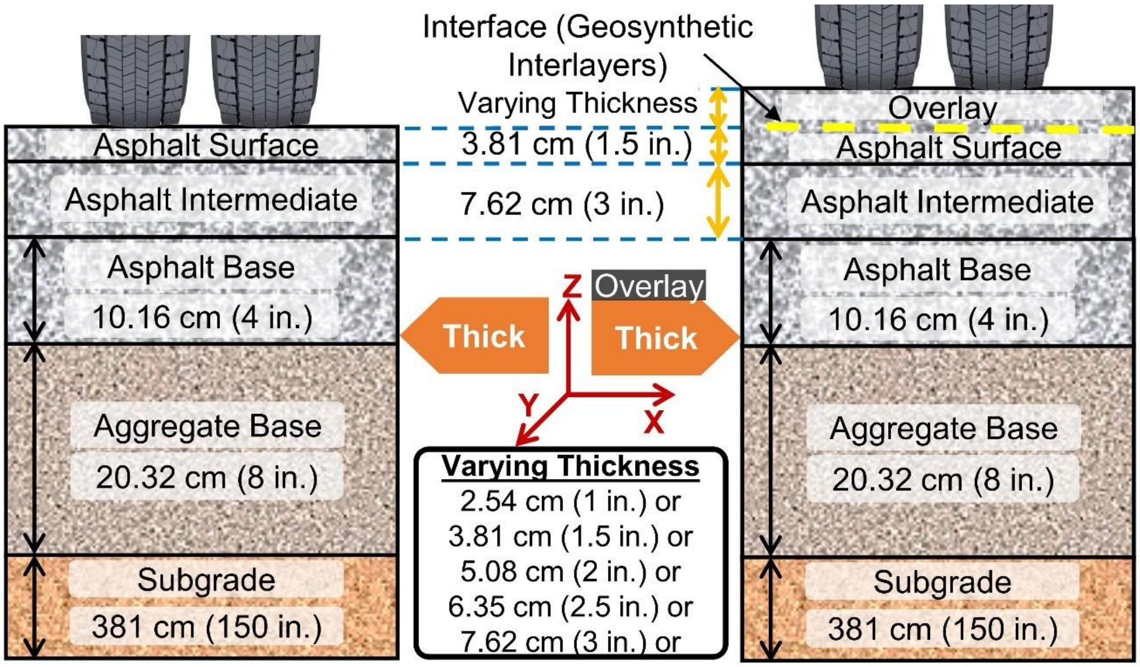

Figure I-2. Thick pavement section used for FlexPAVE™ simulations.

In addition to the FlexPAVE™ simulations, EverstressFE, which is three-dimensional linear elastic finite element software, was used to simulate the pavement responses of the same structure with various thickness and modulus combinations (~1500 combinations). The reason for performing this additional analysis is that EverstressFE allows pavement response simulations to be carried out in batch mode and generates bulk input files using an Excel VBA code, whereas FlexPAVE does not have this capability. The outcomes of nearly 1500 combinations helped to develop a predictive equation to estimate the tensile strain underneath a newly constructed overlay (at the interface) based on falling weight deflectometer (FWD) measurements of the existing damaged pavement. Table I-3 presents the simulation conditions.

Table I-3. Pavement Simulation Conditions Using EverstressFE

<table>
<tr><td rowspan="2">E_{overlay}</td><td>psi</td><td colspan="5">500,000</td></tr>
<tr><td>MPa</td><td colspan="5">3,447</td></tr>
<tr><td>T_{overlay}</td><td>in. (mm)</td><td colspan="5">1.5 (38.1), 3 (76.2), 4 (101.6)</td></tr>
<tr><td rowspan="2">E_{ac}</td><td>psi</td><td>700,000</td><td>500,000</td><td>300,000</td><td>100,000</td><td>50,000</td></tr>
<tr><td>MPa</td><td>4,826</td><td>3,447</td><td>2,068</td><td>689</td><td>345</td></tr>
<tr><td>T_{ac}</td><td>in. (mm)</td><td colspan="5">4 (101.6), 7 (177.8), 10 (25.4)</td></tr>
<tr><td rowspan="2">E_{abc}</td><td>psi</td><td>50,000</td><td>40,000</td><td>30,000</td><td>20,000</td><td>10,000</td></tr>
<tr><td>MPa</td><td>345</td><td>276</td><td>207</td><td>138</td><td>69</td></tr>
<tr><td>T_{abc}</td><td>in. (mm)</td><td colspan="5">8 (203.2)</td></tr>
<tr><td rowspan="2">E_{sg}</td><td>psi</td><td>20,000</td><td>15,000</td><td>10,000</td><td>5,000</td><td>2,500</td></tr>
<tr><td>MPa</td><td>138</td><td>103</td><td>69</td><td>34</td><td>17</td></tr>
<tr><td>T_{sg}</td><td>in. (mm)</td><td colspan="5">Semi-infinite 118 (300)</td></tr>
</table>

Note: $E_{overlay}$ is overlay modulus; $T_{overlay}$ is overlay thickness; E_{ac} is asphalt concrete layer modulus; T_{ac} is asphalt concrete layer thickness; E_{abc} is aggregate base course modulus; T_{abc} is aggregate base course thickness; E_{sg} is subgrade modulus, and T_{sg} is subgrade thickness.

Research Approach

Figure I-3 presents a flow chart of the research approach taken to develop guidelines for selecting geosynthetic products based on the product's ability to resist debonding and reflective crack propagation. The outcomes of this research approach are (1) the ranking of the various geosynthetic products in terms of the load-bearing capacity of the existing pavement for the overlay project and (2) the prediction of the expected mode of failure in the field, i.e., debonding or vertical reflective cracking.

Similarly, Figure I-4 shows the research approach in a flow chart form that aids in determining the appropriate tack coat for the selected geosynthetic product. The outcome of the research approach is the minimum BBS that the chosen tack coat should provide for the selected geosynthetic product, thereby avoiding the debonding distress. This project's experimental and numerical research has resulted in the geosynthetic interlayer selection guidelines shown in Figure I-5. The three-phase research effort that was undertaken to develop these step-by-step guidelines is described briefly in the subsequent text according to the three phases.

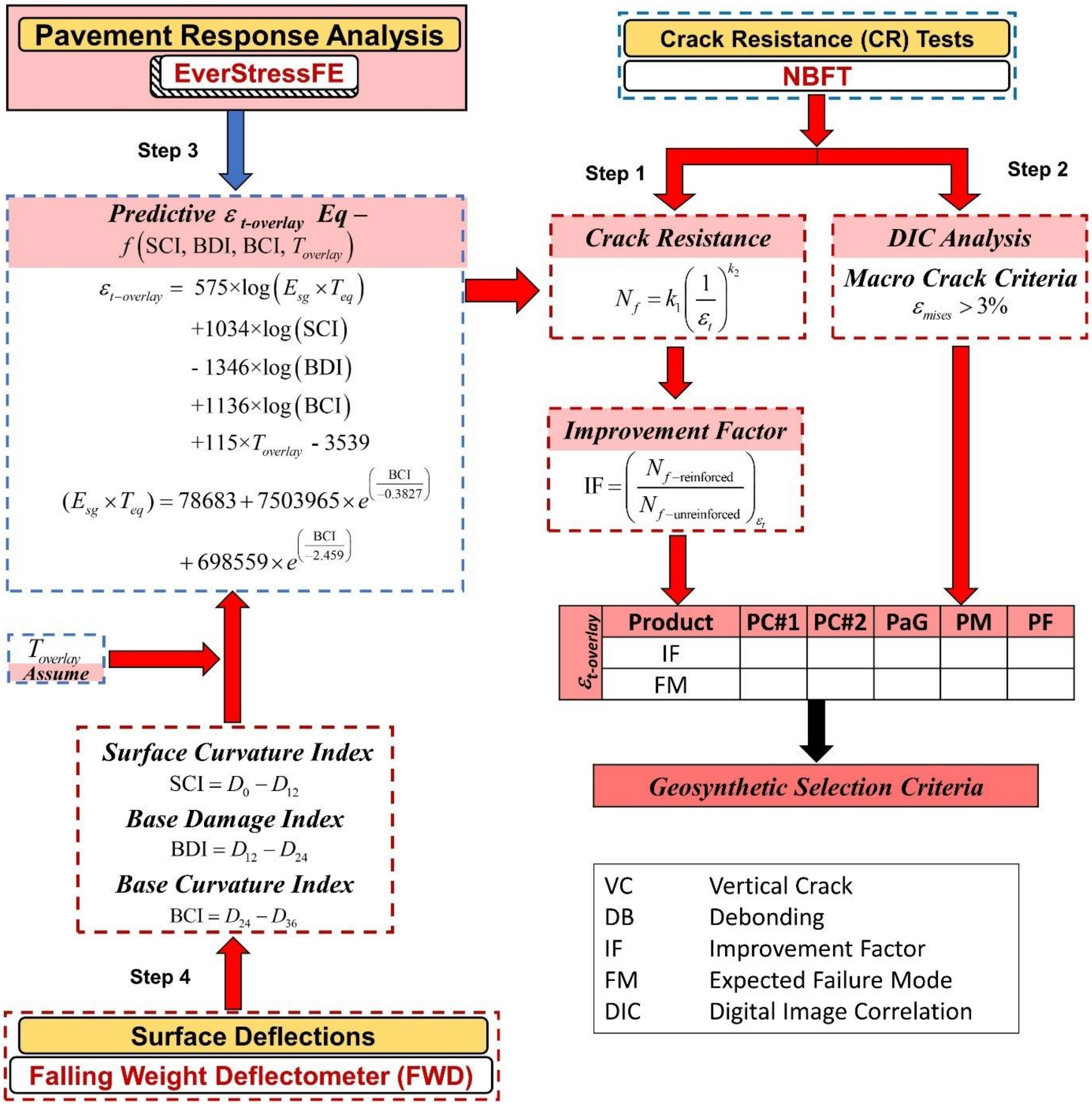

Figure I-3. Flow chart of research approach taken to develop geosynthetic product selection guidelines.

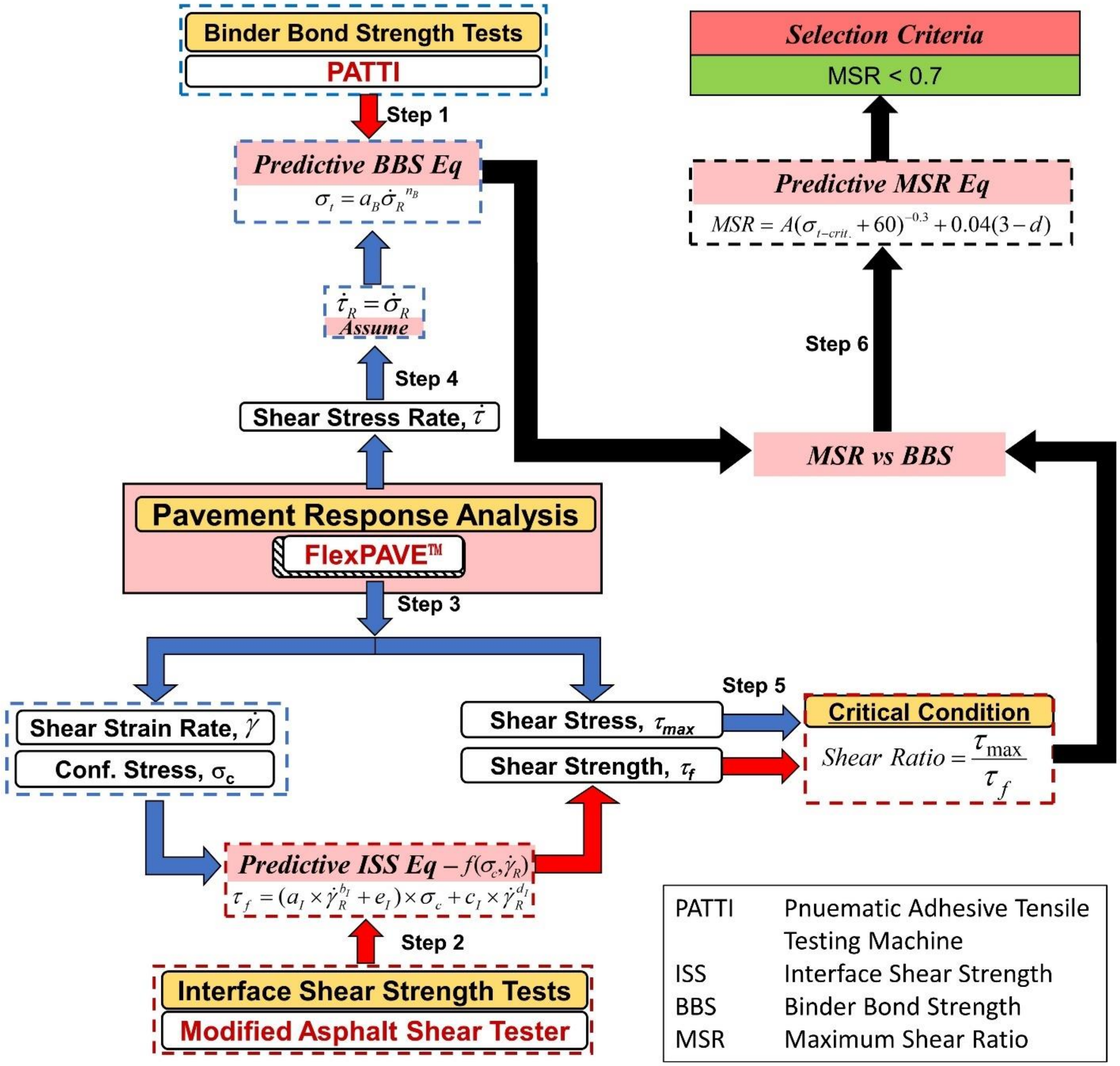

Figure I-4. Flow chart of research approach taken to develop tack coat selection guidelines.

Step 1: Measure the surface deflections.

Falling Weight Deflectometer (FWD)

Surface Curvature Index

$$\text{SCI} = D_0 - D_{12}$$

Base Damage Index

$$\text{BDI} = D_{12} - D_{24}$$

Base Curvature Index

$$\text{BCI} = D_{24} - D_{36}$$

SCI, BDI, BCI in mils

$T_{overlay}$ in inches

Ref. Temp is 23°C (73.4°F)

Step 2: Predict the tensile strain underneath the overlay.

Assume $T_{overlay}$ based on design

Predictive $\varepsilon_{t\text{-}overlay}$ Eq – $f\left(\text{SCI, BDI, BCI}, T_{overlay}\right)$

$$\varepsilon_{t-overlay} = 575\times\log\left(E_{sg}\times T_{eq}\right)+1034\times\log\left(\text{SCI}\right)-1346\times\log\left(\text{BDI}\right)$$
$$+1136\times\log\left(\text{BCI}\right)+115\times T_{overlay} - 3539$$

$$\left(E_{sg}\times T_{eq}\right) = 78683+7503965\times e^{\left(\frac{\text{BCI}}{-0.3827}\right)}+698559\times e^{\left(\frac{\text{BCI}}{-2.459}\right)}$$

Step 3: Select the geosynthetic products based on performance.

Geosynthetic Selection Criteria						
$\varepsilon_{t\text{-}overlay}$	**Products**	**PC#1**	**PaG**	**PM**	**PC#2**	**PF**
40 μ- 60 μ	**IF**	1.7	3.4	32.6	14.2	5.4
	FM	VC	VC	DB	DB	DB
60 μ- 80 μ	**IF**	2.5	2.5	4.1	6.4	5.1
	FM	VC	VC	DB	DB	DB
>80 μ	**IF**	3.3	2.0	1.0	3.5	5.0
	FM	VC	VC	VC	VC	DB/VC

Note: VC-Vertical Crack, DB-Debonding, IF-Improvement Factor, FM-Expected Failure Mode

Step 4: Select the tack coat based on geosynthetic product in use.

Tack Coat Selection Criteria						
Product		**PC#1**	**PC#2**	**PaG**	**PM**	**PF**
Min. BBS	kPa	280	860	455	860	280
	psi	41	125	66	125	41

Figure I-5. Step-by-step selection guidelines for geosynthetic type and tack coat materials.

Phase 1: Evaluate crack resistance in terms of the number of cycles to failure (N_f) and failure mode (debonding and/or vertical cracking) of various geosynthetic products based on laboratory test results.

In Phase 1, the crack resistance and failure mode of the different geosynthetic-reinforced beam specimens were measured using NBFTs. The NBFTs were carried out at different constant actuator tensile strain levels at 23°C (73°F). Chapter 6 of this report presents a critical evaluation of the NBFT results. Analysis of the outcomes led to establishing a relationship between tensile strain and crack resistance, presented here as Equation (I-1).

$$N_f = k_1 \left(\frac{1}{\varepsilon_t} \right)^{k_2} \tag{I-1}$$

where

N_f = number of cycles to failure, representing crack resistance,

k_1, k_2 = regression coefficients, and

ε_t = tensile strain in microns.

Table I-4 presents the parameters k_1 and k_2 for each of the five geosynthetic products and the 'no interlayer' scenario, i.e., the control specimen (CS). Based on the expected tensile strain underneath the overlay, a table was developed that comprises an improvement factor for the crack resistance that corresponds to each geosynthetic product. Figure I-5 contains this table under the description of Step 3. This table will help the designer to choose a product based on his/her engineering judgment.

Table I-4. Measured Parameters k_1 and k_2 Based on On-Specimen Tensile Strain versus Number of Cycles to Failure

Interlayer Type	**CS**	**PC#1**	**PaG**	**PM**	**PC#2**	**PF**
k_1	5.15×10^{-16}	1.42×10^{-11}	8.82×10^{-19}	5.09×10^{-38}	6.38×10^{-24}	8.03×10^{-16}
k_2	5.35	4.25	6.21	11.50	7.72	5.49
R^2	0.78	0.90	0.95	0.42	0.1	0.89

The DIC technique was employed to study the crack propagation patterns throughout the AC beams (Step 2 shown in Figure I-5). The digital images captured using the DIC technique were analyzed using Vic-2D® to determine the Von Mises strain. The Von Mises strain that is measured on the beam surface between the loading points can be used to determine the macro-crack development and, therefore, failure mode. In this study, a comparison between visual observations of the DIC images and Von Mises strain helped identify the macro-crack criterion, which is the point at which the Von Mises strain is greater than or equal to three percent. The debonding area was determined by selecting a region of constant area [150 mm^2 (0.23 in.^{2})] with the dimensions of 60 mm × 2.5 mm (2.36 in. × 0.1 in.) around the interface and then counting the number of pixels that satisfies the Von Mises macro-crack criterion. Correspondingly, the middle one-third area of the beam with a constant area [340 mm^2 (0.53 in.^{2})] and dimensions of 20 mm

× 17 mm (0.79 in. × 0.67 in.) was selected to count the pixels that were used to determine the vertical macro-crack area. The vertical and debonding cracked areas were then plotted against the number of load cycles. The percentages of the vertical and debonding cracked areas helped to determine the failure mode for each test condition.

Figure I-6 shows the Von Mises strain contours that were measured at the failure points during the NBFTs; Chapter 7 presents detailed results. A close investigation of the crack patterns shown in the DIC contour images during the NBFTs of the reinforced and unreinforced beam specimens reveals that each test failure can be classified into two failure modes, vertical cracking and debonding. That is, the energy that is input by repeated loading is dissipated by the creation of new surfaces through either vertical cracking or debonding. The results indicate that all five types of geosynthetic products delay vertical crack propagation but promote debonding. Also, the chance of vertical crack propagation is shown to be greater at higher tensile strain levels. Therefore, depending on the type of geosynthetic product and tensile strain tested, the propensities of vertical cracking and debonding vary.

Figure I-6 also shows that CS, irrespective of the tensile strain set during the NBFT, exhibits vertical cracking at failure. However, at the 180 μ actuator tensile strain level, CS at failure shows signs of debonding strain. The debonding strain becomes debonding cracking once it meets the macro-crack criterion. In all the geosynthetic product cases, the lower strain levels caused predominantly debonding failure, whereas the higher tensile strain levels led to vertical cracking failure. During the high tensile strain tests, both the top and bottom layers served as two independent beams. Decoupled beam behavior occurs once the crack that is generated from the notch passes through the bottom layer and touches the top layer, causing crack initiation at the bottom of the top layer. The delay in the crack initiation from the bottom of the top layer depends on the geosynthetic type and test strain level. This phenomenon indicates the existence of transition tensile strain, which is the tensile strain where the failure mode switches from debonding to vertical cracking when testing specimens at low to high tensile strain levels.

Figure I-6 shows that, in the cases of PC#1 and PaG, debonding failure can be observed only at an interlayer tensile strain that is less than 40 μ. The results for all the tests conducted above 40 μ interlayer tensile strain show vertical cracking failure. Therefore, the transition tensile strain is considered to be 40 μ. In the cases of PC#2 and PM, the transition tensile strain at the interlayer is approximately 70 μ. Note that the application rate recommended by the manufacturer for PC#2 is high compared to the other geosynthetic products due to product thickness. Hence, PC#2 requires a larger quantity of tack coat for complete impregnation. In addition, the thicknesses of PC#2 and PM are greater than the rest of the products. Factors such as the tack coat application rate, product stiffness, and product thickness help the geosynthetic product to absorb the stress near the crack tip, thereby arresting vertical cracking. Unfortunately, the data for PF are not sufficient to determine the transition tensile strain. All the PF tests resulted in debonding failure. Further study using PF at higher tensile strain levels could help identify the transition tensile strain. Therefore, in the geosynthetic interlayer selection guideline presented in Chapter 8, the overlay strain that is greater than the highest tested interlayer tensile strain for PF results in an unidentifiable debonding/vertical cracking failure mode. Any overlay strain that is above the transition tensile strain is defined as vertical cracking, whereas any overlay strain that is below the transition tensile strain is defined as debonding. These observations suggest that the failure mechanism in geosynthetic-reinforced overlays depends on the geosynthetic product type and the strain level at the bottom of the overlay. However, the selection of a suitable geosynthetic product should be made before the overlay is constructed, thus making it necessary to predict the tensile strain at the bottom of the overlay.

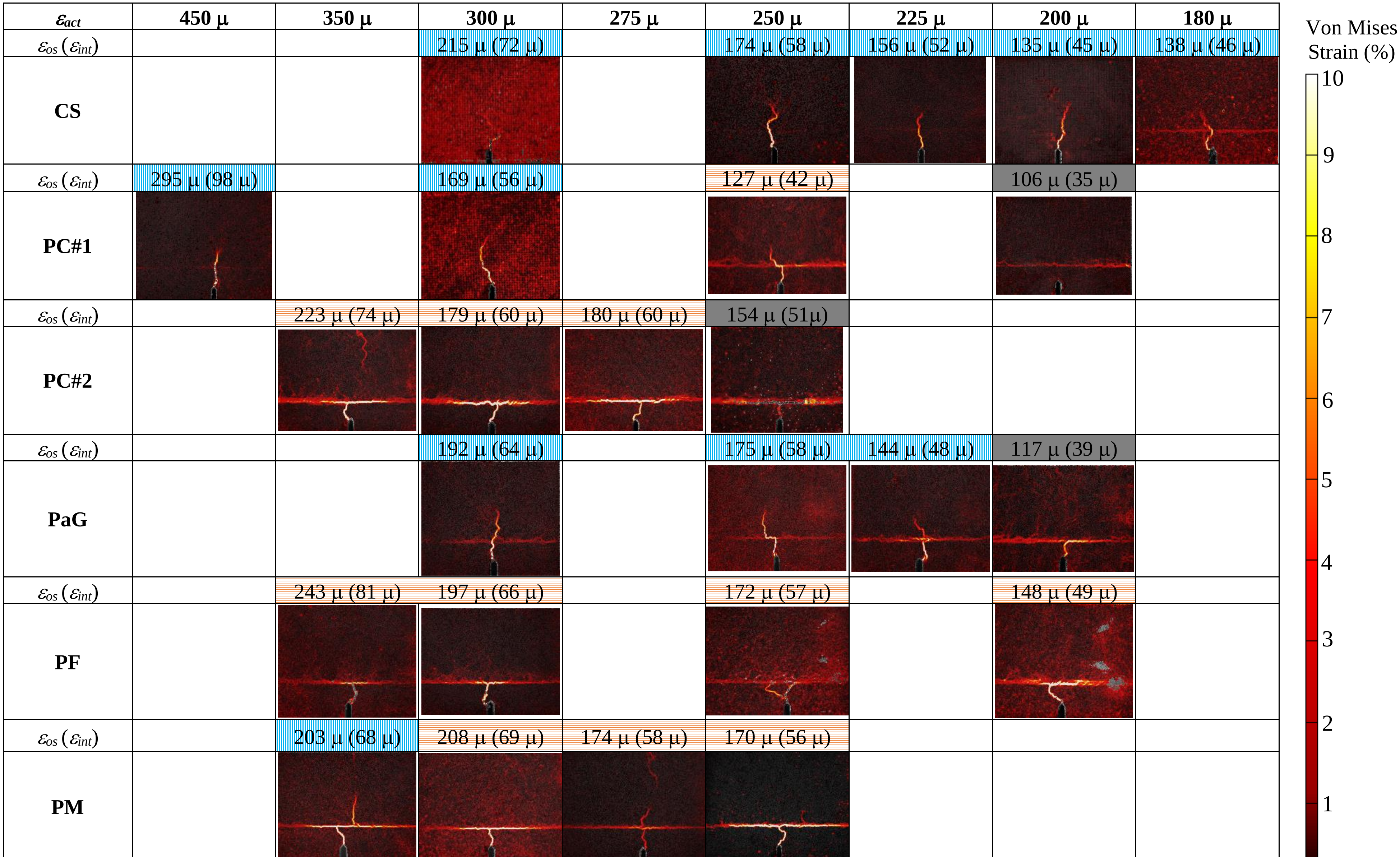

*Note: ε_{act} and ε_{os} are tensile strains calculated using actuator displacement and on-specimen displacement, respectively; and ε_{int} is tensile strain predicted at the interlayer based on on-specimen displacement ($\varepsilon_{int} = \varepsilon_{os}/3$). The failure mode of each test is identified by the shades in each cell with the following patterns:

Vertical Cracking   Debonding Cracking   Failure not recorded using *Stress* × *N*

Figure I-6. Von Mises contours for different interlayer geosynthetic-reinforced beam specimens at failure points in notched beam fatigue tests.

Phase 2: Perform numerical simulations of pavement responses.

Kim et al. (2000) demonstrated that the tensile strain at the bottom of an asphalt layer is closely related to the deflection basin parameters. In order to develop the relationship between the tensile strain at the bottom of an overlay and the deflection basin parameters, pavement response analysis using EverstressFE software for various thickness and modulus combinations (~1500 combinations) was carried out (Step 2 shown in Figure 4). Equation (I-2) was developed based on the numerical simulation study. $E_{sg}{\times}T_{eq}$ in Equation (I-2) is calculated using Equation (I-3). Chapter 4 provides details regarding these numerical solutions.

$$\begin{aligned}\varepsilon_{t-overlay} = \; & 575\times\log\left(E_{sg}\times T_{eq}\right)+1034\times\log\left(\mathrm{SCI}\right)-1346\times\log\left(\mathrm{BDI}\right)+1136\times\log\left(\mathrm{BCI}\right) \\ & +115\times T_{overlay} - 3539\end{aligned} \tag{I-2}$$

$$(E_{sg}\times T_{eq}) = 78683+7503965\times e^{\left(\frac{\mathrm{BCI}}{-0.3827}\right)}+698559\times e^{\left(\frac{\mathrm{BCI}}{-2.459}\right)} \tag{I-3}$$

where

SCI = $D_0 - D_{12}$, surface curvature index (mils),

BDI = $D_{12} - D_{24}$, base damage index (mils),

BCI = $D_{24} - D_{36}$, base curvature index (mils),

D_0, D_{12}, D_{24}, and D_{36} = deflections at the distances of 0 in., 12 in., 24 in., and 36 in. from the center of the FWD loading plate, respectively,

$T_{overlay}$ = thickness of the overlay (in.),

T_{ac} = thickness of the asphalt concrete layer (in.),

T_{abc} = thickness of the aggregate base course (in.),

$$T_{eq} = T_{(ac)eq}+T_{(abc)eq} = h_{ac}\sqrt[3]{\frac{E_{ac}}{E_{sg}}}+h_{abc}\sqrt[3]{\frac{E_{abc}}{E_{sg}}}$$

T_{eq} = equivalent thickness of the pavement structure (in.) in terms of subgrade modulus,

E_{ac} = Young's modulus of the asphalt concrete layer (psi),

E_{abc} = Young's modulus of the aggregate base course (psi),

E_{sg} = Young's modulus of the subgrade (psi).

Equations (I-2) and (I-3) allow the prediction of the tensile strain at the bottom of the overlay ($\varepsilon_{t\text{-}overlay}$) using FWD measurements taken from the existing pavement and the thickness of the overlay ($T_{overlay}$).

Phase 3: Determine the minimum binder bond strength for the different geosynthetic product types.

Figure I-4 presents a flow chart of the research approach that was taken in a previous tack coat study, RP 2018-13 *Development of a Tack Coat Quality Control Program for Mitigating Delamination in Asphalt Pavement Layers*, to control the debonding distress. The same approach was taken in this project to determine the minimum tack coat BBS values for the different geosynthetic interlayer types. The experimental design for this research approach calls for measuring the ISS using the MAST and measuring the BBS using PATTI. The MAST test is carried out at three strain rates and temperatures to build the ISS mastercurve and an ISS predictive equation. Similarly, PATTI is used to measure the BBS of a binder at various temperatures to build the BBS mastercurve and a BBS predictive equation. Further, the braking event of a truck is simulated numerically using FlexPAVE^{TM}, and the *in situ* strain rate and stress rate at the interlayer are predicted. Consequently, the predicted strain and stress rates help in calculating the field ISS and BBS that are experienced by the interlayer using the predictive ISS and BBS equations developed based on experimental data. The outcomes show a universal relationship between the ISS and BBS experienced by the interlayer. The end result of this approach is the minimum BBS value that serves as the criterion for acceptance of the tack coat that corresponds to a specific paving geosynthetic product. The selected tack coat and corresponding geosynthetic product are fully expected to provide sufficient ISS to resist shear stress in the field, thereby avoiding debonding failure.

Figure I-7 shows the failure envelopes of the different geosynthetic products. The MSR versus BBS curves are based on the steps described in Figure I-4. The cut-off value for MSR acceptance is set at 0.7, which is a value proposed for tack coat selection alone (no interlayer). The results show that the MSR value increases, i.e., the shear strength reduces, with different geosynthetic product inclusions between the AC layers. The developed selection criteria will encourage engineers to use a better tack coat than PG 64-22 (used in the present study) with a minimum BBS value, provided in Stage 4 of Figure I-3. The current results show that a better tack coat should improve the performance of the geosynthetic products, similar to the performance of the no-interlayer condition in resisting the debonding distress.

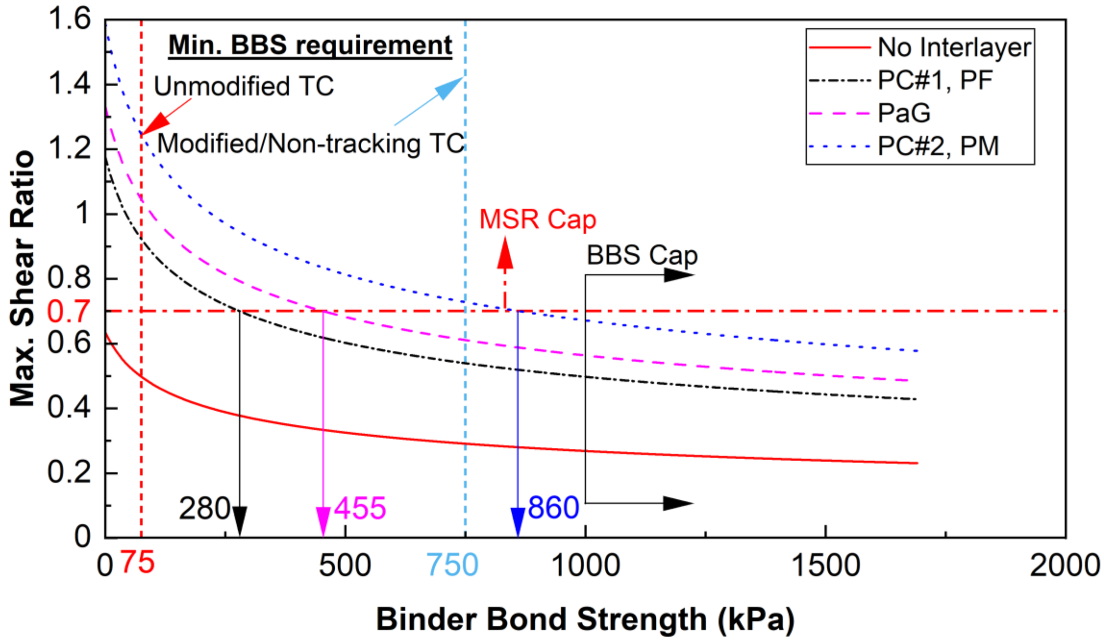

Figure I-7. Failure envelopes showing the minimum binder bond strength required for tack coat (TC) selection.

The current study proposes a threshold shear test protocol to evaluate each geosynthetic product's potential to resist debonding. The confined shear test should be conducted at 50°C (122°F), 5.08 mm/min (0.2 in./min) at the actuator deformation rate (on-specimen reduced shear strain rate of 2.6×10^{-4}/sec) and 275 kPa (40 psi) confining pressure. Based on the MSR information, the minimum required shear strength for acceptance of the geosynthetic-reinforced specimens is 470 kPa (68 psi). Also, for quality control purposes in the field, threshold shear tests should be performed using field cores. Once measured, the ISS must be substituted in Equation (I-4) to verify the acceptance criterion.

$$MSR = \frac{210}{0.6\times ISS} - 0.05 \leq 0.7 \qquad \text{(I-4)}$$

where

MSR = maximum shear ratio, and

ISS = interface shear strength in kPa.

Major Conclusions

This report proposes a framework that practitioners can follow to identify the improvement factors provided by various geosynthetic products as well as the products' failure modes. The results from this study's laboratory tests were linked to field-measured deflections, aided by a regression equation that was developed based on numerical simulations of pavement responses. The findings of this study will help engineers to select the best-fit geosynthetic product based on existing pavement conditions. The study also proposes a minimum BBS requirement for the tack coat that best corresponds to the selected geosynthetic product.

The following conclusions can be drawn based on the experimental work and computational analyses conducted in this research.

Experimental Work Based on Test Results

Interface shear strength tests

The use of the t-T superposition principle to establish ISS and BBS mastercurves was verified in this study. The t-T shift factors determined from DSR measurements of the asphalt binder (PG 64-22 in this study) were used successfully to develop ISS and BBS mastercurves.

- The predictive model equation for ISS developed by Cho (2016) was fitted to obtain coefficients for the double-layered AC specimens with five different geosynthetic types and one unreinforced (CS) condition used in this study. This predictive model can predict the shear strength at a specific pavement depth of interest, which then can be compared against the shear stress at that depth predicted from FlexPAVE™.
- In comparison to the unreinforced specimen (CS), the presence of any geosynthetic product under any test conditions reduced the ISS and increased the chance of interfacial debonding.
- The ISS decreased with an increase in test temperature and a decrease in strain rate. This finding applies to all the tested MAST specimens, independent of geosynthetic product type.
- The shear strength reduced 40% to 65% with a change in temperature from 23°C (73°F) to 54°C (129°F). The difference in the shear strength of the different geosynthetic-reinforced specimens decreased with an increase in the testing temperature.
- Three different confining pressures were applied to determine the effects of confinement on the ISS. The results clearly indicate that ISS is proportional to the applied confinement pressure. The mobilization of aggregate interlocking resulted in increased frictional resistance to the applied shear stress. Therefore, the shear strength increased with an increase in confining pressure. However, the rate of the ISS increase with confining pressure is a function of the geosynthetic product type.
- No effect of the tack coat application rate on the ISS of the geosynthetic-reinforced specimens was readily apparent. Statistical analysis of the ISS data generated in this study also supports the visual observations.
- The bond at the interface will deteriorate with environmental impacts and traffic loading. Hence, a safety factor should be considered to take into account field conditions. The acceptance MSR was set at 0.7 based on findings from this study and NCDOT RP2018-13.
- According to the MSR analysis results, threshold shear strength tests for the evaluation of geosynthetic-reinforced products should be conducted at 50°C (122°F), 5.08 mm/min (0.2 in./min) actuator deformation rate (on-specimen reduced shear strain rate of 2.6×10^{-4}/sec), and 275.8 kPa (40 psi) confining pressure. Based on the MSR information, the minimum required shear strength for geosynthetic-reinforced specimens under these conditions is 470 kPa (68 psi).

Notched beam fatigue tests

- All the geosynthetic products studied can improve crack resistance (in terms of reducing the number of cycles to failure) under in-service conditions (typical tensile strain expected in the field).
- The tack coat application rate affects the pavement's crack resistance whereby an increase in the tack coat rate extends the fatigue life. However, this conclusion is based on three application rates that were applied only to CS and PC#1. Further study is required to confirm the observed results.
- Several failure criteria were applied to the outcome of each NBFT to identify the failure cycle number. However, the stress × N failure criterion eventually was selected for determining failure due to its ease of application and non-dependency on on-specimen deformation measurements. Moreover, the N_f values from the stress × N failure criterion are comparable to those determined by other available failure criteria.
- Full-field displacement and strain contours obtained through the NBFTs using the DIC technique revealed that the failure of geosynthetic-reinforced asphalt beam specimens can be classified into two failure modes, vertical cracking and debonding. The energy that is input by repeated loading is dissipated by the creation of new surfaces through vertical cracking and debonding. Therefore, the increase in interfacial damage effectively mitigates vertical cracking. However, this behavior is not necessarily beneficial to pavement life because the interlayer products that have a greater tendency for interfacial damage will cause debonding pavement failure.
- Strong bonds between geosynthetic interlayers and surrounding asphalt layers that can be provided by high quality tack coat not only prevent the debonding but also allow the full use of the strength of the geosynthetic interlayers in mitigating the reflective cracking.
- DIC analysis revealed that interlayer movement can be significant depending on the geosynthetic product type. Typically, thick and continuous geosynthetic products exhibited greater interlayer movement than thinner and grid-type products.
- When the tip of a vertical crack in the bottom layer nearly reached the interface, the interface damage (if any) started to grow. However, when the vertical crack propagation reached the top layer, i.e., the crack initiated from bottom of top layer, the energy input by the repeated loading was mostly used to propagate the vertical crack and therefore the severity of the interfacial damage did not change significantly.
- During the NBFTs, the failure modes for the PC#1- and PaG-reinforced beam specimens were observed to change from debonding cracking at a low strain level to vertical cracking at a high strain level. Hence, depending on the strain level chosen for testing, the failure mode could change.
- For all the geosynthetic product cases, lower strain levels led to predominantly debonding failure whereas higher tensile strain levels led to vertical cracking failure. During the high tensile strain tests, both the top and bottom layers served as two independent beams due to local debonding at the crack tip. Therefore, vertical cracking at high tensile strain levels could be mitigated if debonding is minimized. This observation emphasizes the importance of sufficient bond strength at the interface of geosynthetic-reinforced asphalt overlays, which is needed to capture the full benefits of geosynthetic products and mitigate reflective cracking.

- The areas of debonding cracking and vertical cracking that were measured on the geosynthetic-reinforced beam specimens corresponded closely to the stress degradation rate that can be measured from load responses without the DIC technique. However, insufficient data led to the inability to establish a relationship. Hence, future research is recommended that could help identify the failure mode without the aid of the DIC technique.

Experimental Work Based on Numerical Simulations

FlexPAVE™ analysis

The FlexPAVE™ analysis of various overlay pavement structures, traffic speeds, temperatures, and overlay thicknesses suggest the following conclusions.

- In this research, 'shear ratio' is defined as the ratio between the shear stress at the interface under vehicular loading and the ISS. The MSR is determined by comparing the shear ratios at various locations in a pavement structure that are determined using the shear stress calculated from FlexPAVE™ and the shear strength calculated from the ISS predictive model. A higher MSR implies greater potential for interface debonding that is due to repeated vehicular braking. An MSR that is greater than one indicates that debonding failure would occur due to the single braking of a dual tire at 80 kN (18 kips). The tack coat considered in this study (PG64-22 binder) generated sufficient shear strength to resist shear stress in the field, based on the numerical simulations. Hence, the potential for interface debonding using this tack coat is minimal.
- The MSR typically is found at the center of the longitudinal axis of the tire at 10 cm (3.9 in.) to 14 cm (5.5 in.) in front of the tire. The MSR location depends on the depth of the interface and the tack coat type.
- The worst field conditions expected in North Carolina for an interface to resist debonding during its service life are as follows: a thick pavement with a dual tire at 80 kN (18 kips) under the braking condition at a speed of 1 mph (1.61 km/hour) at 50°C.
- The difference in the MSR values among different structures typically is between 2.5% and 3.5 percent. The pavement structures considered for the current study did not significantly affect the MSR because shear debonding is a near-the-surface phenomenon.

EverstressFE linear elastic model analysis

- The batch analysis of 1500 combinations of pavement structures with various elastic modulus values and thicknesses was undertaken to predict the overlay tensile strain based on FWD measurements of the existing pavement.
- All the analyses were carried out assuming the temperature of 23°C (73°F). Hence, the deflection measurements had to be corrected for temperature using BELLS equation and the NCDOT deflection correction method.
- The predictive equation for overlay tensile strain is a function of the SCI, BDI, BCI, and $T_{overlay}$. Hence, this approach is not dependent on any back-calculation software to identify the elastic modulus and then analyze simulated responses of an overlay pavement.

Minimum required binder bond strength

- Rigorous numerical simulations for different field conditions helped to develop a universal relationship between the ISS and BBS, followed by the MSR versus BBS relationship. The MSR-BBS relationship is presented as a function of interface depth and was used to determine the BBS threshold values for different interface depths.
- A methodology that was developed under the NCDOT RP 2018-13 project as part of a tack coat quality control program is used in this study to ensure the appropriate bonding of tack coat and provide acceptable field performance. This methodology uses PATTI to measure the BBS of the tack coat material tested at 50°C (122°F). The required stress rate during the test must be maintained at between 90 psi/sec and 115 psi/sec (620 kPa/sec and 792 kPa/sec, respectively).
- Based on the MSR-BBS relationship, the BBS value at 50°C (122°F) that corresponds to the MSR value of 0.7 can be found, as presented in Figure I-7. Therefore, if the BBS of a tack coat at 50°C (122°F) is above that shown in Figure I-5, then the tack coat can be accepted for application with the corresponding geosynthetic product at the manufacturer's recommended rate.
- Employing the selected tack coat that corresponds to a specific geosynthetic product will improve overall pavement performance. Safavizadeh (2015) also reported that a better-performing tack coat will help geosynthetic-reinforced beam specimens exhibit superior performance.

Step-by-Step Procedure for Geosynthetic and Tack Coat Selection Guidelines

Engineers should follow the developed step-by-step process presented in Figure I-5 to select a best-fit geosynthetic product based on expected pavement performance. The appropriate tack coat can then be selected based on the minimum BBS required for the geosynthetic product selected. The main aim of proposing the selection procedure for geosynthetic products is to build a solid research framework. More laboratory and field data will help to reinforce the current approach and eventually assist in developing numerical simulation models.

Step 1: Measure surface deflections.
The existing pavement conditions must be evaluated using an FWD. The deflections must be measured at D_0, D_{12}, D_{24}, and D_{36}. D_r is the surface deflection, and r is the distance from the load center (in.). The measured deflections are used to determine the SCI, BDI, and BCI.

Step 2: Predict the tensile strain underneath the overlay.
The overlay tensile strain predictive equation shown in the Equation (I-2) is a function of the SCI, BDI, BCI, and overlay thickness ($T_{overlay}$). The SCI, BDI, and BCI are measured in Step 1, so the only unknown factor is $T_{overlay}$. The designer must assume a minimum $T_{overlay}$ of 1.5 in. or more. Then, the parameters must be substituted in Equations (I-2) and (I-3) to predict the overlay tensile strain. If the predicted overlay tensile strain is negative because the neutral axis of all the asphalt layers is below the bottom of overlay, then the interface is in the compressive stress state. This case indicates that the existing pavement under the overlay is in good condition. In this case, the selection of the geosynthetic product is at the engineer's discretion. The engineer needs to note that the initial compressive state of the interface would eventually transform to the tensile state as the damage progresses with time and traffic.

If the predicted overlay tensile strain is greater than 100 μ, then the pavement is severely damaged, in which case milling the surface layer followed by a leveling course is recommended before installing the geosynthetic product. Alternatively, increasing the overlay thickness also reduces the tensile strain. If increasing the overlay thickness reduces the interface tensile strain below 100 μ, then the geosynthetic product can be used after standard crack fill and patchwork. These suggestions are based on laboratory test results; a thorough field study based on these recommendations would refine the findings.

Step 3: Select the geosynthetic product based on performance.
Determining the crack resistance of the various geosynthetic products investigated in this study helped to develop the selection table shown in Step 3 of Figure I-5. The improvement factor reported in the table is the ratio of the crack resistance of a geosynthetic-reinforced AC beam at a specific strain level to that of an unreinforced AC beam. The DIC study helped identify the failure mode between debonding and vertical cracking. The presence of vertical cracking accelerates damage by allowing moisture to infiltrate the pavement structure. In general, debonding failure is more prevalent than vertical crack failure.

The strain range in Step 3 is selected based on the tensile strain at the bottom of the overlay that is predicted in Step 2. The improvement factor of the various products for the selected strain range is provided, and the product can then be chosen based on the improvement factor for the predicted strain value in a given project. Note, however, that the improvement factor is insignificant for various products within a certain range of tensile strain. Hence, the engineer's judgment regarding product selection must be based on the cost-benefit ratio. The proposed selection table (Step 3 in Figure I-5) is based on limited laboratory test results. Hence, relying on field improvement factor values is unrealistic. However, the table may offer a ranking pattern of the geosynthetic products' performance for different field conditions.

Step 4: Select the tack coat based on the geosynthetic product selected.
The tack coat is selected based on the minimum BBS of the geosynthetic product selected. PATTI is used to measure the BBS of the tack coat material at 50°C (122°F). The required stress rate during the test must be maintained at between 90 psi/sec and 115 psi/sec (620 kPa/sec and 792 kPa/sec, respectively). If the BBS value meets the minimum BBS reported in Step 4 of Figure I-5, then the tack coat should be applied at the application rate recommended by the manufacturer. The minimum BBS value is based on the MSR of 0.7, which is the value used for tack coat selection (without geosynthetics). A previous NCDOT research project found through laboratory study that the crack resistance of geosynthetic-reinforced products increases with a better-quality tack coat (i.e., greater BBS). The crack resistance of all the geosynthetic products in the current study was evaluated using PG 64-22 binder as the tack. The typical BBS value of PG 64-22 binder is between 75 kPa (11 psi) and 90 kPa (13 psi). However, the recommended tack coat requires a BBS value that is at least three to eight times that of the PG 64-22 binder. Hence, the improvement factor proposed in Step 3 is expected to be observed in the field. Nonetheless, the superiority of one product over another with a better tack coat cannot be confirmed by the current study and remains a topic for future research.

TABLE OF CONTENTS

Chapter 1. Introduction 26
1.1 Background 26
1.2 Research Needs and Significance 26
1.3 Research Objectives and Scope 27
1.4 Research Approach 29
1.5 Report Organization 31
Chapter 2. Materials and Properties 32
2.1 Asphalt Concrete Mixture 32
2.2 Dynamic Modulus (|*E**|) Test of Asphalt Mixture 34
2.3 Tack Coat 37
2.4 Dynamic Shear Rheometer (|*G**|) Test of Tack Coat Binder 38
2.5 Geosynthetic Products 40
Chapter 3. Test Methodology 43
3.1 Interlayer Shear Strength Tests 43
3.1.1 Laboratory Fabrication of MAST Test Specimens 43
3.1.2 Air Void Study 43
3.1.3 Modified Advanced Shear Tester Tests 45
3.2 Crack Resistance Tests 49
3.2.1 Laboratory Fabrication of Beam Specimens 49
3.2.2 Air Void Study 49
3.2.3 Four-Point Bending Beam Fatigue Test 56
3.3 Binder Bond Strength Test 58
3.3.1 Pneumatic Adhesion Tensile Testing Instrument (PATTI) Test 58
3.3.2 Binder Bond Strength Test Methodology Using PATTI 59
3.3.3 Failure Modes in PATTI Test 63
3.4 Calibration of Measurement Systems for Study Test Devices and Methods 64
3.4.1 Digital Image Correlation Technique 64
3.4.2 Calibration of DIC System for MAST Testing 65
3.4.3 Calibration of DIC System for Notched Beam Fatigue Testing 66
3.4.4 Calibration of Deflections for Notched Beam Fatigue Testing 69
Chapter 4. Numerical Simulations of Pavement Responses 75
4.1 Background 75
4.2 Parameters Used for Numerical Simulations 75

4.2.1 Structure Information ... 75
4.2.2 Material Parameters for Each Pavement Layer ... 76
4.2.3 Climate Data ... 77
4.2.4 Traffic Data ... 78
4.2.5 Tire-Pavement Contact Pressure Configuration ... 78
4.3 FlexPAVE™ Analysis Output ... 79
4.4 Parameters Used in EverstressFE Simulations ... 82
4.4.1 Structure Information and Material Parameters ... 83
4.4.2 Climate Data ... 83
4.4.3 Tire Load and Configuration ... 84
4.5 EverstressFE Analysis Output ... 84
Chapter 5. Interface Shear Strength Test Results and Discussion ... 88
5.1 Interface Shear Strength ... 88
5.1.1 Effects of Geosynthetic Interlayer Type on Interface Shear Strength ... 91
5.1.2 Effect of Tack Coat Application Rate on Interface Shear Strength ... 94
5.1.3 Effect of Temperature on Interface Shear Strength ... 97
5.1.4 Effect of Confining Pressure on Interface Shear Strength ... 100
5.2 Statistical Analysis of the Effect of Tack Coat Application Rate ... 104
Chapter 6. Notched Beam Fatigue Test Results and Discussion ... 107
6.1 Fatigue Models and Failure Criteria ... 107
6.1.1 Basic Fatigue Models ... 108
6.1.2 Different Types of Failure Criteria ... 110
6.2 Crack Resistance Capacity of Geosynthetic-Reinforced Beam Specimens ... 131
6.3 Effect of Tack Coat Application Rate on Crack Resistance Capacity ... 138
Chapter 7. Digital Image Correlation Test Results and Discussion ... 142
7.1 Background ... 142
7.2 Digital Image Correlation System Terminology ... 142
7.3 Principle Behind Digital Image Correlation ... 144
7.4 Strain Tensors and Associated Criteria ... 146
7.5 Tracking Crack Propagation Using Digital Image Correlation ... 148
7.6 Quantitative Analysis of DIC Images ... 160
Chapter 8. Development of Selection Criteria and Guidelines for Geosynthetic Products and Corresponding Tack Coats ... 168
8.1 Development of Predictive Model for Crack Resistance Capacity ... 168
8.2 Prediction of Tensile Strain at the Bottom of Asphalt Overlay ... 170

8.3 Temperature Correction for Deflections at Radial Offset Distance 173
8.4 Development of Geosynthetic Product Selection Guidelines Based on Performance . 174
8.5 Development of Predictive Model for Interface Shear Strength 175
8.6 Development of Predictive Model for Binder Bond Strength.................................... 176
8.7 Identification of Interface Debonding Potential for Tack Coats Based on Numerical Simulation 177
8.8 Developing the Maximum Shear Ratio Failure Envelope 183
8.8.1 Measuring Mix Parameter *A* 186
8.8.2 Measuring Binder Bond Strength 186
8.8.3 Quality Control Using Confined Interface Shear Strength Test 187
8.9 Tack Coat Purchase Criteria.. 188
8.10 Geosynthetic and Tack Coat Selection Guidelines 189
Chapter 9. Conclusions and Recommendations for Future Work 192
9.1 Experimental Work Based on Test Results... 192
9.1.1 Interface Shear Strength Tests 192
9.1.2 Notched Beam Fatigue Tests 193
9.2 Experimental Work Based on Numerical Simulations 194
9.2.1 FlexPAVE™ Analysis 194
9.2.2 EverstressFE Linear Elastic Model Analysis... 195
9.3 Minimum Required Binder Bond Strength 195
9.4 Step-by-Step Guidelines for Geosynthetic and Tack Coat Selection.......................... 195
9.5 Recommendations for Further Research 195
REFERENCES 197
Appendix A. Literature Review 208
A.1. Reflective Cracking... 208
A.2. Function of Geosynthetics.. 209
A.2.1 Reinforcing .... **Error! Bookmark not defined.**
A.2.2 Stress Relieving .... **Error! Bookmark not defined.**
A.2.3 Water Barrier .... **Error! Bookmark not defined.**
A.3. Debonding Problem... 209
A.4. Factors Influencing the Bonding 210
A.4.1 Tack Coat Type.. 210
A.4.2 Tack Coat Application Rate.. 210
A.4.3 Curing Time 211
A.4.4 Surface Texture.. 212

A.5. Test Methods 212
A.5.1 Ancona Shear Testing Research and Analysis (ASTRA) Device 213
A.5.2 Louisiana Interlayer Shear Strength Tester (LISST) 214
A.5.3 Sapienza Direct Shear Testing Machine (SDSTM) 214
A.5.4 Advanced Shear Tester (AST) 215
A.5.5 Modified Asphalt Shear Tester (MAST) 216
A.6. Bonding of Geosynthetic-Reinforced Interlayer 218
A.7. Critical Summary 219
Appendix B. Beam Bending Theory and Four-Point Beam Bending Stress/Strain 221
B.1. Bending strain 221
B.2. Bending stress 223
Appendix C. Sinusoidal fitting procedure 229
Appendix D. Laboratory Fabrication of MAST Test Specimens 232
Appendix E. Laboratory Fabrication of Beam Specimens 247

LIST OF FIGURES

Figure I-1. Schematic illustrations for (a) MAST test set-up, (b) PATTI test set-up, and (c) four-point bending beam fatigue test set-up. viii
Figure I-2. Thick pavement section used for FlexPAVE™ simulations. x
Figure I-3. Flow chart of research approach taken to develop geosynthetic product selection guidelines. xii
Figure I-4. Flow chart of research approach taken to develop tack coat selection guidelines. ... xiii
Figure I-5. Step-by-step selection guidelines for geosynthetic type and tack coat materials. xiv
Figure I-6. Von Mises contours for different interlayer geosynthetic-reinforced beam specimens at failure points in notched beam fatigue tests. xviii
Figure I-7. Failure envelopes showing the minimum binder bond strength required for tack coat (TC) selection. 3

Figure 1-1. Flow chart of research approach taken to develop geosynthetic product selection guidelines. 29
Figure 2-1. Aggregate gradation of RAP-40 mixture. 32
Figure 2-2. (a) Removing asphalt concrete loose mix in cloth bag from collection bucket, (b) removing loose mix from cloth bag, and (c) loose mix inside metal bucket. 33
Figure 2-3. (a) Separation pans and (b) cloth bags for preparing a well-mixed asphalt concrete mixture. 33
Figure 2-4. Linear relationship between air void content and weight of gyratory-compacted samples. 35
Figure 2-5. Dynamic modulus mastercurve for RS9.5C RAP-40. 35
Figure 2-6. Dynamic shear modulus mastercurves for PG 64-22 binder tack coat. 39
Figure 2-7. Geosynthetic samples: (a) PC#1, (b) PC#2, (c) PaG, (d) PM, and (e) PF. 42
Figure 3-1. Target and achieved air void content relationship for different layers. 44
Figure 3-2. Loading configurations of MAST test set-up. 45
Figure 3-3. Gluing procedure for MAST test specimen: (a) bottom shoes tightened on gluing jig, (b) application of glue on bottom shoes, (c) specimen placement on bottom shoes, (d) upper shoe installation above specimen, (e) specimen with all shoes in place, and (f) trimming extra glue from shoe edges. 46
Figure 3-4. Preparation of speckled paper for DIC image capture: (a) spray painting paper, (b) finished speckled paper, and (c) speckled paper on MAST shoes to track on-specimen displacement using DIC technique. 47
Figure 3-5. (a) Loading MAST shoes with specimen into MAST jig, (b) installing confining pressure plate with load cell, (c) placing the MAST over the MTS 810, (d) environmental chamber, (e) DIC test set-up, and (f) view through DIC camera. 48
Figure 3-6. MAST test set-up: (a) schematic diagram, (b) loading MAST shoes into loading jig, and (c) test set-up with DIC system. 49
Figure 3-7. Schematic diagram of beam cut into three parts for air void study. 50

Figure 3-8. (a) Beam specimen cut into three equal portions and (b) middle one-third portion cut to create bottom (18-mm thick) and top layer (36-mm thick). 50
Figure 3-9. (a) Measuring height of bottom layer to check the level, (b) side plates of mold removed, (c) bottom layer being pushed out of mold, (d) flipping over bottom layer, (e) pushing flipped bottom layer back into mold, and (f) closing sides of mold. 52
Figure 3-10. Air void study results for RS9.5C RAP-40. 53
Figure 3-11. Air void study results for RS9.5C RAP-20. 54
Figure 3-12. Compaction imprint on side walls of mold. 54
Figure 3-13. Traced imprint of side walls of molds with dimensions of beam overlapping. 55
Figure 3-14. Revised configuration for cutting beams for performance study. 55
Figure 3-15. Air void study results for RS9.5C RAP-40 mixture beam specimens cut from slab. 56
Figure 3-16. Air void study results for RS9.5C RAP-20 mixture beam specimens cut from slab. 56
Figure 3-17. Cox and Sons four-point bending beam test apparatus (ASTM D7460-10). 57
Figure 3-18. Custom-made environmental chamber attached to MTS to control temperature during beam fatigue tests. 58
Figure 3-19. (a) Type IV self-alignment adhesion tester (PATTI) and (b) cross-sectional schematic of self-aligning piston assembly (ASTM D4541-17 (2017)). 59
Figure 3-20. Step-by-step procedure for PATTI testing. 60
Figure 3-21. Test set-up for hot spray gun usage to apply tack coat for PATTI testing. 61
Figure 3-22. Metal caps on pull-off stubs to apply setting pressure. 62
Figure 3-23. Stress rates measured using PATTI under rotating and fixed dial conditions. 63
Figure 3-24. (a) Cohesive failure of binder, (b) adhesive failure of pull stub, and (c) mixture of cohesive failure and adhesive failure of pull stub. 64
Figure 3-25. Digital image correlation analysis of differences between initial image and deformed image (Seo et al. 2002). 65
Figure 3-26. Comparison of MTS actuator and DIC system displacements. 66
Figure 3-27. Typical fulcrum module capturing process during a cyclic fatigue test (from VIC-2D flyer). 67
Figure 3-28. Input parameters for DIC fulcrum module. 68
Figure 3-29. (Top) recorded commands: actuator commands versus DIC trigger commands; (bottom) actuator/LVDT displacements versus DIS displacements over time. 69
Figure 3-30. Four-point bending beam test apparatus housed in MTS. 71
Figure 3-31. Five stages of displacement calibration. 72
Figure 3-32. Tensile strain data points and curve fits for various actuator tensile strain input commands: (a) 250 μ, (b) 500 μ, (c) 1000 μ, (d) 1500 μ, and (e) 2000 μ. 73
Figure 3-33. Relationships between tensile strain based on input commands and tensile strains using measured actuator and on-specimen displacements. 74
Figure 4-1. Thick pavement structure used for FlexPAVE™ computational simulations. 76

Figure 4-2. FlexPAVE™ dual tire-pavement contact configuration. 78
Figure 4-3. Stress distribution at the interface 1.5-inch deep: (a) normal stress and (b) shear stress.. 79
Figure 4-4. (a) Normal stress and (b) resultant shear stress distributions.................................... 81
Figure 4-5. Shear strain: (a) γ_{yz} and (b) γ_{zx}. 82
Figure 4-6. Pavement structures used to analyze pavement responses: (left) without overlay and (right) with overlay. 84
Figure 4-7. Typical falling weight deflectometer deflection bowl and measurement points. 85
Figure 4-8. Falling weight deflectometer deflection bowl with changes in asphalt concrete surface layer thickness. 85
Figure 4-9. Falling weight deflectometer deflection bowl with changes in asphalt concrete surface layer modulus. 86
Figure 4-10. Tensile strain computed for various overlay thicknesses and asphalt concrete thicknesses of existing surface layer. 87
Figure 4-11. Tensile strain computed for various overlay thicknesses and varying asphalt concrete modulus values of existing surface layer. 87
Figure 5-1. Shear strain measured via crosshead LVDT and DIC for interface shear strength tests at 50.8 mm/min, 19°C, and 483 kPa confining for Ultrafuse. 89
Figure 5-2. Pure power form fitting method to evaluate strain rate (k') at 50.8 mm/min, 19°C, and 483 kPa confining pressure for Ultrafuse. 90
Figure 5-3. Mastercurves for different geosynthetic-reinforced asphalt specimens at the confining pressure levels of (a) 172 kPa (25 psi), (b) 276 kPa (40 psi), and (c) 483 kPa (70 psi). 93
Figure 5-4. Tack coat application rate effect at 172 kPa (25 psi) confining pressure on geosynthetic-reinforced specimens: (a) PC#1, (b) PaG, (c) PC#2, (d) PF, and (e) PM. 97
Figure 5-5. Temperature effect on geosynthetic-reinforced specimens: (a) CS, (b) PC#1, (c) PaG, (d) PC#2, (e) PF, and (f) PM... 100
Figure 5-6 Correlation between shear strength and confining pressure at different temperatures: (a) CS, (b) PC#1, (c) PaG, (d) PC#2, (e) PF, and (f) PM. 104
Figure 5-7. Effect of tack coat application rate on ISS: (a) PM and (b) PF............................... 106
Figure 6-1. Schematic diagram of laboratory fatigue test results for asphalt concrete mixture (Chakroborty and Das 2017)... 109
Figure 6-2. Typical relationships between stiffness and number of load repetitions for controlled strain mode vs. controlled stress mode tests. 111
Figure 6-3. Flexural stiffness versus number of cycles during fatigue testing: (a) CS, (b) PC#1, (c) PC#2, (d) PaG, (e) PM, and (f) PF. 113
Figure 6-4. Cyclic stress, strain, and phase lag relationship (Findley and Davis 2013)............ 115
Figure 6-5. Variation in phase angle versus number of cycles. 115
Figure 6-6. Variation in phase angle with load cycles; flexural stiffness versus number of cycles during fatigue tests of (a) CS, (b) PC#1, (c) PC#2, (d) PaG, (e) PM, and (f) PF. 116

Figure 6-7. Evolution of fitted data during fatigue tests of PF specimens at constant actuator strain of 350 μ: (a) 100th cycle, (b) 1000th cycle, (c) 10,000th cycle, and (d) 100,000th cycle.... 117
Figure 6-8. *R*-squared failure criterion (Al-Khateeb and Shenoy 2004). 118
Figure 6-9. Variation of R^2 with load cycles during fatigue tests: (a) CS, (b) PC#1, (c) PC#2, (d) PaG, (e) PM, and (f) PF. 120
Figure 6-10. (a) Stress-strain relationship of viscoelastic material and (b) dissipated energy concept (Luo et al. 2013). 122
Figure 6-11. Dissipated energy failure Criterion 1: Tangent intersection method for dissipated energy ratio in controlled strain mode. 123
Figure 6-12. Dissipated energy failure Criterion 2: Failure point is where the relationship becomes nonlinear for the dissipated energy ratio in controlled stress mode............................ 123
Figure 6-13. Dissipated energy ratios with load cycles during fatigue tests: (a) CS, (b) PC#1, (c) PC#2, (d) PaG, (e) PM, and (f) PF... 125
Figure 6-14. Stiffness degradation ratio.. 127
Figure 6-15. Normalized modulus × load cycles during fatigue tests: (a) CS, (b) PC#1, (c) PC#2, (d) PaG, (e) PM, and (f) PF... 128
Figure 6-16. Stress × N versus number of loading cycles... 129
Figure 6-17. Stress × N (cycles) versus load cycles during fatigue tests: (a) CS, (b) PC#1, (c) PC#2, (d) PaG, (e) PM, and (f) PF... 130
Figure 6-18. Failure curve defined in three stages of Weibull model (Tsai et al. 2005). 133
Figure 6-19. Validation of measured and predicted failure points using Weibull three-stage survivor function.. 134
Figure 6-20. Actuator tensile strain versus fatigue life for reinforced and unreinforced (CS) beam specimens... 137
Figure 6-21. On-specimen tensile strain versus fatigue life for reinforced and unreinforced (CS) beam specimens. 137
Figure 6-22. Comparison of target application rates and application rates measured in the field in other research efforts: (a) NCHRP 712-2012 (Mohammad et al. 2012) and (b) FHWA-ICT-09-035 (Al-Qadi et al. 2009).. 139
Figure 6-23.Change in 'stress × N' with number of cycles for CS... 140
Figure 6-24.Change in 'stress × N' with number of cycles for PC#1.. 141
Figure 6-25. Comparison of crack resistance capacity of CS and PC#1. 141
Figure 7-1. DIC image: (a) shown on a computer screen and (b) stored in the computer's memory. 143
Figure 7-2. Step size in terms of subset size.. 144
Figure 7-3. Schematic of basic underlying principle of digital image correlation. 145
Figure 7-4. Von Mises strain measured for CS and all types of geosynthetic-reinforced beam specimens tested at 250 μ strain. 150
Figure 7-5. Von Mises strain measured for control specimen (CS) tested at different strain levels. 151

Figure 7-6. Von Mises strain measured for PC#1-reinforced beams tested at different strain levels. 152
Figure 7-7. Von Mises strain measured for PC#2-reinforced beams tested at different strain levels. 153
Figure 7-8. Von Mises strain measured for PaG-reinforced beams tested at different strain levels. 154
Figure 7-9. Von Mises strain measured for PF-reinforced beams tested at different strain levels. 155
Figure 7-10. Von Mises strain measured for PM-reinforced beams tested at different strain levels. 156
Figure 7-11. Von Mises contours of NBFT results for interlayer beam specimens at failure points. 157
Figure 7-12. Graphic user interface for interlayer DIC analysis and steps involved in analysis. 160
Figure 7-13. Selecting analysis areas for interlayer DIC analysis. 161
Figure 7-14. Cumulative vertical cracking area measured during NBFTs of CS. 163
Figure 7-15. Cracked area measured during NBFTs of PC#1 specimens. 164
Figure 7-16. Cracked area measured during NBFTs of PC#2 specimens. 165
Figure 7-17. Cracked area measured during NBFTs of PaG specimens. 166
Figure 7-18. Cracked area measured during NBFTs of PM specimens. 167
Figure 8-1. Crack resistance model showing relationship between tensile strain and NBFT failure cycle. 169
Figure 8-2. Odemark's concept of equivalent thickness calculation. 171
Figure 8-3. Relationship between $E_{sg} \times T_{eq}$ and BCI. 172
Figure 8-4. Predicted and measured overlay tensile strain using Equation (8-2). 172
Figure 8-5. Flow chart of research approach to develop geosynthetic product selection guidelines. 175
Figure 8-6. Shear ratio, shear strength (CRS-2 (Source1)), and shear and normal stress levels in longitudinal direction under the central axis of tire at layer interface to determine maximum shear strength (MSR). 178
Figure 8-7. Typical interface layer shear strain history. 179
Figure 8-8. Typical interface layer shear stress history. 180
Figure 8-9. Shear ratio distribution under dual tires: (a) PC#1 results in 3-D, (b) PM results in 3-D, (c) PC#1 results in 2-D, and (d) PM results in 2-D. 182
Figure 8-10. Flow chart of research approach taken to develop tack coat selection guidelines. 183
Figure 8-11. A schematic depicting the braking event that leads to the worst condition causing debonding. 184
Figure 8-12. Maximum shear ratio (MSR) failure envelope for different mixtures. 184
Figure 8-13. Change in maximum shear ratio (MSR) with depth (in.). 185
Figure 8-14. Failure envelopes showing minimum binder bond strength (BBS) required for tack coat selection. 188

Figure 8-15. Step-by-step selection guidelines for geosynthetic products and tack coats......... 191

Figure A- 1. Mechanism of reflective cracking (Sudarsanan et al. 2015). 208
Figure A- 2. Stress at interlayer caused by moving traffic (Raab and Partl 2004). 210
Figure A- 3. Fracture mechanics crack mode 212
Figure A- 4. Shear stress distribution (a) Direct Shear Test; (b) Simple Shear Test (Raab et al. 2009). 213
Figure A- 5. Ancona Shear Testing Research and Analysis (ASTRA) Device (Pasquini et al. 2015). 214
Figure A- 6. Louisiana interlayer shear strength tester (LISST) (Mohammad et al. 2018). 214
Figure A- 7. Sapienza Direct Shear Testing Machine (SDSTM) (Tozzo et al. 2014). 215
Figure A- 8. Advanced Shear Tester (AST) (Zofka et al. 2015). 215
Figure A- 9. Modified asphalt shear tester (MAST) (Cho et al. 2017b)...... **Error! Bookmark not defined.**
Figure A- 10. Typical MAST test result. 217
Figure A- 11. Shear ratio concept. 218

Figure B- 1. Beam bending of a small element: (a) before bending, (b) after bending, and (c) sectional view... 221
Figure B- 2. Four-pont bending beam fatigue test configuration: (a) front view and (b) sectional view. 225

Figure D- 1. (a) Superpave gyratory compactor (Pine Test Equipment, Inc.) and (b) compaction molds. 232
Figure D- 2. Compaction procedure for double-layered MAST test sample: (a) bottom layer fabrication, (b) bottom layer placement in hot mold with tack coat, and (c) completed MAST test sample. 233
Figure D- 3. Alignment of placement of geosynthetic product in the field. 234
Figure D- 4. Geosynthetic interlayer sample cutting process. 234
Figure D- 5. (a) Tracing the cutting pattern, (b) completed template pattern, and (c) cutting/extracting the geosynthetic sample using a cloth cutter. 235
Figure D- 6. Tack coat application process: (a) pouring hot binder from metal canister with perforated lid and (b) spreading binder uniformly using a heat gun and metal spatula............. 236
Figure D- 7. Non-uniform application of tack coat applied to bottom layer surface of MAST test samples... 236
Figure D- 8. Hot spray gun test set-up for tack coat application: (a) test set-up, (b) control panel, and (c) hot spray gun.. 237
Figure D- 9.. Hot spray gun components: (a) gun, cartridge, and nozzles, (b) air spray nozzle, and (c) liquid nozzle. 238

Figure D- 10. (a) Attaching nozzle to hot spray gun cartridge, (b) pouring liquid asphalt into cartridge, (c) loading cartridge into heating chamber of spray gun, (d) cartridge with asphalt inside spray gun, (e) closing spray gun mouth, and (f) measuring temperature at nozzle tip. ... 239
Figure D- 11. (a) Sheet cover above gyratory-compacted sample, (b) small gap between cover sheet and sample, and (c) application of hot asphalt using hot spray gun. 240
Figure D- 12. Tack coat applied to the bottom layer surface of MAST test samples: (a) non-uniformity (metal canister) and (b) uniformity (hot spray gun). 241
Figure D- 13. Placement of geosynthetic interlayer products (view from top towards top of bottom layer): (a) PC#1, (b) PC#2, (c) PaG, (d) PM, and (e) PF. 242
Figure D- 14. (a) Bottom layer after tack coat application, (b) liquified asphalt binder after placing the bottom layer with tack coat in the oven at 145°C for two minutes, and (c) setting pressure application by rolling metal rod over PC#1... 243
Figure D- 15. Tracking the geosynthetic reinforcement placement direction: (a) bottom layer of MAST test sample and (b) final cored MAST test specimens.. 244
Figure D- 16. Procedure for coring and cutting cylindrical specimens: (a) cored MAST test sample, (b) trimming the top/bottom layer, and (c) finished specimens. 245
Figure D- 17. Process for protecting geosynthetic-reinforced sample with PVC pipe: (a) sample placed on canister, (b) the PVC pipe with leveling marks matched with the bottom of the specimen, and (c) completed sample with PVC pipe protection. 246
Figure D- 18. Side views of geosynthetic-reinforced specimens made with (a) PC#1, (b) PC#2, (c) PaG, (d) PM, and (e) PF. 246

Figure E- 1. Pneumatic roller compactor with vibrator (CRT-RC2S)....................................... 247
Figure E- 2. (a) Weighing loose mix in cloth bag and (2) two pans of loose mix obtained from two cloth bags in the oven at the compaction temperature (145°C). 248
Figure E- 3. (a) Batching the necessary quantity of loose mix into pans, (b) spreading loose mix in the pans for uniform heating, (c) batched pans, and (d) batched pans, mold, and necessary accessories in the oven at mix temperature.. 249
Figure E- 4. (a) Separation compartment in mold with collar, (b) pouring loose mix into each compartment, (c) heaps of loose mix in each compartment, (d) leveling the heaps in the compartment, (e) removing separation compartment, (f) leveling slab surface, (g) plowing contents of slab in length direction, (h) plowing contents of slab in width direction, (i) measuring surface temperature of loose mix before compaction using an infrared heat gun, and (j) loading mold onto compaction platform. 252
Figure E- 5. (a) Height adjustment scale in compactor, (b) channel sections set above aluminum plate for precision measurements, and (c) compactor face about to abut channels. 253
Figure E- 6. Details of each compaction level and number of cycles at respective applied pressure. 253
Figure E- 7. (a) Template used for cutting pattern and (b) tracing the template over PC#2. 254

Figure E- 8. (a) Tack coat application test set-up and (b) applying tack coat using hot spray gun. 255
Figure E- 9. Placement of geosynthetic product above bottom layer: (a) before and (b) after placement. 255
Figure E- 10. Layout pattern of grid for (a) PC#1, (b) PC#2, and (c) PaG. 256
Figure E- 11. Procedure for cutting beam specimens: (a) slab dimensions and slab prior to sawing beam specimens and (b) before trimming top and bottom layers.................................. 257
Figure E- 12. Beam specimens fastened in a holding jig.. 258
Figure E- 13. Drill bits used for making tapered notches. 259
Figure E- 14. Tapered notches made by drilling: (a) and (b) chipped edges under a unidirectional pass, and (c) non-chipped edge under a bidirectional pass. 260
Figure E- 15. (a) Components of roller stamp and (b) using roller stamp for speckling. 261
Figure E- 16. (a) Spraying the base coat on a beam specimen and (b) speckle patterns with different dot sizes on beam specimens... 262

LIST OF TABLES

Table I-1. Tack Coat Rates for Different Geosynthetic Types vii
Table I-2. Test Conditions Used in Study........ ix
Table I-3. Pavement Simulation Conditions Using EverstressFE xi
Table I-4. Measured Parameters k_1 and k_2 Based on On-Specimen Tensile Strain versus Number of Cycles to Failure........ xv

Table 2-1. Shift Factor Coefficients of RS9.5C RAP-40 Study Mixture 37
Table 2-2. Summary of Tack Coat Application Rates for Geosynthetic Products Used in Study 37
Table 2-3. Shift Factor Coefficients of PG 64-22 Binder Tack Coat Used in Study........ 39
Table 2-4. Nomenclature Details for Different Geosynthetics Types 40
Table 2-5. Properties of Study Geosynthetic Products 41
Table 3-1. Interlayer Shear Strength Test Conditions 43
Table 3-2. MAST Specimens: Air Void Content........ 44
Table 3-3. Verification of Air Void Study Results 44
Table 3-4. Nomenclature Details for Slab Specimens 51
Table 3-5. Predicted On-Specimen Tensile Strain Based on Compliance-Displacement Relationship for the Study RS9.5C Mixture 74
Table 4-1. Prony Coefficients for Relaxation Modulus........ 77
Table 4-2. Pavement Simulation Conditions Using EverstressFE 83
Table 5-1. Summary of ANCOVA Results 105
Table 5-2. Tukey HSD Analysis Results for PM........ 105
Table 5-3. Tukey HSD Analysis Results for PF........ 105
Table 6-1. Conventional Failure Criteria........ 112
Table 6-2. Failure Life Based on Different Failure Criteria for Control and Geosynthetic-Reinforced Beam Specimens 132
Table 6-3. Failure Life Based on Stress × N Failure Criterion for Control and Geosynthetic-Reinforced Beam Specimens 135
Table 6-4. Life Extension Ratios of Geosynthetic-Reinforced Beam Specimens Compared to Control Specimens........ 136
Table 6-5. Fatigue Coefficients of Actuator Tensile Strain versus N_f for Unreinforced and Reinforced Specimens 138
Table 6-6. Fatigue Coefficients of On-Specimen Tensile Strain versus N_f for Unreinforced and Reinforced Specimens 138
Table 8-1. Fatigue Coefficients of Interlayer Tensile Strain versus Number of Loading Cycles for Unreinforced and Reinforced Specimens 169
Table 8-2. C_0 and A Values for Each North Carolina Region and Statewide Values........ 174
Table 8-3. Coefficients of Interface Shear Strength Prediction Equation for Different Asphalt Layer Interface Conditions at Reference Temperature of 35°C 176
Table 8-4. Coefficients of Binder Bond Strength Prediction Equation for PG 64-22 Tack Coat177

Table 8-5. Material Parameter *A* for Different Geosynthetic Products 186
Table 8-6. Minimum BBS Required for Tack Coat for Different Geosynthetic Products 189

Table A- 1. NCHRP report 712 tack coat application rate (Mohammad et al. 2012). 211
Table A- 2. FHWA tech brief tack coat application rate (FHWA 2016)................................... 211

Table E- 1. Material and Dimensions of Drill Bits Used for Current Study 259
Table E- 2. Dot Size Selection Table for Speckling Process in DIC Testing............................. 261

SYMBOLS AND ABBREVIATIONS

β	=	Slope of the linear regression in the second stage
ξ	=	Reduced time at reference temperature
ε	=	Strain
ω	=	Angular loading frequency (Hz)
θ	=	Bending angle
$\dot{\sigma}$	=	Axial stress rate (kPa/s)
δ	=	Minimum value of $\|E^*\|$ (MPa)
ρ	=	Radius of curvature
β, γ	=	Constants, material parameters for the sigmoidal function
$\delta+\alpha$	=	Maximum value of $\|E^*\|$ (MPa)
ε_1, ε_2	=	Principal strains at an element
ε_{act}	=	Actuator based tensile strain at the bottom of the asphalt layer
σ_c	=	Normal confining stress (kPa)
ω_c	=	Constant, location parameter where loss modulus equals storage modulus
$\tau_{cohesion}$	=	Cohesion component of shear strength (kPa)
τ_f	=	Shear strength at the layer interface (kPa)
ϕ_i	=	Phase angle between stress and strain at load cycle i
ρ_i	=	Relaxation times (sec)
ε_{int}	=	On-specimen based tensile strain at the interlayer
ε_{os}	=	On-specimen based tensile strain at the bottom of the asphalt layer
$\dot{\sigma}_R$	=	Reduced axial stress rate (kPa/s)
ω_R	=	Reduced angular frequency (Hz)
τ_s	=	Shear stress (kPa)
ε_t	=	Tensile strain at the bottom of the asphalt layer
σ_t	=	Tensile strength / binder bond strength (kPa)
$\sigma_{t\text{-}crit}$	=	Critical tensile strength / binder bond strength at 50°C (kPa)
ε^v	=	Von Mises strain
λ_w	=	Temperature correction factor
ε_{xx}	=	Strain along the x-axis
ε_{xy}	=	Shear strain tensor
τ_{xz}	=	Shear stress in transverse direction under the tire (kPa)
γ_{xz}	=	Shear strain in the transverse direction under the tire
ε_{yy}	=	Strain along the y-axis
γ_{yz}	=	Shear strain in the longitudinal direction under the tire
τ_{yz}	=	Shear stress in longitudinal direction under the tire (kPa)
a	=	center-to-center spacing between clamps (Cox: 119 mm)
A	=	Constant, asphalt concrete mix material parameter used for maximum shear ratio predictive equation
A_0, A_1, and B_1	=	Fitting parameters
a_1, a_2, a_3	=	Functions of temperature
a_B, n_B	=	Material parameter constants for binder bond strength predictive equation
A_{cs}	=	Cross-sectional area of specimen (m^2)

a_I, b_I, c_I, d_I, e_I	=	Material parameter constants for interface shear strength predictive equation
a_T	=	Time-temperature shift factor
b	=	Average specimen width (mm)
BBS	=	Binder bond strength (kPa)
BCI	=	Base curvature index (mils)
BDI	=	Base damage index (mils)
C_0 and A	=	Regression constants
CS	=	Control Specimen
D	=	Damage
d	=	Depth of interface from asphalt surface (in.)
D_0, D_{12}, D_{24}, and D_{36}	=	Deflections at distances of 0, 12, 24, and 36 inches from the center of the falling weight deflectometer loading plate, respectively
DIC	=	Digital image correlation
E	=	Modulus of the asphalt concrete
E_∞	=	Equilibrium modulus (MPa)
$E(t)$	=	Relaxation modulus (MPa)
E^*	=	Dynamic modulus (MPa)
E_0	=	Initial stiffness (modulus) of the material, and
E_{abc}	=	Young's modulus of aggregate base course (psi)
E_{ac}	=	Young's modulus of asphalt concrete layer (psi)
E_i	=	Relaxation strength (MPa)
E_{sg}	=	Young's modulus of subgrade (psi)
f	=	Loading frequency (Hz)
F_A	=	Axial force (kN)
F_c	=	Confining force (kN)
f_R	=	Reduced frequency (Hz)
FWD	=	Falling Weight Deflectometer
G^*	=	Dynamic shear modulus (MPa)
G^*_g	=	Glassy dynamic shear modulus when frequency tends to infinite
h	=	Average specimen height (mm)
H_{ac}	=	Asphalt concrete layer thickness (in.)
ISS	=	Interface shear strength (kPa)
I_{zz}	=	Area moment of inertia
k	=	Reduced strain rate at reference temperature
k'	=	Slope of strain vs. time at temperature T
k_1, k_2, k_3	=	Material properties (calibration parameters)
$\ln(\alpha)$	=	Intercept of the linear regression of the second stage.
m	=	Number of Maxwell elements
M	=	Total moment of the forces
m_e, ν	=	Constant, dimensionless, shape parameter
MSR	=	Maximum shear ratio
N or n or N_i	=	Number of cycles
NBFT	=	Notched beam fatigue test
N_f	=	Number of cycles to failure
P	=	Load applied by the actuator (N)

PaG	=	Paving grid
PATTI	=	Pneumatic Adhesion Tension Testing Instrument
PC#1	=	Paving composite #1
PC#2	=	Paving composite #2
PF	=	Paving fabric
PM	=	Paving mat
r	=	Radial distance from center of load plate (in.)
R^2	=	Coefficient of determination
SCI	=	Surface curvature index (mils)
SG	=	Shear gap (mm)
S_i	=	Stiffness at the i^{th} cycle
S_o	=	Initial stiffness measured at the 50th load cycle
SR	=	Flexural beam stiffness ratio, beam stiffness at the cycle of interest divided by initial beam stiffness
SS_{res}	=	Sum of squared residual errors
SS_{tot}	=	Sum of squared total errors
t	=	Time (sec)
T	=	Total number of periods
T_{abc}	=	Thickness of aggregate base course (in.)
T_{ac}	=	Thickness of asphalt concrete layer (in.)
T_{eq}	=	Equivalent thickness (in.) of pavement structure in terms of subgrade modulus
$T_{overlay}$	=	Thickness of the overlay (in.)
u and v	=	Displacements
$u_{A\text{-}act}$	=	Actuator-based axial displacement (mm)
$u_{A\text{-}DIC}$	=	Digital image correlation-based axial displacement (mm)
W_0	=	Energy dissipated in the first cycle
W_i	=	Dissipated energy at load cycle i
W_n	=	Energy dissipated in the n^{th} cycle
w_T	=	Deflection at temperature T
w_{T0}	=	Deflection corrected to temperature T_0
$\overline{x}$	=	Global mean for covariate x
x_i	=	Independent predictor, or explanatory variable
x_{ij}	=	Covariates
$\bar{y}$	=	Mean value of y (measured values)
$\hat{y}$	=	Predicted value of y
$\hat{Y}$	=	Dependent or response variable
y_i	=	Measured values
Y_{ij}	=	j^{th} observation under the i^{th} categorical group
$\hat{\beta}$	=	Regression coefficient for the relationship between the response and covariate
$\dot{\gamma}$	=	Shear strain rate
$\dot{\gamma}_R$	=	Reduced shear strain rate
ϵ_{ij}	=	Random errors
μ	=	Overall mean

Chapter 1. Introduction

1.1 Background

One common form of pavement rehabilitation that is quick and reliable for treating pavement distress is asphalt concrete (AC) overlays. The phenomenon of crack propagation through a new overlay from the underlying pavement structure is known as reflective cracking. Many interlayer reinforcement technologies can be employed to mitigate reflective cracking, but geosynthetic products are gaining attention due to their ease of installation, low cost, and wide availability. The primary functions of geosynthetics are reinforcement, stress relief, and waterproofing. The reinforcing function requires the geosynthetic material to have a significantly higher modulus value than the surrounding asphalt. Such reinforcement can redirect cracking at the interlayer, thereby delaying or mitigating reflective cracking indefinitely. Stress-relieving geosynthetic products have low stiffness values and can store strain at low stress levels. With regard to the waterproofing function, when a crack penetrates through the overlay, the geosynthetic acts as a barrier to prevent water infiltration and protects the underlying structure. A geosynthetic product that is fully impregnated by the tack coat significantly reduces water permeability. Proper installation, control of the overlay thickness, and oversight of the compaction quality are required to achieve the three primary geosynthetic functions. Similarly, ensuring a proper bond between adjacent asphalt layers to allow the pavement structure to act monolithically in resisting vehicular and thermal loads is of critical importance for solid pavement performance. A weak bond between the layers and the geosynthetic product eventually leads to premature failure due to debonding, followed by a reduction in the service life of the asphalt pavement. Therefore, proper selection criteria are needed for geosynthetic products to meet the variable pavement conditions. Numerous types of geosynthetic products are available in the market, and the primary goal of each product for paving applications is to control reflective cracking and improve the pavement's longevity. Unfortunately, limited studies have been undertaken to establish selection guidelines for the various geosynthetic products based on field conditions.

1.2 Research Needs and Significance

In recent years, the North Carolina Department of Transportation (NCDOT) has been working with the Geosynthetic Materials Association (GMA) to develop a special provision for improved geosynthetic pavement interlayer materials and create a distress chart that provides valuable data for product selection. The GMA has recently addressed both needs by developing five standard categories of geosynthetic materials for pavement applications. These categories (which were developed based on the Virginia DOT's geosynthetic specifications) are (1) Paving Fabrics Types I & II, (2) Paving Mats Types I, II, & III, (3) Paving Grids Types I, II, & III, (4) Composite Paving Grids Types I, II, & III, and (5) Pavement Repair and Bridge Deck Waterproofing Strip Membranes. Although these five categories provide the NCDOT with an excellent foundation to develop the special provision and distress chart, further research is needed to identify a list of properties and performance criteria that geosynthetic products must meet to perform adequately for their intended function. The main goal of this research effort is to ensure that NCDOT engineers can choose the appropriate geosynthetic pavement interlayer products for a specific application based on performance data.

Because specifying and testing the material properties (tensile strength, elongation percentage, melting point, etc.) of the geosynthetics themselves are relatively straightforward tasks, the major challenge with this effort is the identification or development of tests that can adequately capture the specific mechanisms that can cause or mitigate distress in actual pavement structures in a realistic manner, all while remaining practical enough for routine testing by agencies and manufacturers. One common example of this challenge is fatigue testing. Fatigue tests that are performed at realistic strain levels may take weeks to run and thus are impractical. However, fatigue tests that are performed at higher strain levels may not adequately represent field distress mechanisms and material behavior. Thus, test results from these fatigue tests need to be verified based on more realistic strain levels.

Findings from two recently completed research projects, funded by the NCDOT and conducted by North Carolina State University (NCSU) researchers, serve to aid this joint effort by the NCDOT and GMA. These projects are NCDOT HWY-2012-02 *Performance of Cracking Mitigation Strategies on Cracked Flexible Pavements* (Kim et al. 2015a) and NCDOT HWY-2013-04 *Surface Layer Bond Stresses and Strength* (Kim et al. 2015b). The NCDOT HWY-2012-02 project used both laboratory and field studies to investigate the ability of geosynthetic interlayer products to mitigate reflective cracking in asphalt overlays. A flexible pavement section of U.S. 1 in Moore County was selected for field trials, and five interlayer research segments that incorporated three geosynthetic products, a chip seal, and a control (tack coat only) segment were placed. Cores obtained from the field pavements and specimens fabricated in the laboratory using a slab compactor were tested using four-point bending notched beam fatigue tests (hereinafter called NBFTs) and direct shear tests. The results from the laboratory tests clearly demonstrated the benefits of geosynthetics in mitigating reflective cracking, as long as the bond between the geosynthetic product and surrounding AC is sufficiently strong to resist shear stress at the layer interface. These findings were verified based on the results of a condition survey of the U.S. 1 field trial sections. As part of the NCDOT HWY-2013-04 project, the NCSU research team developed a computational, experimental methodology to determine shear failure in asphalt overlays reinforced by interlayer systems.

The findings from both the NCDOT HWY-2012-02 and NCDOT HWY-2013-04 projects were used to develop shear strength threshold values that can be applied to accept or reject asphalt overlays reinforced by interlayer systems. The current study critically evaluates the findings from these two projects, and Appendix A provides a comprehensive literature review. Based on the earlier work, the current research effort includes the development of a comprehensive test methodology for evaluating pavement interlayer geosynthetic products, development of selection criteria for pavement interlayer geosynthetic products and tack coats based on performance data, and the synthesis of this information to provide technical documents for use by the NCDOT.

1.3 Research Objectives and Scope

The primary objective of the proposed research is to develop performance testing methodologies and performance criteria for geosynthetic products used in pavement interlayer applications that can be used in developing performance specifications and product selection guidelines for the NCDOT. Another study objective is to develop a tack coat selection criterion for specific geosynthetic types to safeguard against debonding failure. The scope of the test plan includes five different geosynthetic products designated as paving composite #1 (PC#1), paving composite #2 (PC#2), paving grid (PaG), paving mat (PM), and paving fabric (PF). This scope also encompasses geosynthetic applications for asphalt overlays that are placed over damaged

AC pavement. The damaged AC layer is mimicked by creating a notch on the underside of an AC beam test specimen. A geosynthetic product would be placed one-third from the bottom of the asphalt beam, which represents the surface of the damaged AC pavement.

Gyratory and slab compactors were used to fabricate double-layered geosynthetic-reinforced and unreinforced (control) specimens. The AC mixture used for the current study is classified as RS9.5C with 40% reclaimed asphalt pavement (RAP). The geosynthetic products were sandwiched between the layers with a tack coat (PG 64-22) applied at the rate recommended by the manufacturer. Binder bond strength (BBS) tests were performed using the hot binder (PG 64-22) as a tack coat. The geosynthetic-reinforced and unreinforced specimens were tested using NBFT equipment and a Modified Asphalt Shear Tester (MAST) to measure the specimens' crack resistance capacity and interface shear strength (ISS), respectively.

In the case of an asphalt overlay placed above Portland concrete cement, the major fracture modes that drive cracking are Modes I and II, which indicate thermal loads + wheel loads and wheel loading, respectively. An overlay tester, the Belgium laboratory test, the Ecole Nationale des Travaux Publics de l'Etat (ENTPE) test, or the University of Illinois test are designed to mimic thermal cracking (Mode I) in the field. Three-point beam tests and four-point beam tests represent Mode I fracture that is due to bending under vehicular loading. However, these Mode I types of fracture that are caused by thermal and vehicular loading differ as the AC experiences both compression and tension during vehicle loading (top portion under compression and bottom under tension), but usually experiences a single force (either tension or compression throughout the section) during thermal loading. Limited research has been undertaken for Mode II fracture; the only Mode II cracking tests for AC are wheel-tracking tests and four-point shear tests. Although both Mode I and Mode II are similar in terms of driving pavement cracking, only damage caused by vehicular loading was considered for the present study. Hence, only NBFTs were conducted in this study to capture the crack resistance of geosynthetic-reinforced AC beams under vehicular loading.

The tasks for the goals considered during the study are as follows.

- Evaluate the effects of geosynthetic product type, confining pressure, temperature, and shear strain rate on geosynthetic-reinforced interlayer bonding performance. Then, develop bond shear strength prediction models.
- Perform FlexPAVE™ analysis of various overlay pavement structures, speeds, temperatures, and overlay thicknesses to determine the critical debonding conditions for geosynthetic-reinforced specimens.
- Determine a tack coat selection criterion for installing debonding-resistant geosynthetic products and establishing a tack coat quality control program.
- Develop a prediction equation for field interface tensile strain using falling weight deflectometer (FWD) measurements based on numerical simulations.
- Evaluate the crack resistance capacity of different geosynthetic products and establish a relationship between crack resistance capacity and tensile strain by conducting NBFTs at at least four different constant actuator strain levels.
- Identify the failure mode of the tested geosynthetic products by monitoring their crack propagation patterns using the digital image correlation (DIC) technique.

1.4 Research Approach

Figure 1-1 presents a flow chart of the research approach taken to develop guidelines for selecting geosynthetic products based on the product's ability to resist debonding and reflective crack propagation. The outcomes of this research approach are (1) the ranking of the various geosynthetic products in terms of the load-bearing capacity of the existing pavement for the overlay project and (2) the prediction of the expected mode of failure in the field, i.e., debonding or vertical reflective cracks. The three-phase research effort to develop step-by-step guidelines for geosynthetic product and tack coat selection is briefly described in the following.

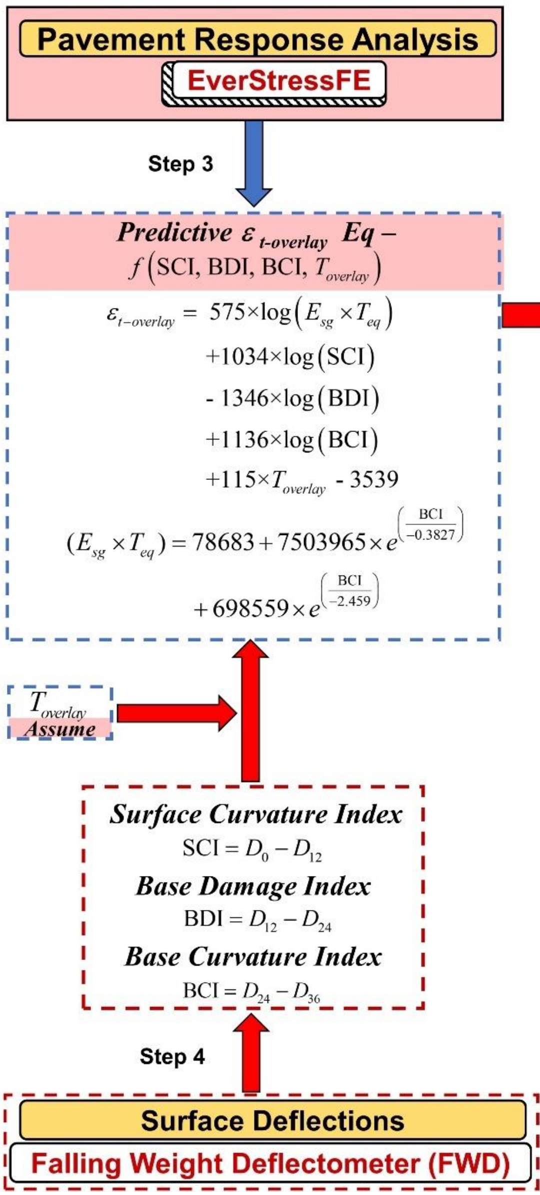

Figure 1-1. Flow chart of research approach taken to develop geosynthetic product selection guidelines.

Phase 1: Evaluate crack resistance in terms of the number of cycles to failure (N_f) and failure mode (debonding and/or vertical cracking) of various geosynthetic products based on laboratory test results.

In Phase 1, the crack resistance and failure mode of the different geosynthetic-reinforced beam specimens were measured using NBFTs and the DIC technique. The NBFTs were carried out at different constant actuator tensile strain levels at 23°C (73°F). The DIC technique was employed to study the crack propagation patterns in the AC beams subjected to the repeated bending. The digital images captured using the DIC technique were analyzed using Vic-2D® to determine the Von Mises strain. The Von Mises strain that is measured on the beam surface between the loading points was used to determine the macro-crack development and, therefore, failure mode. Chapter 6 and Chapter 7 of this report presents a critical evaluation of the NBFT and DIC results respectively.

Phase 2: Perform numerical simulations of pavement responses.

The NBFT results and DIC analyses revealed that different geosynthetic interlayer products produce different crack resistance at different tensile strain levels and the failure mode in geosynthetic-reinforced AC beams depends on the magnitude of tensile strain at the bottom of the beams. Therefore, selection of proper geosynthetic interlayer products requires prior knowledge of the tensile strain at the bottom of AC overlay. Phase 2 is designed to develop a predictive equation for the tensile strain at the bottom of asphalt overlay using surface deflections measured from a FWD).

Phase 3: Determine the minimum binder bond strength for different geosynthetic types.

The performance of a geosynthetic-reinforced AC overlay depends on the quality of the tack coat. The research team used the research approach that was developed in an earlier tack coat study, RP 2018-13 *Development of a Tack Coat Quality Control Program for Mitigating Delamination in Asphalt Pavement Layers*, to determine the minimum tack coat BBS values for the different geosynthetic interlayer types. The experimental design for this research approach is to measure the ISS using the MAST and to measure the BBS using PATTI. The MAST is a monotonic shear tester that is used to measure the ISS of a double-layered AC specimen with or without a geosynthetic interlayer (impregnated with asphalt) sandwiched between the layers. The MAST test is carried out at three strain rates and temperatures to build the ISS mastercurve and an ISS predictive equation. Similarly, PATTI measures the BBS of a binder at various temperatures to build the BBS mastercurve and a BBS predictive equation. Further, the braking event of a truck is simulated numerically using pavement response software, and the *in situ* strain rate and stress rate at the interlayer are measured. Consequently, the measured strain and stress rates help in calculating the field ISS and BBS experienced by the interlayer using the predictive ISS and BBS equations developed based on experimental data. The outcomes show a universal relationship between the ISS and BBS experienced by the interlayer. The relationships between the tack coat BBS and the ISS of geosynthetic-reinforced AC specimens were developed and used to determine the minimum BBS value that serves as the criterion for acceptance of the tack coat that corresponds to a specific paving geosynthetic product. The development of the tack coat selection criterion is detailed in Chapter 8.

1.5 Report Organization

Chapter 1 is an introductory chapter that provides background information about the research needs, highlights the importance of geosynthetic-reinforced pavement performance and the relevance of proper bonding at the AC layer interface, and lists the objectives of this research. Chapter 2 provides details regarding the materials and their properties that were used for the current study. Chapter 3 discusses the different test methods, experimental program, and testing methodology used for this research. Chapter 4 presents the numerical simulation conditions considered for the analyses, the material models, and the parameters and outcomes. Chapter 5 discusses the results of the ISS tests conducted under various conditions and the effects of each influential factor. Chapter 6 and Chapter 7 discuss the NBFT and DIC test results, respectively. Chapter 8 explains the step-by-step procedure followed to develop the geosynthetic product selection guidelines and tack coat selection criteria. The predictive equation for tensile strain at the interface also is discussed in detail. Chapter 8 also presents pavement response analysis that describes the comprehensive stress intensity distribution at the layer interface under actual loading conditions. Chapter 9 concludes the findings of the research and offers recommendations for future work. Details regarding supporting test results for the respective chapters, including the literature review, are provided in the appendices.

Chapter 2. Materials and Properties

2.1 Asphalt Concrete Mixture

The AC used in this study to fabricate the MAST and NBFT specimens was obtained as a loose mix from Lane Construction, Inc. in Raleigh, North Carolina. The NCDOT categorizes the procured loose hot-mix as RS9.5C, where the letter 'R' indicates the presence of RAP, 'S' stands for the surface mixture on the pavement, 9.5 reflects the nominal maximum aggregate size (mm), and 'C' represents the middle level of traffic (3-30 million equivalent single axle loads, or ESALs). The RS9.5C mix contains 40% fractionated RAP (hereafter referred to as the RAP-40 mixture). The virgin binder used for the RAP-40 mixture is PG 58-22. The total binder content in this mixture is 6.0 percent. The material characterization and verification of the reported parameters in the job mix formula were carried out as the initial step prior to performance testing. Figure 2-1 presents the aggregate gradation of the RAP-40 mix. Considering the high RAP content in RAP-40, the compaction temperature was selected as 145°C.

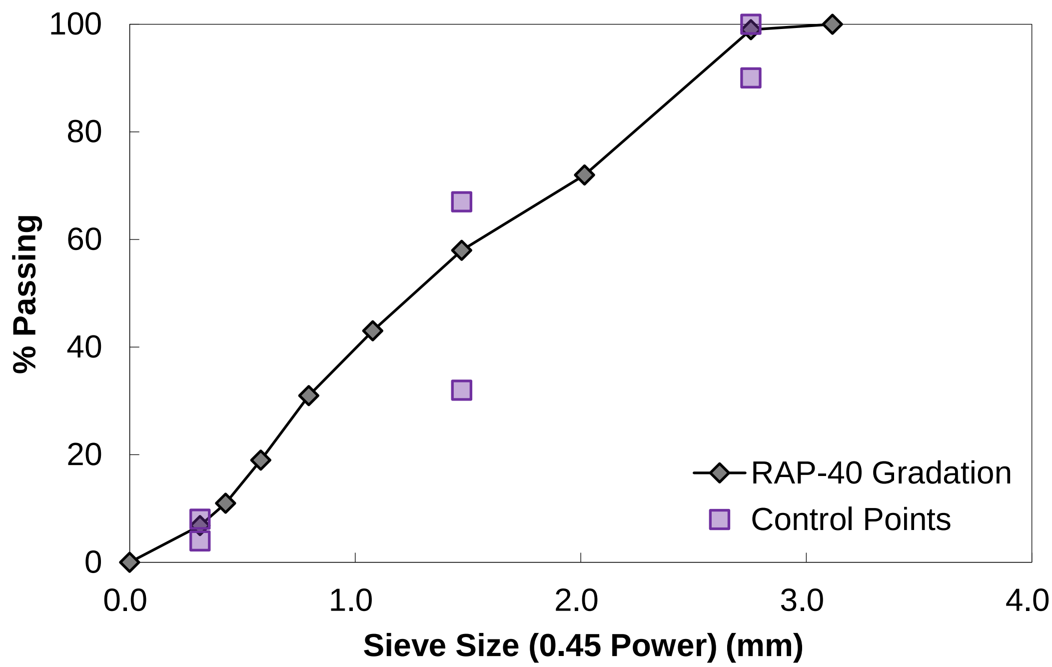

Figure 2-1. Aggregate gradation of RAP-40 mixture.

Even though the loose mix was collected from a hot mix asphalt plant, the likelihood of fine and coarse particle segregation was anticipated while shoveling the AC mix into collection buckets. Hence, a homogenization process was undertaken before fabricating any samples using the loose mix in the laboratory. First, the loose mix was collected in cloth bags and plastic buckets. Figure 2-2 (a) shows the removal of the loose mix in a cloth bag from the plastic bucket as a single unit. Then, Figure 2-2 (b) shows the careful removal of the cloth bag from the mix, achieving minimal loss of loose mix. Figure 2-2 (c) shows the obtained single AC mix lump that has been transferred to a metal bucket.

Figure 2-2. (a) Removing asphalt concrete loose mix in cloth bag from collection bucket, (b) removing loose mix from cloth bag, and (c) loose mix inside metal bucket.

For the separation process, one batch includes four five-gallon buckets, with the total AC mix weighing more than 100 kg (200 pounds). The metal buckets with the loose mix are heated to a temperature of 10°C less than the compaction temperature for two hours. Next, one-fourth portion from each bucket is poured into four separation pans; each pan is further divided into 12 small boxes. This procedure aids in producing a well-mixed asphalt mix. The four buckets of the loose mix are divided into 12 cloth bags for easy storage (three bags per bucket). A storage bag consists of four small boxes, each randomly selected from four separation pans. Figure 2-3 (a) and (b) respectively show the separation pans and cloth bags used for storage. These separated mixes in the cloth bags are used later for sample fabrication and the material characterization study. Depending on the material requirements, this separation process could be repeated.

(a) (b)

Figure 2-3. (a) Separation pans and (b) cloth bags for preparing a well-mixed asphalt concrete mixture.

The theoretical specific gravity and the bulk specific gravity of the loose mix with 40% RAP were measured as per AASHTO T 209-20 (AASHTO 2020a) and AASHTO T 331-17 (AASHTO 2017a), respectively. The maximum specific gravity for the AC mix was found to be 2.44 g/cm^3.

2.2 Dynamic Modulus (|*E**|) Test of Asphalt Mixture

The linear viscoelastic properties of AC mixtures can be determined via dynamic modulus ($|E^*|$) tests that measure a specimen's stress-strain relationship under continuous sinusoidal loading. The parameters obtained are the complex modulus values and time-temperature (t-T) shift factors. The shift factor (a_T) aids in representing the effects of time and temperature via a unique parameter referred to as 'reduced time/frequency', f_R , defined here as Equation (2-1).

$$f_R = f \times a_T \tag{2-1}$$

where

f_R	=	reduced frequency, Hz,
f	=	loading frequency, Hz, and
a_T	=	time-temperature shift factor.

Figure 2-4 explains the linear relationship between the air void content and weight of gyratory-compacted samples. The test specimens are cylindrical specimens 38 mm in diameter and 110 mm in height, cored and cut from a gyratory-compacted sample of 180-mm height. The air void content of each specimen obtained from the gyratory-compacted samples should be maintained at 6 percent. In order to prepare 38-mm cylindrical specimens for performance tests with 6% air void contents, an air void study of the gyratory-compacted samples must be carried out as per AASHTO R 83-17 (AASHTO 2021). The gyratory-compacted samples with different weights of AC mix were compacted to a consistent height of 180 mm. Then, the air void contents were measured for the four 38-mm diameter cylindrical specimens that were cored from each gyratory-compacted sample. Figure 2-4 presents the results of the air void study. A linear relationship is established between the weight of the gyratory-compacted sample and the air void content. This relationship helps to predict the exact weight required for a 180-mm tall gyratory sample to produce four 38-mm diameter and 110-mm tall cylindrical samples with 6% air void content. Figure 2-5 presents the dynamic modulus test results for three replicates of each sample made of the RS9.5C RAP-40 mixture at different temperature/frequency combinations conducted as per AASHTO TP 132-19 (AASHTO 2019).

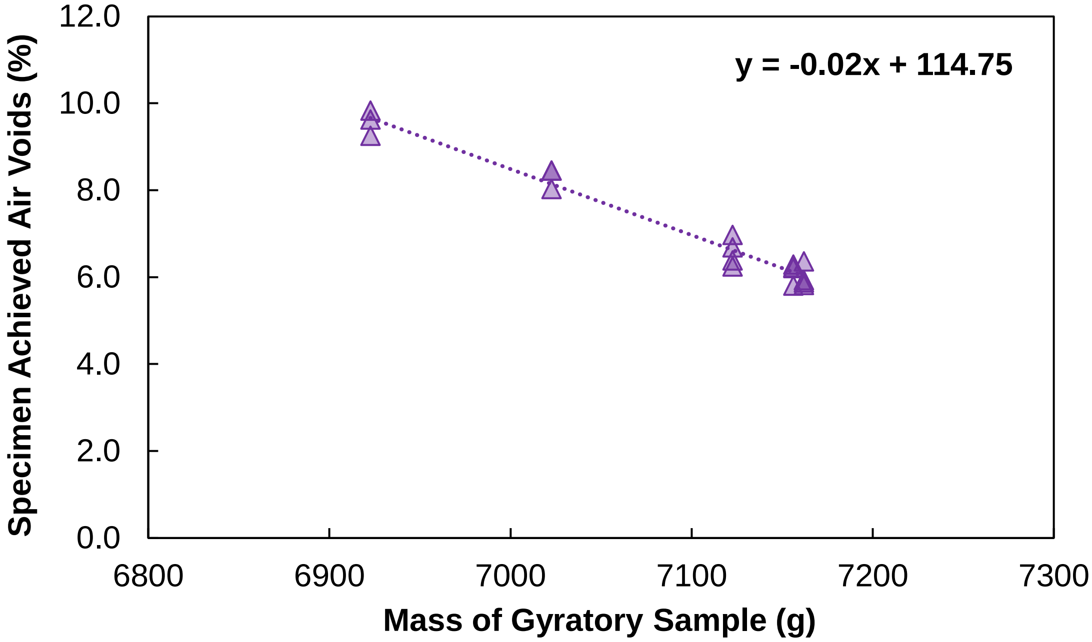

Figure 2-4. Linear relationship between air void content and weight of gyratory-compacted samples.

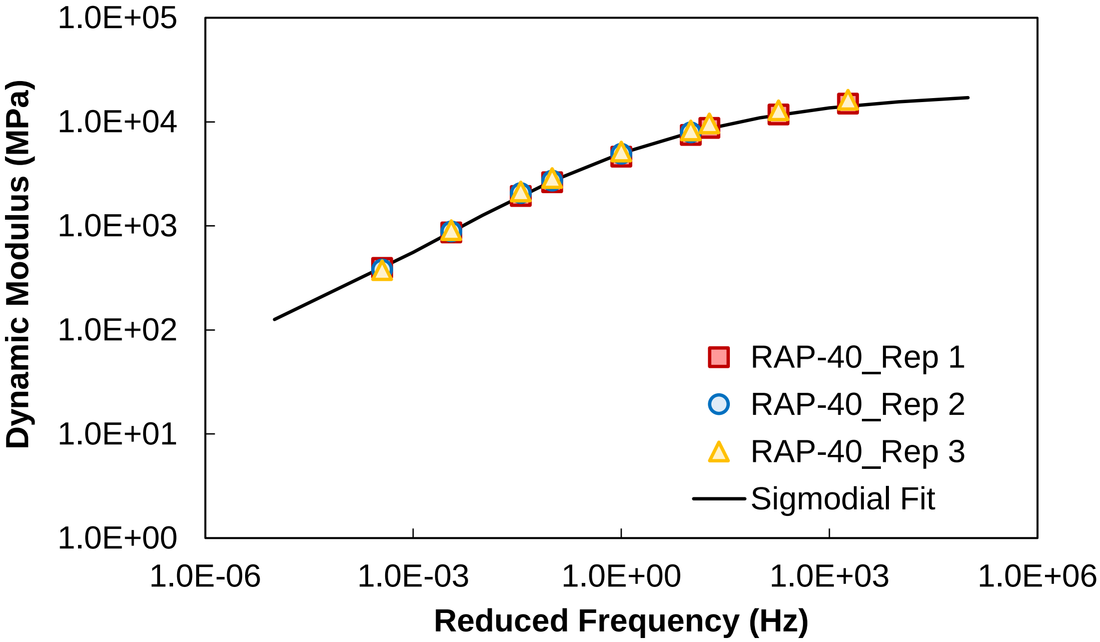

Figure 2-5. Dynamic modulus mastercurve for RS9.5C RAP-40.

An Asphalt Mixture Performance Tester (AMPT) Pro was used as the testing device, and the tests were performed at three temperatures, 4°C, 20°C, and 40°C, and six frequencies, 25 Hz, 10 Hz, 5 Hz, 1 Hz, 0.5 Hz, and 0.1 Hz. A mastercurve was developed by shifting the data points of each replicate horizontally at an arbitrarily selected reference temperature, in this case, 20°C. Equation (2-2) is the sigmoidal function used to fit the dynamic modulus mastercurve. Equation (2-3) represents the time-temperature shift factor in a quadratic function. The Prony series coefficients are obtained by fitting the storage modulus with the function shown in Equation (2-4) using the collocation method (Park et al. 1996, Schapery 1962).

$$\log\left|E^*\right| = \delta + \frac{\alpha}{1+\frac{1}{e^{\beta+\gamma\log(f_R)}}} \tag{2-2}$$

$$\log(a_T) = a_1T^2 + a_2T + a_3 \tag{2-3}$$

$$E(t) = E_\infty + \sum_{i=1}^{m} E_i e^{-t/\rho_i} \tag{2-4}$$

where

a_1, a_2, a_3	=	regression coefficients,
$\|E^*\|$	=	dynamic modulus, MPa,
δ	=	minimum value of dynamic modulus,
$\delta+\alpha$	=	maximum value of dynamic modulus,
β, γ	=	material constants describing the shape of the sigmoidal function,
$E(t)$	=	relaxation modulus, MPa,
E_∞	=	equilibrium modulus, MPa,
E_i	=	relaxation strength, MPa,
ρ_i	=	relaxation times, s,
m	=	number of Maxwell elements, and
t	=	time, s.

An Excel solver developed at NCSU, named FlexMAT™, automates the above steps and provides the Prony series representation of the relaxation modulus. The output parameters obtained are used as material model property inputs for the numerical modeling software, FlexPAVE™ 1.1. Table 2-1 presents the t-T shift factor function coefficients for the mixture obtained while fitting Equation (2-2).

Table 2-1. Shift Factor Coefficients of RS9.5C RAP-40 Study Mixture

Shift Factor Coefficient	Value
a_1	9.63×10^{-4}
a_2	-0.167
a_3	3.084

2.3 Tack Coat

The NCDOT Quality Management Service manual (NCDOT 2018), Table 605-1, stipulates an optimal application rate of 0.181 L/m^2 (0.04 gal/yd^2) for emulsified tack coats, which eventually leaves a residue of 0.03 gal/yd^2. Emulsified tack coats generally are not recommended for geosynthetic product applications for several reasons. First, the optimal tack coat application rate for geosynthetic-reinforced pavements is 12 to 50 times higher than the optimal residual application rate for unreinforced pavements, depending on the selected geosynthetic product. Such an increase in the tack coat application rate does not allow the emulsion to cure effectively due to the thick emulsion layer that forms on the pavement surface. Further, although emulsified asphalt has been used successfully as a tack coat in some cases, the bond strength has developed more slowly than when using hot binder and sufficient time should be provided for emulsions to break and set before the geosynthetic product is placed (Button and Lytton 2007). In addition, an increase in the tack coat application rate during geosynthetic application facilitates run-off of the emulsion, causes a non-uniform distribution of the tack coat, and increases the potential for debonding. Hence, a hot binder of PG 64-22 was selected as the tack coat for this study.

Earlier studies have reported that the variability in the target and achieved application rates of tack coats in the field ranges from 4% to 106% (Al-Qadi et al. 2008, Mohammad et al. 2012). Based on such variability, the dry and wet conditions in the field can be mimicked by varying the residual application rate by ± 66% of the optimal residual application rate for unreinforced sections, i.e., ± 0.091 L/m^2 (0.02 gal/yd^2). Hence, for the unreinforced control specimens in this study, three residual application rates of PG 64-22 asphalt binder, 0.045 L/m^2 (0.01 gal/yd^2), 0.136 L/m^2 (0.03 gal/yd^2), and 0.226 L/m^2 (0.05 gal/yd^2), were used. The optimal application rates used for the geosynthetic-reinforced specimens follow the manufacturers' recommendations. The dry and wet application rate conditions were determined by adding and reducing ± 0.091 L/m^2 (0.02 gal/yd^2) from the manufacturer's optimal application rate, respectively. Table 2-2 provides a summary the tack coat application rates used in this project.

Table 2-2. Summary of Tack Coat Application Rates for Geosynthetic Products Used in Study

Nomenclature	**CS**	**PC#1**	**PC#2**	**PM**	**PF**	**PaG**
Tack coat type	PG 64-22					
Application rate, gal/yd^2 (L/m^2)	0.03 (0.14)	0.14 (0.63)	0.33 (1.49)	0.12 (0.59)	0.08 (0.36)	0.23 (1.04)

2.4 Dynamic Shear Rheometer (|G*|) Test of Tack Coat Binder

The application of the t-T superposition principle to determine the ISS and interface shear stiffness of geosynthetic-reinforced AC was verified by Cho and Kim (2016). In that study, GlasGrid-reinforced asphalt concrete core specimens were sheared in a MAST under constant displacement to measure the ISS at different test temperatures. The t-T shift factors (a_T) of the AC mixture measured via dynamic modulus testing were used initially to verify the t-T superposition principle for the MAST test outcomes. The MAST test results obtained from the unreinforced specimens were used to create a mastercurve with the aid of the mixture's a_T. However, the MAST tests of the geosynthetic-reinforced specimens demonstrated spurious results using the same mixture's a_T. Therefore, using a dynamic shear rheometer (DSR), frequency sweep tests were conducted using a tack coat asphalt binder to obtain the asphalt binder a_T. The asphalt binder a_T was used successfully to construct an ISS mastercurve for the geosynthetic-reinforced specimens. Thus, the conclusion drawn from the Cho et al. (2017b) study is that the mixture a_T applies to unreinforced MAST test specimens, whereas the asphalt binder a_T is applicable for geosynthetic-reinforced specimens.

In this study, ISS tests using the MAST were carried out on geosynthetic-reinforced specimens. Asphalt binder PG 64-22 was used as the tack coat. As explained, the tack coat asphalt binder a_T is a requirement for mastercurve construction. The DSR measures the dynamic shear modulus ($|G^*|$) and determines the t-T shift factors of the asphalt binder. The DSR model used in this study, Anton Paar MCR 302, is a user-friendly device that is capable of wide temperature ranges, as low as -160°C to as high as 1000°C, in minutes for any type or combination of rheological tests. These mechanical tests were performed as frequency sweep tests at 5°C, 20°C, 35°C, 50°C, and 64°C. The loading frequency ranged from 0.1 Hz to 30 Hz at 1% shear strain amplitude. The frequency sweep tests were designed to help construct mastercurves of the dynamic shear modulus values and obtain t-T shift factors for the binder and emulsion residue used in this study. The asphalt residue used for DSR testing was recovered according to AASHTO R 78-16 (AASHTO 2020b) Method B.

Analysis of DSR test outcomes is a simple process due to the long-established standards and practice of the device. If the results of any two tests of the same emulsion type exceed the recommended 6.4% difference specified in AASHTO T 315-12 (AASHTO 2020c), then neither result should be used, and the emulsion must be retested. In this study, the DSR test results were averaged per emulsion and input into a mastercurve template builder using an Excel spreadsheet. This Excel spreadsheet uses the dynamic shear modulus, frequency, and temperature from the DSR tests to calculate the shift factors for each emulsion by fitting the data points to the Christenson–Anderson–Marasteanu (CAM) model (Christensen and Anderson 1992) at a reference temperature, as given in Equation (2-5). The general form of the t-T shift factor equation is given in Equation (2-6), where $|G^*|_g$ is the glassy dynamic shear modulus and is equal to 1 GPa for asphalt binder. ω_c, m, and v are the CAM model fitting parameters for the dynamic shear modulus mastercurve. Equation (2-6) describes the reduced frequency, ω_R, where a_T is the shift factor at temperature T and ω is the actual testing angular frequency.

$$\left|G^*\right|(\omega_R) = \left|G^*\right|_g \left[1+\left(\frac{\omega_c}{\omega_R}\right)^{v}\right]^{-\frac{m_e}{v}} \tag{2-5}$$

$$\omega_R = a_T \times \omega \tag{2-6}$$

where

$\lvert G^*\rvert$	=	dynamic shear modulus,
$\lvert G^*\rvert_g$	=	glassy dynamic shear modulus when frequency tends to infinite,
ω_c	=	constant, location parameter where loss modulus equals storage modulus,
m_e, v	=	constant, dimensionless shape parameter.

Equation (2-3) was employed to fit the t-T shift factor. Table 2-3 presents the shift factor coefficients for each emulsion in this study, measured at the reference temperature of 20°C. Figure 2-6 shows the dynamic shear modulus mastercurves for various tack coats.

Table 2-3. Shift Factor Coefficients of PG 64-22 Binder Tack Coat Used in Study

Shift Factor Coefficients	**a_1**	**a_2**	**a_3**
PG 64-22	0.000823	-0.15368	2.741548

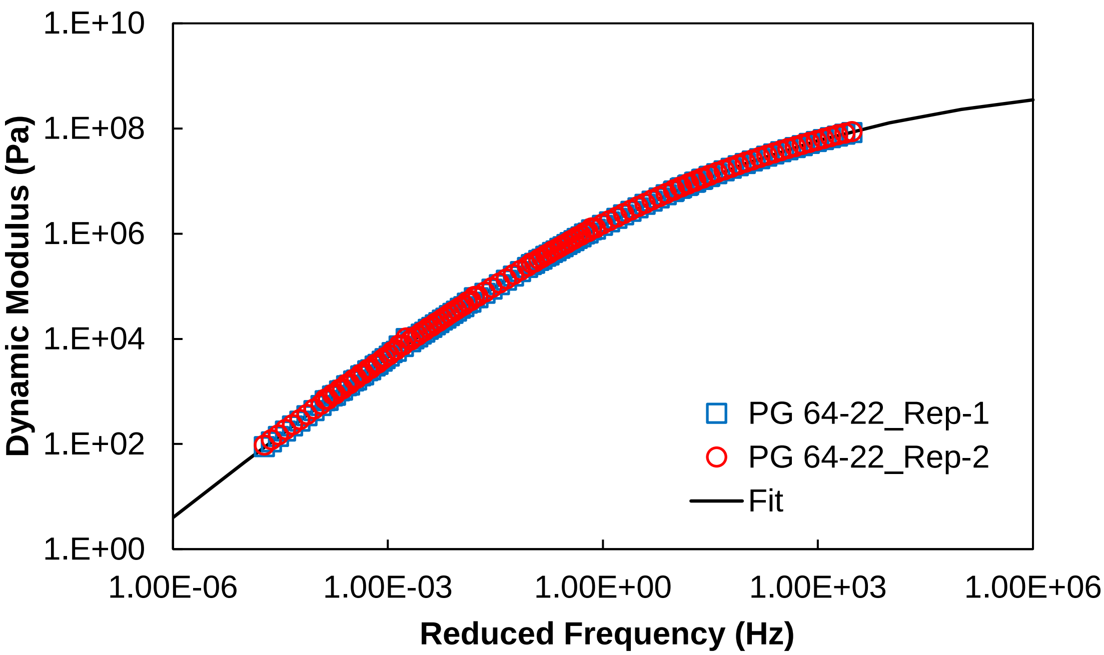

Figure 2-6. Dynamic shear modulus mastercurves for PG 64-22 binder tack coat.

2.5 Geosynthetic Products

The current project used five different geosynthetic reinforcements as interlayers. Table 2-4 provides the nomenclature details for each geosynthetic product type, and the acronyms are used hereafter. Table 2-5 presents the properties of each geosynthetic product supplied by the manufacturer. Figure 2-7 presents images of these five different geosynthetic products.

Table 2-4. Nomenclature Details for Different Geosynthetics Types

Acronym	Acronym Expansion
PC#1	Paving Composite #1
PC#2	Paving Composite #1
PM	Paving Mat
PF	Paving Fabric
PaG	Paving Grid

Table 2-5. Properties of Study Geosynthetic Products

Physical Properties			Mass/unit area	Tensile strength (kN/m)	Strip tensile strength (N/50 mm)	Grab tensile strength	Tensile elongation	Melting point	Asphalt retention
Units	Metric		g/m^2	kN/m	N/50 mm	N	%	°C	L/m^2
	Imperial		oz/yd^2	lb/in.	lb/2 in.	lb	%	°F	gal/yd^2
Paving Composite	PC#1	Metric	270	50	-	-	≤ 3%	255	(Bitumen coated > 60%)
		Imperial	8	285	-	-	≤ 3%	490	
	PC#2	Metric	678	115	-	-	≤ 3%	800	1.2
		Imperial	20	655	-	-	≤ 3%	1472	0.27
Paving Mat	PM	Metric	237	50			<5	>232	0.47
		Imperial	7	280			<5	>450	0.1
Paving Grid	PaG	Metric	405	100			≤ 3%	>232/>820	Pressure-sensitive adhesive backing
		Imperial	12	571			≤ 3%	>450/>1508	
Paving Fabric	PF	Metric	139	-	-	449	50%	160	0.91
		Imperial	4.1	-	-	101	50%	320	0.2

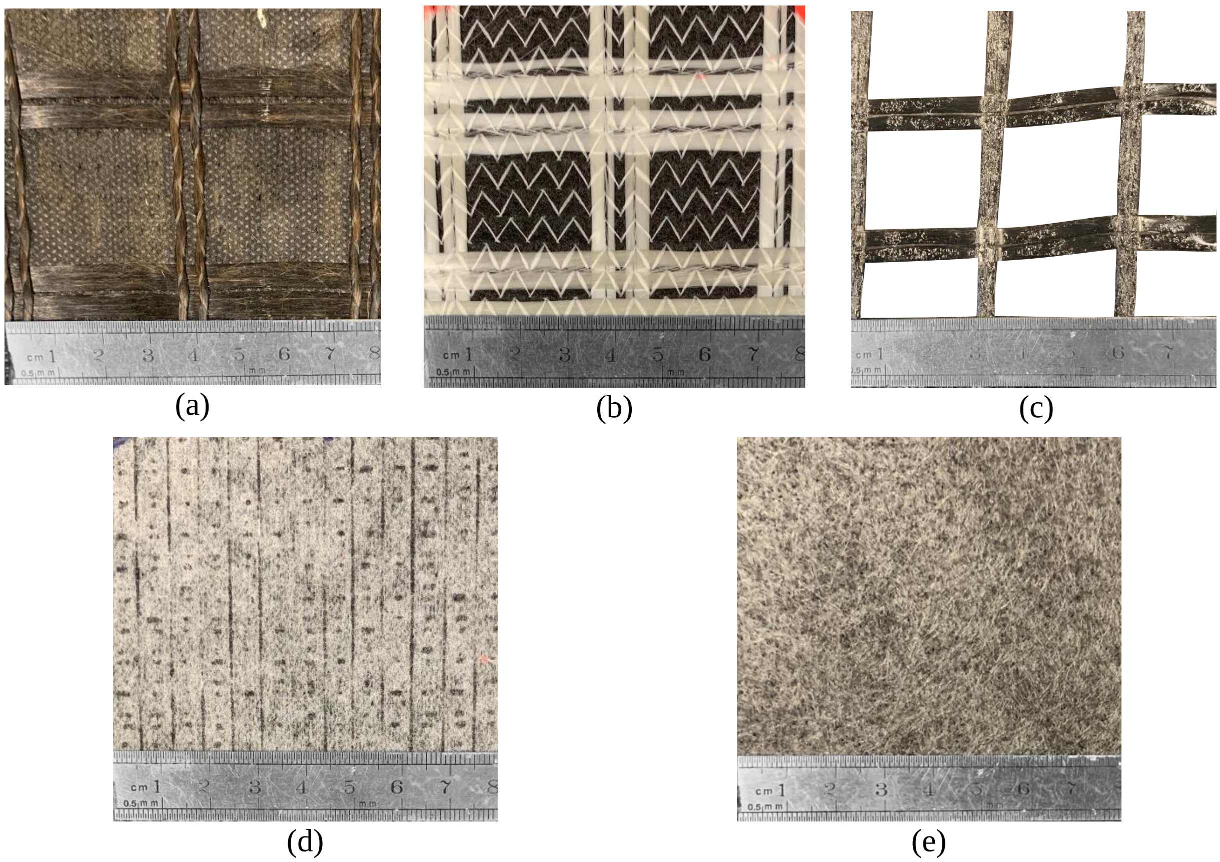

Figure 2-7. Geosynthetic samples: (a) PC#1, (b) PC#2, (c) PaG, (d) PM, and (e) PF.

Chapter 3. Test Methodology

3.1 Interlayer Shear Strength Tests

The MAST was employed in this project to measure the ISS of various tack coat interfaces. Five different geosynthetic-reinforced AC specimens were tested for ISS under various test conditions. All the MAST test specimens were loaded in monotonic mode to shear in order to investigate the effects of temperature, loading rate, confining pressure, and application rate on the ISS of the materials. Table 3-1 presents the factors and parameters used to create the various ISS test conditions.

Table 3-1. Interlayer Shear Strength Test Conditions

Factors	**Number of Levels**
Geosynthetic Type	6 (CS, PC#1, PC#2, PaG, PF, and PM)
Temperature	3 (23°C, 35°C, 54°C)
Loading Rate	1 (0.2 in./min)
Confining Pressure (Normal Stress)	3 (69 kPa, 276 kPa, 483 kPa)
Application Rate (Residual)	3 (Wet, Optimal, Dry)

3.1.1 Laboratory Fabrication of MAST Test Specimens

Several steps are involved in the fabrication of double-layered MAST test specimens: (1) MAST test sample compaction using a Superpave gyratory compactor, (2) geosynthetic material preparation of the MAST test samples, (3) geosynthetic interlayer installation of the MAST test samples, (4) tack coat applied to MAST test samples, and (5) MAST test specimens extracted from the MAST test samples. The detailed explanation of each step is provided in Appendix D.

3.1.2 Air Void Study

The production of consistent MAST test specimens plays a crucial role in interface shear tests. In order to achieve uniform samples in this project, the research team investigated the air void contents of the gyratory-compacted specimens. The major aim of the air void study was to obtain the same air void content for both the bottom and top layers.

Table 3-2 presents the air void contents of the MAST test specimens obtained using the saturated surface-dry method. A clear difference in the achieved air voids is evident when the target air void content of the same sample was used for the top and bottom layers. Moreover, when targeting an air void content below 6% for the bottom layer, the number of gyrations exceeds 130, which is far above the design number of gyrations (N_{design}) of 75. The resultant excessive shear causes the aggregate to break, negatively affecting the asphalt mixture's performance as well as the interface bond. Hence, in this study, the air void content of 7% was targeted for the MAST test specimens. Table 3-3 presents further air void content study verification.

Table 3-2. MAST Specimens: Air Void Content

No.		1	2	3	4
Sample Target Air Void Content		8.7%	8.2%	7.8%	7.3%
No. of Gyrations	Bottom	73	94	139	140
	Top	21	27	29	35
Achieved Air Void Content	Sample	8.1%	7.5%	7.0%	6.1%
	Specimen	7.3%	6.6%	6.4%	5.5%
	Top Layer	7.4%	7.2%	7.0%	6.3%
	Bottom Layer	6.9%	6.1%	5.9%	5.0%

Table 3-3. Verification of Air Void Study Results

Sample Target Air Void Content		No. of Gyrations		Achieved Air Void Content		
Top	Bottom	Bottom	Top	Specimen	Top Layer	Bottom Layer
8.70%	8.00%	70	22	6.94%	7.15%	6.76%

Figure 3-1 shows the relationship between the target air void contents and the achieved air void contents for the different beam specimen layers. Based on these results, the design air void contents of 8.7% and 8.0% were chosen for the top and bottom layer compaction, respectively.

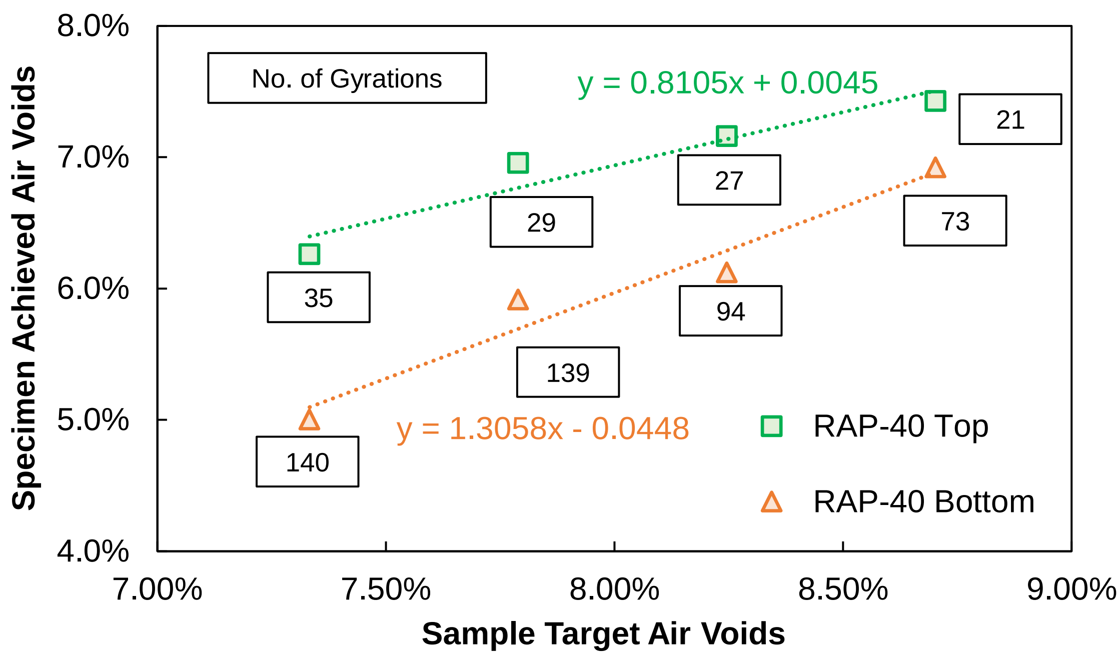

Figure 3-1. Target and achieved air void content relationship for different layers.

3.1.3 Modified Advanced Shear Tester Tests

Recent work at NCSU has utilized the MAST, a shear test device that is used to perform confined shear tests of layered asphalt specimens, both with and without geosynthetic interlayer systems. This NCSU work notably led to the development of shear strength mastercurves for bond strength levels at various combinations of loading rate, temperature, tack coat material, and confining pressure. Figure 3-2 presents the loading configurations and components used in MAST testing.

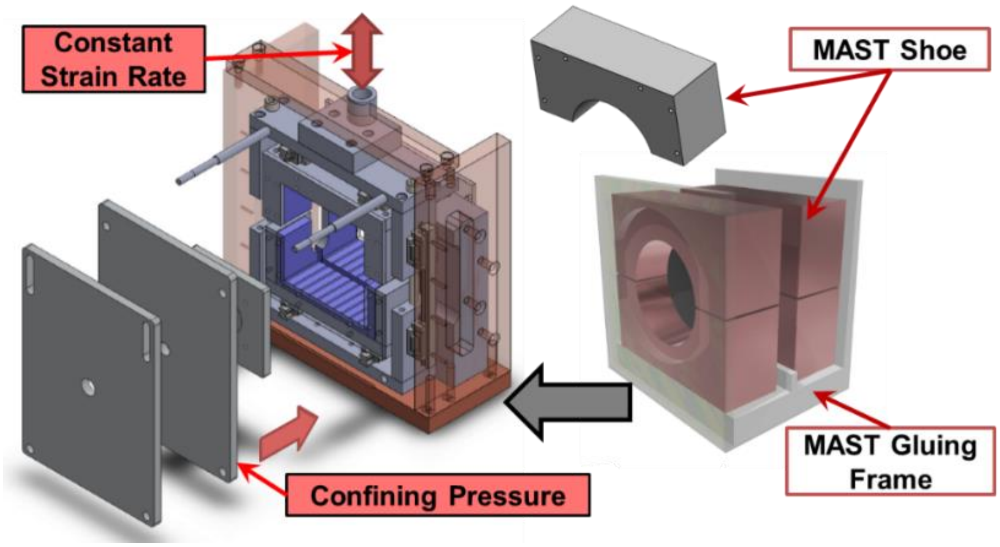

Figure 3-2. Loading configurations of MAST test set-up.

Procedure for gluing specimen to MAST shoes

The MAST shear test is a quick test that induces substantial loading in a short time at the specimen interface. The boundary conditions of the MAST test set-up support the development of bending moments within each layer of the specimen that rotate the specimen. However, a weak grip between the specimen and the testing jig could lead to slippage in the normal/confinement direction and thus to erroneous outcomes. Therefore, utmost care was taken in this study to affix the specimen to the jig with the aid of metal 'shoes'. A MAST shoe set consists of two pairs of shoes and a shoe frame that holds the specimen in the shoes for gluing with epoxy. An 8-mm gap is present between the shoes in each pair. The step-by-step procedure for gluing the specimen to the jig is shown in Figure 3-3 (a) through (f), followed by a written description of the process.

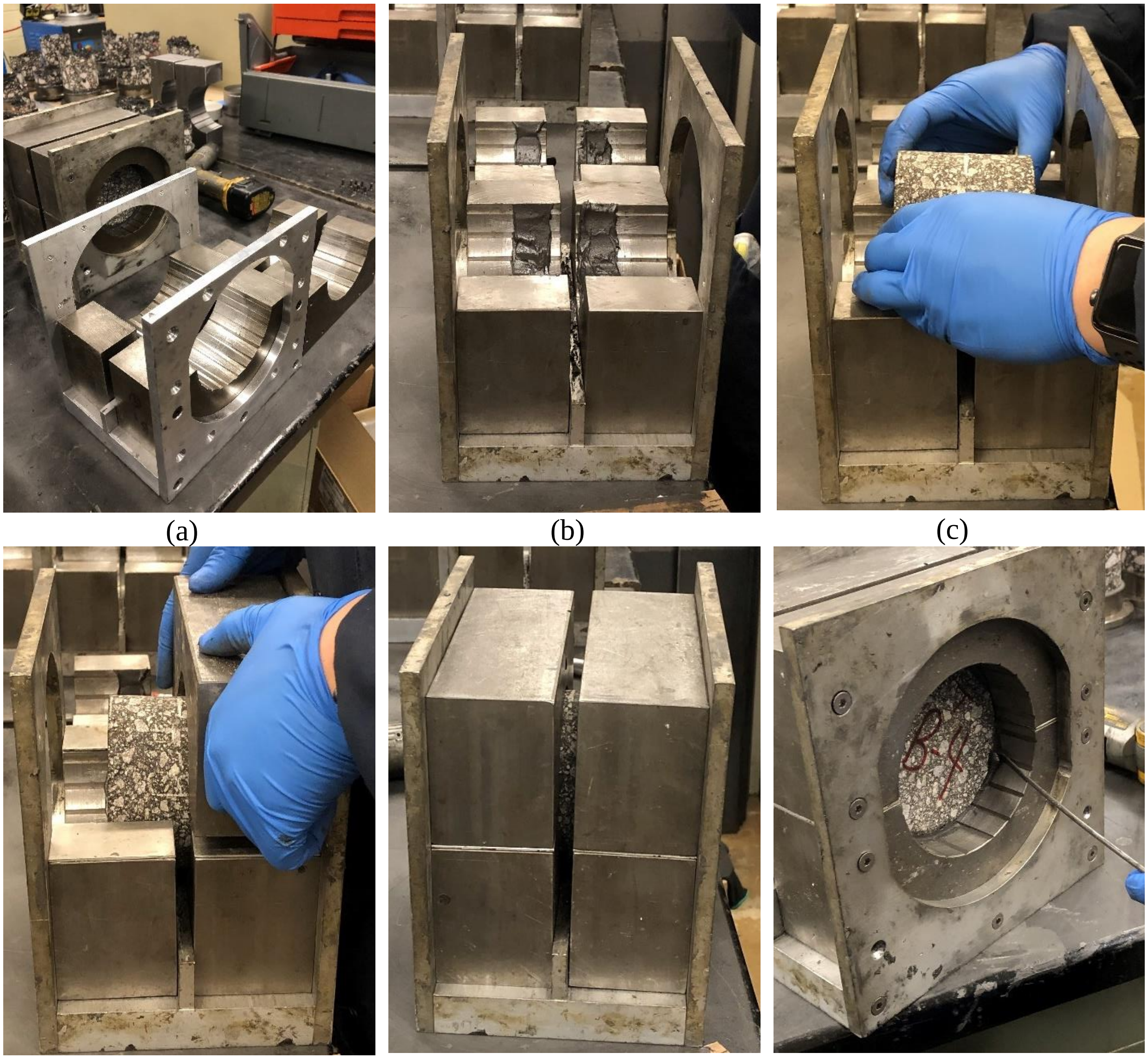

(d) (e) (f)

Figure 3-3. Gluing procedure for MAST test specimen: (a) bottom shoes tightened on gluing jig, (b) application of glue on bottom shoes, (c) specimen placement on bottom shoes, (d) upper shoe installation above specimen, (e) specimen with all shoes in place, and (f) trimming extra glue from shoe edges.

1. In accordance with the manufacturer's recommendation to prepare epoxy glue, mix the glue agents at a ratio of 6:1, i.e., 54 g of plastic steel putty (black) and 9 g of putty hardener (white) for one pair of shoes. Place the necessary quantity of the glue agents on mixing cardboard and mix well for two minutes to achieve a uniform grey paste.
2. Place the bottom shoe on the metal frame and affix it to the frame using screws, as shown in Figure 3-3 (a).
3. Divide the glue on the mixing card into four equal portions and apply two portions, as shown in Figure 3-21 (b). Repeat for the second pair of shoes.

4. Carefully place the specimen on the bottom shoe, as shown in Figure 3-3 (c). Position the interface of the specimen such that it is at the center of the gap between the shoes. Note: The geosynthetic installation direction marked on the specimen must be in line with the shearing direction, i.e., perpendicular to the ground.
5. Place the upper shoes over the specimen, as shown in Figure 3-21 (d) and (e), and tighten the frame. Fill any gap between the lower and upper shoes with metal plates.
6. Remove any excess epoxy glue that extrudes at the specimen edges using a spatula, as shown in Figure 3-21 (f).
7. Allow a glue curing period of 16 hours prior to using with the MAST.

Preparation and gluing of speckled paper for DIC testing

The DIC technique was employed to measure on-specimen displacements. A detailed description of the technique is given in Section 3.4.1, Digital Image Correlation Technique. The DIC algorithm needs a distinct random point to track the specimen's movement between consecutive images and determine the displacement. Speckled paper is used for this purpose. Pieces of speckled paper were cut to dimensions of 3.75 cm (1.48 in.) by 2.45 cm (1 in.). The samples were placed in a tray and sprayed with matte black paint from a specified distance, as shown in Figure 3-4 (a). Figure 3-4 (b) shows the resultant speckled paper. The other side of the speckled paper was sprayed with glue and pasted onto the MAST shoes, as shown in Figure 3-4 (c).

(a) (b) (c)

Figure 3-4. Preparation of speckled paper for DIC image capture: (a) spray painting paper, (b) finished speckled paper, and (c) speckled paper on MAST shoes to track on-specimen displacement using DIC technique.

Procedure for loading the specimen glued to the shoes into MAST jig

Once the MAST test specimen is glued to the shoes and the speckled paper is pasted onto the surface of the shoes, the shoes must be loaded into the MAST testing jig, as shown in Figure 3-5 (a). The horizontal translation of the MAST shoes is constrained by installing a collar that essentially ties the shoes to the jig. Figure 3-5 (b) shows the confining plate with a load cell added to the jig. Figure 3-5 (c) shows the MAST placed over the material test system (MTS – 810). Once the necessary connection between the actuator piston and the MAST vertical loading rod is established, then the environmental chamber is installed for conditioning the specimen to the test temperature, as shown in Figure 3-5 (d). Figure 3-5 (e) shows the DIC test set-up, and

Figure 3-5 (f) shows the view through the charge-coupled camera. After three hours of conditioning, the MAST test can commence.

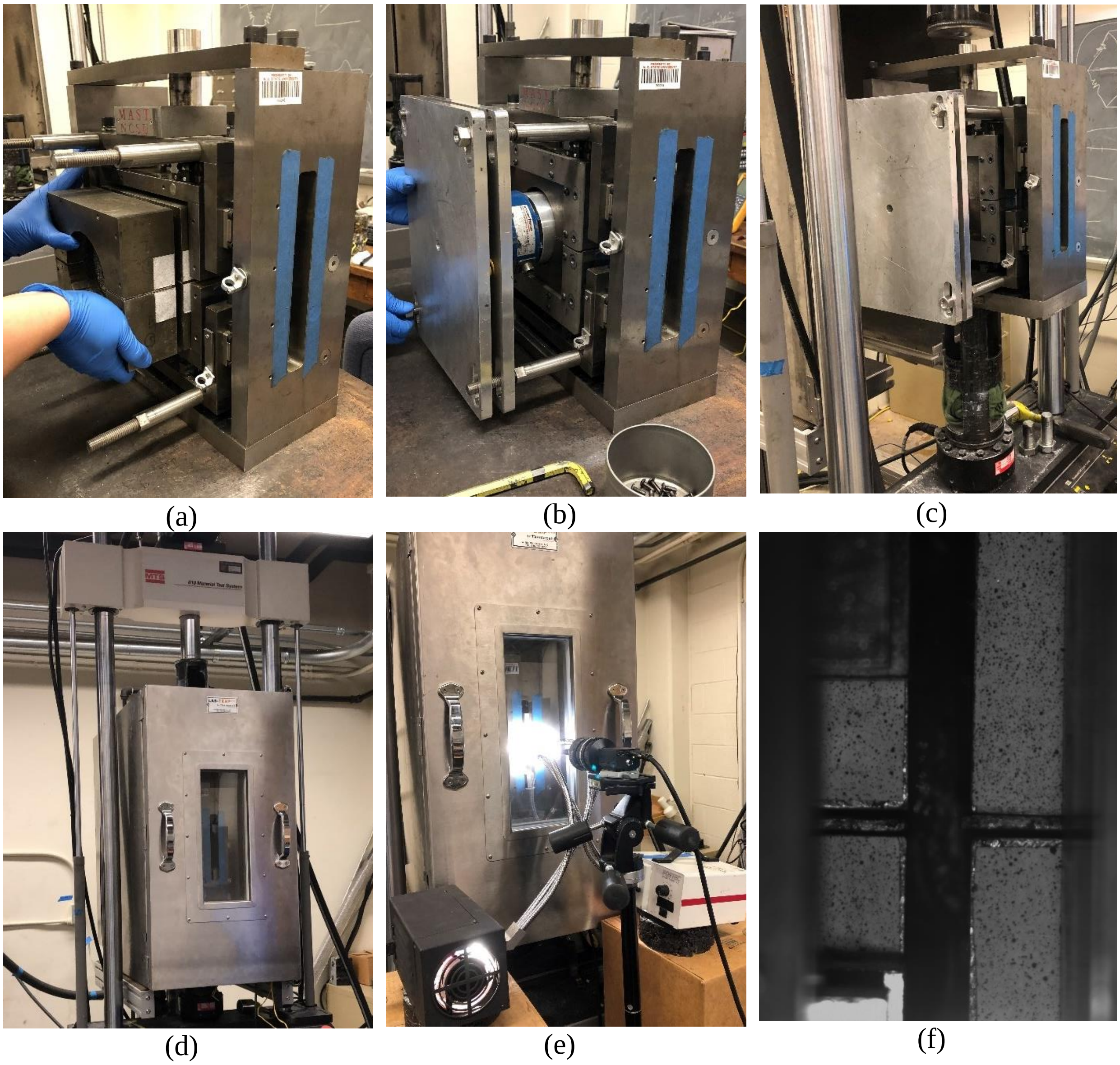

Figure 3-5. (a) Loading MAST shoes with specimen into MAST jig, (b) installing confining pressure plate with load cell, (c) placing the MAST over the MTS 810, (d) environmental chamber, (e) DIC test set-up, and (f) view through DIC camera.

MAST test configuration

The geosynthetic-reinforced specimens were subjected to monotonic shear tests in this study once the specimens reached the test temperature after three hours of conditioning. A load that corresponds to normal stress was applied by tightening the confinement plate against the specimen, as shown in Figure 3-2. All the geosynthetic-reinforced specimens were sheared at a constant displacement (crosshead) rate of 5.08 mm/min (0.2 in./min). The shear force, normal vertical stress, and horizontal displacement were recorded continuously throughout the test. In addition, the DIC technique was used to measure any on-specimen displacement. Figure 3-6 shows the DIC set-up with the MAST.

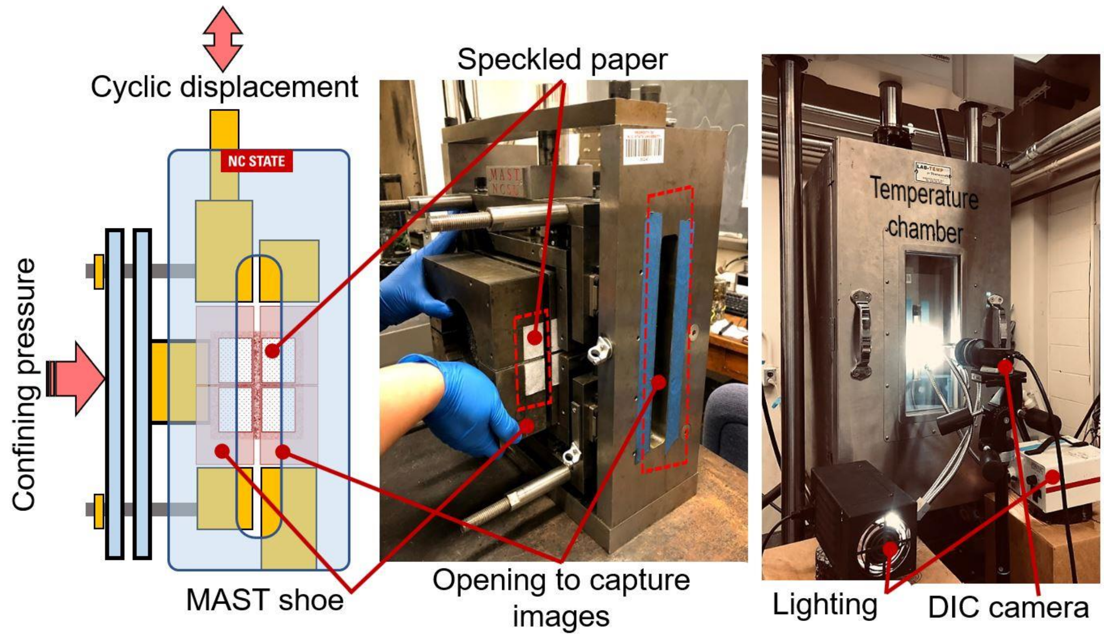

Figure 3-6. MAST test set-up: (a) schematic diagram, (b) loading MAST shoes into loading jig, and (c) test set-up with DIC system.

3.2 Crack Resistance Tests

3.2.1 Laboratory Fabrication of Beam Specimens

The major steps involved in the laboratory fabrication of beam specimens for the NBFTs are (1) compact the slab sample using a roller compactor, (2) prepare the geosynthetic product for slab samples, (3) apply the tack coat using a hot spray gun, (4) place the geosynthetic product on the slab sample, (5) prepare the beam specimen, (6) prepare the beam holding jig, (7) cut a notch in the beam specimen, and (8) speckle the beam specimen for DIC testing. A detailed description of each step is provided below. The detailed explanation of each step is provided in Appendix E.

3.2.2 Air Void Study

Figure 3-7 schematically presents the dimensions of a beam cut into three parts for the air void study. Figure 3-8 (a) shows the actual beam specimens cut into three equal portions. Figure 3-8 (b) shows that the middle one-third of each beam is cut into two pieces, thus creating the bottom layer that is 18-mm (0.7-in.) thick and the top layer that is 36-mm (1.42-in.) thick.

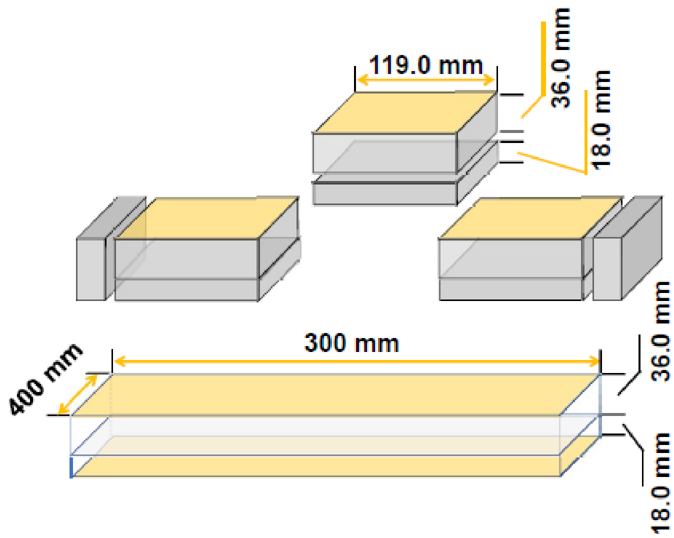

Figure 3-7. Schematic diagram of beam cut into three parts for air void study.

(a)

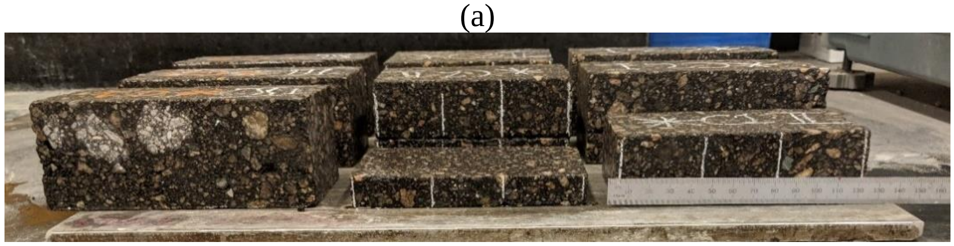

(b)

Figure 3-8. (a) Beam specimen cut into three equal portions and (b) middle one-third portion cut to create bottom (18-mm thick) and top layer (36-mm thick).

The nomenclature used to identify the beam specimens is ‘SYM’ ‘X’ ‘#’ and is ‘SYM’ ‘X’ – ‘Y’ ‘SYM’ for the air void study specimens.

Table 3-4 presents details of each designation.

Table 3-4. Nomenclature Details for Slab Specimens

Designation	Symbol/Acronym	Details
SYM	*	40% RAP
	+	20% RAP
	↑	Top part of top/bottom slab layer
	↓	Bottom part of top/bottom slab layer
X	A, B, C, etc.	Tag for slab sample
Y	T	Top of beam specimen
	B	Bottom of beam specimen
#	1,2,3	Beam specimens cut from a slab, beam in front of forwarding direction is '1'.

For the *B and +B specimens, the target air void content of 8.5% in the top layer resulted in a measured air void content of 12 percent. Visual inspection and height measurements of the slab surface proved the compactor's inability to achieve the target height, thus leading to a higher achieved air void content. However, the bottom layer of the beam specimen in all cases showed an achieved air void content of 10% or greater, irrespective of the target air void content and even after achieving the target height. This difference for the bottom layer of the specimen raises the concern that an air void gradient is present throughout the height of the specimen. The cold compacting face of the roller compactor could be attributed to the cause as well. Hence, the decision was made to flip the bottom layer prior to the top layer compaction. The step-by-step procedure followed for flipping the slab is shown in Figure 3-9.

(a)

(b)

(c)

(d)

(e)

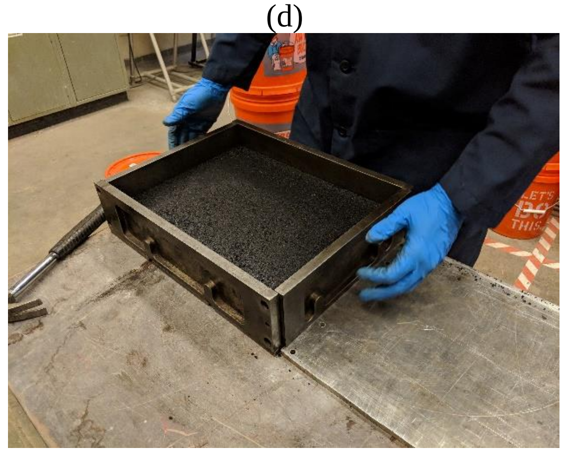

(f)

Figure 3-9. (a) Measuring height of bottom layer to check the level, (b) side plates of mold removed, (c) bottom layer being pushed out of mold, (d) flipping over bottom layer, (e) pushing flipped bottom layer back into mold, and (f) closing sides of mold.

The air void study of the slabs with the bottom layer flipped shows that, for both the RAP-40 and RAP-20 mixtures, the air void content of the bottom layer of the beam specimen (top portion of the bottom layer of the slab) matches the achieved air void content of the top layer whose target air void is higher than 8.5 percent. Figure 3-10 and Figure 3-11 present the air void study results for RAP-40 and RAP-20, respectively. The bottom portion of the same slab sample's bottom layer was measured, and a 2% to 3% difference in the achieved air void content was found. The difference in air void contents indicates an air void gradient in the layers. Because the top layer uses the bottom portion of the layer for the specimen, the air void gradient is not evident, whereas the top portion of the bottom layer (which would become the bottom layer in the beam specimen) shows a higher air void content. Therefore, all the beam specimens were made with the bottom layer flipped before the top layer is placed to achieve a consistent air void content throughout the specimen. However, flipping the bottom layer did not guarantee the consistency of the air void content along the beam depth for all target air void contents. Once the target air void content is below 8.5%, the top layer's air void content does not match the linear trend that is found in the flipped bottom layer. The resistance provided by the RAP coupled with the difficulty in compacting under the constraint of the mold size in the laboratory could be reasons for this outcome. Therefore, to achieve an adequate air void content comfortably under the limited laboratory conditions, the research team decided to achieve an air void content of 10%, which is achievable for both mixtures (RAP-40 and RAP-20), thus allowing comparison of the air void study results.

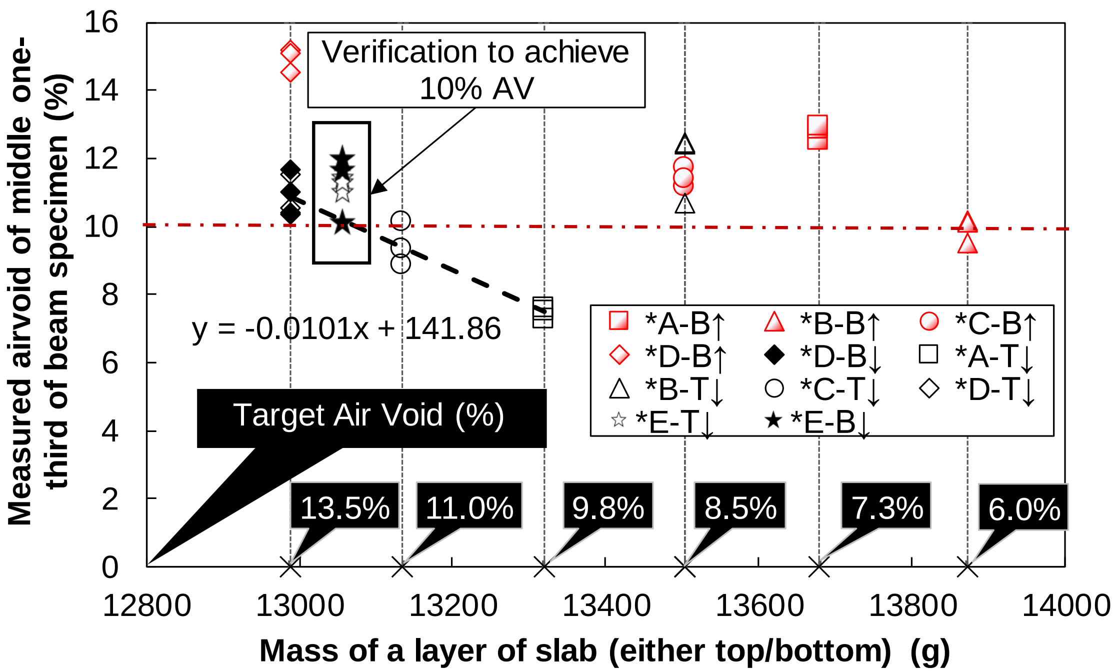

Figure 3-10. Air void study results for RS9.5C RAP-40.

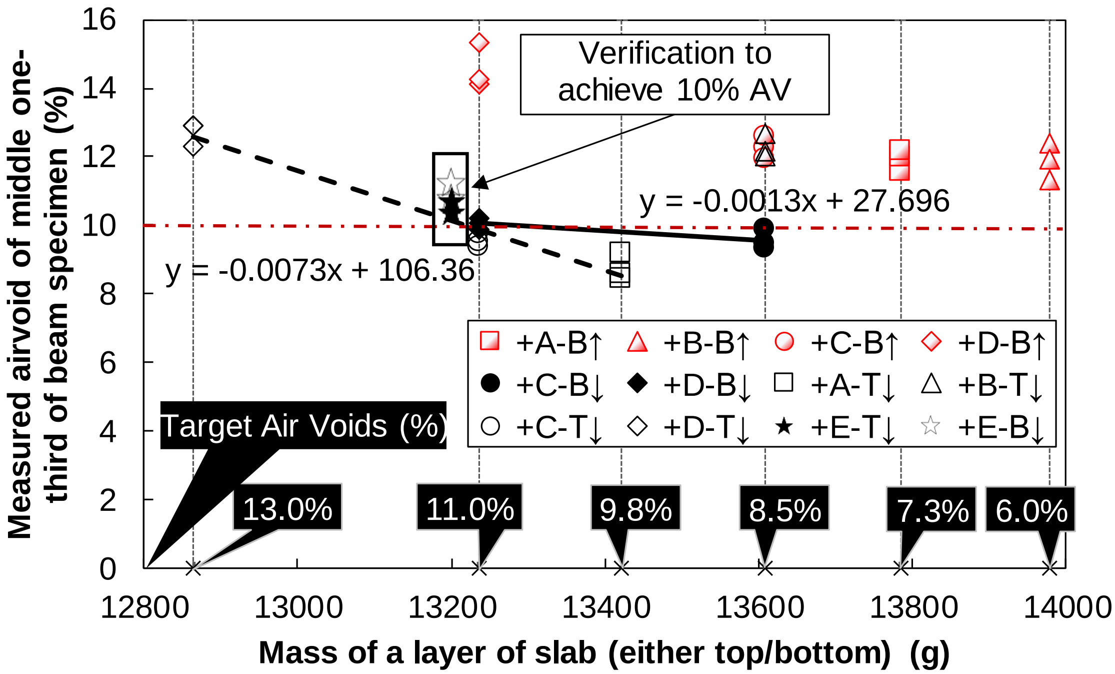

Figure 3-11. Air void study results for RS9.5C RAP-20.

Also, a visual inspection of the side walls of the molds in the compaction direction indicated an imprint of the compaction pattern. Figure 3-46 shows the compaction imprint and indicates the likelihood of an air void gradient in the samples. The imprint was traced and was found to overlap with the beam dimensions, as shown in Figure 3-13, which served to indicate the cause for the air void content variability among the three beam specimens cut from the same slab. The research team then decided to use only two beams from each slab for the performance study in order to maintain air void content uniformity. Figure 3-14 depicts the revised configuration for cutting beams from the slab.

Figure 3-12. Compaction imprint on side walls of mold.

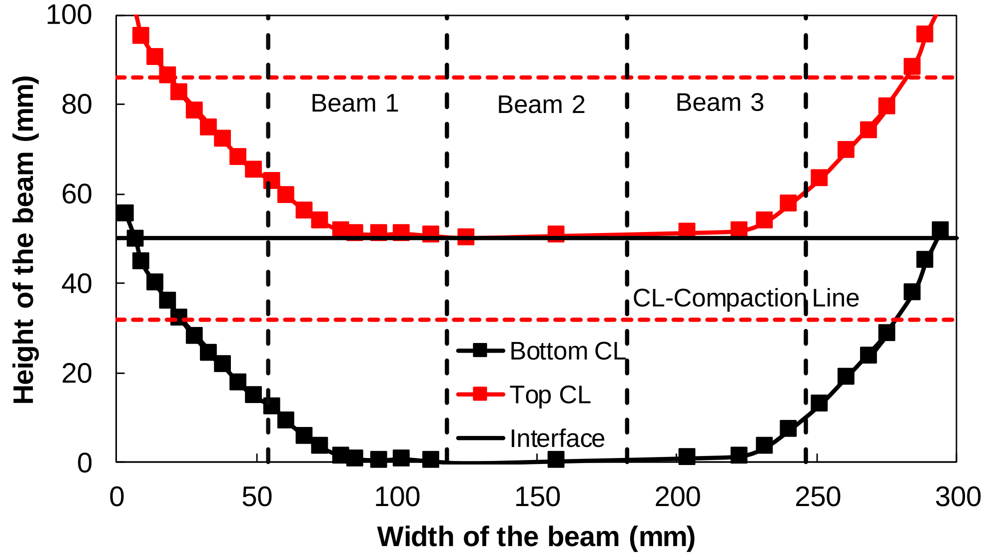

Figure 3-13. Traced imprint of side walls of molds with dimensions of beam overlapping.

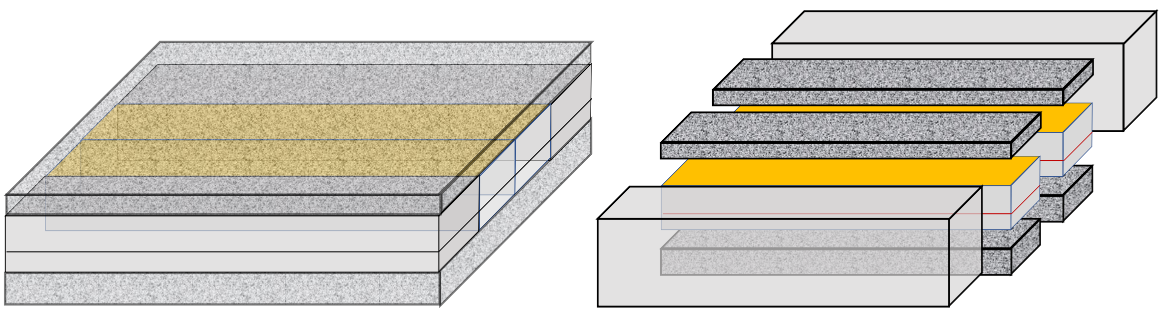

Figure 3-14. Revised configuration for cutting beams for performance study.

In order to confirm these findings, the research team carried out a study of two slab samples, each from a particular mixture type i.e., RS9.5C RAP-40 or RAP-20. In the case of the RAP-40 mixture, three beams were made from the slab. Figure 3-15 shows the variability of the air void content in the RS9.5C RAP-40 slab, with an average air void content of 11.7% and standard deviation of 0.8 for the three beam specimens. Figure 3-16 shows that the two beams made from the RAP-20 mixture had an average air void content of 11% and standard deviation of 0.6. The reduction in the standard deviation of the RAP-20 two-beam configuration compared to the RAP-40 results could be attributed to the absence of the air void gradient that is expected at the edge of the beam in a three-beam configuration.

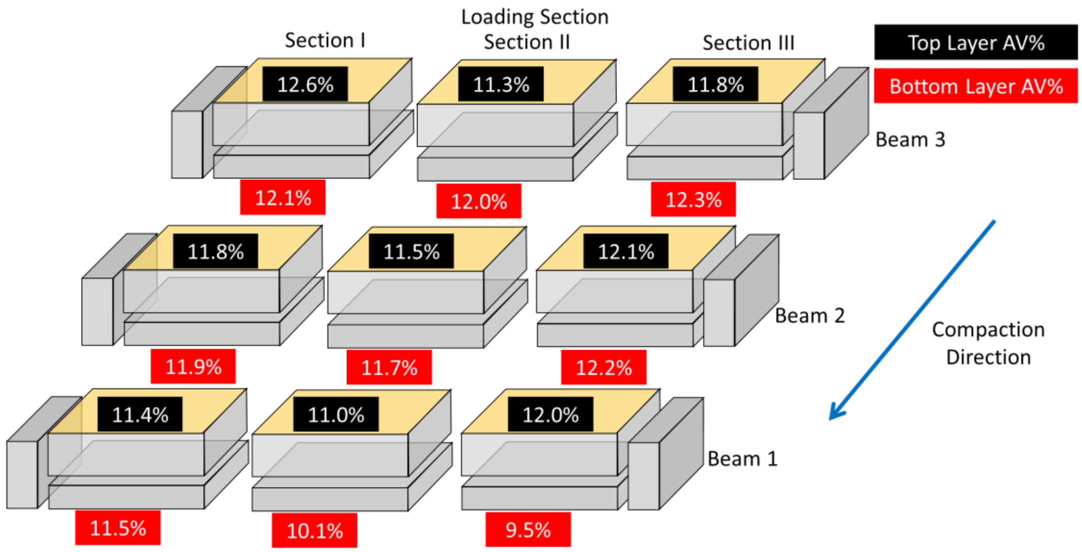

Figure 3-15. Air void study results for RS9.5C RAP-40 mixture beam specimens cut from slab.

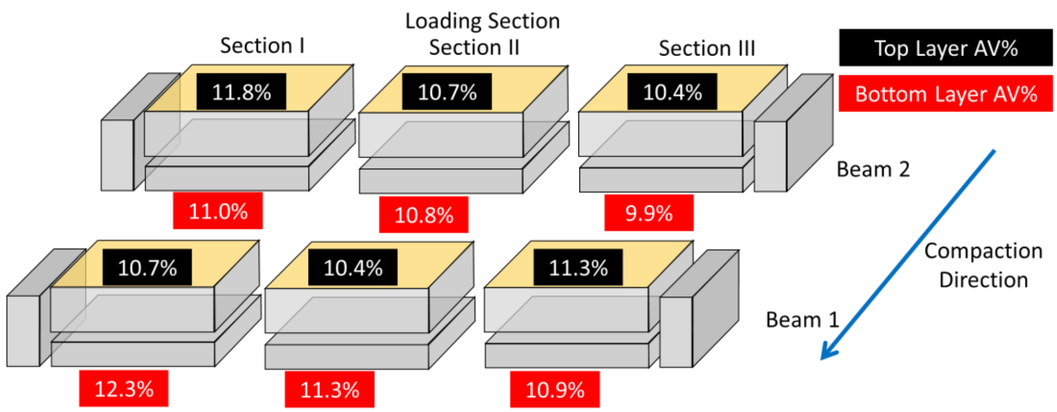

Figure 3-16. Air void study results for RS9.5C RAP-20 mixture beam specimens cut from slab.

3.2.3 Four-Point Bending Beam Fatigue Test

The four-point bending beam test device used in this study simulates the Mode I pavement cracking mechanism via beam bending. Standard beam fatigue tests, ASTM D7460-10 (ASTM 2010) and AASHTO T 321-17 (AASHTO 2017b), were carried out using an AC beam specimen (from a single layer of a slab sample) with dimensions of 50 mm × 63 mm × 380 mm (1.97 in. × 2.48 in. × 14.96 in.) subjected to cyclic loading (control stress/control strain) at a frequency of 10 Hz. AASHTO T 321-17 (AASHTO 2017b) stipulates that a four-point beam loading device should be capable of (1) providing repeated sinusoidal loading at a frequency range of 5 Hz to 10 Hz, (2) subjecting specimens to four-point bending with free rotation and horizontal translation at all load and reaction points, and (3) forcing the specimen back to its original position (i.e., zero deflection) at the end of each load pulse.

The test device from Cox and Sons used in this study complies with AASHTO T 321-17 (AASHTO 2017b). The apparatus was adapted to fit in the MTS 810 Universal Testing Machine (UTM) that is available at the NCSU laboratory. Figure 3-17 shows the loading and free rotation points in the device.

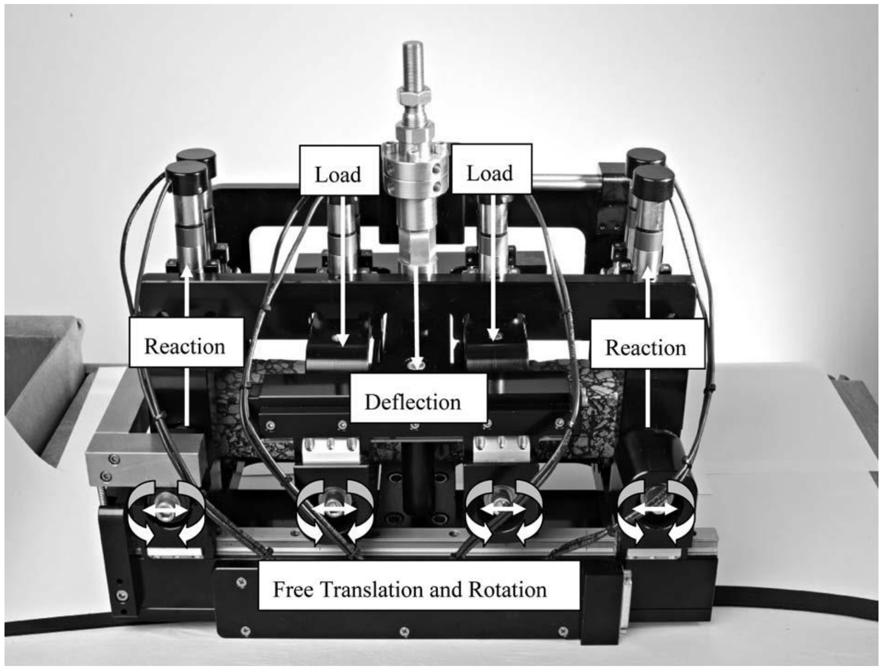

Figure 3-17. Cox and Sons four-point bending beam test apparatus (ASTM D7460-10).

The spacing between the clamps is 119 mm (4.69 in.), and the beam length between the outside clamps is 357 mm (14.06 in.) in this apparatus. A customized environmental chamber with a glass-covered opening, shown in Figure 3-18, was used to fit the apparatus and to condition all the beam fatigue test specimens.

ASTM D7460-10 (ASTM 2010) and AASHTO T 321-17 (AASHTO 2017b) call for the on-specimen displacement control mode; however, the Material Testing System, the servo-hydraulic testing machine used in this study, does not have a feedback system from the on-specimen LVDT. Therefore, the NBFTs were conducted in constant actuator displacement control mode at the frequency of 10 Hz at 23°C. In addition to the displacements measured by the actuator LVDT, on-specimen displacements were measured by an additional LVDT mounted on the neutral axis (i.e., mid-depth) of the beam.

Three different strain values were calculated and used in this study: tensile strain at the bottom of the beam, calculated from the actuator displacement (denoted as ε_{act}); tensile strain at the bottom of the beam, calculated from the on-specimen displacement (denoted as ε_{os}), and tensile strain at the interlayer, calculated from the on-specimen displacement (denoted as ε_{int}). Note that ε_{int} is one-third of ε_{os} and that ε_{int} in the NBFT is the strain of interest when the findings from this study are extended to overlays in the field. Note also that, in actuator displacement control mode, the on-specimen displacement amplitude and therefore ε_{os} will change as the loading continues and the damage in the beam increases, even though the actuator displacement amplitude and ε_{act} are constant throughout the NBFT. In this study, ε_{os} at the 50th loading cycle was used as the initial strain in the NBFTs.

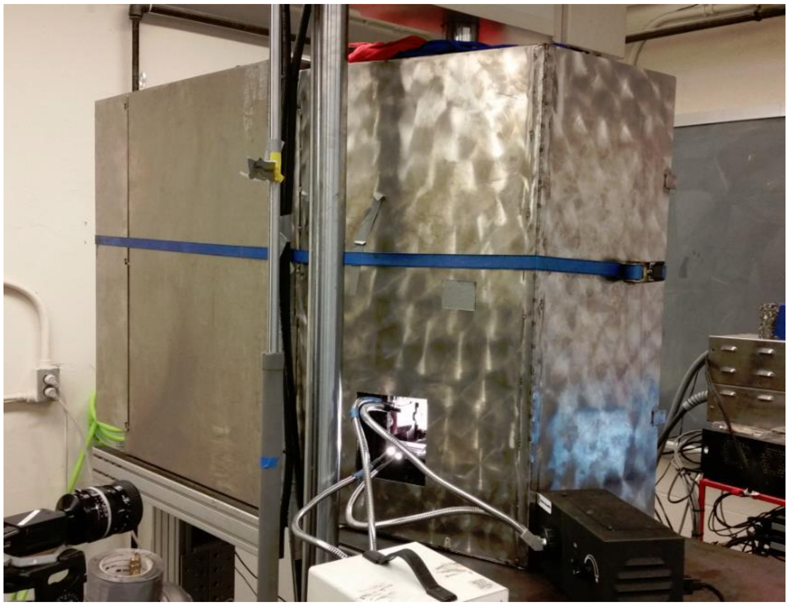

Figure 3-18. Custom-made environmental chamber attached to MTS to control temperature during beam fatigue tests.

3.3 Binder Bond Strength Test

3.3.1 Pneumatic Adhesion Tensile Testing Instrument (PATTI) Test

AASHTO T 361-16 (AASHTO 2020d) details the laboratory test procedure for adhesion testing but does not consider different application rates and cannot be used for field testing. In response, Karshenas (2015) developed a procedure based on AASHTO T 361-16 (AASHTO 2020d) and described the use of an adhesion tester in the field and in the laboratory. Karshenas (2015) also established a strong prediction relationship between the BBS and bond shear strength of AC specimens. The current research extends the Karshenas research by investigating the possibility of applying the t-T superposition principle to the measured tensile strength to build mastercurves.

In this study, PATTI was used to measure the BBS of asphalt binder. PATTI is a self-aligning pneumatic device that is used to measure the pull-off tensile strength of tack coats and the corresponding stress rate at different test temperatures. Figure 3-19 (a) shows the PATTI test set-up used in this study that includes a Quantum Series Gold model, categorized as a Type IV/ Method D test device in ASTM D4541-17 (ASTM 2017). The system applies a true axial force relative to the pull stub to obtain a tensile strength value, as illustrated in the schematic drawing shown in Figure 3-19 (b). This value can quantitatively represent the tensile bond strength between the tack coat and substrate. Note that the PATTI test is not limited to asphalt binder but also can be used to test paint, film, coatings, or most adhesives on a smooth, rough, porous, flat, or curved substrate. The PATTI system can test bond strength levels up to 68,948 kPa (10,000 psi).

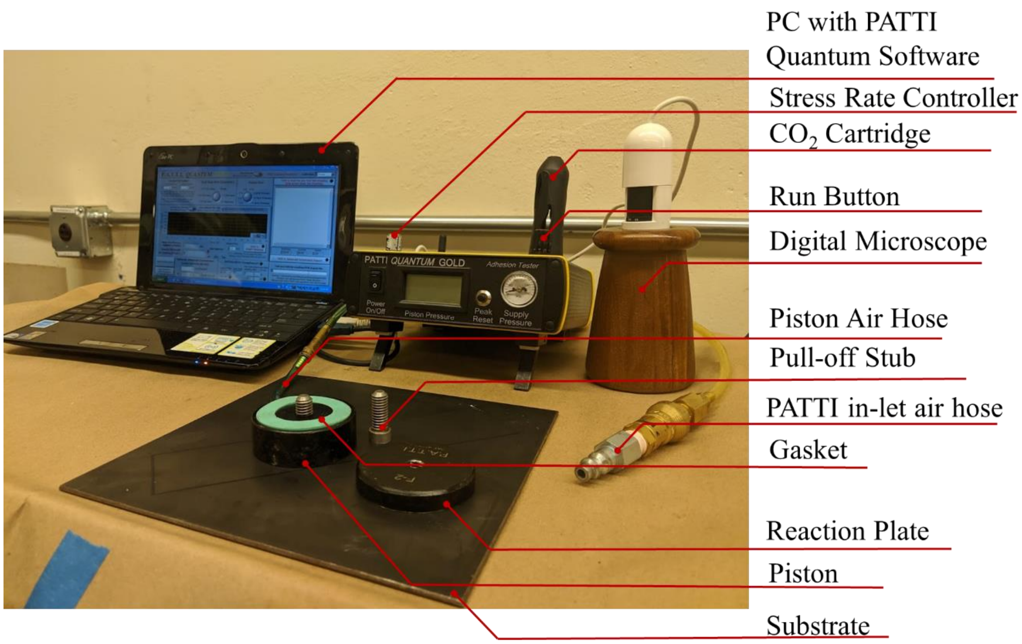

(a)

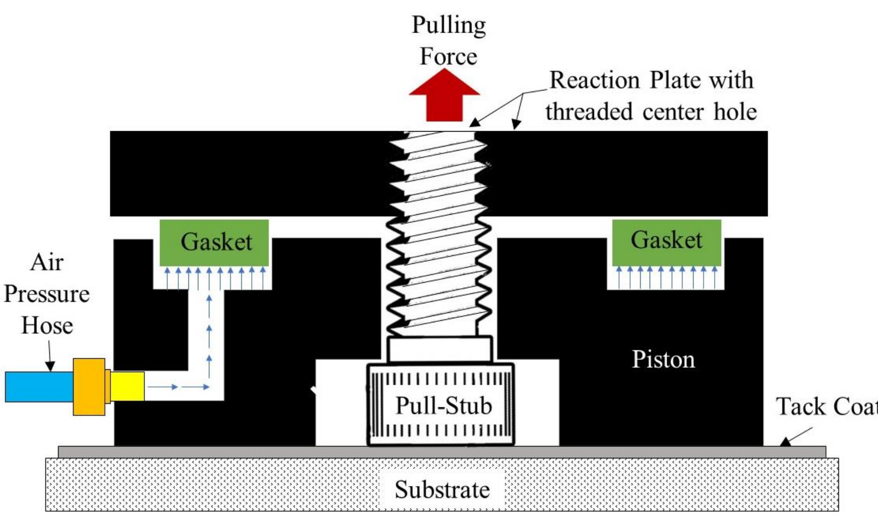

(b)

Figure 3-19. (a) Type IV self-alignment adhesion tester (PATTI) and (b) cross-sectional schematic of self-aligning piston assembly (ASTM D4541-17 (2017)).

3.3.2 Binder Bond Strength Test Methodology Using PATTI

The PATTI test procedure that is described in this section draws from previous research conducted at NCSU (Cho 2016, Karshenas 2015). The fundamental procedure is derived from ASTM D4541-17 (ASTM 2017) and later AASHTO TP 91-13, now AASHTO T 361-16 (AASHTO 2020d). The goal of this guideline is to allow both laboratory and field-testing using

PATTI. Figure 3-20 illustrates the step-by-step procedure for conducting PATTI pull-off tests and the subsequent text provides details regarding each step.

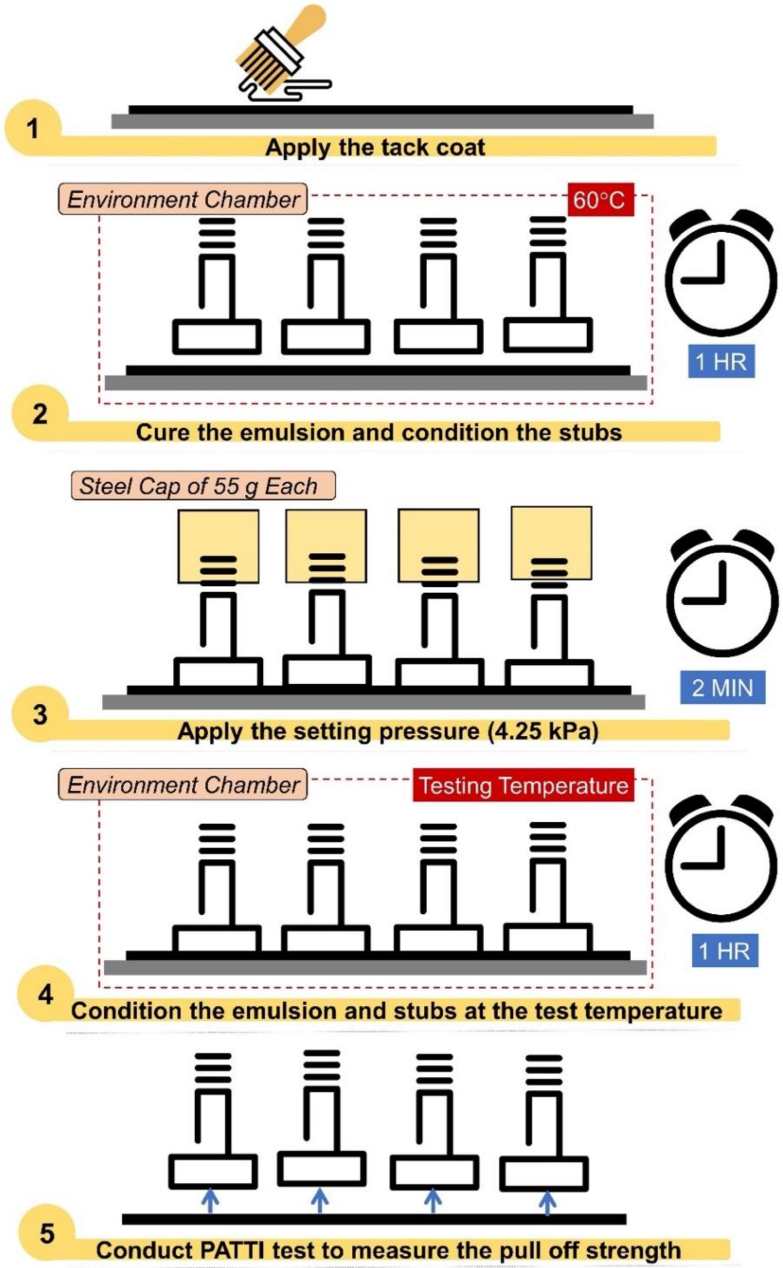

Figure 3-20. Step-by-step procedure for PATTI testing.

Step 1: Prepare tack coat sample and apply tack coat.
The tack coat sample used for PATTI tests can be obtained either by placing a metal plate (substrate) on the existing asphalt surface prior to the application of the tack coat at the construction site or by applying a tack coat with the specified application rate using a foam paintbrush in the laboratory. According to ASTM D4541 (ASTM 2017), a metal substrate should be used when testing pull-off strength. However, the rigidity and surface texture of the substrate

will affect the results of the test, and these characteristics are not controllable variables in field measurements. In this study, the research team used the recommended standard substrate, which is an 11-gauge cold-rolled steel plate with matte finish, in accordance with ASTM A568/A568M-17a (ASTM 2019). The team used this specific plate because of its availability, ease of production, and standardization. Note that a foam paintbrush is to be used only for emulsions, and a hot spray gun is employed to apply hot binder onto the substrate in the lab. Figure 3-21 shows the hot spray gun used to spray Ultrafuse hot binder onto a metal substrate in this study. The metal template is used to confine the spray within the testing area.

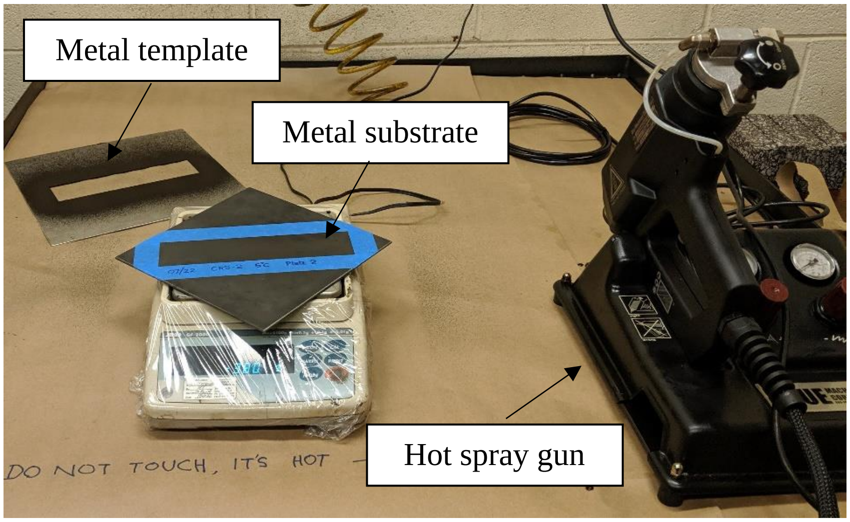

Figure 3-21. Test set-up for hot spray gun usage to apply tack coat for PATTI testing.

Step 2: Cure the emulsion.

The improper curing of emulsion can cause a weak bond. Therefore, allowing sufficient time for curing is crucial for gaining inherent pavement strength, and the length of the curing time depends on the tack coat type. For example, rapid-setting emulsions require a curing period of 30 minutes, whereas slow-setting emulsions need at least an hour to cure. In either case, the pull stubs and substrate with tack coat are heated to the application temperature of 60°C in an oven for their respective curing time. Each substrate sample requires at least three pull stubs or replicates. In the case of hot binder, the substrate with tack coat and pull stubs are heated to the compaction temperature (typically 145°C) for ten minutes to liquefy the binder and activate the tackiness of the binder to bond with the pull-off stub. This heating time of ten minutes was found to be the most appropriate time for this purpose based on the outcome consistency of all the stubs placed after different heating times.

Step 3: Apply setting pressure.

During preliminary testing, once a sample has cured, the heated pull stubs are placed on the tack coat sample, and the pull-off strength is measured after conditioning. In this study, the dominant adhesive failure was observed for the hard and non-tracking tack coats. To mitigate this problem, a metal cap weighing 55.0 g ±1.0 g was placed on top of each pull stub for two minutes at the ambient temperature of the laboratory to ensure the formation of a good bond with the tack coat, as shown in Figure 3-22. This overburden weight was intended to mimic the dead load (stress) of typical surface layers.

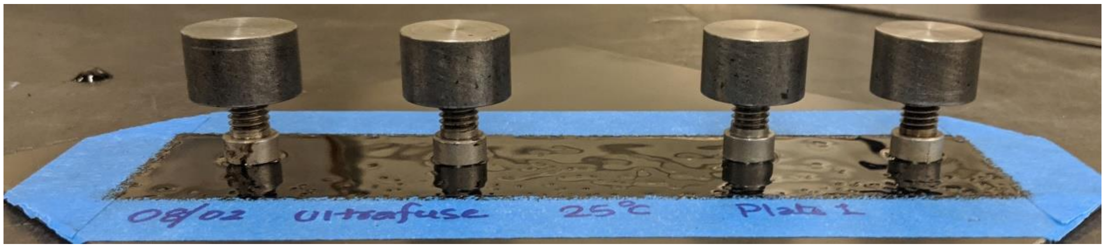

Figure 3-22. Metal caps on pull-off stubs to apply setting pressure.

Step 4: Condition the substrate and stubs.

After two minutes of setting pressure application, the metal caps were removed, and the tack coat sample was conditioned in an environmental chamber at the testing temperature for one hour. Asphalt binder properties are highly dependent on temperature. ASTM D4541-17 (ASTM 2017) recommends that the stress rate range should fall within a small bandwidth of 345 kPa/s to 1,034 kPa/s (50 psi/s to 150 psi/s) such that the PATTI test is conducted at numerous temperatures to obtain the necessary overlap among the pull-off strength values, which in turn aids the mastercurve construction. For this study, tests were run at 5°C, 7°C, 10°C, 13°C, 15°C, 17°C, 19°C, 22°C, 25°C, 30°C, 35°C, 44°C, and 53°C using the residual application rate of 0.14 L/m^2 (0.03 gal/yd^2).

Step 5: Conduct PATTI tests to determine pull-off tensile strength.

The standard practice specified in ASTM D4541-17 (ASTM 2017) is to pull off the stubs for at least three substrate replicates (four stubs per substrate) at the same conditioning temperature. The PATTI Quantum software that accompanies the device records the peak tensile strength and changes in stress with time. However, this tensile strength value may not be a legitimate result because it depends on the failure mode of the pull stub, the load rate, and the repeatability.

The PATTI system can apply only a limited range of loading rates during BBS tests of asphalt binder to meet acceptability standards. ASTM D4541-17 (ASTM 2017) and the PATTI owner's manual state that the load rate shall not exceed 1,034 kPa/s (150 psi/s), as the variability in the measured BBS values for asphalt binder are too high after this point. Therefore, most of the load rates used in this research fell within 345 kPa/s to 1,034 kPa/s (50 psi/s to 150 psi/s). According to ASTM D4541-17 (ASTM 2017), the procedure is to start with the load dial in the 'off' position and slowly turn the dial counterclockwise to release the air pressure after pressing the 'Run' button until the desired stress rate is achieved. The major difficulty of the stipulated procedure is maintaining a constant stress rate. In fact, a nonlinear stress-growth curve was observed in this study, as shown in Figure 3-23 by the black 'rotating knob' curve. An alternative to this procedure is to set the load dial to a specific position prior to running the test. This position is determined based on multiple trials and is usually below the quarter of the dial circle. The dial is left at this position for the entire test series. As shown in Figure 3-23 by the red 'fixed knob' curve, this alternative method results in a linear stress-growth curve that is both repeatable and eases the calculation of the stress rate (the slope of the line). Hence, this alternative method was used for the remainder of this study.

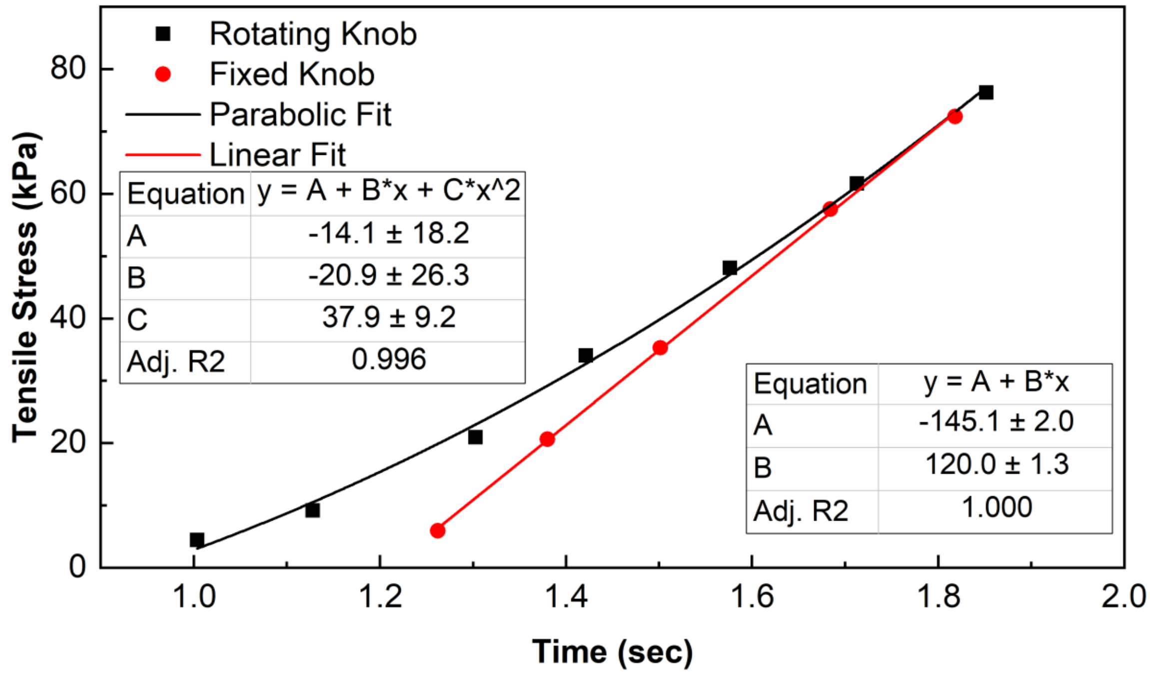

Figure 3-23. Stress rates measured using PATTI under rotating and fixed dial conditions.

3.3.3 Failure Modes in PATTI Test

Once the binder achieves its tensile strength under the specific PATTI test conditions, the pull-off stub detaches from the substrate. This detachment is considered a pull stub failure and occurs in three primary ways that define three respective failure modes. Cohesive failure mode occurs within the asphalt binder, leaving a uniform layer of binder on the stub and substrate, as shown in Figure 3-24 (a). Adhesive failure mode, shown in Figure 3-24 (b), occurs when the pull stub completely detaches from the binder, leaving the binder entirely on the substrate, or when the pull stub pulls the binder layer along with the stub, leaving no trace of the binder on the substrate. A test can also fail in a combination of these two modes, which is termed ‘mixed failure’, as shown in Figure 3-24 (c). During mixed failure, some portion of the asphalt binder remains on either the stub or substrate. Other miscellaneous types of failure are possible when sliding or twisting occurs during the initial application of the pull stub or during the placement of the piston. The ideal type of failure for this research is cohesive failure because it demonstrates the tensile strength of the binder itself and not its adhesive capabilities. During the data analysis performed in this study, if the failure mode was outside the cohesive type of failure, then the results were dismissed.

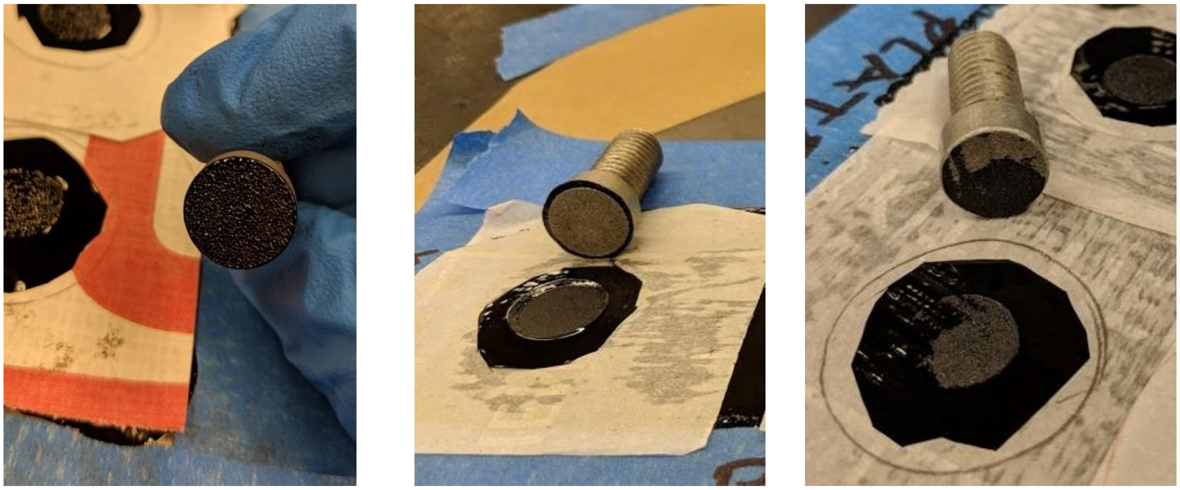

(a) (b) (c)

Figure 3-24. (a) Cohesive failure of binder, (b) adhesive failure of pull stub, and (c) mixture of cohesive failure and adhesive failure of pull stub.

The final stage of PATTI test analysis should follow the repeatability criteria stipulated in ASTM D4541-17 (ASTM 2017). According to this standard, the difference between each test in terms of intra-laboratory results should be less than 14.8%, and the difference in inter-laboratory test results should be a maximum of 28.4% for a D-type tester. In this research, if the results were found to differ more than 14.8%, then they were dismissed as outliers.

3.4 Calibration of Measurement Systems for Study Test Devices and Methods

3.4.1 Digital Image Correlation Technique

A DIC system is a non-contact measurement system that can be employed to compute the relative displacements and strain activity in a 2-D plane by comparing images of a deformed specimen with images of an initial, undeformed reference specimen using advanced mathematical techniques. To implement DIC analysis of the differences between the initial image and the deformed images, the undeformed reference image is divided into small subsets, and then the corresponding locations of these subsets in the deformed images are tracked by matching their grayscale pixel levels, as shown in Figure 3-25. By monitoring the location of the subsets, the horizontal and vertical displacements of the center point of each subset in the pixels can be determined at different stages of the testing (Seo et al. 2002).

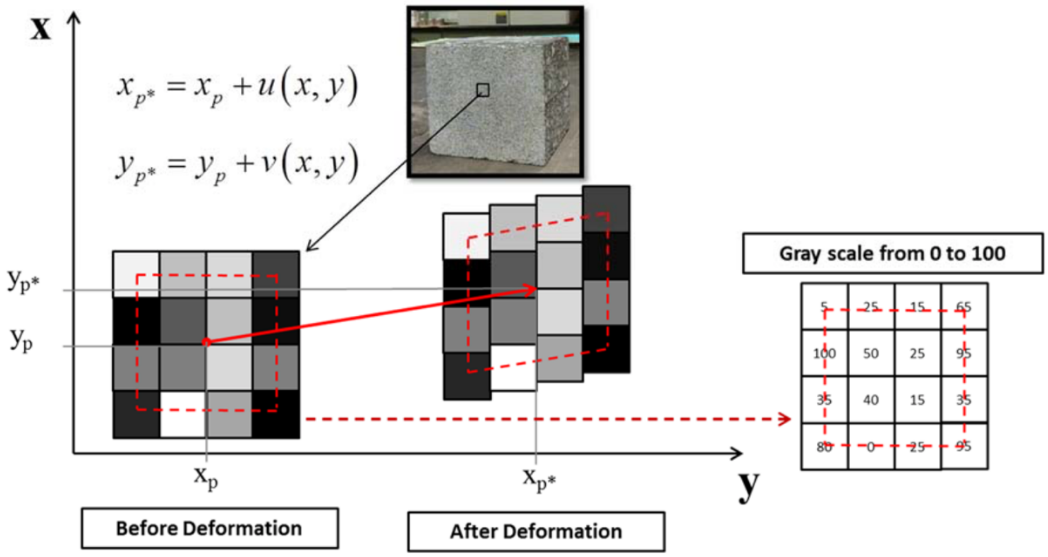

Figure 3-25. Digital image correlation analysis of differences between initial image and deformed image (Seo et al. 2002).

The DIC system set-up includes a 5-megapixel camera along with a 35–75 mm f: 3.3–4.5 manual focus lens to capture images. Two dual-fiber optical gooseneck lights were used in this study to provide consistent, cool, and sufficient lighting on the specimen surface. An adjustable tripod stand with built-in bubble levels was used to level the camera and place it at an approximate distance of 75 cm from the specimen and at the same height and lateral position as the specimen. A relatively high shutter speed of 1.5 ms was used to prevent blurry images. An f-stop of 3.3, a fairly wide lens aperture size, was used to let the maximum possible light hit the camera sensor. A relatively low gain setting close to -3.9 db was used to prevent unwanted image noise. The DIC camera was connected to a computer that was installed with two commercially available DIC software packages developed by Correlated Solutions, Inc: Vic-Snap and Vic-2D. Vic-Snap is used to acquire images during testing and control the camera shutter speed, position, and lighting levels. VIC-2D is 2-D DIC analysis software that is used to calibrate the scale, analyze the captured images, and calculate the displacements and strain through comparisons of images using advanced mathematical algorithms. Key aspects and details regarding DIC analysis can be found in Safavizadeh and Kim (2017).

3.4.2 Calibration of DIC System for MAST Testing

Even though the principle behind a monotonic asphalt shear test is simple, the MAST is a complex device. It has numerous components that must be assembled and disassembled during specimen loading and unloading. The major challenge during MAST testing is ensuring that shearing occurs only along the interface, which is achieved by securely attaching shoes to the jig through threaded bolts and screw fasteners. Even then, the moment that is induced on the shoes is so high during the test that it causes a rocking action. The degree of the rocking action depends on the temperature at which the test is carried out, thus indicating that the cause of the rocking is a machine compliance issue. Furthermore, many connections and bearings are located between the actuator and the MAST, adding deformation to the actuator linear variable differential transformer (LVDT) measurements. At a glance, an on-specimen LVDT should be a quick solution, but the rocking action makes those measurements inaccurate. Hence, the on-specimen displacement that occurs in shear tests is measured using an external non-contact DIC system.

The accuracy of a DIC system is dependent on the system set-up, which includes the amount of lighting, speckle pattern, aperture opening, etc. (Safavizadeh and Kim 2017). Therefore, the DIC system's accuracy must be checked carefully before conducting shear tests. This aim can be achieved by conducting a trial test at a constant displacement rate without any attached load using the DIC system and then comparing the results to the recorded actuator displacement(s). All of the measurement system settings should mimic real shear test conditions, except that the speckled paper that is used to track motion is glued to the MTS actuator. An environmental chamber also is used in this validation test because, during a monotonic shear test, the image of the test specimen is captured through the transparent window of the environmental chamber. The refraction of light through the window influences the DIC measurements. During the test, a constant displacement rate of 5.08 mm/min (0.2 in./min) is applied by the MTS machine. Images are taken by the DIC camera at a constant capture rate of 150 milliseconds. Figure 3-26 shows the displacements that were measured using an actuator and DIC system in this study. As shown, the DIC system measurements match the actuator displacements, thus validating the accuracy of the DIC system for taking displacement measurements during MAST tests.

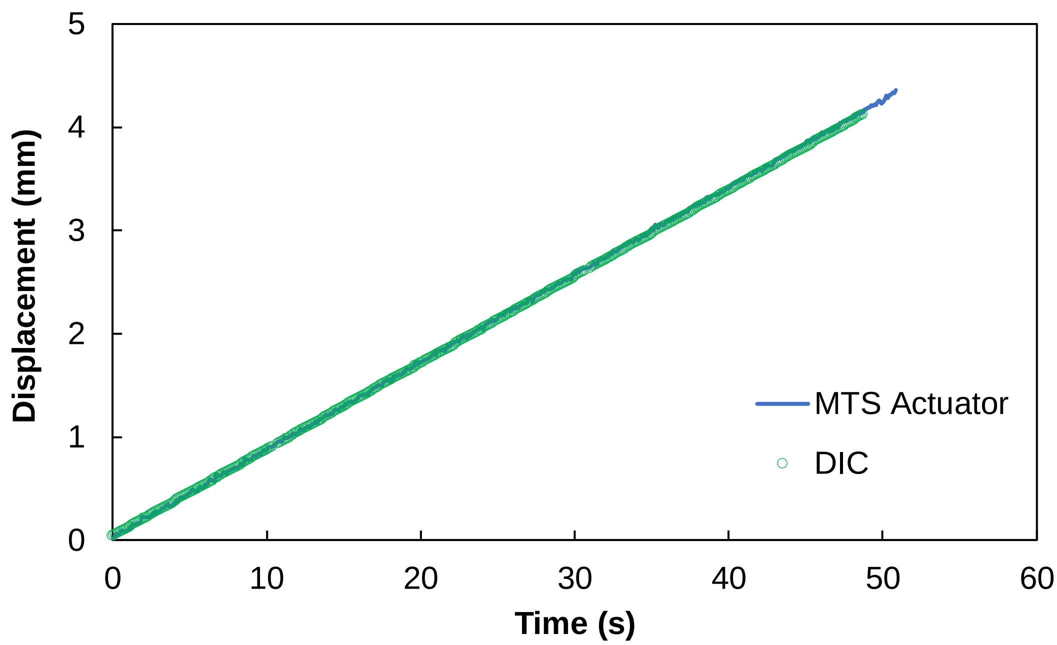

Figure 3-26. Comparison of MTS actuator and DIC system displacements.

3.4.3 Calibration of DIC System for Notched Beam Fatigue Testing

One of the primary reasons for conducting NBFTs in this research was to track the crack propagation in AC beams with and without geosynthetic reinforcement. The NBFTs were conducted in constant actuator displacement mode at 10 Hz frequency and the DIC technique was employed to capture and measure the crack lengths and widths. The full crack path at a specific loading cycle can be captured at its peak displacement amplitude. However, triggering the DIC camera at that exact time is tedious. The DIC system commonly uses the same cable to send the trigger signal and receive the captured image data between the computer and camera. This process results in inaccuracy in the timing of image acquisition if the time interval is too short due to the delay in the communication with the camera and saving the image. Therefore, a hardware trigger is preferred for high-frequency tests, which involves an external camera triggering signal. A new fulcrum module was procured for this study to trigger the camera depending upon the drive signal sent to the actuator. This section explains the calibration of the fulcrum module to check its reliability prior to conducting the NBFTs.

The maximum frame per second of the new DIC camera is 71. Thus, for a 10 Hz test, the maximum number of data points/images acquired per cycle (0.1 s) is seven. However, this number of data points may not be sufficient to construct a sinusoidal fit. Therefore, capturing images at the alternate load cycle and at a constant phase angle difference helps create a complete cycle. Figure 3-27 shows a single DIC cycle measured during a cyclic test. Typical DIC system software sets the trigger voltage signal depending on the MTS controller's drive signal that simulates the constant displacement amplitude. The MTS controller sends the drive signal to the actuator valves; the drive signal is read out via an analog reader and fed to the DIC system's data acquisition system (DAQ). VIC-Snap, the DIC image capturing software, with the aid of the DAQ sets the trigger voltage and sends a trigger signal through a cable to the camera; this cable is separate from the image-saving cable to the computer. This process allows the accurate acquisition of DIC images.

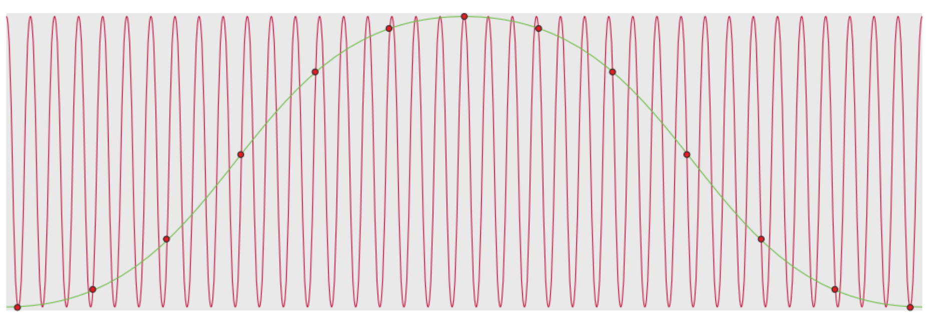

Figure 3-27. Typical fulcrum module capturing process during a cyclic fatigue test (from VIC-2D flyer).

Figure 3-28 shows the typical input options available in VIC-Snap's fulcrum module. In this study, a sequence recording was activated at a constant phase step for every n^{th} cycle depending on the user's requirement. For instance, a 15° phase step at every 200 cycles triggers the camera to capture images that provide a full cycle with 24 images (360/15 = 24). However, the number of actuator cycles between two consecutive images for a 10 Hz test is four. The software must monitor one cycle to check the current frequency and limits, monitor another cycle to obtain the waveform/voltage, and then trigger the camera. Thus, to obtain a single DIC cycle (360°) that contains 24 images, the actuator must complete 96 cycles. Then, the next sequence initiates at the 200th actuator cycle, and so on.

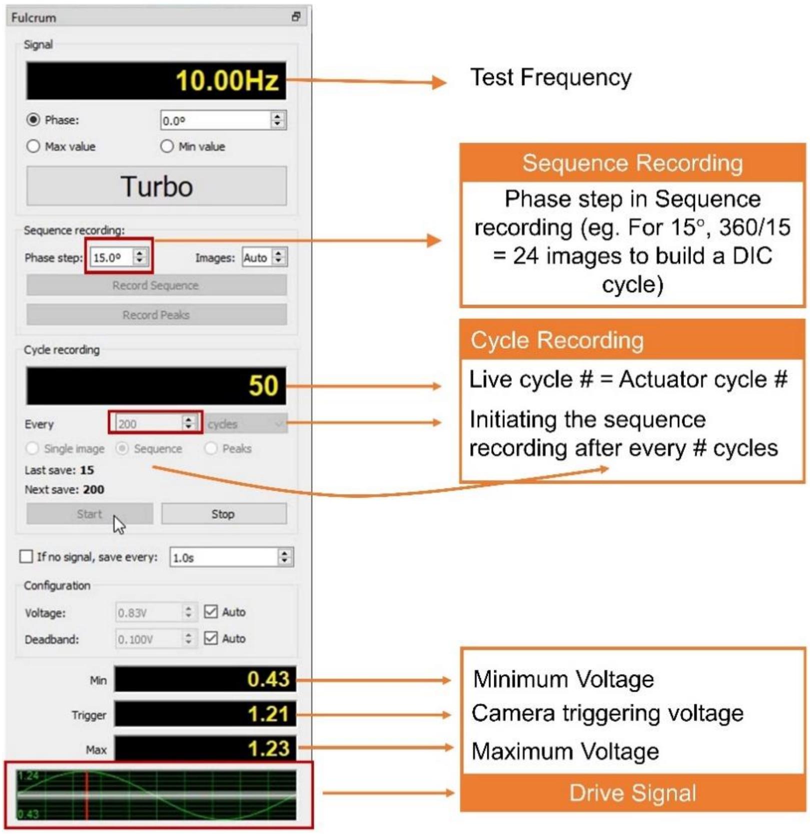

Figure 3-28. Input parameters for DIC fulcrum module.

Figure 3-29 shows the displacements measured using the actuator and DIC system in this study. As shown, the DIC system measurements match the actuator displacements, thus validating the accuracy of the DIC system for taking displacement measurements during fatigue tests.

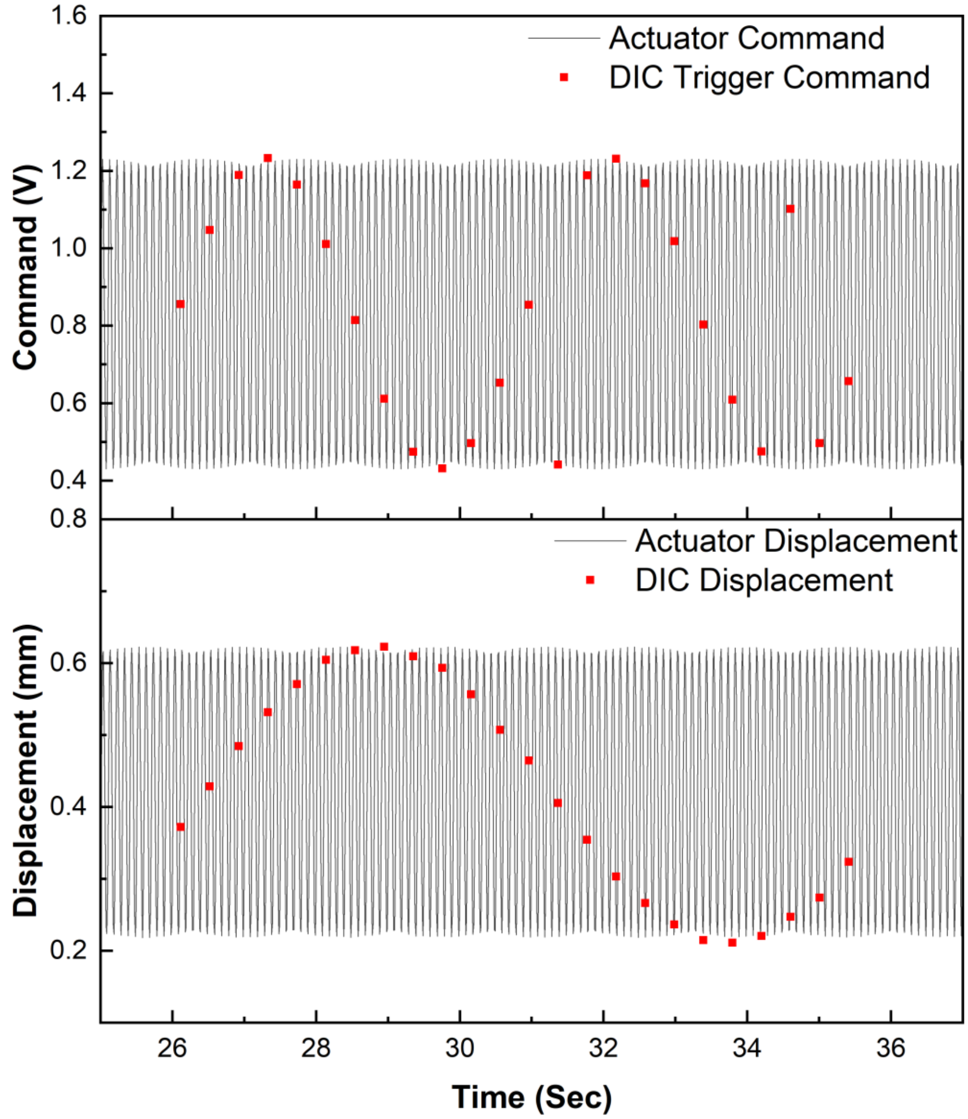

Figure 3-29. (Top) recorded commands: actuator commands versus DIC trigger commands; (bottom) actuator/LVDT displacements versus DIS displacements over time.

3.4.4 Calibration of Deflections for Notched Beam Fatigue Testing

Based on elastic beam deflection calculation methods, such as double integration or energy (Castigliano's theorem), the deflection at the center of a beam under four-point bending beam loading is 1.15 times greater than the deflection at the loading points (two points on the specimen, distance *a* from both ends). The current loading system at NCSU measures the displacement at the loading point using an actuator LVDT. Several connections and bearings must be set up before the specimen experiences the load, which raises the question of whether the cited difference between four- and two-point loading remains valid, as machine compliance might cause additional deformations. Therefore, the NCSU research team decided to use an on-specimen LVDT that measures the deflection at the neutral axis. The displacements measured using the on-specimen LVDT and the actuator LVDT were compared to the DIC system measurements to establish a relationship between the applied and measured displacements.

Also, a closed-loop system that could control the loading based on the on-specimen deflections would be useful for these types of tests. The current MTS system at NCSU, shown in Figure 3-30, does not support an add-on to configure the on-specimen displacement-controlled test. Hence, the NCSU team independently measured the on-specimen deflections and loads using an LVDT and load cell. The two main reasons for this decision are that (1) most laboratories do not have an on-specimen controlled actuator loading system, so a method that a larger user group could use would be welcome, and (2) the current MTS actuator capacity at NCSU is 100 kN (22,000 lb) and has a maximum displacement range of 200 mm (7.87 in.). Controlling the actuator to accommodate a displacement that is less than a millimeter using a 150-kN capacity closed-loop system would cause a surge in loading and eventually lead to sudden specimen failure. Therefore, an actuator displacement control test would be ideal for avoiding catastrophic specimen failure. Also, an on-specimen LVDT and load cell can provide accurate displacement and load measurements, respectively.

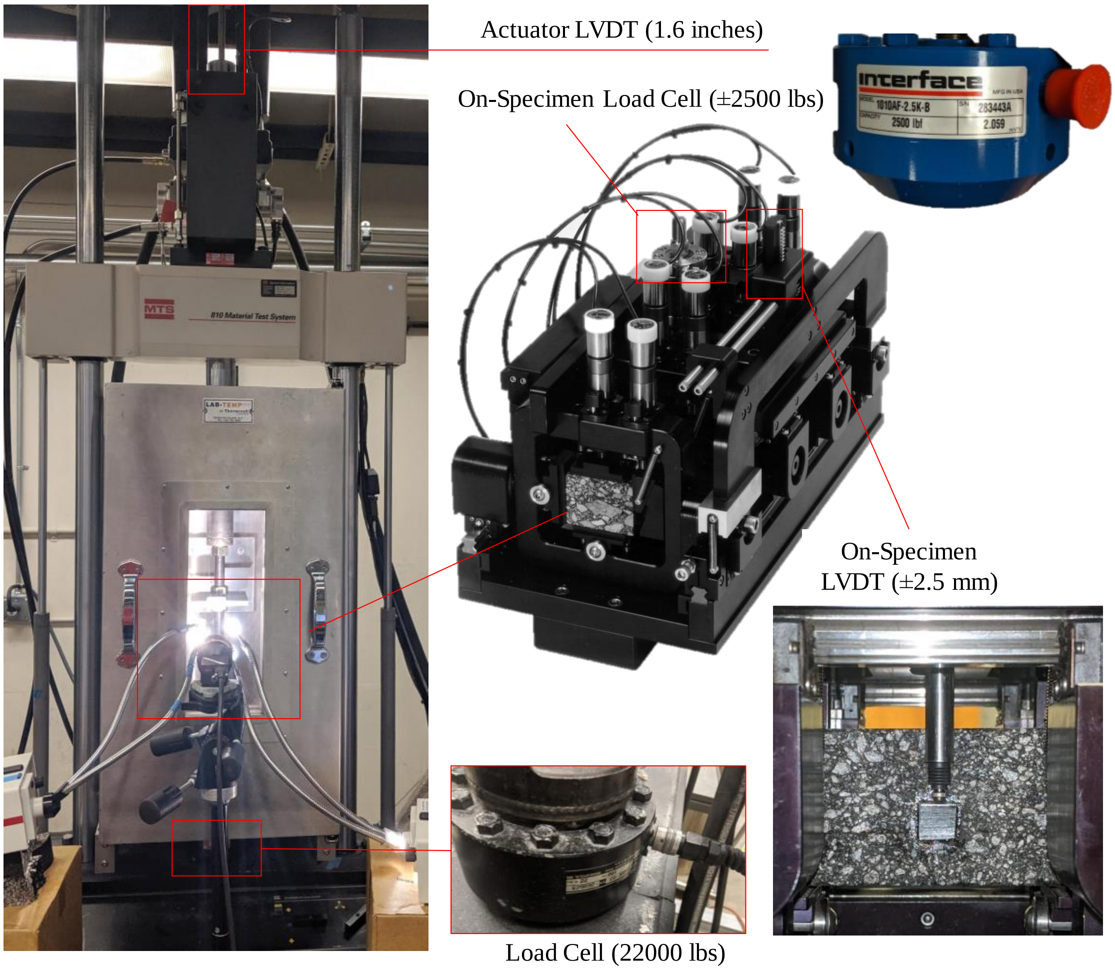

Figure 3-30. Four-point bending beam test apparatus housed in MTS.

The calibration process was designed to accommodate the deflection ranges from the lowest to highest expected tensile strain levels (250 μ - 2000 μ) during the NBFTs. The calibration phase is composed of five stages, ranging from 250 μ, 500 μ, 1000 μ, 1500 μ, and 2000 μ tensile strain. The corresponding theoretical deflections were back-calculated to find 0.105 mm, 0.215 mm, 0.425 mm, 0.64 mm, and 0.85 mm, respectively. For each stage, 100 cycles of respective deflections were applied via actuator displacement, as shown in Figure 3-31. The rest periods between the two stages were fixed at two and three seconds.

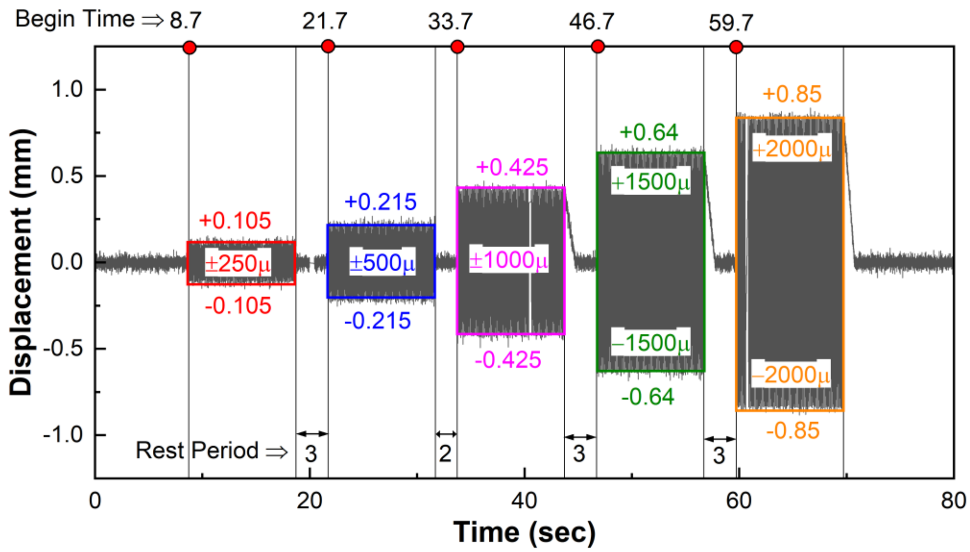

Figure 3-31. Five stages of displacement calibration.

LabVIEW logging software was employed to capture the displacements and loads. The deflections measured from the actuator and on-specimen LVDTs at different stages were used to calculate the tensile strain values. The data logging was configured to capture 1000 data points per second, i.e., 100 data points per cycle for the 10 Hz test. These data points must be fitted with a sinusoidal waveform to measure the amplitudes accurately. This fitting procedure is described in Appendix C. The described fitting procedure was used to measure the tensile strain that was recorded during each stage. Figure 3-32 (a) through (e) show the data noise and fitted lines for each of the five calibration stages, respectively. Two major observations can be made from Figure 3-32. First, the noise of the data points from the actuator is high at the lower tensile strain values of 250 μ (δ = 0.105 mm) and 500 μ (δ = 0.215 mm) whereas the on-specimen measurements at the same deflections remain smooth. The higher noise level for the actuator measurements of the smaller deflections is caused by the wide measurement range of the actuator LVDT. Second, the on-specimen tensile strain measurements are lower than the actuator-based tensile strain measurements, which indicates system compliance with regard to the displacement measurements.

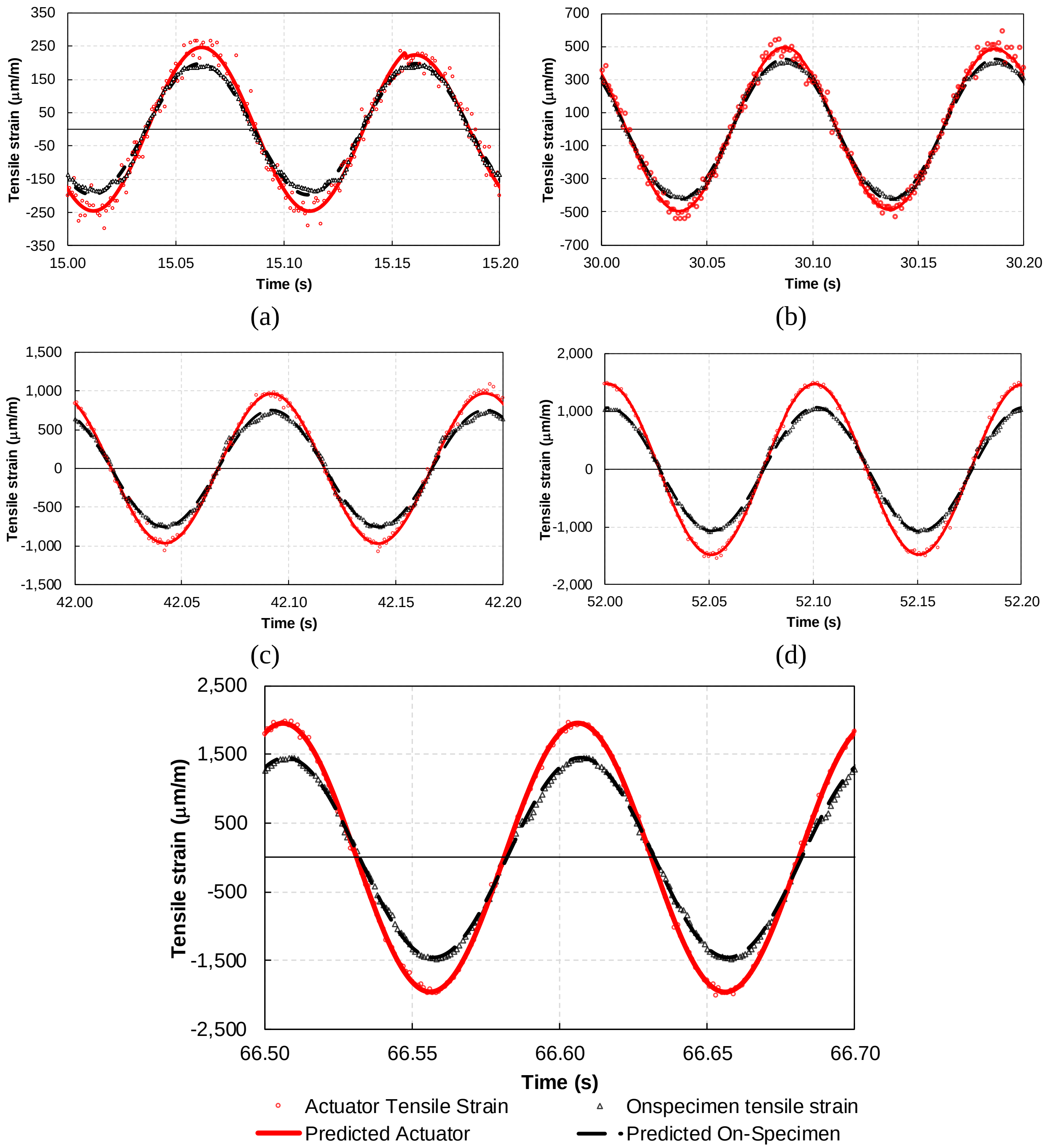

(e)

Figure 3-32. Tensile strain data points and curve fits for various actuator tensile strain input commands: (a) 250 μ, (b) 500 μ, (c) 1000 μ, (d) 1500 μ, and (e) 2000 μ.

Based on these observations, relationships between the tensile strain based on actuator input command and tensile strains based on measured actuator and on-specimen displacements could be established, as shown in Figure 3-33.

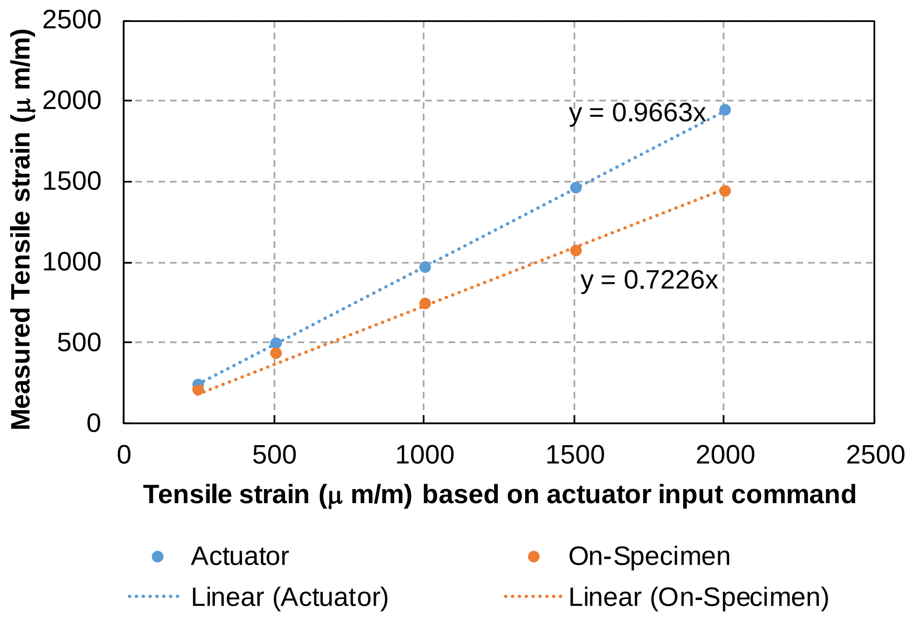

Figure 3-33. Relationships between tensile strain based on input commands and tensile strains using measured actuator and on-specimen displacements.

The relationship shown in Figure 3-33 clearly indicates that only 72% of the input command displacement is reflected in the specimen deflection. Hence, the research team highly recommends that any laboratory should establish its own compliance-displacement relationship for the specific mixture of interest at a specific temperature so that the expected initial tensile strain can be predicted during the test. This exercise is essential, as system compliance varies among different laboratories. For the study mixture, RS9.5C, at room temperature, Table 3-5 presents the predicted tensile strain values that fit most of the tensile strain levels of the current project. Note that this compliance-displacement relationship remains valid only during the initial few cycles before damage initiation. Once the stiffness of the mixture degrades, the relationship for the current set-up does not remain valid. Therefore, the on-specimen deflections should be measured throughout the test for accuracy.

Table 3-5. Predicted On-Specimen Tensile Strain Based on Compliance-Displacement Relationship for the Study RS9.5C Mixture

Actuator input deflection (mm)	Predicted on-specimen deflection (mm)	Predicted actuator tensile strain (µm/m)	Predicted on-specimen tensile strain (µm/m)
1.043	0.754	2006	1500
0.835	0.603	1605	1200
0.626	0.452	1204	900
0.417	0.302	802	600
0.209	0.151	401	300
0.104	0.075	201	150

Chapter 4. Numerical Simulations of Pavement Responses

4.1 Background

The presence of (in)sufficient interface bond strength between pavement layers can be evaluated by understanding and quantifying the distribution of the stress within the pavement section under realistic traffic conditions. The NCSU research group has developed a fast Fourier transform-based 3-D viscoelastic finite element analysis tool known as FlexPAVE™ (formerly known as the LVECD program) to evaluate pavement responses under moving vehicle loads. FlexPAVE™ can simulate actual climatic conditions as generated by the Enhanced Integrated Climatic Model. Moreover, FlexPAVE™ is zipped with the Simplified ViscoElastic Continuum Damage model and permanent deformation shift model that can predict pavement responses and distresses, namely, fatigue cracking and rutting, for any temperature and traffic conditions. In this study, FlexPAVE™ was used to determine the critical stress types that are involved in debonding.

Cho (2016) conducted extensive pavement response analysis of three typical pavement sections constructed in North Carolina that are categorized as thin, intermediate, and thick structures. The analysis was carried out at 5°C, 20°C, 40°C, and 60°C, three different speeds, 8 km/hour (5 mph), 40 km/hour (25 mph), and 88 km/hour (55 mph), three-axle loads, 106.8 kN (24 kips), 160 kN (36 kips), and 213.6 kN (48 kips), and two types of tire rolling conditions, i.e., free-rolling and braking, to determine the worst field condition that encourages debonding. The findings show that the worst stress state that leads to debonding is created by a single tire with a single-axle single-tire load of 213.6 kN (48 kips) on a thick pavement structure at a fixed vehicular speed of 8 km/h (5 mph) under the braking condition. Henceforth, that specific condition is considered for the current study except that the tire loading is assumed as a 80-kN (18-kip) single-axle dual-tire configuration.

4.2 Parameters Used for Numerical Simulations

4.2.1 Structure Information

Among the typical pavement sections found in North Carolina, a thick pavement is more susceptible to debonding than a thin pavement (Cho 2016). Figure 4-1 presents a cross-section that provides the thickness of each layer assumed for the thick pavement structure used in the present study for the FlexPAVE™ simulations. The top three layers, i.e., surface, intermediate, and base layers, are composed of AC mixtures with different gradations. The standard thickness for a surface course constructed with an asphalt mixture that has a 9.5-mm nominal maximum aggregate size usually ranges between 38.1 mm (1.5 in.) and 63.5 mm (2.5 in.). Hence, for this study, thicknesses of 25.4 mm (1 in.), 38.1 mm (1.5 in.), 50.8 mm (2 in.), 63.5 mm (2.5 in.), and 76.2 mm (3 in.) were chosen to analyze the worst field loading condition.

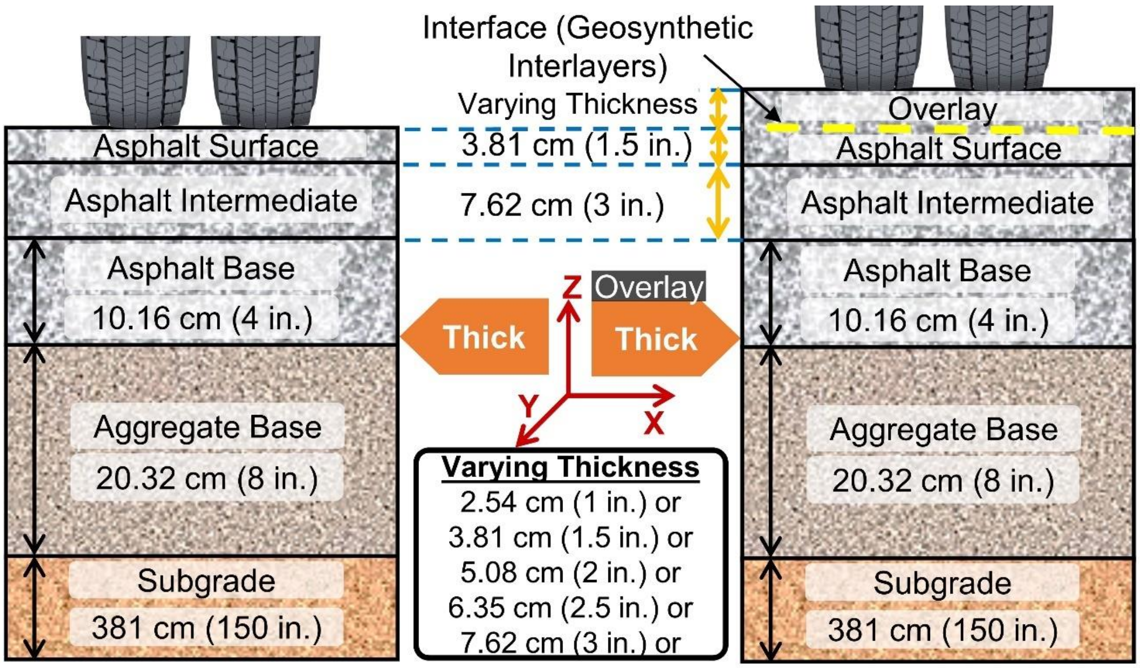

Figure 4-1. Thick pavement structure used for FlexPAVE™ computational simulations.

4.2.2 Material Parameters for Each Pavement Layer

Asphalt concrete

The three top layers of the thick pavement structure are assigned the material properties of AC as follows. The surface course is assigned either a warm mix (RS9.5B RAP-35) or hot mix (RS9.5B RAP-30) depending on the mixture under consideration, whereas the intermediate and base layers have the properties of typical RI19B and RB25B mixtures, respectively.

The viscoelastic nature of AC is defined using Prony series coefficients/parameters in FlexPAVE™ and is achieved through the interconversion from the dynamic modulus to the relaxation modulus over a wide time range using the generalized Maxwell model shown in Equation (2-4). The number of Maxwell elements decides the prediction accuracy – the more elements, the greater the accuracy – but leads to more complexity at the same time. FlexMAT™, Excel-based software, was used in this study to analyze the dynamic modulus outcomes to calculate the Prony series coefficients, as shown in

Table 4-1. The material properties for I19B and B25B are adopted from Cho (2016).

Table 4-1. Prony Coefficients for Relaxation Modulus

ρ_i (sec)	E_i (MPa)		
	S9.5C	**I19B**	**B25B**
2.00E+08	46.25	15.86	10.71
2.00E+07	28.63	31.18	21.24
2.00E+06	83.97	65.98	45.3
2.00E+05	202.61	150.13	105.76
2.00E+04	533.62	356.33	268.88
2.00E+03	1414.45	823.24	702.8
2.00E+02	3534.75	1685.67	1676.39
2.00E+01	7775.77	2821.99	3194.19
2.00E+00	14342.18	3759.34	4550.7
2.00E-01	21764.79	3476.25	4160.3
2.00E-02	27406.48	3756.6	4357.92
2.00E-03	29391.90	3081.01	3337.35
2.00E-04	27736.27	2440.15	2452.81
2.00E-05	23763.77	1802	1669.18
2.00E-06	18977.34	1286.44	1099.82
2.00E-07	14398.53	893.45	705.84
2.00E-08	10955.97	610.14	446.61
E_∞	14.04	38.24	51.59
Ref Temp (°C)	21.1	5	5
Poissons ratio	0.3	0.35	0.35
$\alpha 1$	6.7454e-04	5.9500e-04	7.1300e-04
$\alpha 2$	-0.1691	-0.1611	-0.1690
$\alpha 3$	3.2678	0.7909	0.8270

Note: ρ_i is the relaxation time of element i; E_i is the relaxation modulus of element i; and E_∞ is long term modulus.

Subgrade

The subgrade is assumed as linear elastic material for the FlexPAVE™ simulations, and the modulus value used in this study's analysis is 68.95 MPa (10,000 psi).

4.2.3 Climate Data

Although FlexPAVE™ has the ability to simulate the pavement's behavior under changing temperatures as a function of time and pavement depth, the isothermal temperature profile at

50°C was used in this study because high temperature was found to be the worst condition for debonding (Kim et al. 2015b).

4.2.4 Traffic Data

The design vehicle configuration for the response analysis was chosen as a dual-tire system to replicate the tire loading of half a single-axle dual-tire condition. The axle load of 80 kN thus is distributed through the dual tire configuration as 40 kN (9 kips) with 827.4-kPa (120-psi) tire-pavement contact pressure.

4.2.5 Tire-Pavement Contact Pressure Configuration

The tire-pavement contact pressure distribution is non-uniform, and simulating the pressure distribution is essential for accurate pavement response computations. Moreover, the tire-pavement contact pressure distribution is affected significantly by the tire inflation pressure, tire type, and tire load. The NCSU research team determined the FlexPAVE™ tire-pavement contact area using stress-in-motion (SIM) technology under a moving load (De Beer et al. 2004). The area is considered rectangular with an aspect ratio of 11:7 (length:width) assumed in FlexPAVE™. The tire-pavement contact pressure distribution is based on fitting a quadratic function to the actual pressure in both the longitudinal and transverse directions. The test outcomes after carrying out different combinations of numerical simulations are reported in Chapter 6. Figure 4-2 shows the FlexPAVE™ dual tire-pavement contact configuration.

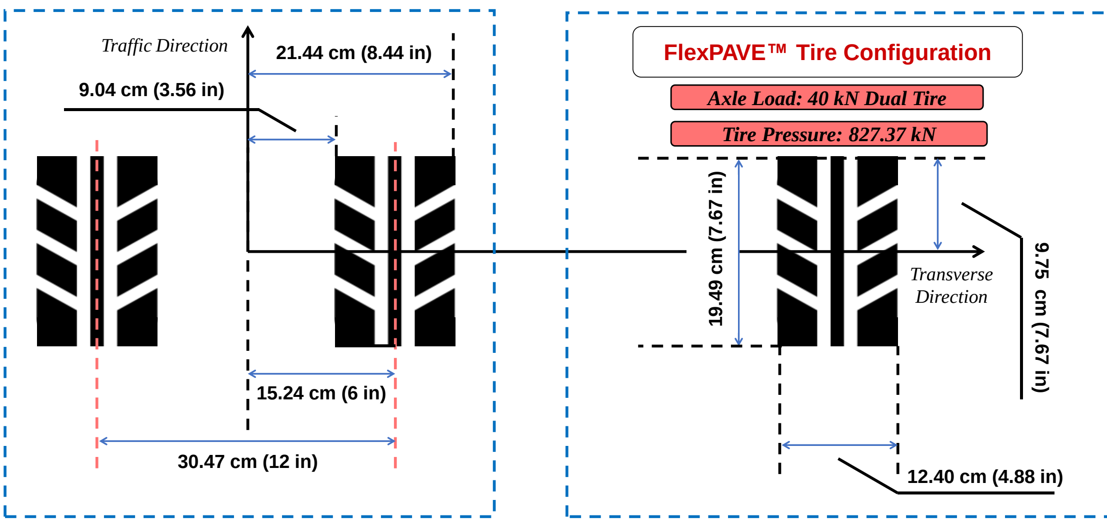

Figure 4-2. FlexPAVE™ dual tire-pavement contact configuration.

Shear traction due to tire braking condition
The tire-pavement contact stress is affected directly by the tire rolling conditions and thus the stress response. Cho et al. (2017a) considered two types of tire rolling conditions. i.e., free-rolling and braking. A study conducted by the National Highway Traffic Safety Administration on the stopping distances of truck tractors found that the rolling resistance coefficient (shear

traction) varies from 0.35 to 0.55. The pavement response analysis showed that 0.55 shear traction is the most critical condition for debonding and hence was used for this study's analysis.

4.3 FlexPAVE™ Analysis Output

Figure 4-3 presents the FlexPAVE™ analysis results of the interface stress distribution at a depth of 3.81-cm (1.5-in.) for the thick structure. Figure 4-3 (a) and (b) present the normal stress and shear stress results, respectively. The 3-D contour plots helped to identify the critical conditions at the interface.

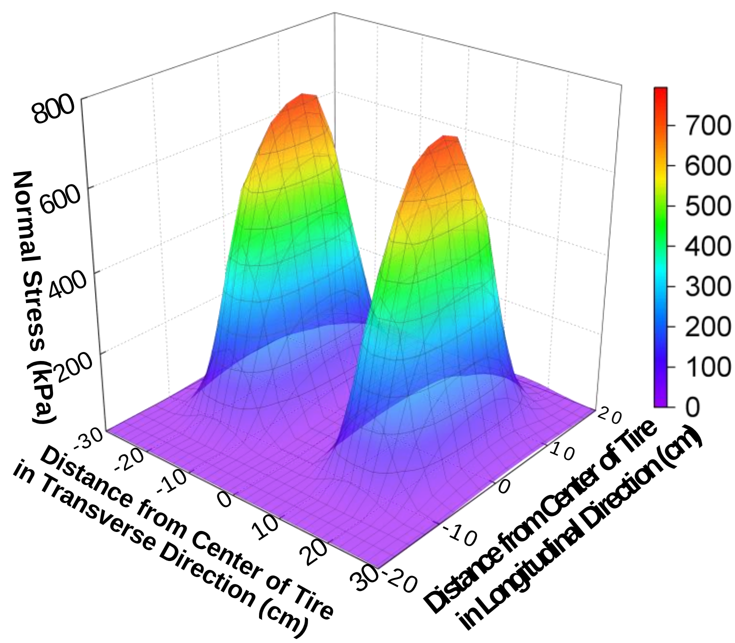

(a)

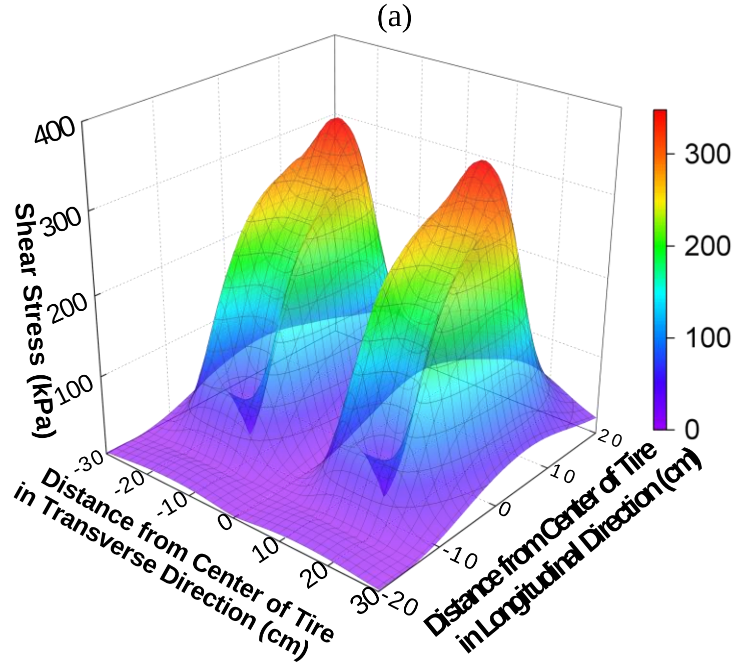

(b)

Figure 4-3. Stress distribution at the interface 1.5-inch deep: (a) normal stress and (b) shear stress.

OriginPro 2018 was employed to create 3-D and 2-D contours of both the normal and shear stress distributions. The contour profile option in the software helped to draw the stress/strain responses along the transverse/longitudinal direction, as shown in Figure 4-4. The maximum normal stress ($\sigma_{zz\text{-}max}$) is 740 kPa, as shown in Figure 4-4 (a). The magnitudes of the resultant shear stresses in the longitudinal and transverse directions at any location along the interface plane are determined and the maximum resultant shear stress (τ_{max}) of 303 kPa was found to occur at the center of the tire, as shown in Figure 4-4 (b).

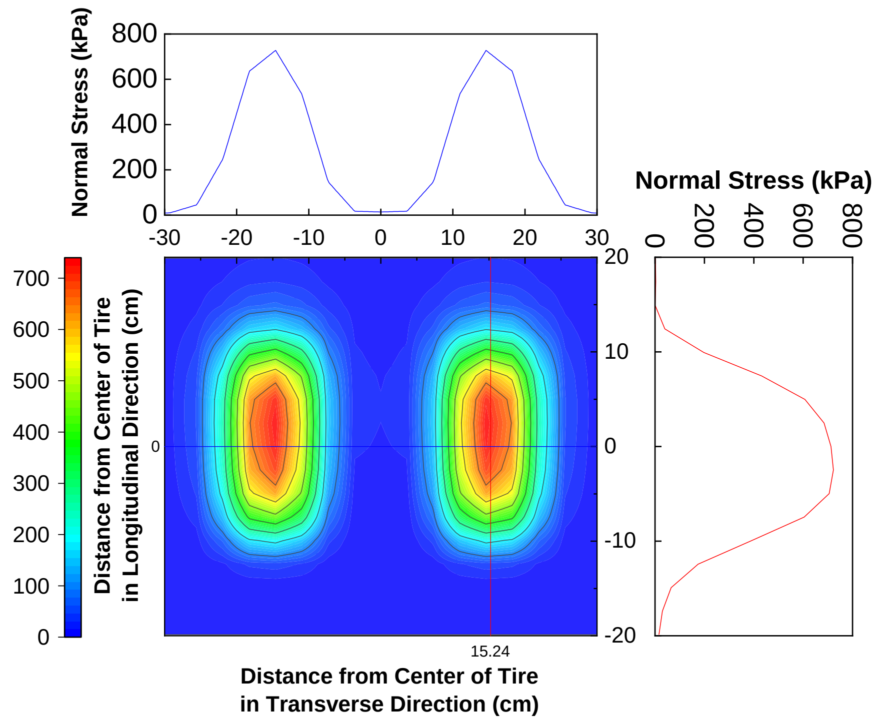

(a)

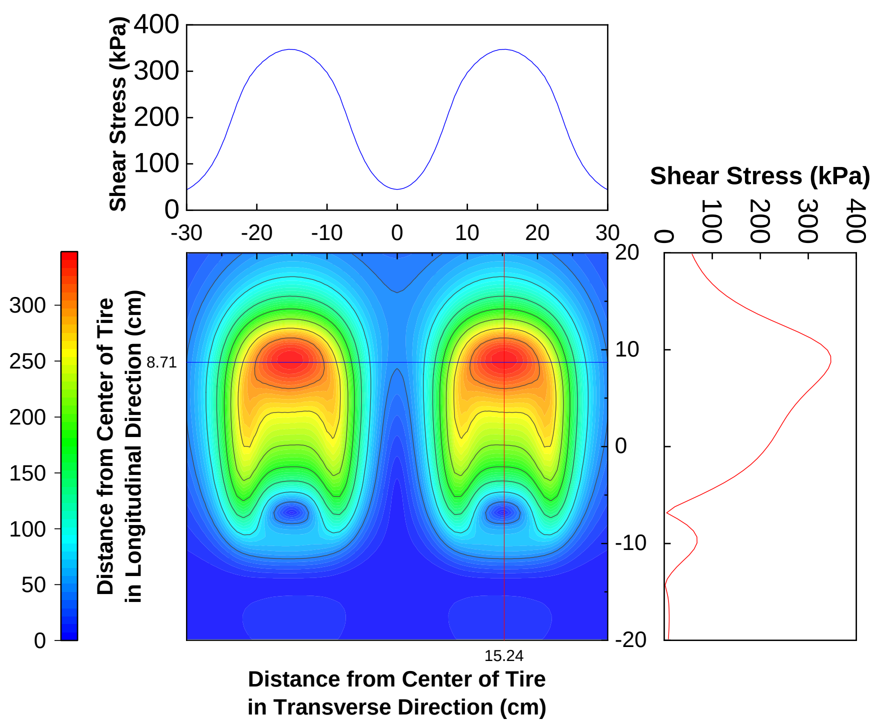

(b)

Figure 4-4. (a) Normal stress and (b) resultant shear stress distributions.

Figure 4-5 (a) and (b) illustrate the shear strain that occurred in the longitudinal (γ_{yz}) and transverse (γ_{zx}) directions, respectively.

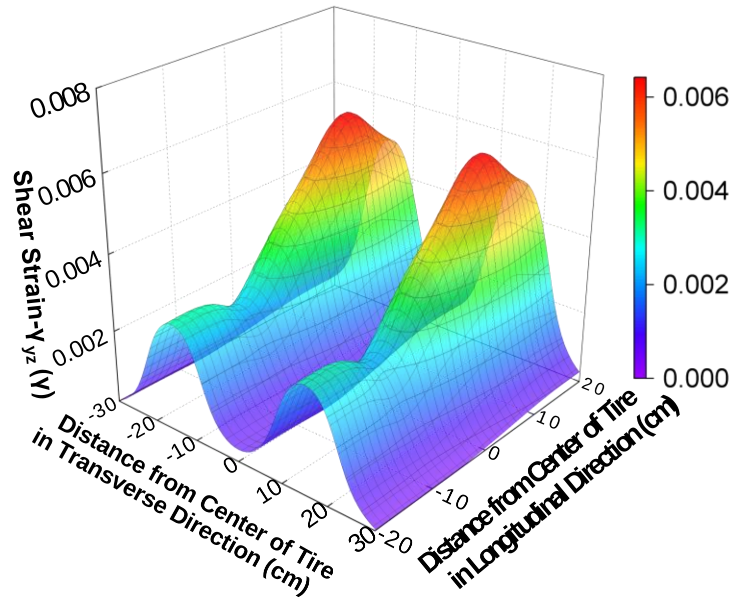

(a)

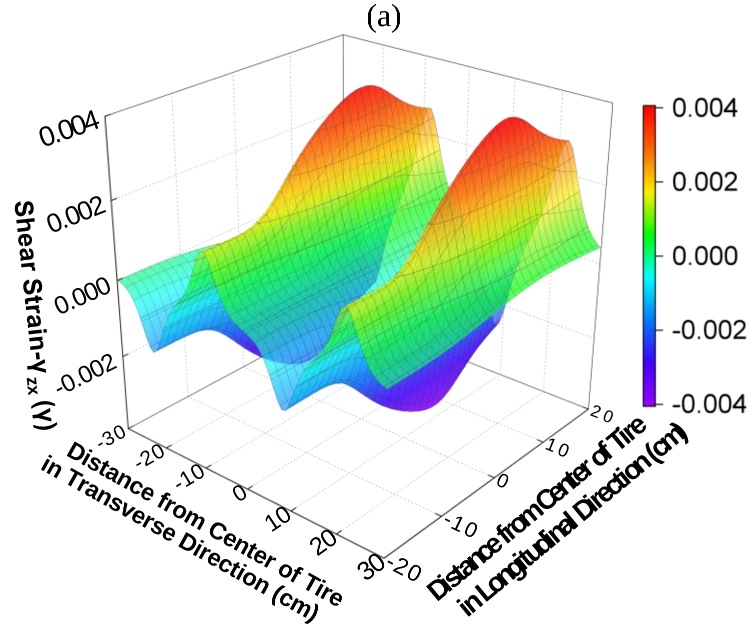

(b)

Figure 4-5. Shear strain: (a) γ_{yz} and (b) γ_{zx}.

4.4 Parameters Used in EverstressFE Simulations

EverstressFE is 3-D linear elastic finite element software that can run pavement response analysis in batch mode. The advantage of EverstressFE over FlexPAVE™ is that an Excel VBA code will suffice to create numerous combinations of structural and material input files. Moreover, a VBA code can easily extract the analyzed test results from the EverstressFE output file. Also, linear elastic pavement response analysis is popular in the pavement community; therefore, a predictive equation that is based on linear elastic analysis can be easily verified.

4.4.1 Structure Information and Material Parameters

The pavement responses of standard structures with an overlay and surface, base, and subgrade layers were simulated using EverstressFE by combining various thicknesses and modulus values (~1500 combinations). The loading conditions differ depending on the required parameter output. Table 4-2 presents the material parameters and structural conditions considered for this study. Note that the aggregate base course thickness was fixed at 203.2 mm (8 in.) while the subgrade was assumed as semi-infinite by providing a large depth of 300 mm (118 in.). The thicknesses of the existing AC surface layer and overlay were varied to accommodate different pavement designs for various field conditions. The modulus values were varied to mimic variously damaged and aged conditions of different layers in the field. The Poisson's ratios (υ) of the asphaltic, unbound, and subgrade layers were assumed as 0.35, 0.40, and 0.45, respectively. All the layers were considered to be fully bonded. Eventually, the outcome of nearly 1500 combinations helped to develop a predictive equation to measure the tensile strain underneath the newly constructed overlay, based on FWD deflection measurements of the existing damaged/aged pavement.

Table 4-2. Pavement Simulation Conditions Using EverstressFE

$E_{overlay}$	**psi**	500,000				
	MPa	3,447				
$T_{overlay}$	**in. (mm)**	1.5 (38.1), 3 (76.2), 4 (101.6)				
E_{ac}	**psi**	700,000	500,000	300,000	100,000	50,000
	MPa	4,826	3,447	2,068	689	345
T_{ac}	**in. (mm)**	4 (101.6), 7 (177.8), 10 (25.4)				
E_{abc}	**psi**	50,000	40,000	30,000	20,000	10,000
	MPa	345	276	207	138	69
T_{abc}	**in. (mm)**	8 (203.2)				
E_{sg}	**psi**	20,000	15,000	10,000	5,000	2,500
	MPa	138	103	69	34	17
T_{sg}	**in. (mm)**	Semi-infinite 118 (300)				

Note: $E_{overlay}$ is overlay modulus; $T_{overlay}$ is overlay thickness; E_{ac} is asphalt concrete layer modulus; T_{ac} is asphalt concrete layer thickness; E_{abc} is aggregate base course modulus; T_{abc} is aggregate base course thickness; E_{sg} is subgrade modulus, and T_{sg} is subgrade thickness.

4.4.2 Climate Data

EverstressFE pavement response analysis is linear elastic analysis. The input modulus value is assumed to be a representative condition (damaged or aged or both) of the pavement at 23°C.

4.4.3 Tire Load and Configuration

Two main types of structures were assumed for the study to analyze pavement responses, and the loading condition differs for each type. The first type is a structure without overlay, shown on the left side of Figure 4-6, where FWD testing was expected to be carried out. However, in EvestressFE, the load parameters are wheel type, axle type, tire contact, and tire pressure. Hence, the load conditions were identified to fit the FWD load of 40 kN (9000 lb) applied through a loading plate with the diameter of 600 mm (12 in.). Thus, a 'single tire' wheel type in a 'single' axle with an applied tire load of 40 kN and tire pressure of 565 kPa that leaves a 'circular' imprint on the pavement was assumed for this study. The second type of structure is an overlay structure, illustrated on the right side of Figure 4-7, which was used to measure the tensile strain underneath the overlay (at the interface). The load parameters are applied through a single wheel and single axle. The load on the tire is 40 kN, and the tire pressure is 827 kPa. The tire contact shape is rectangular, with a tire width of 175 mm.

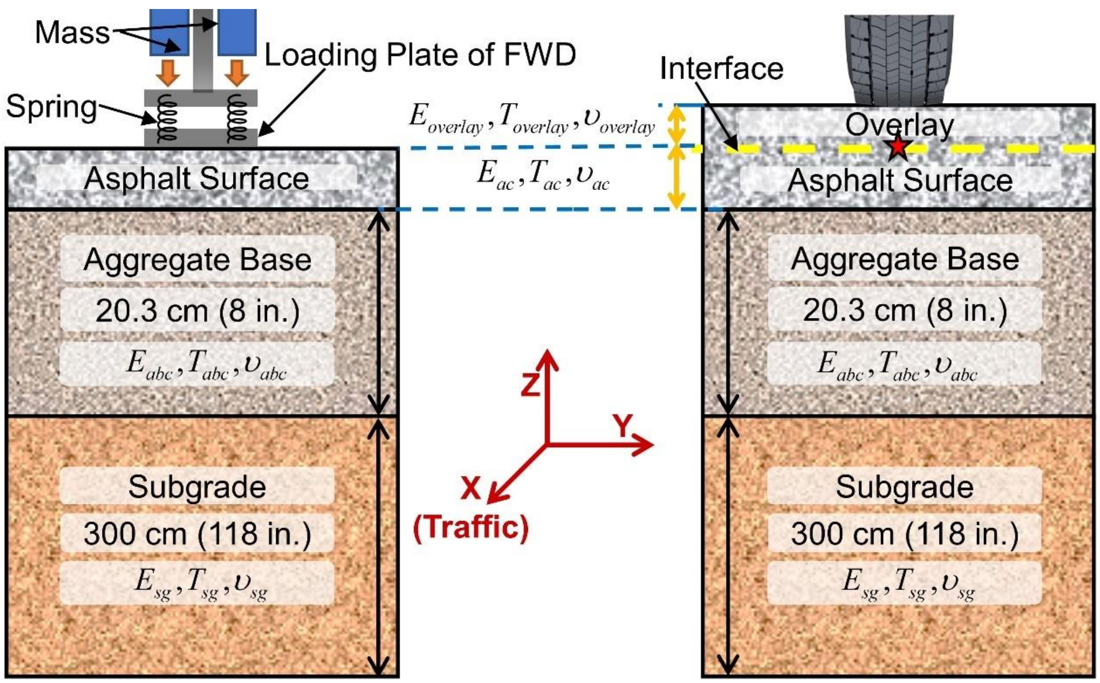

Figure 4-6. Pavement structures used to analyze pavement responses: (left) without overlay and (right) with overlay.

4.5 EverstressFE Analysis Output

The output measured for the two types of structures differs due to the difference in the requirements. The output of the structure without an overlay includes only the deflection measurements on the pavement surface that was subjected to FWD loading. The deflection points were measured 0 in., 8 in., 12 in., 18 in., 24 in., 36 in., and 48 in. from the loading center. Figure 4-7 shows the typical deflection bowl and deflection measurement points for the structure without an overlay. Similarly, Figure 4-8 and Figure 4-9 show the difference in the deflection bowl due to changes in the surface layer thickness and modulus, respectively.

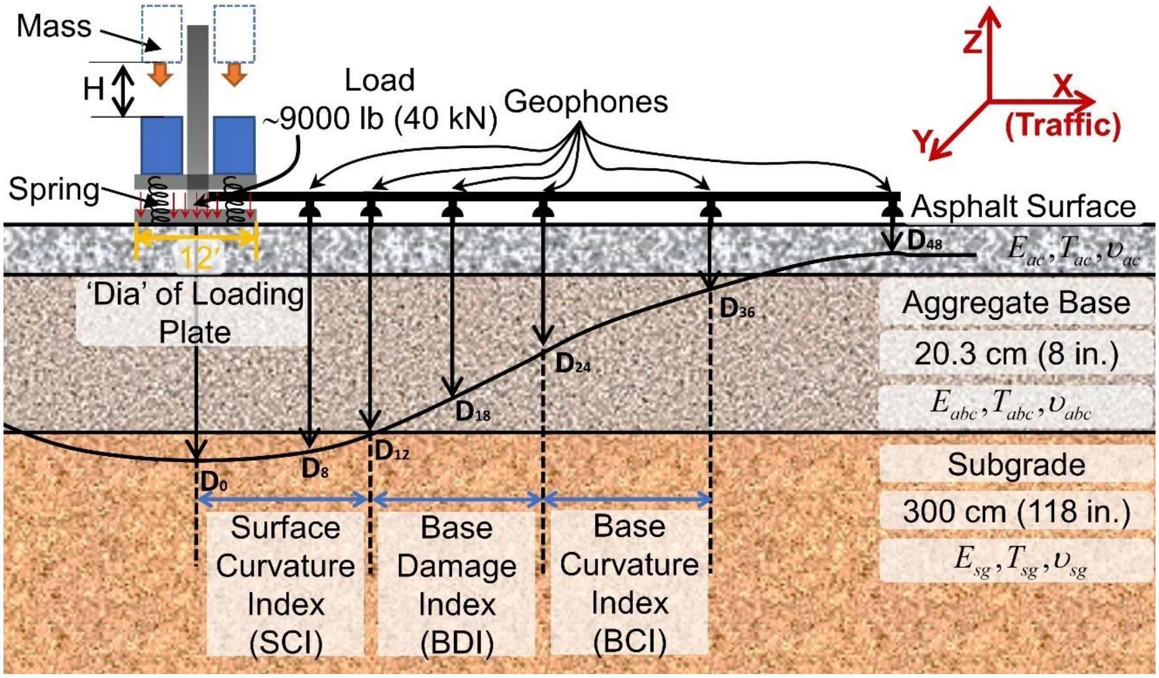

Figure 4-7. Typical falling weight deflectometer deflection bowl and measurement points.

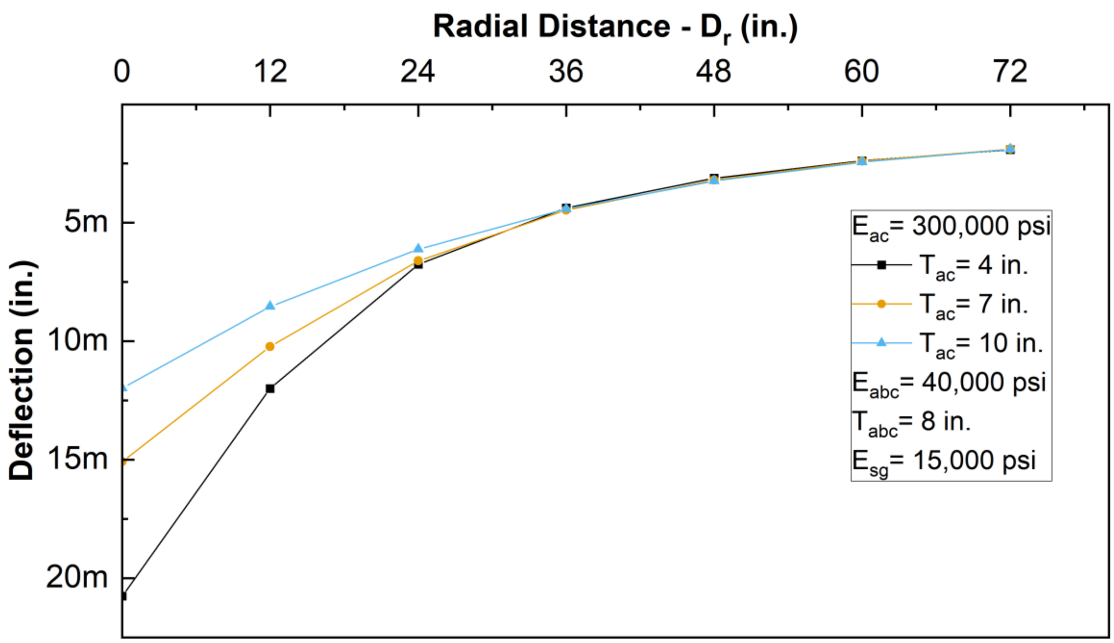

Figure 4-8. Falling weight deflectometer deflection bowl with changes in asphalt concrete surface layer thickness.

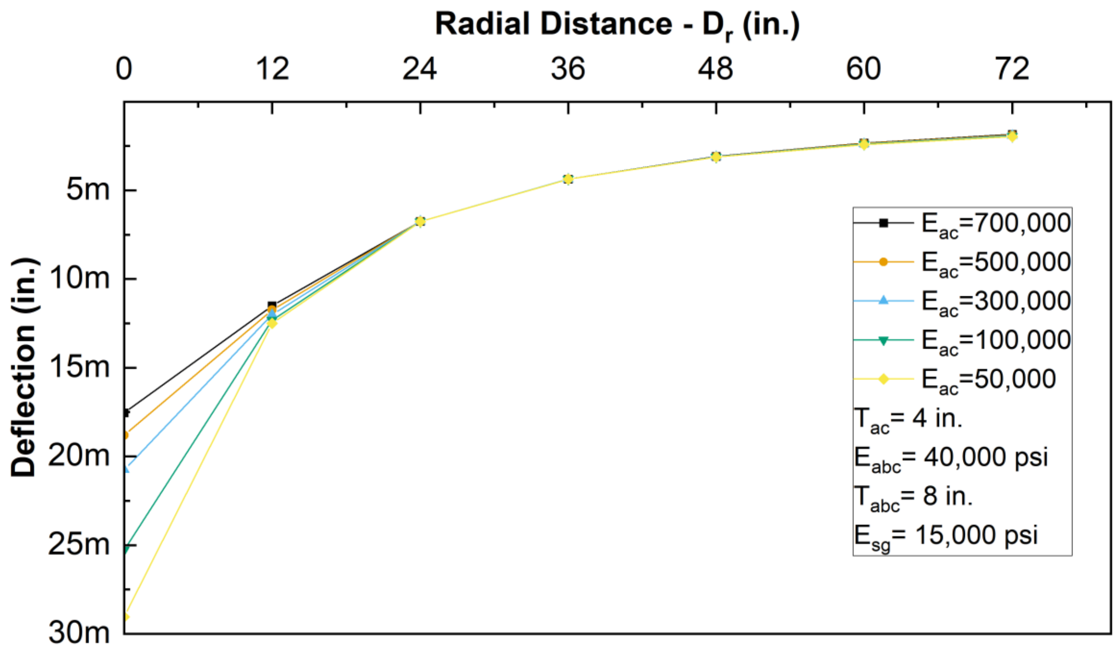

Figure 4-9. Falling weight deflectometer deflection bowl with changes in asphalt concrete surface layer modulus.

Intuitively, with an increase in AC thickness or modulus value, the deflections reduce by keeping the other structural and material parameters constant. Similar responses were observed during the pavement response analysis.

The second type of structure, the structure with an overlay, was used to measure the tensile strain underneath the overlay. Typically, for a specific structure without an overlay, three structures with overlays are simulated with overlay thicknesses of 1.5-in., 3-in., and 4-inches. Figure 4-10 and Figure 4-11 present the results for such a set of simulations of structures with overlays for thicknesses and modulus values, respectively. The results indicate that the thickness and modulus of the overlay have a more significant influence on the tensile strain measured at the interface than the thickness and modulus of the existing pavement layer.

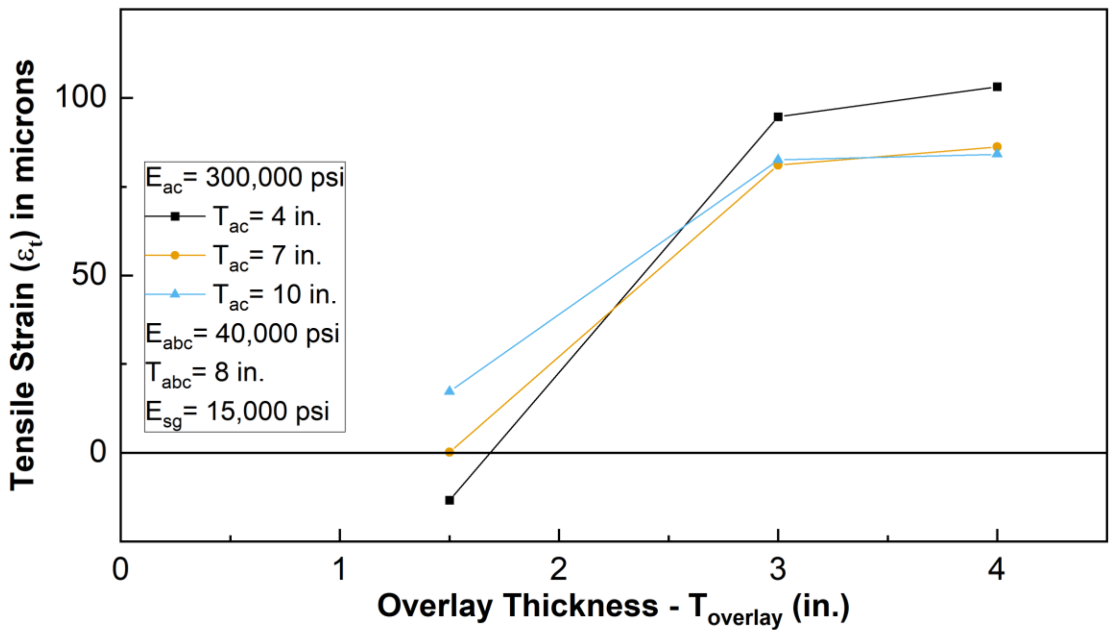

Figure 4-10. Tensile strain computed for various overlay thicknesses and asphalt concrete thicknesses of existing surface layer.

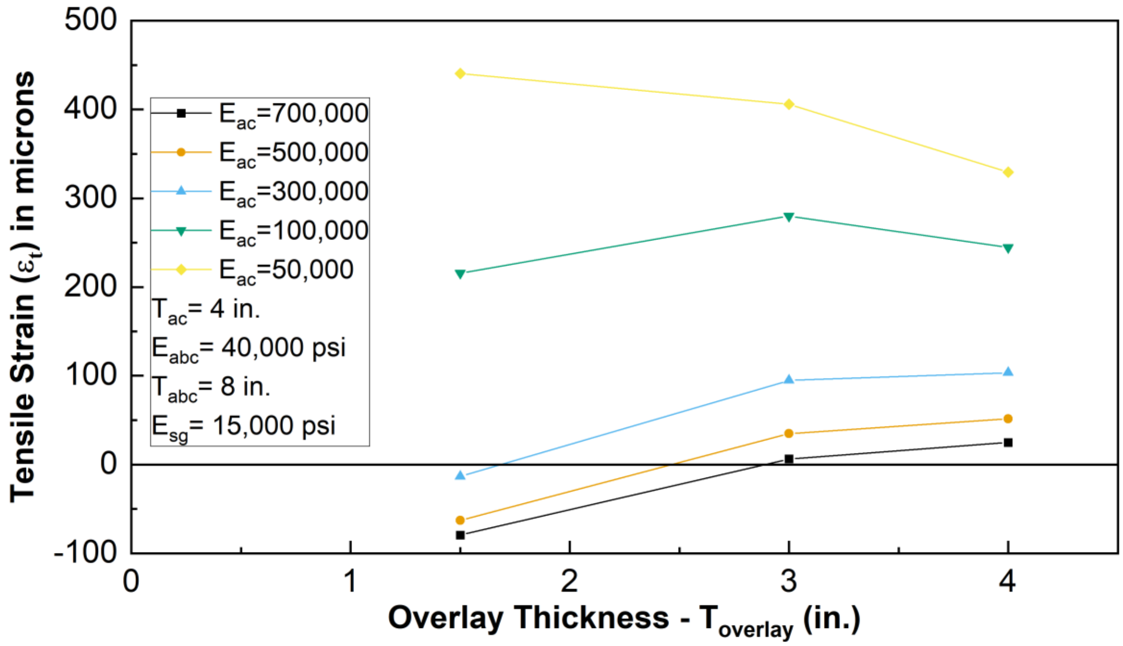

Figure 4-11. Tensile strain computed for various overlay thicknesses and varying asphalt concrete modulus values of existing surface layer.

Chapter 5. Interface Shear Strength Test Results and Discussion

5.1 Interface Shear Strength

During the MAST tests, four measurements were recorded to analyze the ISS test results: actuator displacement, actuator force, on-specimen displacement using DIC, and confining force. The actuator displacement, actuator force, and confinement load measurements were acquired using a 16-bit National Instruments data acquisition board and recorded using LabVIEW software. VIC-2D software was employed to measure the on-specimen displacements.

Actuator displacement was used only to verify the input constant displacement rate for the test and not used for the analysis. Actuator force measurements can be used to calculate the shear stress (τ_s) at any time during the test, as shown in Equation (5-1).

$$\tau_s = \frac{F_A}{A_{cs}} \tag{5-1}$$

where

F_A = axial force, kN, and

A_{cs} = cross-sectional area of the specimen, m^2.

The on-specimen displacement that was measured via DIC was used to calculate the DIC shear strain (γ) to avoid any effects of machine compliance on the actuator strain, as shown in Equation (5-2).

$$\gamma = \frac{u_{A-DIC}}{SG} \tag{5-2}$$

where

u_{A-DIC} = DIC-based axial displacement, and

SG = shear gap [8 mm (0.3 in.) in this study].

The confining force that was measured using a load cell placed in the platen parallel to the specimen is used to calculate the normal stress that is present in real field conditions, as defined in Equation (5-3).

$$\sigma_c = \frac{F_c}{A_{cs}} \tag{5-3}$$

where

F_c = confining force.

On-specimen strain values typically are lower than crosshead LVDT (actuator) measured strain values and differ depending on the stiffness of the specimen that affects machine compliance. As shown in Figure 5-1, the crosshead strain rate remained constant throughout the test, while the DIC strain rate follows a nonlinear trend. Chehab et al. (2002) proposed a pure power form fitting method to measure the strain rates for such nonlinear responses. The on-specimen strain rate in power form is shown in Equations (5-4), (5-5), and (5-6).

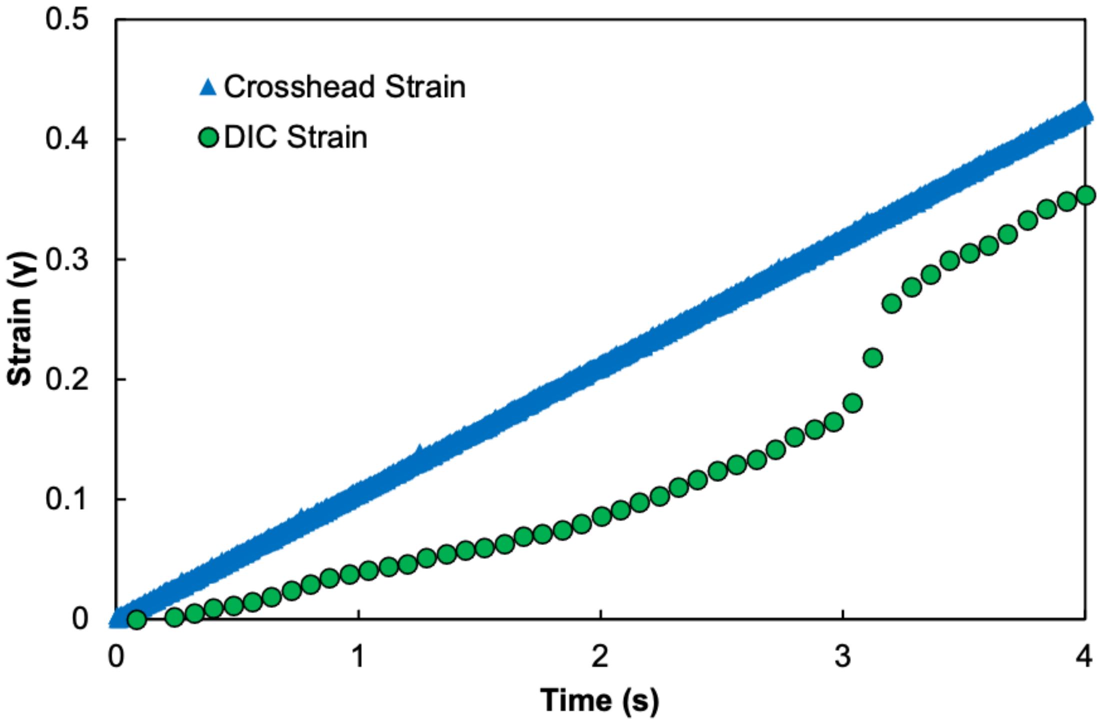

Figure 5-1. Shear strain measured via crosshead LVDT and DIC for interface shear strength tests at 50.8 mm/min, 19°C, and 483 kPa confining for Ultrafuse.

$$\varepsilon = k' \times t^n \tag{5-4}$$

$$\varepsilon = k' \times a_T^n \times \left(\frac{t}{a_T}\right)^n \tag{5-5}$$

$$\varepsilon = k \times \xi^n \tag{5-6}$$

where

ε = strain,

k' = slope of strain vs. time at temperature T,

ξ = reduced time at reference temperature, and

k = reduced strain rate at reference temperature.

Figure 5-2 shows the fitting technique used to obtain the strain rate. For this process, only the data before failure were used. In other words, if the data deviate from a power law, they should be excluded from the fitting process to obtain the strain rate.

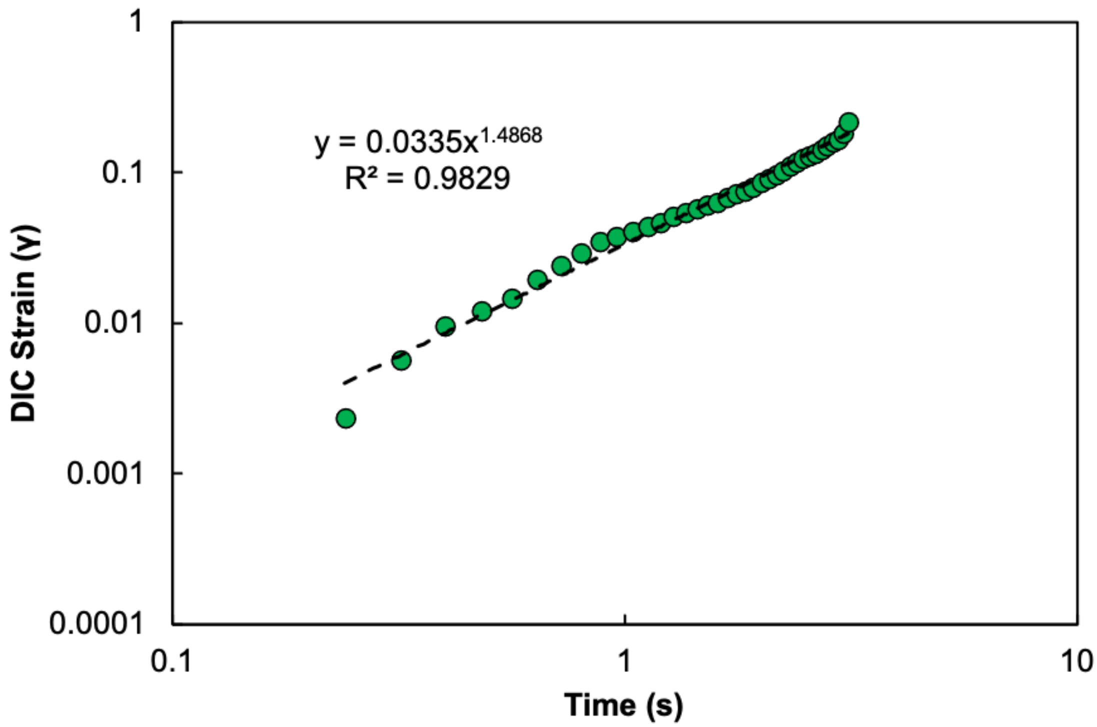

Figure 5-2. Pure power form fitting method to evaluate strain rate (k') at 50.8 mm/min, 19°C, and 483 kPa confining pressure for Ultrafuse.

In this research, k' is considered the DIC shear strain rate ($\dot{\gamma}$) measured based on the method proposed by Chehab et al. (2002). The reduced shear strain rate ($\dot{\gamma}_R$) was calculated by multiplying the DIC shear strain rate by the shift factor (a_T) measured from dynamic shear modulus tests of the corresponding tack coat material used for the MAST specimen, as shown in Equation (5-7).

$$\dot{\gamma}_R = \dot{\gamma} \times a_T \tag{5-7}$$

where

$\dot{\gamma}_R$ = reduced shear strain rate, and

$\dot{\gamma}$ = shear strain rate.

5.1.1 Effects of Geosynthetic Interlayer Type on Interface Shear Strength

Safavizadeh (2015) demonstrated that the t-T superposition principle is valid for constructing an ISS mastercurve based on MAST test results for geosynthetic-reinforced AC specimens and based on DSR test results for tack coats. Following the same methodology, in this research, mastercurves were constructed for the different geosynthetic-reinforced specimens based on tests carried out at three different temperatures and a constant actuator displacement rate of 5.08 mm/min (0.2 in./min). Figure 5-3 shows that the presence of any type of geosynthetic product under any testing conditions reduces the ISS and increases the chances of debonding. The shear resistance of MAST specimens at the confining pressure levels of 172 kPa (25 psi) and 483 kPa (70 psi) can be divided into three clear categories based on the shear strength mastercurves. The control specimen (labeled ‘CS-Opt-0.03’ in Figure 5-3) shows the best shear resistance in comparison to any of the geosynthetic-reinforced specimens under any specific testing condition. PC#1 and PaG display the highest shear strength values among the geosynthetic-reinforced specimens, and PM, PF, and PC#2 show the lowest shear strength values.

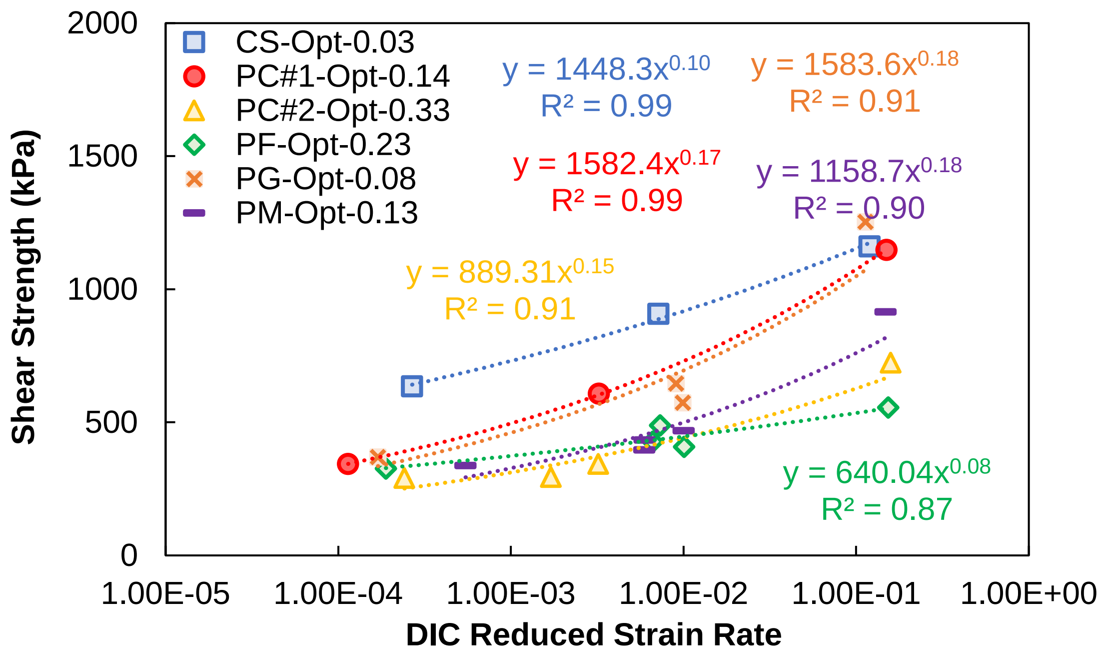

2000
1500
1000
500
0
Shear Strength (kPa)
CS-Opt-0.03
PC#1-Opt-0.14
PC#2-Opt-0.33
PF-Opt-0.23
PG-Opt-0.08
PM-Opt-0.13
y = 1448.3x^0.10
R² = 0.99
y = 1583.6x^0.18
R² = 0.91
y = 1582.4x^0.17
R² = 0.99
y = 1158.7x^0.18
R² = 0.90
y = 889.31x^0.15
R² = 0.91
y = 640.04x^0.08
R² = 0.87
1.00E-05
1.00E-04
1.00E-03
1.00E-02
1.00E-01
1.00E+00
DIC Reduced Strain Rate

(a)

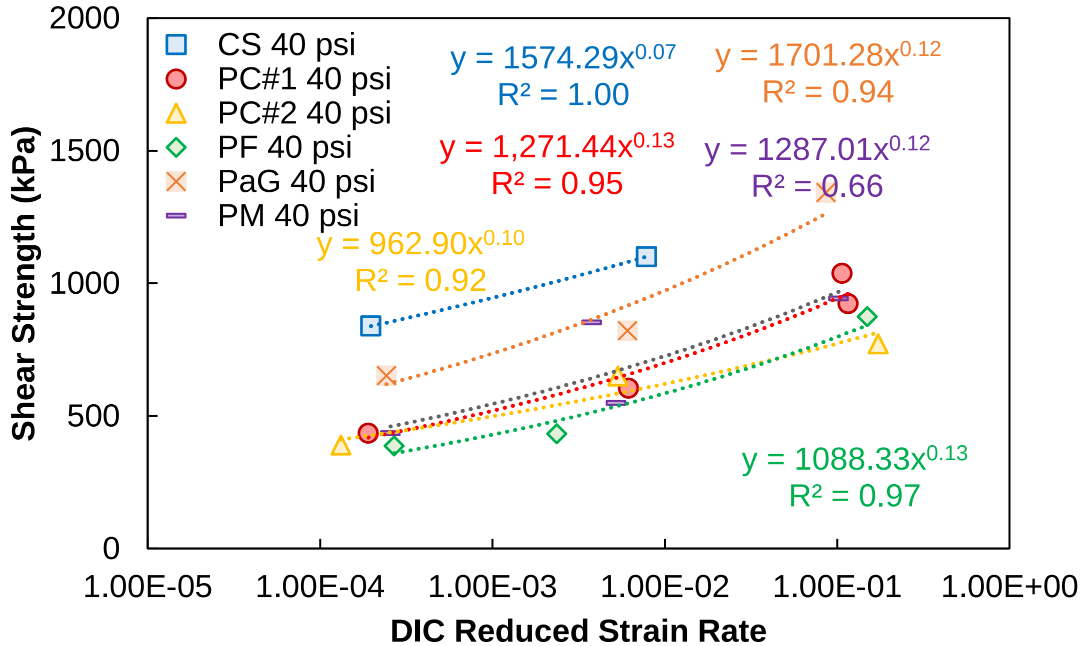

2000
1500
1000
500
0
Shear Strength (kPa)
CS 40 psi
PC#1 40 psi
PC#2 40 psi
PF 40 psi
PaG 40 psi
PM 40 psi
y = 1574.29x^0.07
R² = 1.00
y = 1701.28x^0.12
R² = 0.94
y = 1,271.44x^0.13
R² = 0.95
y = 1287.01x^0.12
R² = 0.66
y = 962.90x^0.10
R² = 0.92
y = 1088.33x^0.13
R² = 0.97
1.00E-05
1.00E-04
1.00E-03
1.00E-02
1.00E-01
1.00E+00
DIC Reduced Strain Rate

(b)

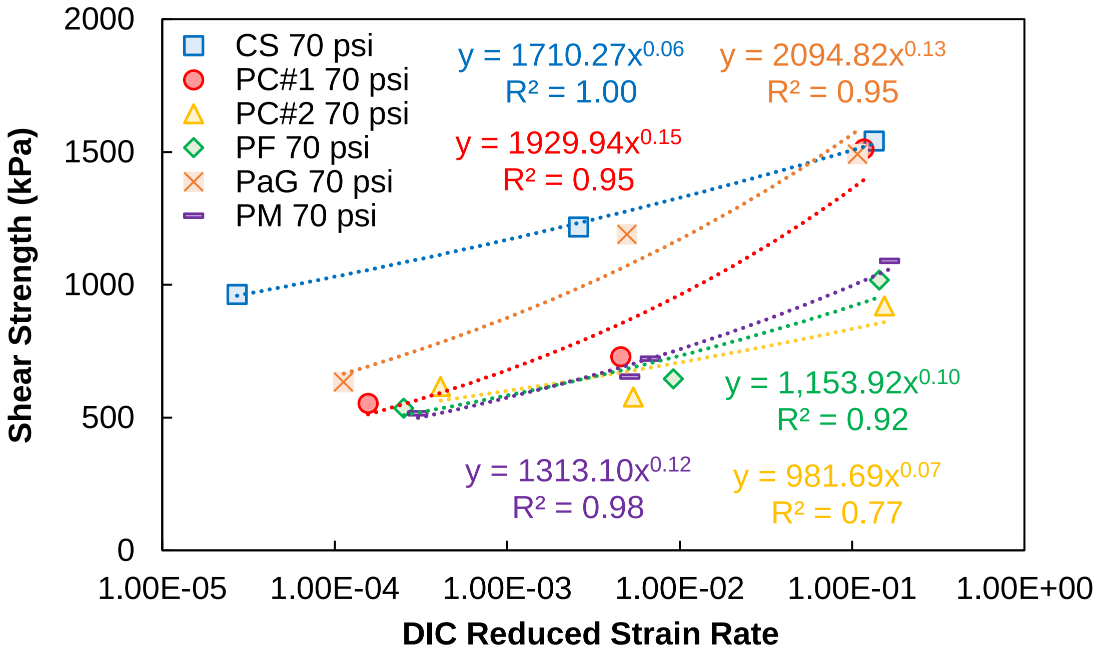

(c)

Figure 5-3. Mastercurves for different geosynthetic-reinforced asphalt specimens at the confining pressure levels of (a) 172 kPa (25 psi), (b) 276 kPa (40 psi), and (c) 483 kPa (70 psi).

Table 2-2 in Chapter 2 presents the tack coat application rates applied for the different geosynthetic interlayer products. The optimum tack coat application rates for PC#2 and PF are 1.36 L/m^2 (0.3 gal/yd^2) and 1.04 L/m^2 (0.23 gal/yd^2), respectively. PC#2 and PF exhibit greater asphalt retention capacity as they are the thickest products among the five, thereby demanding a high tack coat application rate. However, the effective tack coat application rate, which is the total tack coat application rate minus the asphalt retention rate, is the same for all the geosynthetic materials for each of the dry, optimum, and wet conditions. Thus, the major cause of the weak ISS of PC#2 and PF, as shown in Figure 5-3, is the greater geosynthetic thickness of 2 mm to 3 mm (0.08 in. - 0.12 in.) compared to the average thickness of 1 mm (0.04 in.) for the other three products. Consequently, this thickness factor forces the reinforced interface to act as a soft shearing plane, which contributes to easy failure. The viscoelastic nature of asphalt makes the tack coat-impregnated geosynthetic interface behave as a stiffer interface layer at 23°C (73°F) than at the higher temperatures of 35°C (95°F) and 54°C (129°F). This viscoelasticity causes geosynthetic products such as PC#1 and PaG with similar thicknesses to yield comparable ISS values at 23°C (73°F). However, Figure 5-3 shows that the PaG-reinforced specimen has the highest shear strength values among all the geosynthetic-reinforced specimens. The grid openings in the PaG product allow direct contact between the upper and lower AC layers, which activates an additional interlocking action due to friction. The other four geosynthetic products are continuous structures that avoid direct AC layer contact. These products demand a high asphalt application rate compared to PaG's tack coat application rate of 0.36 L/m^2 (0.08 gal/yd^2); thus, they behave as a softer interlayer at higher temperatures. The effect of temperature on the tack coat has less impact on the PaG-reinforced specimens than the other specimens. The combination of these two factors (grid opening size and temperature dependency) explains the high ISS value for the PaG-reinforced specimens at high temperatures.

5.1.2 Effect of Tack Coat Application Rate on Interface Shear Strength

Five geosynthetic-reinforced MAST specimens with three different application rates that correspond to dry, optimum, and wet conditions were tested to measure the ISS; Figure 5-4 (a) through (e) respectively present the results. The application rate for each specimen in gal/yd^2 is given in the legends. Figure 5-4 provides no clear trend between the ISS and tack coat application rate that can be seen among all different geosynthetic materials. That is, based solely on visual observations of the graphical representations of the results, the effect of the tack coat rate on the ISS that is universal for all five geosynthetic products is difficult to determine. However, note that the ISS from the optimum rate for the PM and PF products is clearly lower than those from the dry and wet rate. Statistical analysis on the data shown in Figure 5-4, which is described in Section 5.2, supports this observation. The research team could not explain why the optimum rate for the PM and PF products yielded the lowest ISS values, other than the fact that these two products have flat surface whereas other products have grid patterns that would affect the shear behavior of geosynthetic-reinforced specimens. More replicates and probably a more sensitive test, such as the shear fatigue test, are needed to accurately evaluate the effect of tack coat rate on the ISS. Ragni et al. (2021) has conducted a preliminary study to vet this idea and found that cyclic tests are sensitive to tack coat.

The indeterminate outcomes are in line with the results from a study carried out for the NCDOT RP2018-13 project (Kim et al. 2021) in which three different tack coat application rates (0.01, 0.03, and 0.05 gal/yd^2) were investigated. In that study, MAST specimens were fabricated with three application rates for five different tack coats, and the results did not show any effect of tack coat application rate on the ISS. The conclusions reached in the RP2018-13 study include that the real effect and implications of the application rate cannot be captured completely using the ISS test, because it is a quick monotonic shear test that serves primarily as a quality control test. Cyclic shear fatigue tests are considered to be more reliable for understanding the effect of application rate because the loading mode is similar to real field conditions.

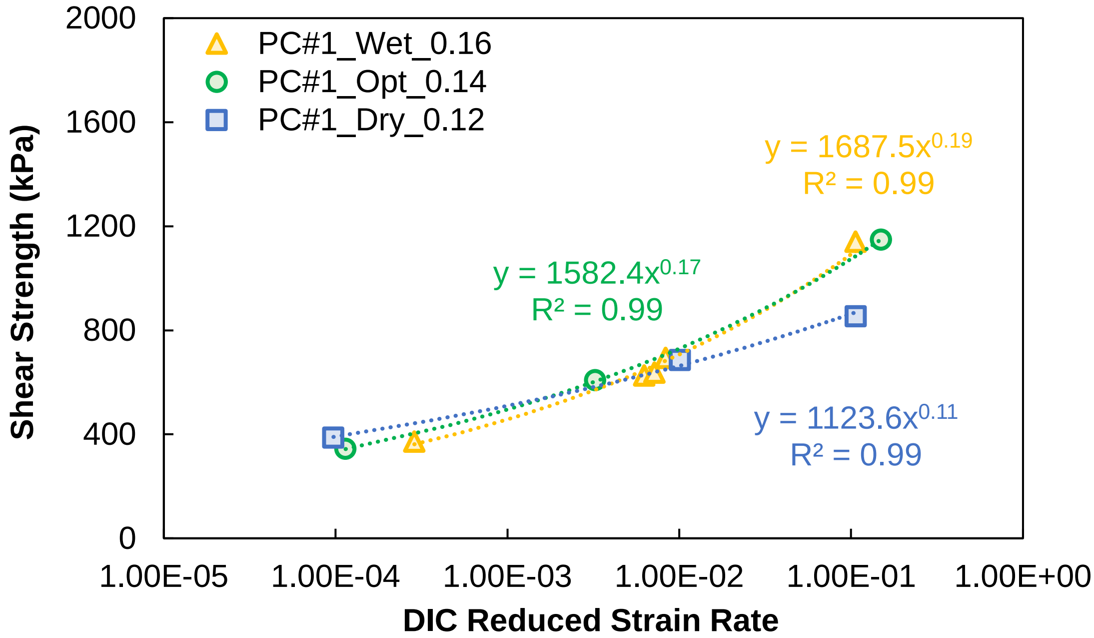

PC#1_Wet_0.16
PC#1_Opt_0.14
PC#1_Dry_0.12
y = 1687.5x^0.19
R² = 0.99
y = 1582.4x^0.17
R² = 0.99
y = 1123.6x^0.11
R² = 0.99
Shear Strength (kPa)
DIC Reduced Strain Rate

(a)

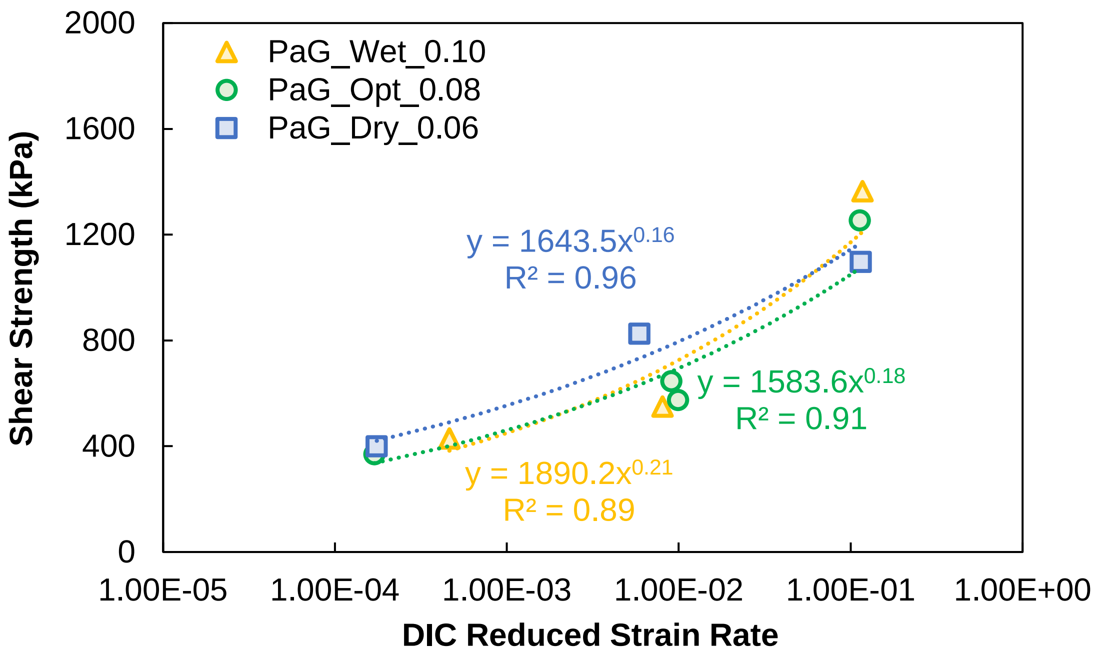

PaG_Wet_0.10
PaG_Opt_0.08
PaG_Dry_0.06
y = 1643.5x^0.16
R² = 0.96
y = 1583.6x^0.18
R² = 0.91
y = 1890.2x^0.21
R² = 0.89
Shear Strength (kPa)
DIC Reduced Strain Rate

(b)

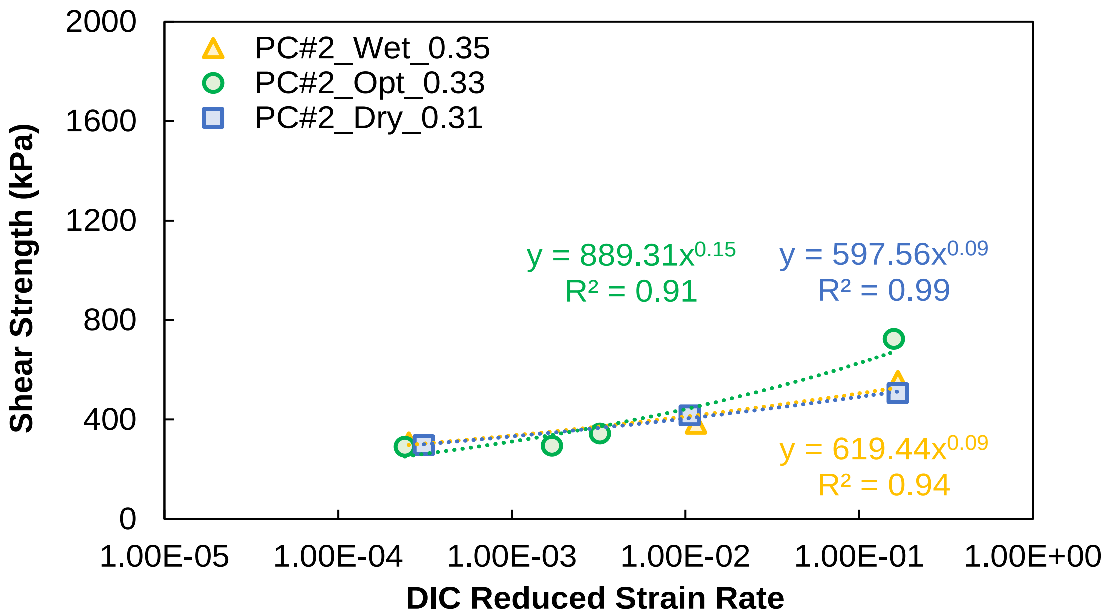

Shear Strength (kPa)
2000
1600
1200
800
400
0
1.00E-05
1.00E-04
1.00E-03
1.00E-02
1.00E-01
1.00E+00
DIC Reduced Strain Rate
PC#2_Wet_0.35
PC#2_Opt_0.33
PC#2_Dry_0.31
y = 889.31x^0.15
R² = 0.91
y = 597.56x^0.09
R² = 0.99
y = 619.44x^0.09
R² = 0.94

(c)

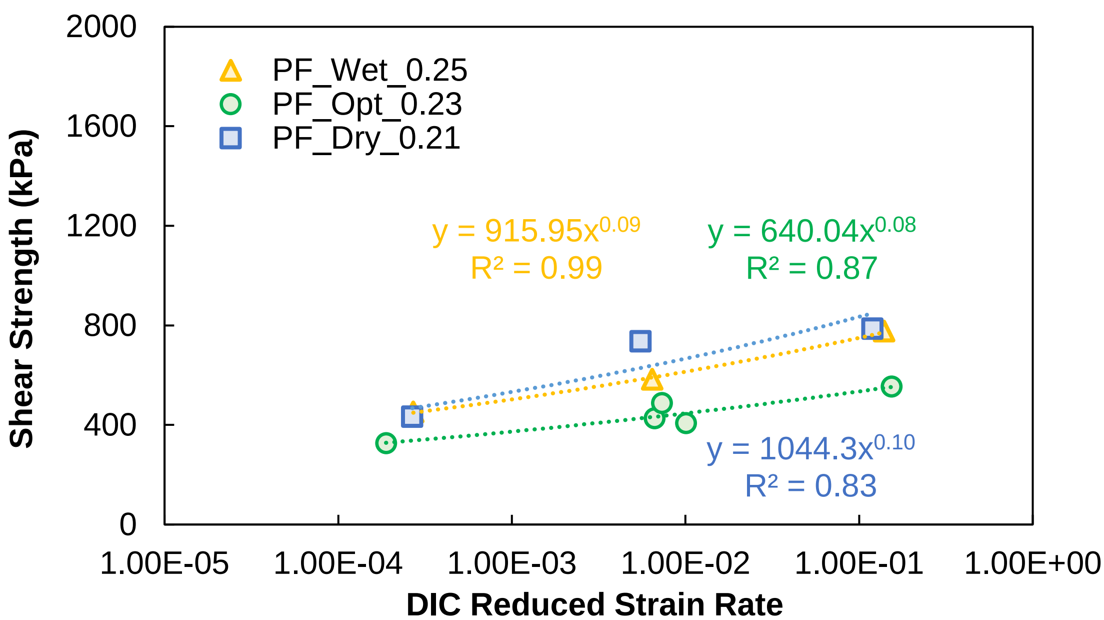

Shear Strength (kPa)
2000
1600
1200
800
400
0
1.00E-05
1.00E-04
1.00E-03
1.00E-02
1.00E-01
1.00E+00
DIC Reduced Strain Rate
PF_Wet_0.25
PF_Opt_0.23
PF_Dry_0.21
y = 915.95x^0.09
R² = 0.99
y = 640.04x^0.08
R² = 0.87
y = 1044.3x^0.10
R² = 0.83

(d)

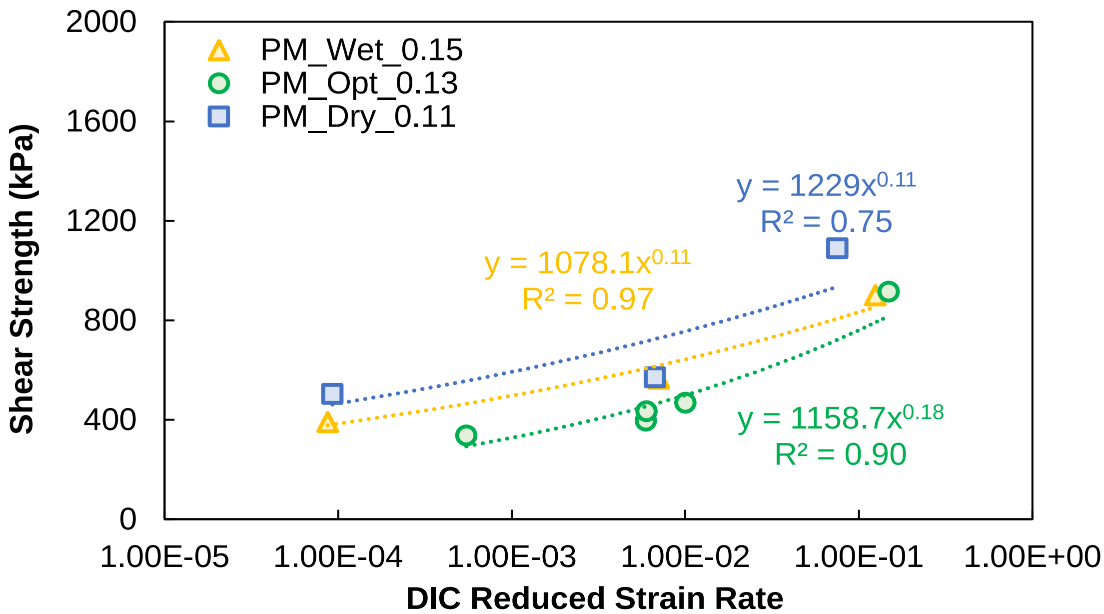

(e)

Figure 5-4. Tack coat application rate effect at 172 kPa (25 psi) confining pressure on geosynthetic-reinforced specimens: (a) PC#1, (b) PaG, (c) PC#2, (d) PF, and (e) PM.

5.1.3 Effect of Temperature on Interface Shear Strength

The MAST tests were conducted using five different geosynthetic products at three different temperatures to find the effects of temperature on the ISS. Figure 5-5 (a) through (f) present comparisons of the ISS of control and geosynthetic-reinforced specimens at different temperatures. At the intermediate temperature, 35°C (95°F), at least two shear replicate tests were conducted under selected conditions at the confining pressure of 172.37 kPa (25 psi) to check for test variability. For the same type of geosynthetic-reinforced specimens, the shear strength decreased with an increase in temperature. Note that the effect of geosynthetic type on the ISS is evident at the low temperature of 23°C (73.4°F) but is nullified at the high temperature of 54°C (129.2°F).

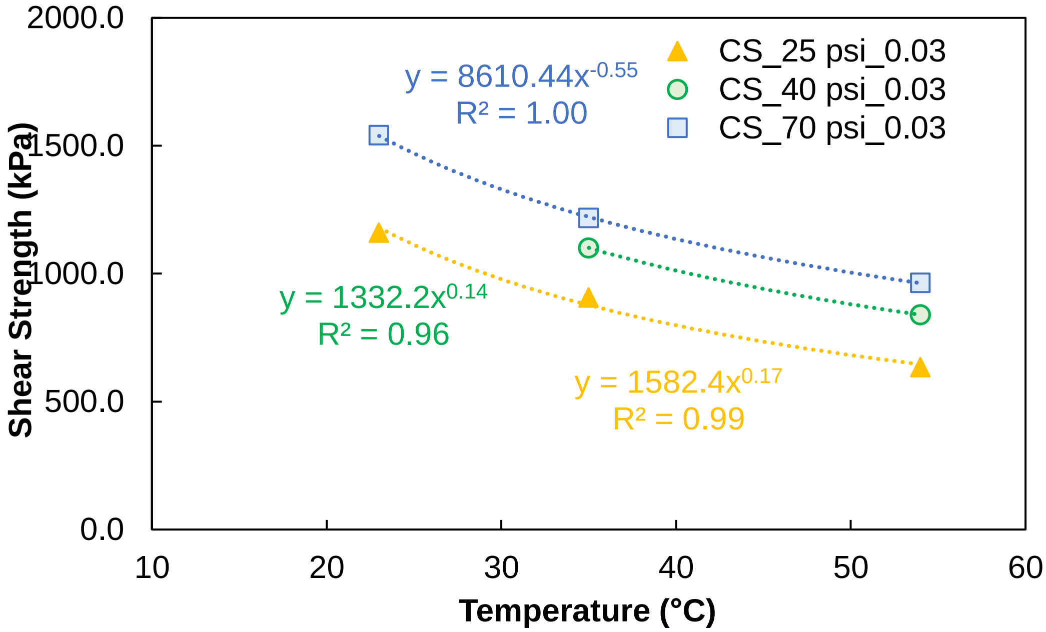

2000.0
1500.0
1000.0
500.0
0.0
Shear Strength (kPa)
10
20
30
40
50
60
Temperature (°C)
CS_25 psi_0.03
CS_40 psi_0.03
CS_70 psi_0.03
y = 8610.44x-0.55
R² = 1.00
y = 1332.2x0.14
R² = 0.96
y = 1582.4x0.17
R² = 0.99

(a)

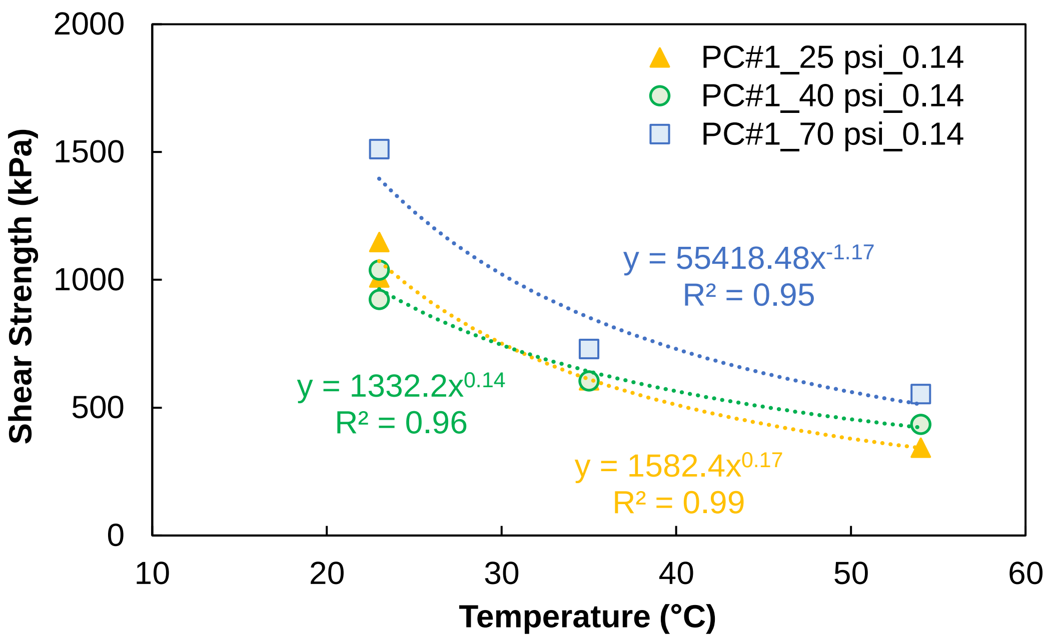

2000
1500
1000
500
0
Shear Strength (kPa)
10
20
30
40
50
60
Temperature (°C)
PC#1_25 psi_0.14
PC#1_40 psi_0.14
PC#1_70 psi_0.14
y = 55418.48x-1.17
R² = 0.95
y = 1332.2x0.14
R² = 0.96
y = 1582.4x0.17
R² = 0.99

(b)

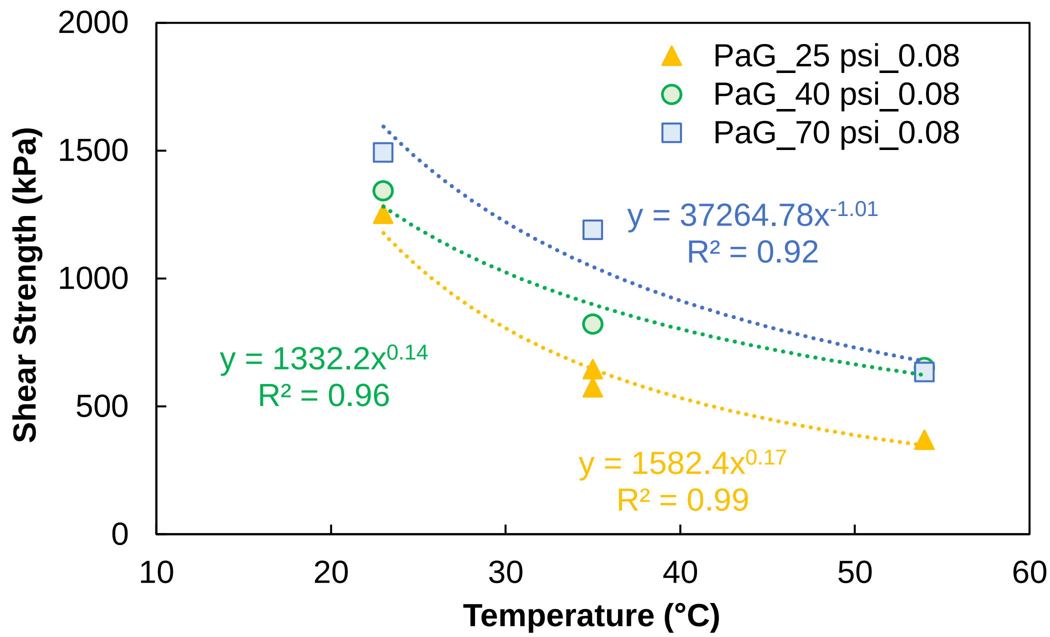

PaG_25 psi_0.08
PaG_40 psi_0.08
PaG_70 psi_0.08
y = 37264.78x-1.01
R² = 0.92
y = 1332.2x0.14
R² = 0.96
y = 1582.4x0.17
R² = 0.99
Shear Strength (kPa)
Temperature (°C)
2000
1500
1000
500
0
10
20
30
40
50
60

(c)

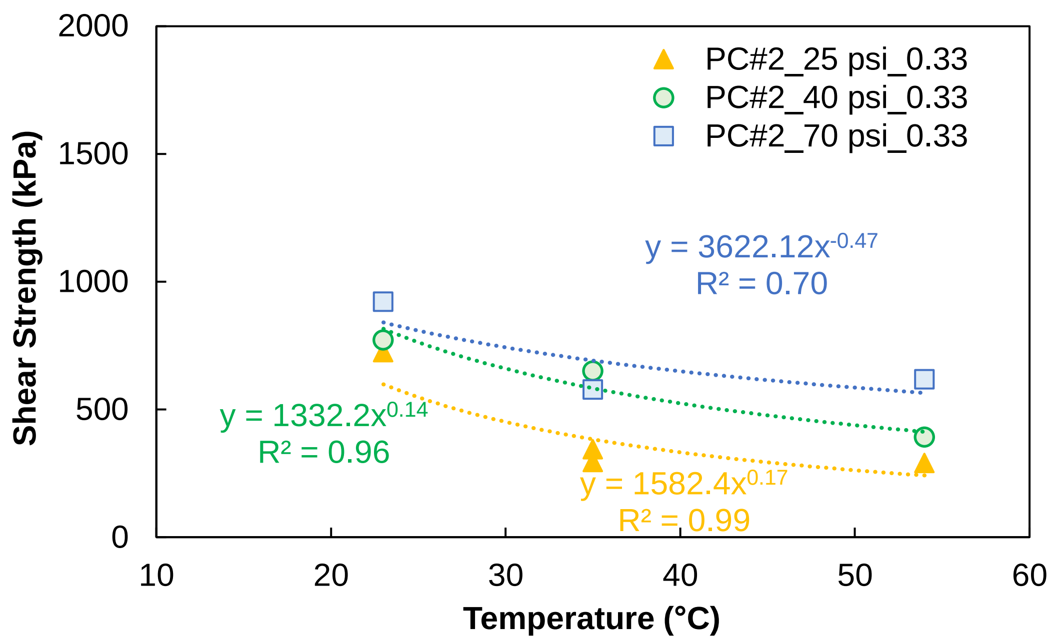

PC#2_25 psi_0.33
PC#2_40 psi_0.33
PC#2_70 psi_0.33
y = 3622.12x-0.47
R² = 0.70
y = 1332.2x0.14
R² = 0.96
y = 1582.4x0.17
R² = 0.99
Shear Strength (kPa)
Temperature (°C)
2000
1500
1000
500
0
10
20
30
40
50
60

(d)

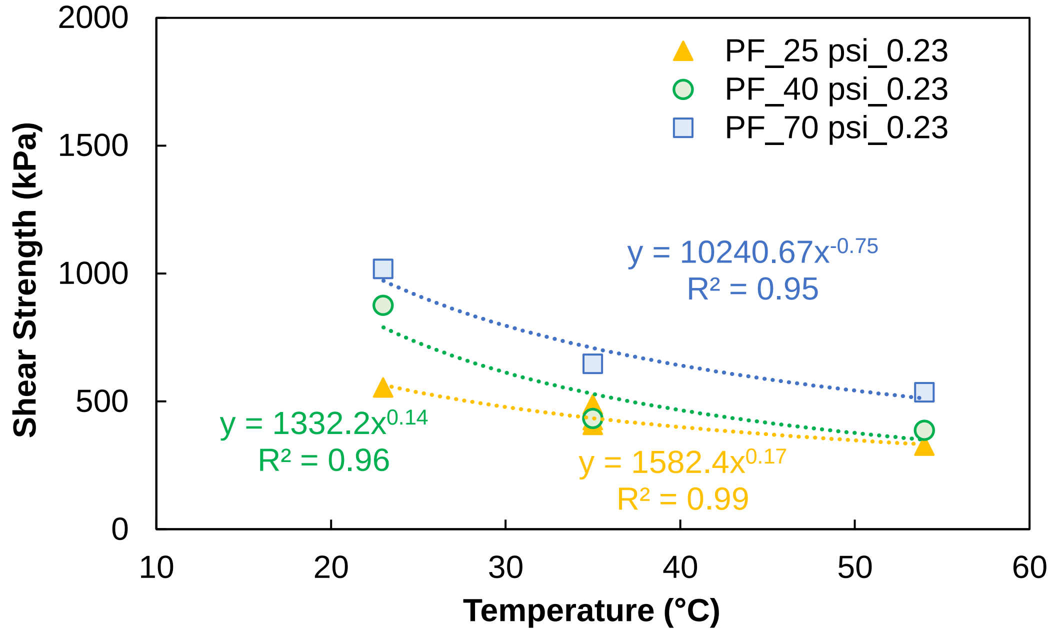

(e)

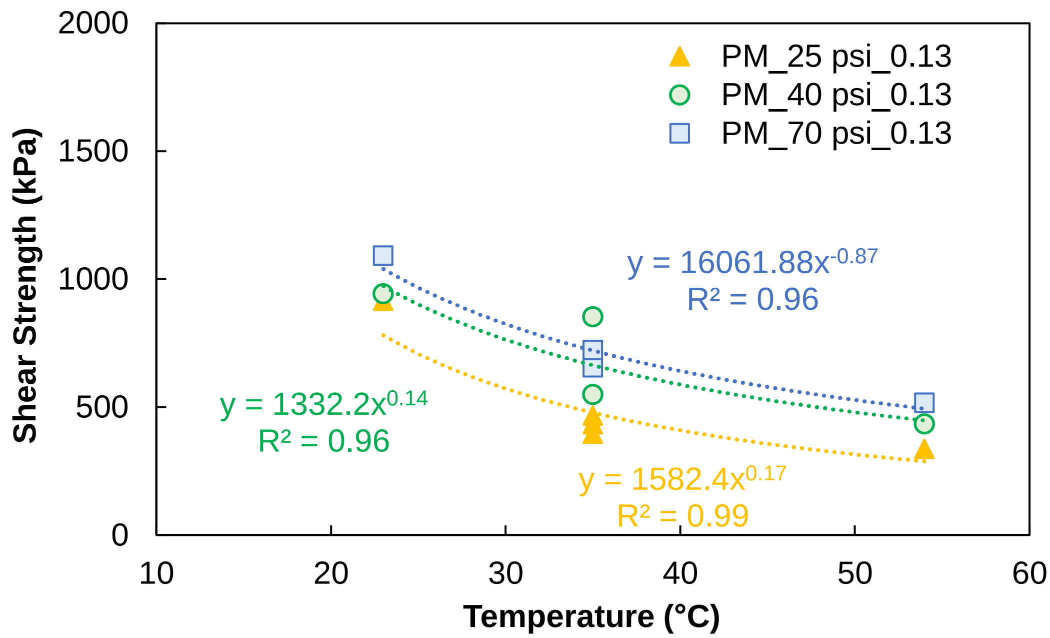

(f)

Figure 5-5. Temperature effect on geosynthetic-reinforced specimens: (a) CS, (b) PC#1, (c) PaG, (d) PC#2, (e) PF, and (f) PM.

5.1.4 Effect of Confining Pressure on Interface Shear Strength

Three different normal (confining) pressure levels, 172.37 kPa (25 psi), 275.79 kPa (40 psi), and 482.63 kPa (70 psi), were selected to conduct the MAST tests. The normal stress was applied by tightening the confinement plate against the specimen prior to testing. The change in confinement load during the test was recorded using a load cell.

Figure 5-6 shows that the effect of confinement pressure. The tack coat only control specimens (CS) show a clear linear trend between shear strength and confining pressure at the three different temperatures. However, the geosynthetic-reinforced specimens show a nonlinear trend and high variability. The results clearly show that an increase from 172 kPa (25 psi) to 483 kPa (70 psi) confining pressure increases the shear strength irrespective of the geosynthetic type used for specimen fabrication. However, the confining pressure levels of 172 kPa (25 psi) and 276 kPa (40 psi) show the comparable shear strength for all geosynthetic types. The nonlinear trend shown in Figure 5-6 is contrary to the typical linear trend found by previous researchers. For example, Canestrari's research group extensively studied the relationship between confining pressure and shear strength for geosynthetic-reinforced specimens (Canestrari et al. 2016a, Ferrotti et al. 2011, Partl et al. 2018, Pasquini et al. 2013). They found that ISS envelopes with confining pressure follow a linear trend. Also, Cho and Kim (2016) found a similar linear trend between shear strength and confining pressure at different strain rates during their ISS study of specimens fabricated using various tack coat emulsions. The limited data set available for the current research has created difficulty in ascertaining the credibility of the nonlinear trend, but it could be attributed to test variability. Therefore, considering the experience of previous researchers, a linear fit was used to develop the ISS prediction model in this study. However, an ISS study with a wider spectrum of confining pressure and higher number of replicates is recommended as a future research goal to establish a clear trend regarding the effect of confining pressure on the ISS of geosynthetic-reinforced specimens.

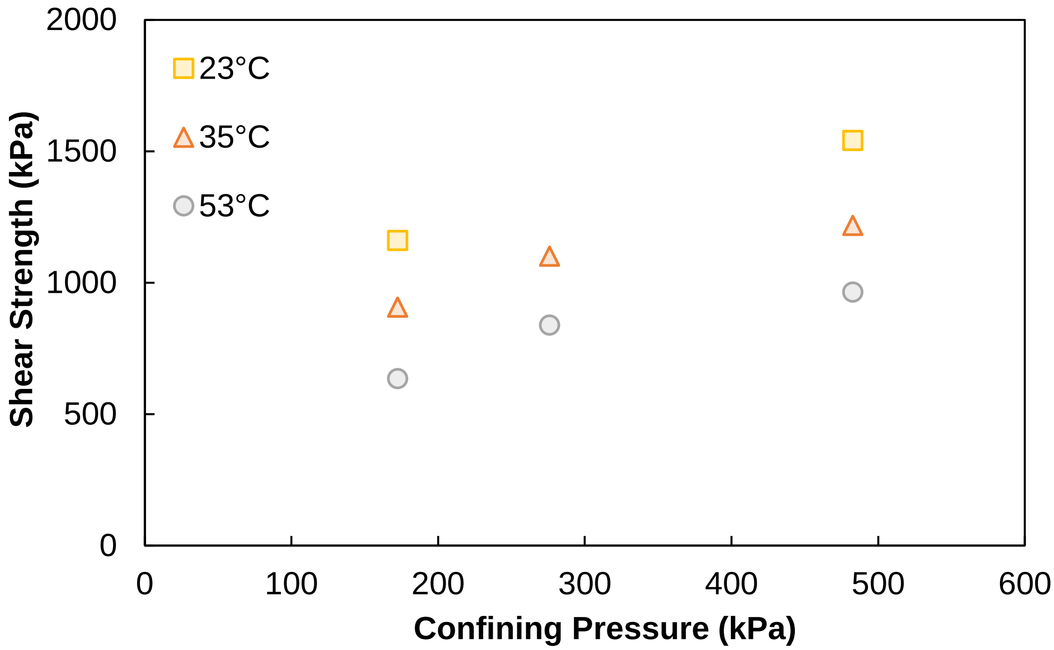

(a)

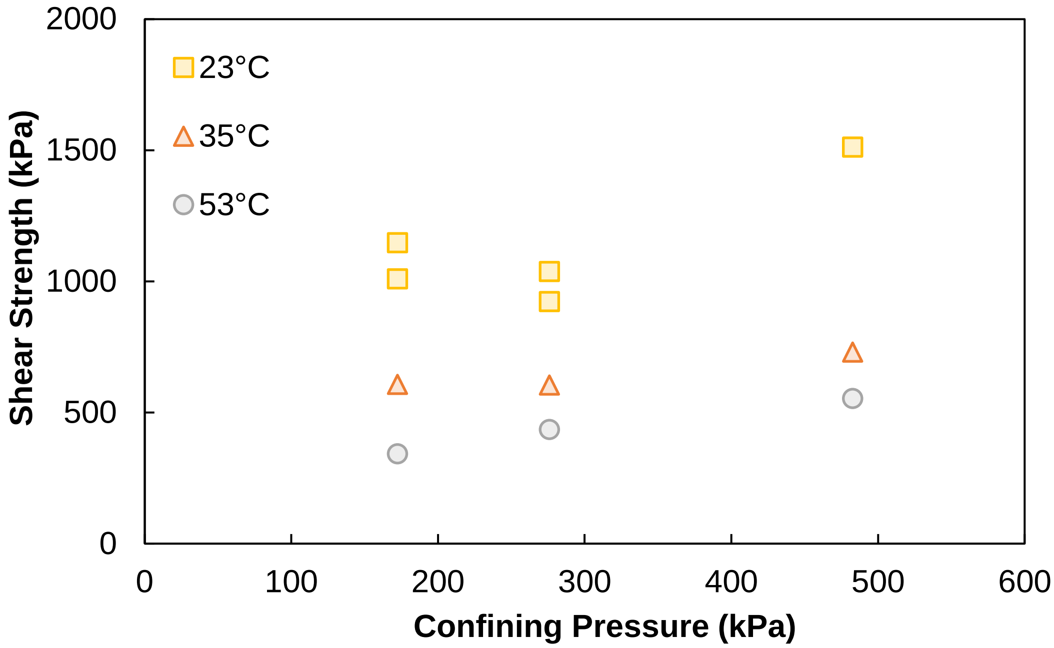
2000
1500
1000
500
0
0
100
200
300
400
500
600
23°C
35°C
53°C
Shear Strength (kPa)
Confining Pressure (kPa)

(b)

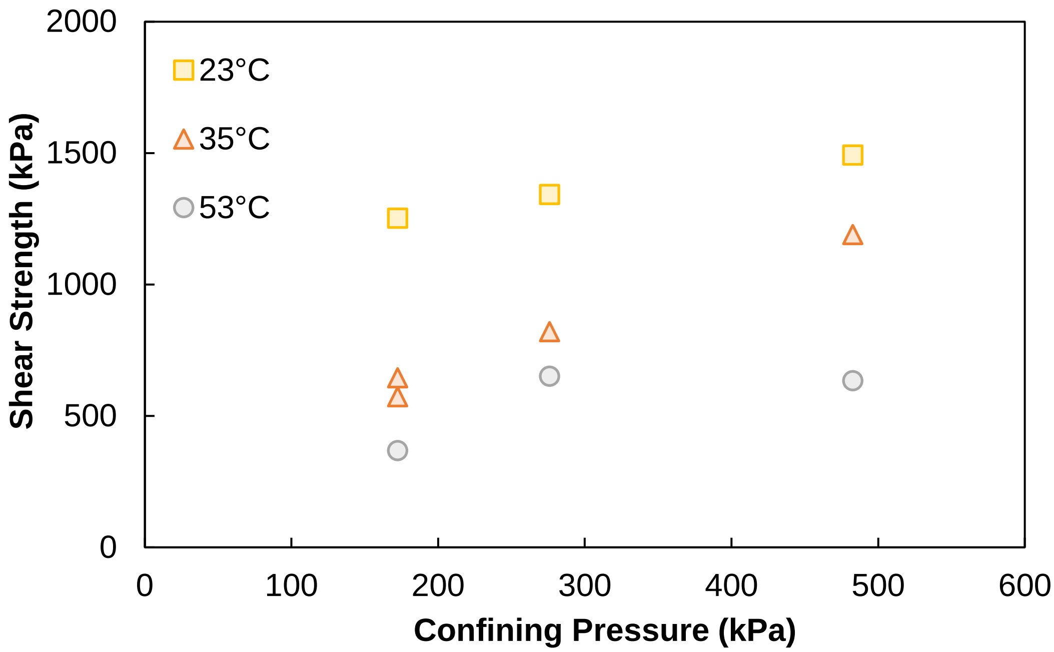
2000
1500
1000
500
0
0
100
200
300
400
500
600
23°C
35°C
53°C
Shear Strength (kPa)
Confining Pressure (kPa)

(c)

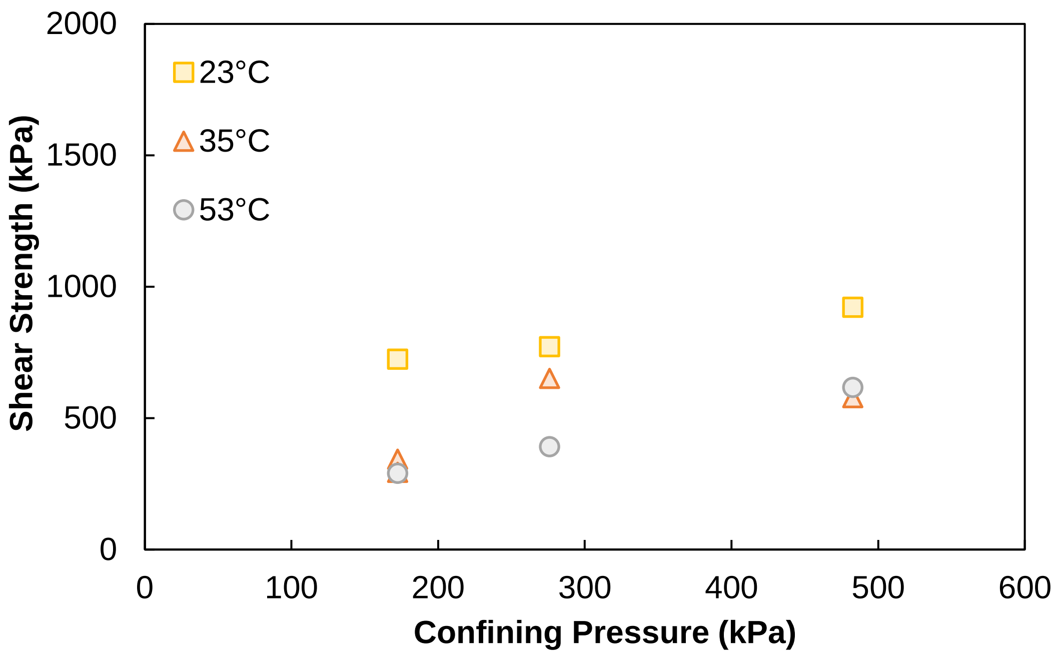

2000
1500
1000
500
0
Shear Strength (kPa)
23°C
35°C
53°C
0
100
200
300
400
500
600
Confining Pressure (kPa)

(d)

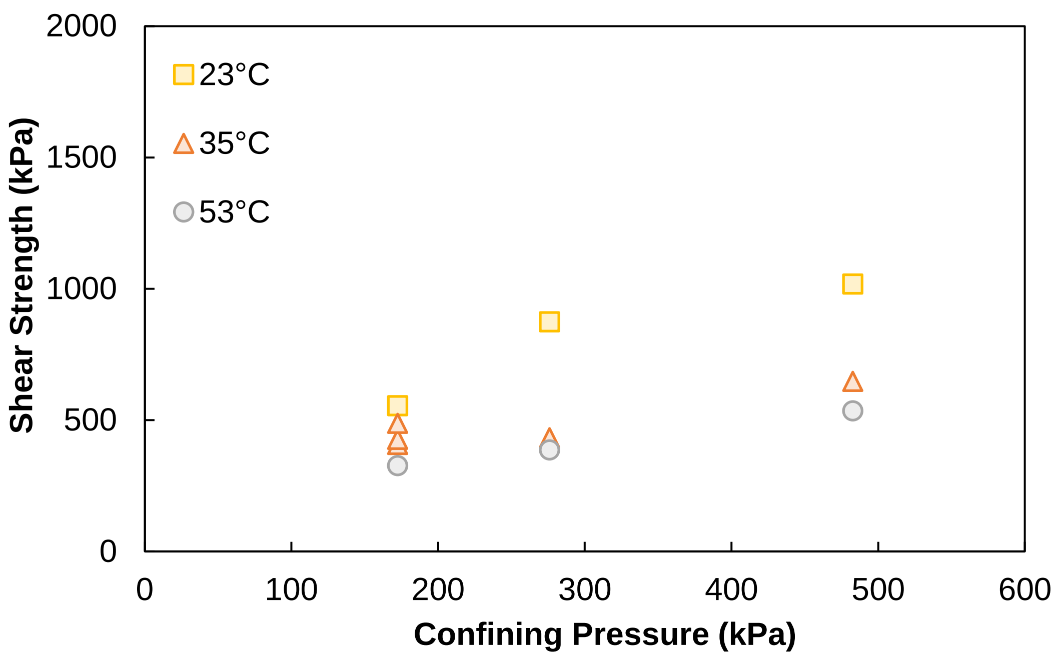

2000
1500
1000
500
0
Shear Strength (kPa)
23°C
35°C
53°C
0
100
200
300
400
500
600
Confining Pressure (kPa)

(e)

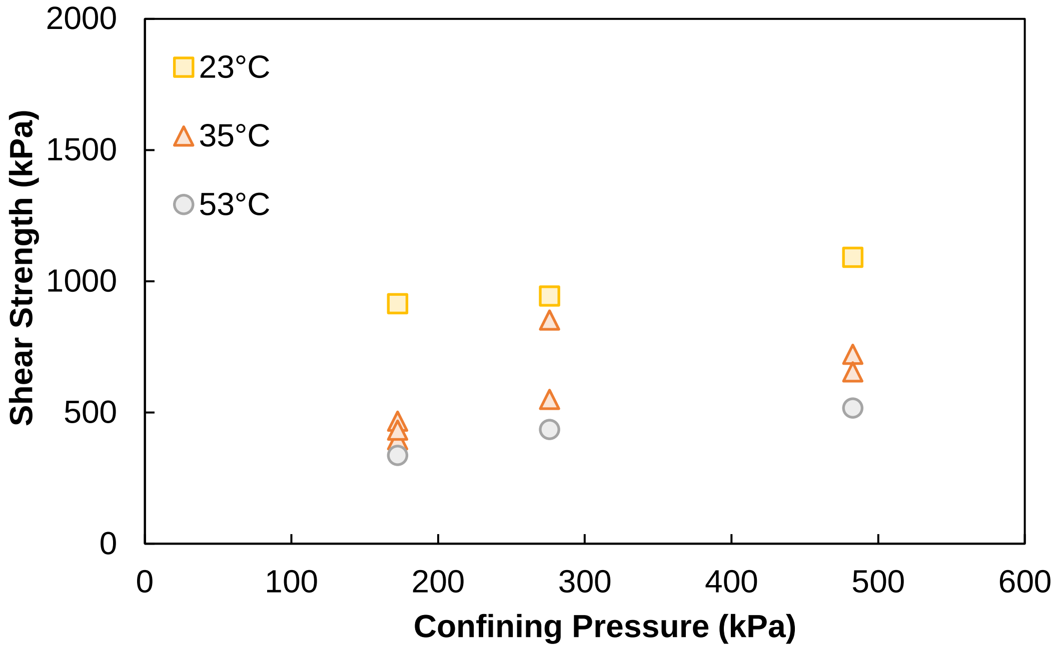

(f)

Figure 5-6 Correlation between shear strength and confining pressure at different temperatures: (a) CS, (b) PC#1, (c) PaG, (d) PC#2, (e) PF, and (f) PM.

5.2 Statistical Analysis of the Effect of Tack Coat Application Rate

The effect of the tack coat application rate on ISS was statistically analyzed in this study using the analysis of covariance (ANCOVA) model. The statistical software JMP 14 was used to conduct the single-factor ANCOVA, as shown in Equation (5-8).

$$Y_{ij} = \mu + \widehat{\beta}(x_{ij} - \overline{x}..) + \varepsilon_{ij} \qquad (5\text{-}8)$$

where

μ = the overall mean,

i = 1, 2, 3, …, r,

j = 1, 2, 3, …, n,

Y_{ij} = j^{th} observation under the i^{th} categorical group,

$\hat{\beta}$ = regression coefficient for the relationship between the response and covariate,

x_{ij} = covariates, and

ϵ_{ij} = random errors.

$\overline{x}$ = global mean for covariate x.

Table 5-1 presents the ANCOVA results. In this analysis, the tack coat application rate is the independent variable and the reduced strain rate is the covariate. At $\alpha = 0.05$, the tack coat application rates for PM and PF show a significant difference, which indicates that the effect of these tack coat application rates on the ISS is significant for PM and PF, but not for the other three geosynthetic types. Further, Table 5-2 and Table 5-3 present the results of Tukey honest significant difference (HSD) analysis for PM and PF, respectively. The confidence level used in this analysis is 95%, and 'Lower CL' and 'Upper CL' in Table 5-2 and Table 5-3 indicate the lower and upper boundaries of the confidence limit, respectively. The *p*-values shown in these tables indicate that the change in rate from dry to optimum has a significant effect on the ISS of PM and PF. Also, the effect of the rate changing from optimum to wet on the ISS is significant for PF but not for PM. A comparison of the ISS measured at the wet and optimum application rates as well as at the dry and wet application rates shows an insignificant effect ($p > 0.05$) of the application rate on ISS for PM. Also, the rate change from dry to wet shows an insignificant effect on the ISS for PF.

Table 5-1. Summary of ANCOVA Results

Geosynthetic Type	Sum of Squares	F Ratio	Prob > F
PC#1	0.001	2.31	0.19
PC#2	0.001	0.08	0.92
PM	0.076	6.30	0.03
PF	0.065	19.57	0.001
PaG	0.007	0.58	0.58

Table 5-2. Tukey HSD Analysis Results for PM

Level	Level	Difference	Std Err Dif	Lower CL	Upper CL	*p*-Value
Dry	Opt	0.196	0.057	0.028	0.364	0.0259
Wet	Opt	0.122	0.057	-0.046	0.289	0.1505
Dry	Wet	0.074	0.063	-0.112	0.261	0.5044

Note: Lower CL and Upper CL indicate the boundaries of the confidence limit.

Table 5-3. Tukey HSD Analysis Results for PF

Level	Level	Difference	Std Err Dif	Lower CL	Upper CL	*p*-Value
Dry	Opt	0.169	0.030	0.081	0.257	0.0019
Wet	Opt	0.136	0.030	0.049	0.224	0.0063
Dry	Wet	0.033	0.033	-0.065	0.131	0.6065

Note: Lower CL and Upper CL indicate the boundaries of the confidence limit.

Figure 5-7 (a) and (b) show a pictorial representation of the effect of the tack coat application rate on ISS for PM and PF, respectively. The data shown in Figure 5-7 do not follow the expected trend, i.e., the optimum tack coat application rate is expected to yield greater shear strength than the dry and wet rates. Reasons for this unexpected trend are difficult to find within the data generated in this study. Further study involving more tests is needed to explain this unexpected behavior.

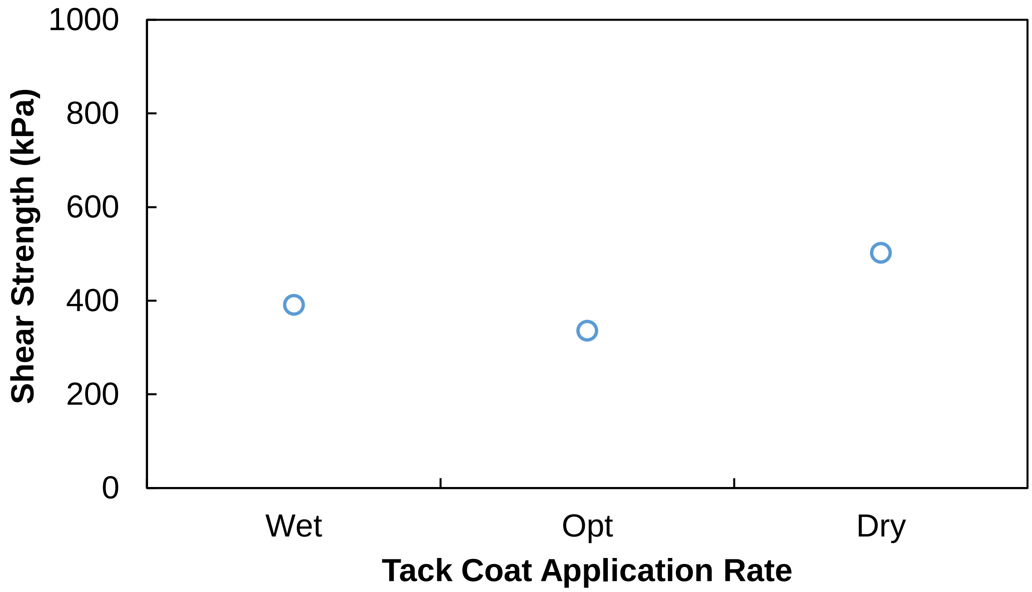

(a)

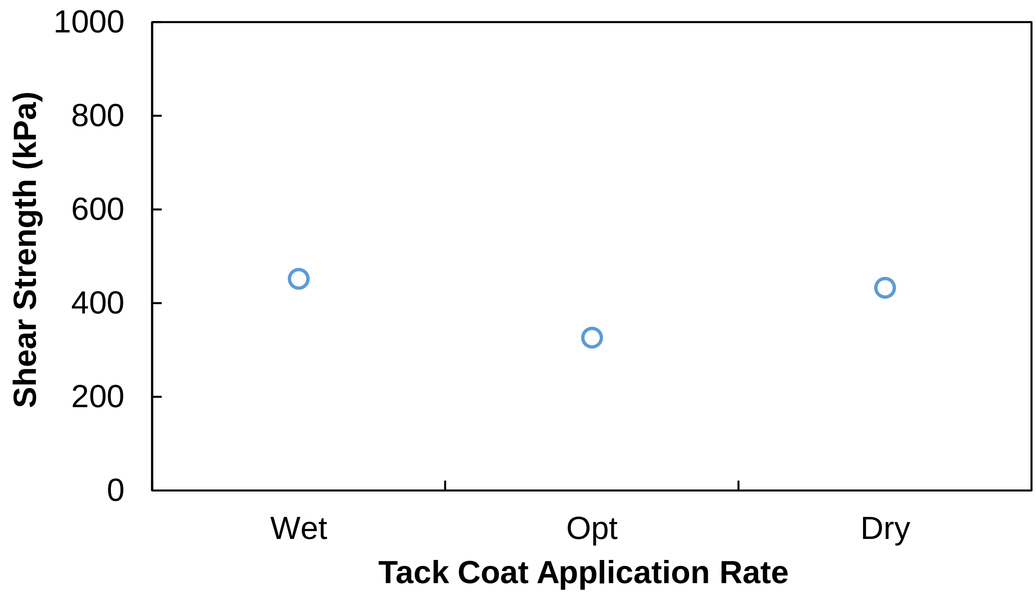

(b)

Figure 5-7. Effect of tack coat application rate on ISS: (a) PM and (b) PF.

Chapter 6. Notched Beam Fatigue Test Results and Discussion

The major driving force for reflective cracking is fatigue loading (a combination of traffic and thermal loads) that is experienced by pavement in the field. Hence, the reflective crack resistance capacity of geosynthetic-reinforced AC in this study was quantified using fatigue (repeated cycle) load tests. Numerous fatigue load configurations are readily available for such tests, and the outcomes can be correlated to field behavior depending on the fatigue test type and failure criteria applied to the results. The fatigue test selected to measure the crack resistance of geosynthetic-reinforced AC in this study is a modified version of the four-point beam fatigue test, i.e., the notched beam fatigue test (NBFT). The crack resistance capacity is the number of load cycles the geosynthetic-reinforced beam specimen will resist before reaching the failure threshold. A detailed explanation of the reflective cracking mechanism is provided in the Appendix A.

The selection of an appropriate failure criterion is a common consideration for laboratory asphalt fatigue testing. Many factors should be taken into consideration when developing an ideal failure criterion, but the criterion should involve only simple measurements, such as the load and displacement of the specimen, and avoid dependency on visual crack monitoring and advanced techniques such as DIC. However, correlating DIC results with traditional failure criteria is essential for this investigation in order to eliminate DIC for future test conditions. Also, a DIC study will help designers anticipate a particular failure mode in the field when using a geosynthetic product for paving applications.

6.1 Fatigue Models and Failure Criteria

The primary reason for conducting fatigue tests of AC mixtures is to find the parameters that allow models to predict the fatigue life of the tested mixture for a given pavement structure. In this case, the parameters were used to predict the crack resistance of geosynthetic-reinforced AC in a layered pavement structure. The crack resistance capacity of a geosynthetic-reinforced beam is measured similarly to the fatigue life of a homogenous AC beam specimen. In general, fatigue models that are used to predict the responses of AC pavements can be categorized into phenomenological and mechanistic approaches. In the phenomenological approach, the fatigue characteristics of the asphalt mixture usually are expressed as the relationship between the initial stress or strain and the number of load repetitions to failure. The mechanistic approach employs two major damage theories to predict pavement performance. One theory works on the principle of fracture mechanics, while the other is continuum damage theory to define the fatigue behavior of AC. Phenomenological models are used more commonly than mechanistic models to evaluate pavement performance. A phenomenological approach was adopted in this study to evaluate fatigue life in terms of crack resistance.

In the phenomenological approach, the pavement's structural responses are compared against laboratory-developed fatigue failure criteria. The most widely used structural response factor is the tensile strain at the bottom of the AC layer for bottom-up cracking, whereas the tensile strain and shear strain at the pavement's surface layer are used for top-down cracking. The initial number of load repetitions (N_i) and the number of cycles to failure (N_f) that separate the different phases during a fatigue test must be determined arbitrarily by individual experiments. Because the main objective of flexure fatigue testing is to determine how many load repetitions the material will sustain before failure, an accurate, standardized, and consistent definition of failure is needed to maintain the integrity of the test results and provide a consistent basis for any implementation scheme. In general, under controlled strain testing, the fatigue life of stiff mixtures is relatively short and that of softer mixtures is relatively long (Benedetto et al. 2004, Witczak et al. 2007). Many researchers have proposed various failure criteria to find the number of cycles to failure. The most common criteria are 'conventional' criteria as well as the phase angle criterion, *R*-squared criterion, dissipated energy ratio criterion, stiffness degradation ratio criterion, and stress × N failure criterion.

6.1.1 Basic Fatigue Models

Miner's cumulative damage principle typically is applied to predict fatigue cracking in AC pavements (Wilkins 1956). The ratio of predicted repetitions of traffic loading to the allowed repetitions of traffic during a specific period represents the pavement damage during that season. The damage ratios for various seasons are added to determine the cumulative fatigue damage to the pavement, as shown in Equation (6-1). When the cumulative damage ratio over a period exceeds one, that pavement is considered to be failed due to the fatigue cracking. Transfer functions are employed to convert the cumulative damage to the percentage of the area that is cracked.

$$D = \sum_{i=1}^{T} \frac{n_i}{N_i} \qquad (6\text{-}1)$$

where

D = damage,

T = total number of periods,

n_i = actual traffic for period i, and

N_i = allowable failure repetitions under conditions prevailing in period i.

Equation (6-2) is the general mathematical form found in the literature that is used to measure the number of load repetitions to fatigue failure. This model is a function of the initial tensile strain response at a given location and the modulus of the asphalt layer considered for the initial tensile strain.

$$N_f = \beta_3 k_1 \varepsilon_t^{k_2} E^{k_3} \qquad (6\text{-}2)$$

where

N_f = number of load repetitions to failure (i.e., fatigue cracking in this case),

ε_t = tensile strain at the bottom of the asphalt layer,

E = modulus of the asphalt concrete,

k_1, k_2, k_3 = material properties (calibration parameters), and

β_3 = field calibration factor (shift factor) that depends on the location and climatic conditions.

The material properties k_1, k_2, and k_3 in Equation (6-2) are measured by conducting four-point beam fatigue tests. Figure 6-1 presents a typical fatigue life relationship obtained from beam fatigue test results by Chakroborty and Das (2017). The beam fatigue tests were conducted at different tensile strain levels and various temperatures. The initial tensile strain was measured at the 50th cycle. Each data point in Figure 6-1 is the fatigue life (number of cycles to failure) for the four-point beam fatigue test conducted at a specific temperature, frequency, and strain/stress level.

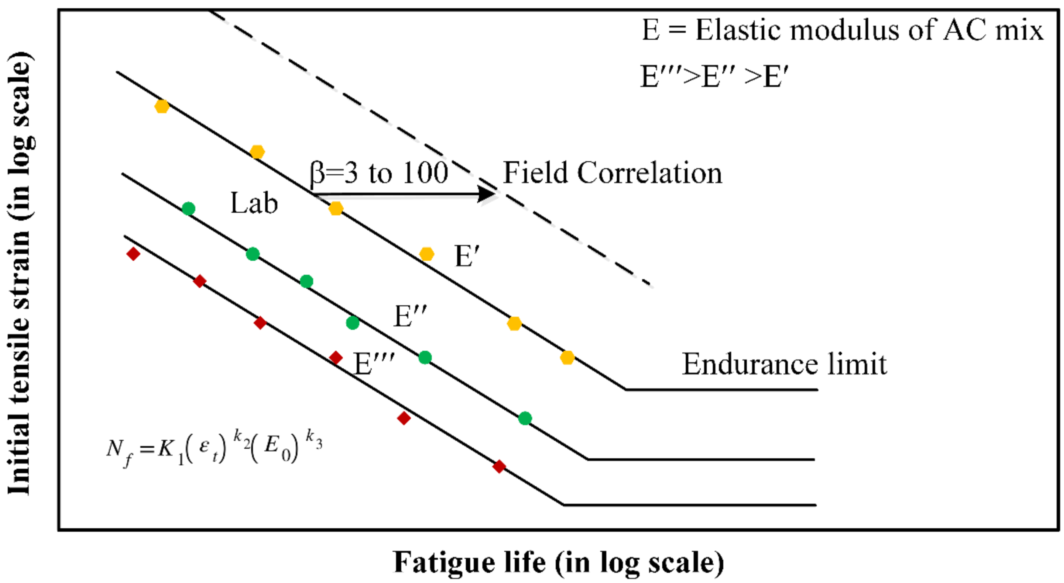

Figure 6-1. Schematic diagram of laboratory fatigue test results for asphalt concrete mixture (Chakroborty and Das 2017).

The fatigue life/specimen failure cycle can be measured using any of the failure criteria proposed in the following Section 6.1.2. Typically, the number of load cycles required for 50% reduction in flexural stiffness is considered the failure criterion for a homogenous AC mix. The phenomenological relationship for fatigue life for laboratory test results is mathematically expressed by Equation (6-3) (Asphalt Institute 1991, Monismith et al. 1985, Shell International Petroleum Company 1978, Si et al. 2002, Tayebali et al. 1994). The Equation (6-3) coefficients are obtained by fitting the expression to the data points shown in Figure 6-1. The trend indicates that an increase in the mixture modulus reduces the fatigue life. This response is attributable to the brittle nature of the binder at higher modulus values and vice versa in terms of fatigue failure. However, the fatigue life that is predicted using Equation (6-3) cannot be applied directly to predict field performance due to complexities in the field. Hence, users of this equation develop local calibration factors (β) based on field studies to help relate lab study results to the field.

$$N_f = K_1 \left(\varepsilon_t\right)^{k_2} \left(E_0\right)^{k_3} \tag{6-3}$$

where

N_f = the number of load cycles to failure,

ε_t = initial tensile strain,

E_0 = initial stiffness (modulus) of the material, and

k_1, k_2, k_3 = regression coefficients.

The failure criterion that is selected to define failure determines the fatigue life. The following Section 6.1.2 describes commonly used criteria and ways that each criterion can help determine the crack resistance of geosynthetic-reinforced AC mixes.

6.1.2 Different Types of Failure Criteria

Conventional Criteria

During a beam fatigue test, the data obtained from the test device are the load and displacement data. This information is substituted in the relationships shown in Equations (6-4), (6-5), and (6-6) and used to measure the maximum stress, strain, and flexural stiffness, respectively, of beam specimens during four-point bending beam fatigue tests. A detailed derivation of the equations is provided in the Appendix B.

$$\sigma_t = \frac{3 \times a \times P}{b \times h^2} \tag{6-4}$$

where

a = center-to-center spacing between clamps (Cox: 119 mm),

P = load applied by the actuator (N),

b = average specimen width (mm), and

h = average specimen height (mm).

$$\varepsilon_t = \frac{12 \times \delta \times h}{\left(3 \times L^2\right) - \left(4 \times a^2\right)} \tag{6-5}$$

where

δ = maximum deflection at the center of the beam (mm) and

L = length of the beam between outside clamps (Cox: 357 mm).

Equation (6-6) is used for calculating the flexural beam stiffness (MPa) that is referred to as stiffness (S) in this research.

$$S = \frac{\sigma_t}{\varepsilon_t} \tag{6-6}$$

Once the stiffness value is calculated for each data point during the test, it can be plotted against the number of cycles.

The flexural stiffness degradation of the beam that occurs with an increase in the number of load cycles in constant strain and constant stress mode tests follows a typical trend, as shown in Figure 6-2 (axes in linear-linear scale). The three stiffness reduction phases are the primary, secondary, and tertiary stages, described in the following text.

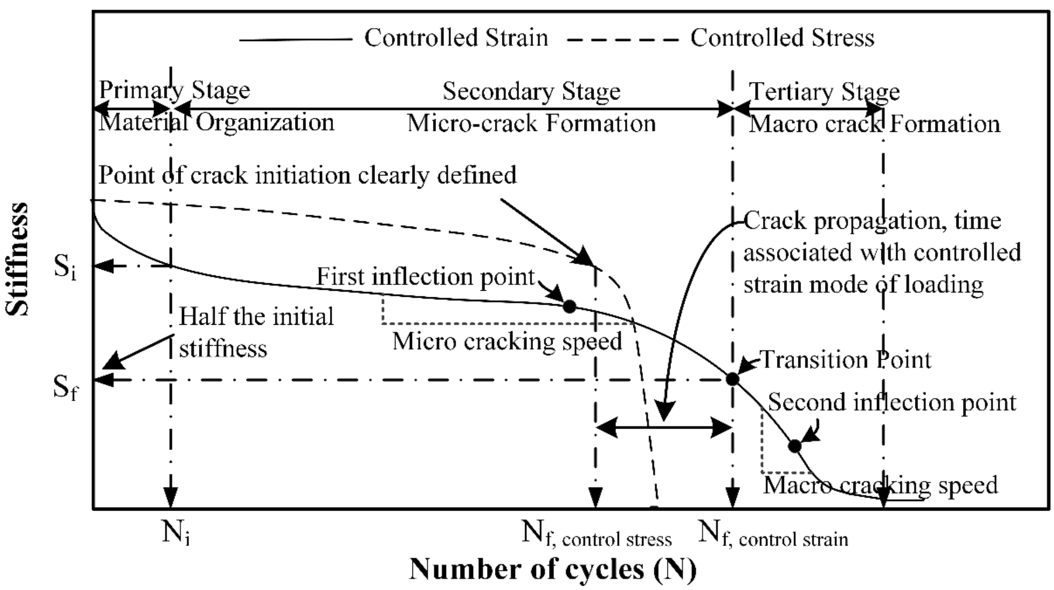

Figure 6-2. Typical relationships between stiffness and number of load repetitions for controlled strain mode vs. controlled stress mode tests.

Phase I or adaptation phase: The primary phase is associated with a rapid decrease in stiffness. The material reorganization, equipment seating effects, and heat development can contribute to the sudden loss in stiffness. However, this stiffness is readily recoverable once the test is paused during this phase.

Phase II or quasi-stationary phase: The secondary phase is characterized by a steady linear decrease in stiffness at a slower rate than in the primary phase. The reduction in stiffness is due mainly to the formation of microcracks.

Phase III or failure phase: The tertiary stage starts with the formation of macrocracks. That is, the microcracks formed during Phase II coalesce to form macrocracks in Phase III. In both modes of loading (controlled strain and controlled stress), clear and definite transition points between the different phases are tedious to mark as the formation of microcracks and macrocracks cannot be tracked easily during the test.

Different researchers have arbitrarily defined initial conditions and failure criteria for fatigue testing. The initial condition (tensile strain/stress) is taken as 50, 200, or 500 cycles for both stress- and strain-controlled tests (Tayebali et al. 1994). The stiffness, or modulus value, is considered the failure criterion in the conventional approaches instead of the overall material properties. Any variation in stiffness depends on the specimen's test temperature, internal heating phenomenon, and material composition. The complex and heterogeneous nature of AC invites variability in its material composition. A minor change in the material composition of a specimen, such as the asphalt content or aggregate gradation, can cause a significant difference in the stiffness degradation pattern and, thus, the failure stiffness. Table 6-1 presents the conventional failure criteria used in different research efforts.

Table 6-1. Conventional Failure Criteria

Reference	**Failure Criterion**	**Loading condition**
Van Dijk (1975)	Strain becomes double the initial strain	Constant stress
Tayebali et al. (1994)	90% reduction in initial stiffness	Constant stress
AASHTO T 321 (2017c)	50% reduction in initial stiffness	Constant strain

Figure 6-3 shows the stiffness degradation with the increase in the number of fatigue cycles for each of the test specimens in this study during actuator-controlled constant strain tests. As shown, failure occurred rapidly. The stiffness degradation rate is high during the high tensile strain test, irrespective of the reinforcement product used. The failure criterion of 50% reduction in initial stiffness was used for the constant strain load condition; the stars in the plots indicate the failure points.

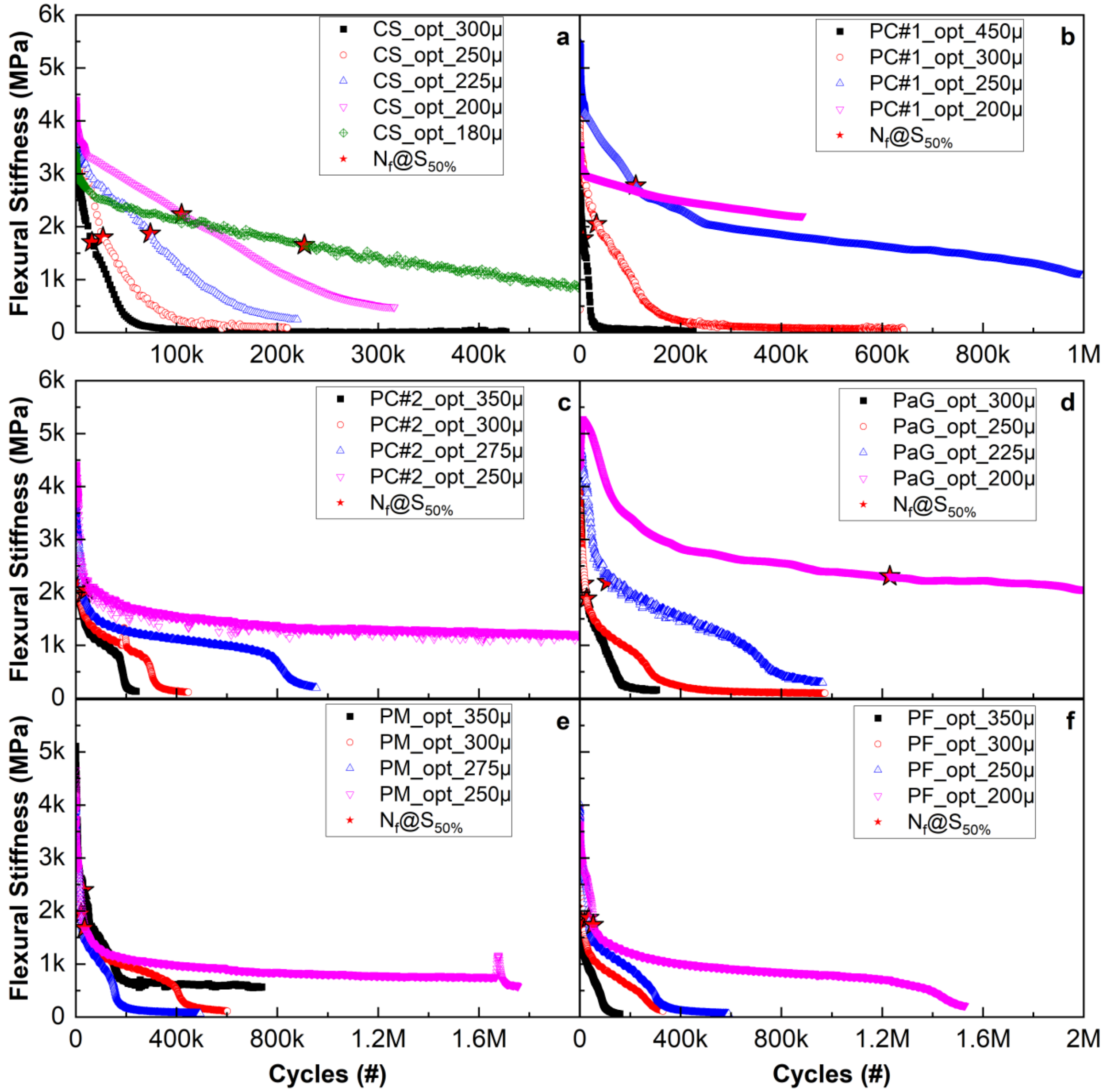

Figure 6-3. Flexural stiffness versus number of cycles during fatigue testing: (a) CS, (b) PC#1, (c) PC#2, (d) PaG, (e) PM, and (f) PF.

The tensile stress and strain were calculated based on elastic beam theory, which ignores stress concentrations and localization caused by a notched and layered beam specimen. Thus, the results shown in Figure 6-3 represent theoretical rather than the actual stress and strain experienced by the beam specimens. Nevertheless, stiffness curves constructed from real test data tend to be more challenging to interpret because they have less distinct regions. When it comes to finding specific points and regions on stiffness degradation graphs, DIC information is often a more accurate tool than simply looking at the curve itself. The accuracy of this type of analysis also is based on the scale of the graph and therefore can be subjective, even when clearly defined regions are present (Wargo 2015).

Previous research studies at NCSU show that replicate stiffness curves can differ significantly due to specimen-to-specimen variability. Such variability is not unexpected in four-point bending beam fatigue tests of geosynthetic-reinforced asphalt beam specimens. Even though asphalt is a heterogeneous material, composite AC material that consists of aggregate, mastic, and air voids is expected to cause variability in fatigue and fracture tests. Moreover, two layers of asphalt with an interlayer system installed between them is expected to increase the variability even further (Safavizadeh 2015).

Phase Angle Criterion

A viscoelastic material under cyclic loading causes the strain to lag behind the stress by an angle called the phase angle (δ), as illustrated in Figure 6-4. The time lag between the peak displacement/strain to peak load/stress in a cyclic test typically is used to measure the phase angle. The measured load and displacement are fitted with the waveform selected for the test to find the time difference (Δt) between the peak load and displacement. Further, Equation (6-7) can be used to measure the phase angle by knowing the load frequency. The fitting is based on high variability among the cycles. Experimental results reveal a stable increase in the measured phase angle of AC followed by a sharp decrease (Reese 1997). The fatigue failure of the material is defined as the number of cycles to failure, N_f, which causes a sharp decline in the phase angle, as illustrated in Figure 6-5. The reverse in the phase angle represents the transformation of the material's dominant mechanism and probably contributes to the formation of macrocracks. Hence, this approach holds more theoretical support and is considered a better indicator of fracture/failure than conventional approaches. The phase angle varies depending on the temperature; the usual range of phase angle failure is between 10° and 50° (Airey et al. 2002). For a constant strain test, the drop in phase angle is caused by the distortion of the load response that affects the sinusoidal curve that is fitted to that load shape. For this reason, the phase angle shown in Figure 6-5 is not a true phase angle; even so, this ability of the fitted phase angle to detect changes in load shape means that it can be used also to help detect specimen failure.

$$\delta = \frac{2\pi\Delta t}{T} \tag{6-7}$$

where

δ = phase angle.

Δt = time lag between peak displacement and peak load, and

T = period of the waveform.

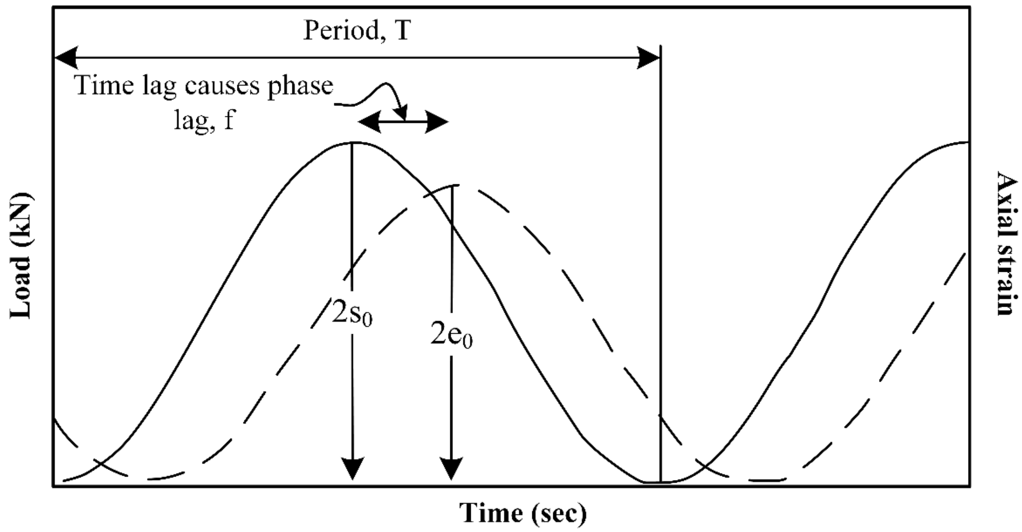

Figure 6-4. Cyclic stress, strain, and phase lag relationship (Findley and Davis 2013).

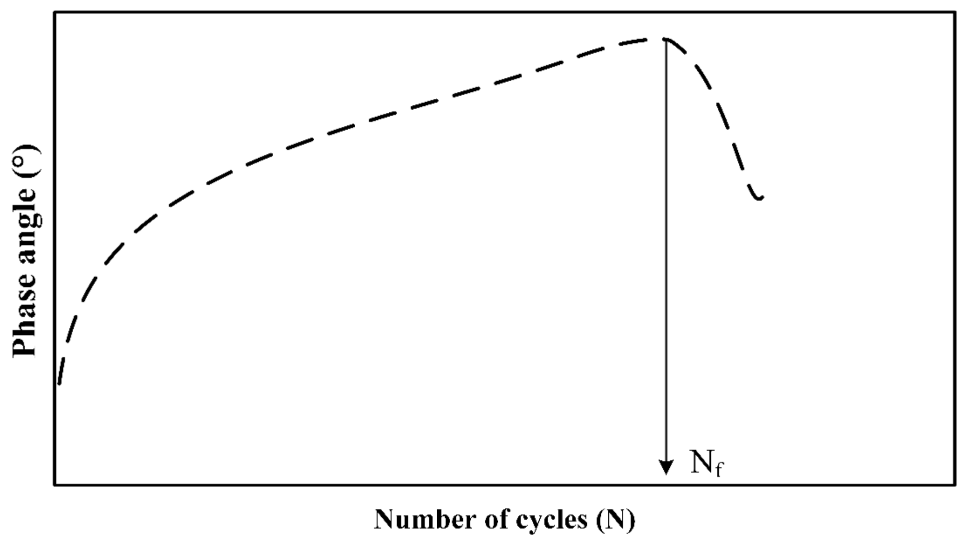

Figure 6-5. Variation in phase angle versus number of cycles.

Figure 6-6 shows that, for the control and five geosynthetic-reinforced beam specimens tested in this study, an apparent increase in phase angle occurs during the initial cycle followed by a drop. A comparison with the DIC results reveals that the phase angle increases when crack propagation occurs at the bottom layer. However, the decline in the phase angle occurs once the crack initiation starts to penetrate to the top layer or a top-down crack occurs. The distortion in the waveform of the stress/strain is minimal while the cracks are in the bottom layer; however, the calculated phase angle value remains low due to crack propagation and debonding at the interface. Once the crack propagates to the top layer, the distortion becomes prominent, resulting in the reversal of the phase angle.

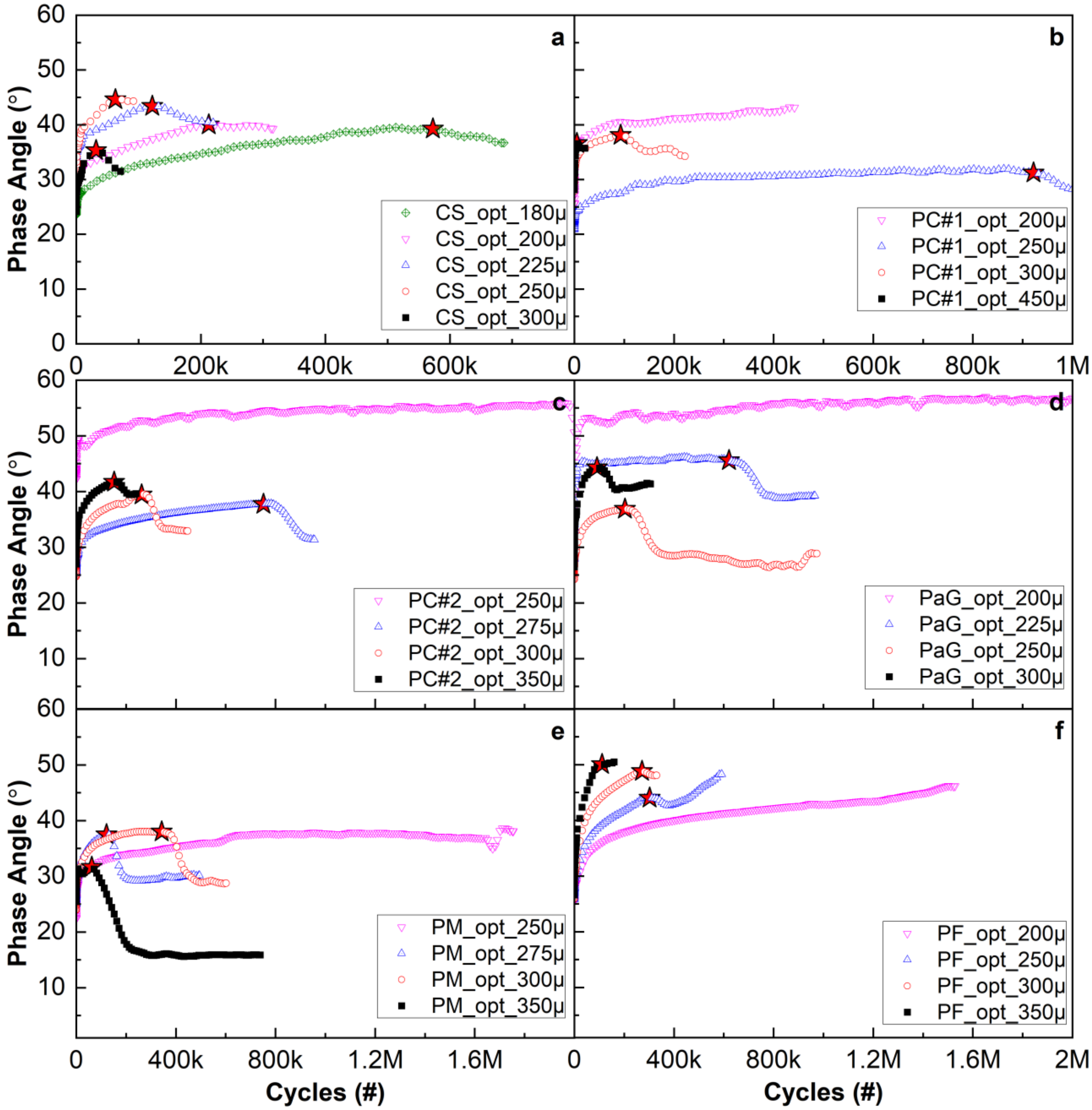

Figure 6-6. Variation in phase angle with load cycles; flexural stiffness versus number of cycles during fatigue tests of (a) CS, (b) PC#1, (c) PC#2, (d) PaG, (e) PM, and (f) PF.

Figure 6-7 shows the evolution of the distortion for the stress for PF-reinforced beam specimens as an example. Figure 6-7 (a) to (d) demonstrate that fitting the distorted load shape greatly affects the calculated phase angle. The actual peak values of the load versus peak displacement curves are noteworthy because these peak values shift much more than the fitted curve; so, a ‘phase angle’ based on these values would show a greater drop than the fitted curve. This behavior is expected because cracks, which reflect lack of material, can open and close quickly and thus should be closer to the displacement peaks and minima than to the peaks and minima in the overall fitted data. However, because the entire load history is important to the understanding of damage, a fitted curve is believed to provide a better representation of the material's behavior than simply looking at the peak values (Wargo 2015).

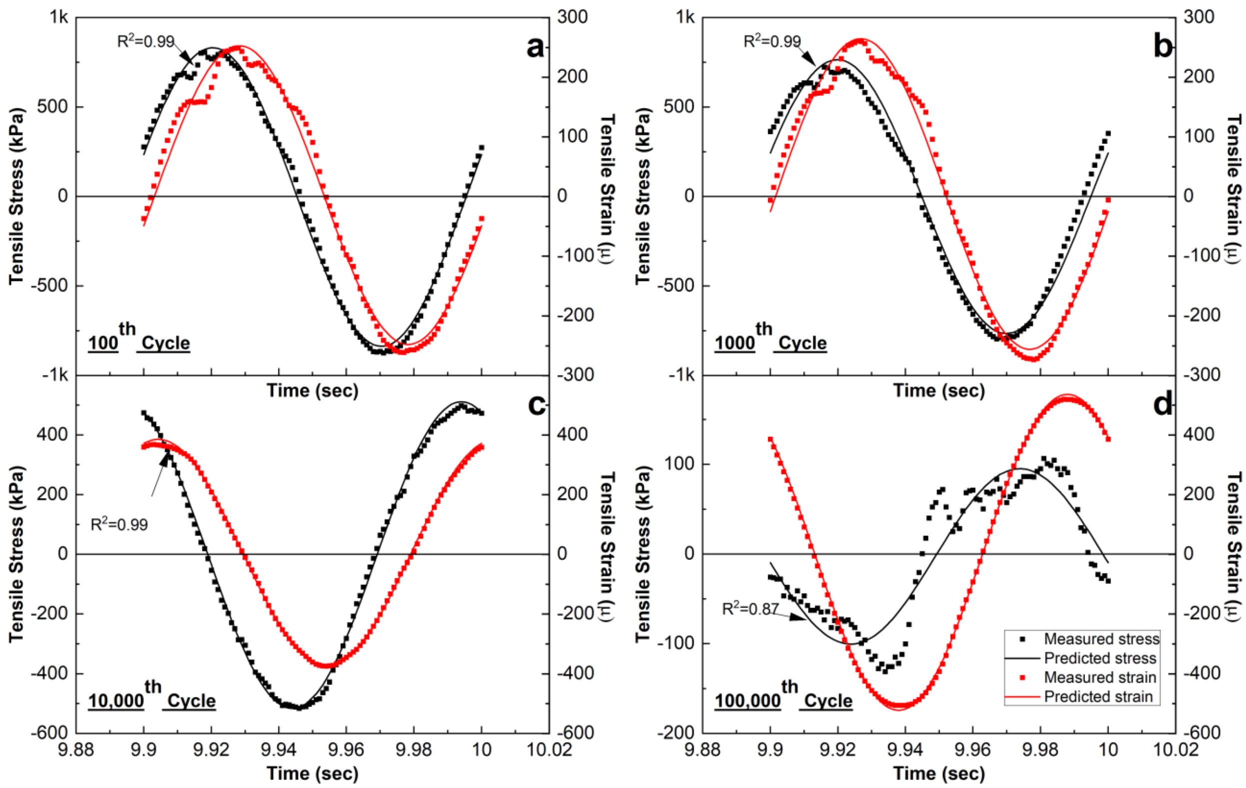

Figure 6-7. Evolution of fitted data during fatigue tests of PF specimens at constant actuator strain of 350 µ: (a) 100th cycle, (b) 1000th cycle, (c) 10,000th cycle, and (d) 100,000th cycle.

R-squared Criterion

Al-Khateeb and Shenoy (2004) used a statistical approach known as the *R*-squared approach to determine fatigue life based on variations in the stress and strain responses. The loading waveform (sinusoidal, haversine, trapezoidal, triangular, etc.) chosen for a test varies depending on the test protocol or objectives. During the first few cycles of the test, before the specimen begins to undergo damage, the stress/strain response of the specimen follows the same shape as the input displacement/load waveform. However, as the test goes on, the specimen's response data begin to scatter from the input shape function due to damage. In the case of a typical strain-controlled sinusoidal cyclic test, the initial undamaged stress cycle information that is fitted with a sinusoidal function gives an R^2 value close to 1. However, as the test progresses, damage occurs to the specimen, and the sinusoidal function that is fitted to the measured stress data starts to show a reduction in the R^2 value. Figure 6-8 shows that the first point of fatigue failure occurs when the R^2 value decreases sharply. The material undergoes complete failure/rupture once the R^2 value reaches zero.

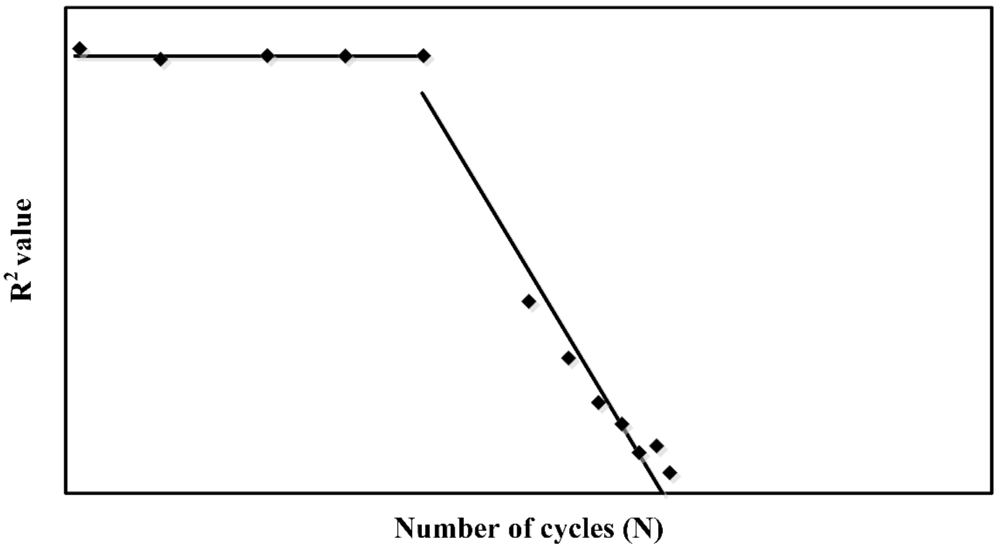

Figure 6-8. *R*-squared failure criterion (Al-Khateeb and Shenoy 2004).

A least-squares regression technique that first assumes that the stress and strain are represented by a functional form is presented in Equation (6-8). Appendix C provides a detailed description of the fitting method.

$$y(t) = A_0 + A_1 \cos(2\pi ft) + B_1 \sin(2\pi ft) \tag{6-8}$$

where

A_0, A_1, and B_1 are fitting parameters,

t = time (sec), and

f = frequency (Hz).

The step-by-step procedure that is used to fit the measured data via Equation (6-8) is detailed in the Appendix. Once the measured data are fitted, the A_0, A_1, and B_1 coefficients are obtained. Thus, stress/strain at any time (t) can be predicted using Equation (6-8). Further, the R^2 value for each cycle of data can be calculated using Equation (6-9).

$$R^2 = 1 - \frac{SS_{res}}{SS_{tot}} = 1 - \frac{\sum (y_i - \hat{y})^2}{\sum (y_i - \bar{y})^2} \tag{6-9}$$

where

R^2 = coefficient of determination,

SS_{res} = sum of squared residual errors,

SS_{tot} = sum of squared total errors,

$\hat{y}$ = predicted value of y,

$\bar{y}$ = mean value of y (measured values), and

y_i = measured values.

Figure 6-9 presents R^2 values versus number of load cycles for the CS and five geosynthetic-reinforced beam specimens. The initial region of each plot appears as a straight line, with little or no change in R^2 value, which indicates that the sinusoidal curve fit for the measured stress data approximates the response reasonably well. Even though macrocrack propagation through the bottom layer and debonding at the interlayer are predominant during the initial portion, the distortion in the load response is subtle. However, once the crack enters and propagates through the top layer, the load shape becomes severely distorted and starts to cause the R^2 value to drop. However, defining an objective point to classify failure based on this drop is difficult, especially in cases where the decline is relatively gradual. Also, the suggested failure-identifying method proposed by Al-Khabeeb and Shenoy (2011) recommends two criteria; one defines the beginning of fatigue failure and the second describes complete fatigue failure/rupture. The fitted linear line of the initial region intersects at R^2 = 1, while the fitted linear line for the end region projects to the x-axis for an R^2 value of zero, which indicates complete fatigue failure. The fatigue failure initiation point seems to underpredict the failure cycle, and the complete failure point seems to overpredict the failure cycle (Wargo 2015). Hence, a piecewise linear function with two segments was used in this study to find the fatigue failure point. The function used for fitting is shown in Equation (31).

$$\begin{aligned} y &= a_1 + k_1 x \quad (x < x_i) \\ y &= a_2 + k_2 (x - x_i) \quad (x \geq x_i) \\ y_i &= a_1 + k_1 x_i \end{aligned} \tag{6-10}$$

where

a_1 = intercept of initial region,

k_1= slope of initial region,

k_2= slope of end region, and

x_i = intersection of initial and end regions, defined as the failure point.

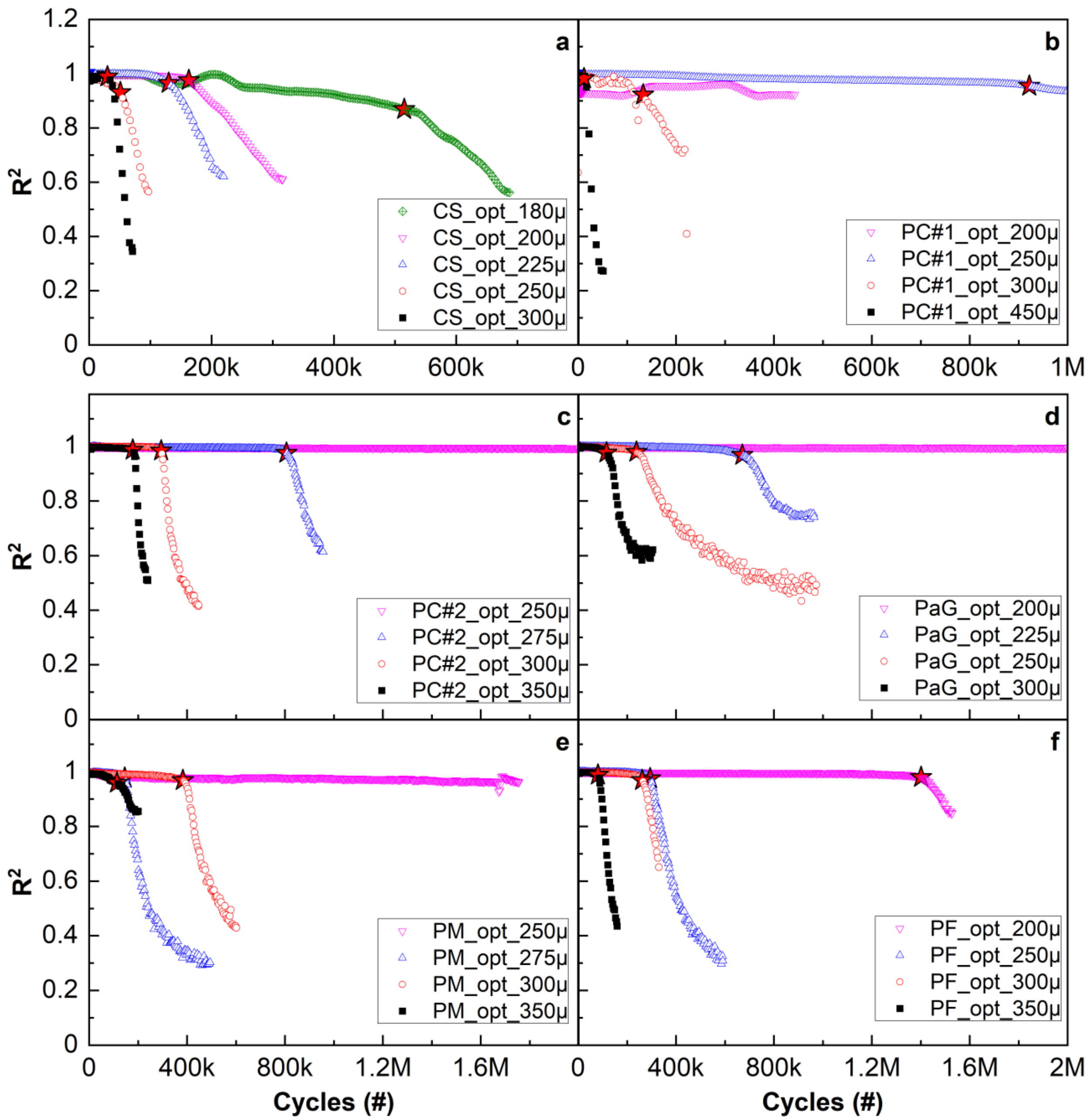

Figure 6-9. Variation of R^2 with load cycles during fatigue tests: (a) CS, (b) PC#1, (c) PC#2, (d) PaG, (e) PM, and (f) PF.

Two Dissipated Energy Ratio Criteria

Dissipated energy is the damping energy or energy loss per cycle in any repeated dynamic load test. The rheological behavior of viscoelastic materials is the fundamental factor that influences dissipated energy. This factor depends on the number of load cycles, levels of strain and stress, and temperature. The viscoelastic material absorbs and stores part of the deformation energy as potential energy and dissipates the rest through viscous forces (Tschoegl 2012). The asphalt mix’s resistance to fatigue crack propagation can distribute the deformation energy and dissipation rate. The irreversible damage process in terms of energy dissipation occurs in the vicinity of the crack tip (Aglan and Figueroa 1993). A significant portion of the energy dissipated during fatigue tests is converted to heat energy. The dissipated energy per unit volume per cycle, W_i, is given by Equation (6-11).

$$W_i = \pi \sigma_i \varepsilon_i \sin \phi_i = \pi \varepsilon_i^2 \left(S_{mix} \right)_i \sin \phi_i \tag{6-11}$$

where

W_i = dissipated energy at load cycle i,

i = strain amplitude at load cycle i,

S_i = mix stiffness at load cycle i, and

ϕ_i = phase angle between stress and strain at load cycle i.

Pronk and Hopman (1991) developed the concept of a dissipated energy ratio as a function of the number of load cycles, as shown in Equation (6-12).

$$\left(R_E \right)_n = \frac{n.W_0}{W_n} \tag{6-12}$$

where

n = number of loading cycles,

W_0 = energy dissipated in the first cycle, and

W_n = energy dissipated in the n^{th} cycle.

Figure 6-10 (a) and (b) respectively show the stress-strain relationship for viscoelastic material and the concept of dissipated energy whereby energy is dissipated during the loading-unloading process.

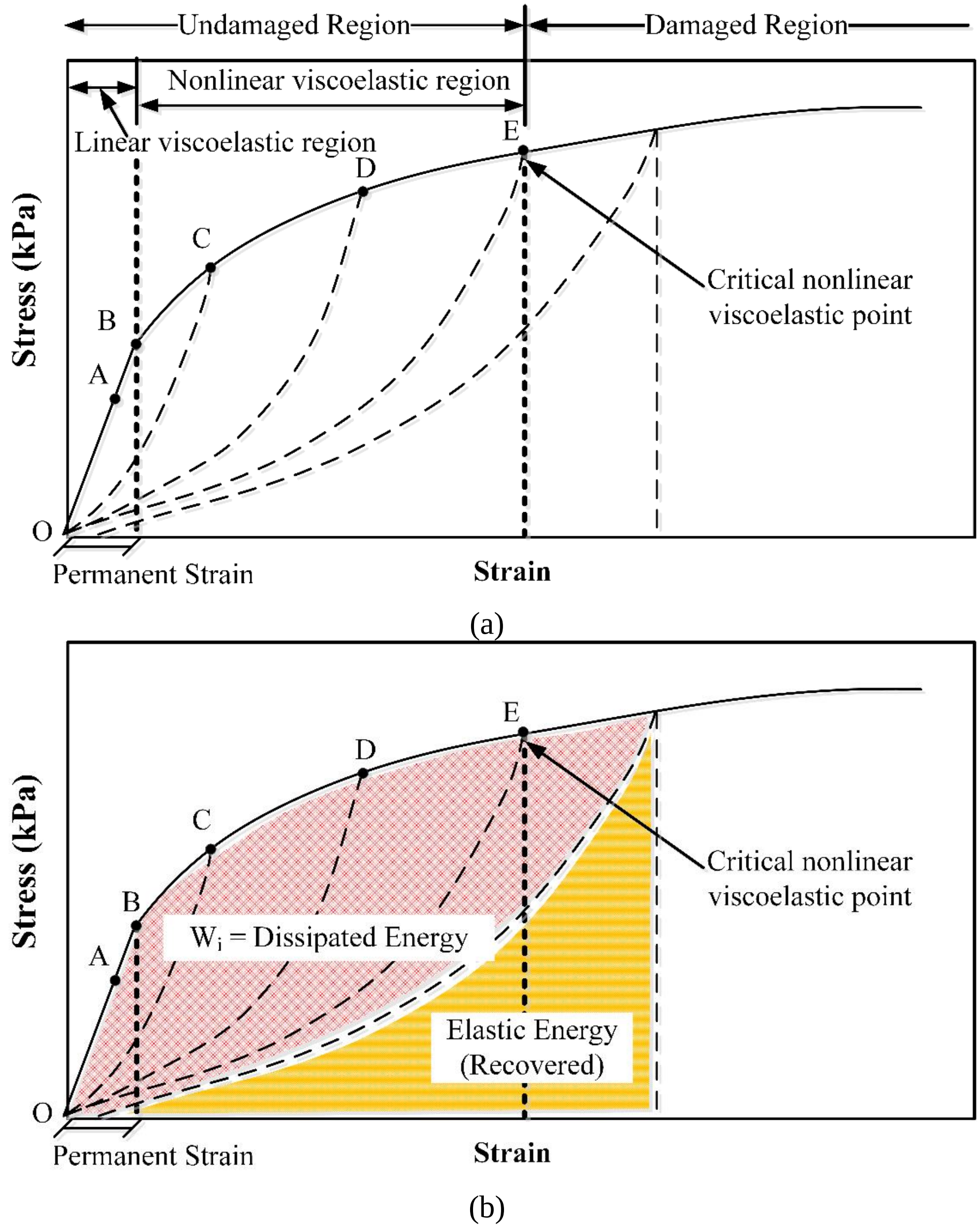

Figure 6-10. (a) Stress-strain relationship of viscoelastic material and (b) dissipated energy concept (Luo et al. 2013).

The fatigue life that is based on the dissipated energy ratio can be defined according to two criteria. Both criteria are based on the relationship between the energy ratios for different cycles versus the number of load cycles. Criterion 1 is the tangent intersection method (Point A) that is to determine the fatigue failure for a control strain test, as shown in Figure 6-11. This method overestimates the number of cycles to failure.

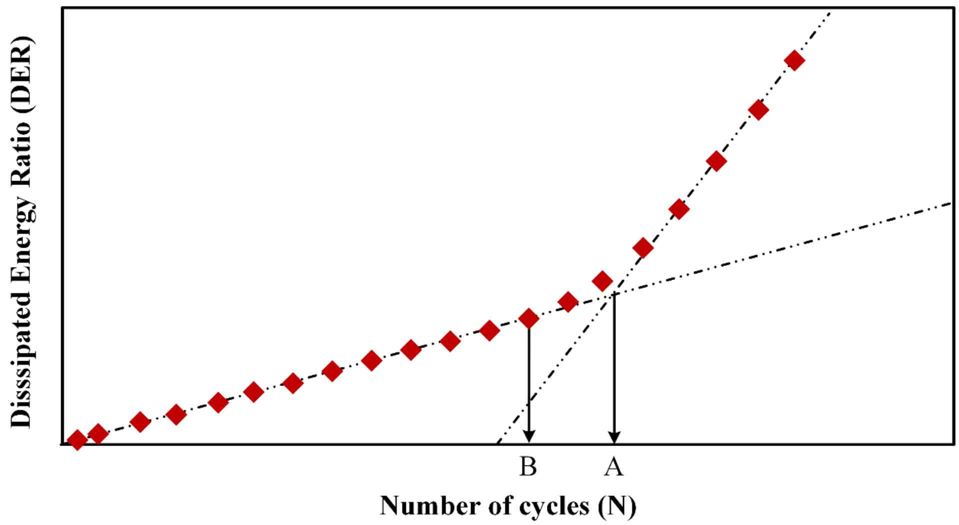

Figure 6-11. Dissipated energy failure Criterion 1: Tangent intersection method for dissipated energy ratio in controlled strain mode.

Criterion 2 is used to find the failure point in a controlled stress mode fatigue test. The point where the linearity of the relationship between the dissipated energy ratio and the number of cycles ends (Point B) is considered the failure point, as shown in Figure 6-12. The chance of error is high when using this criterion, as such failure points are subjective depending on the user's capability, the density of the points, the scale of the graph, etc. Hence, a consistent method is required for determining the fatigue life objectively and precisely.

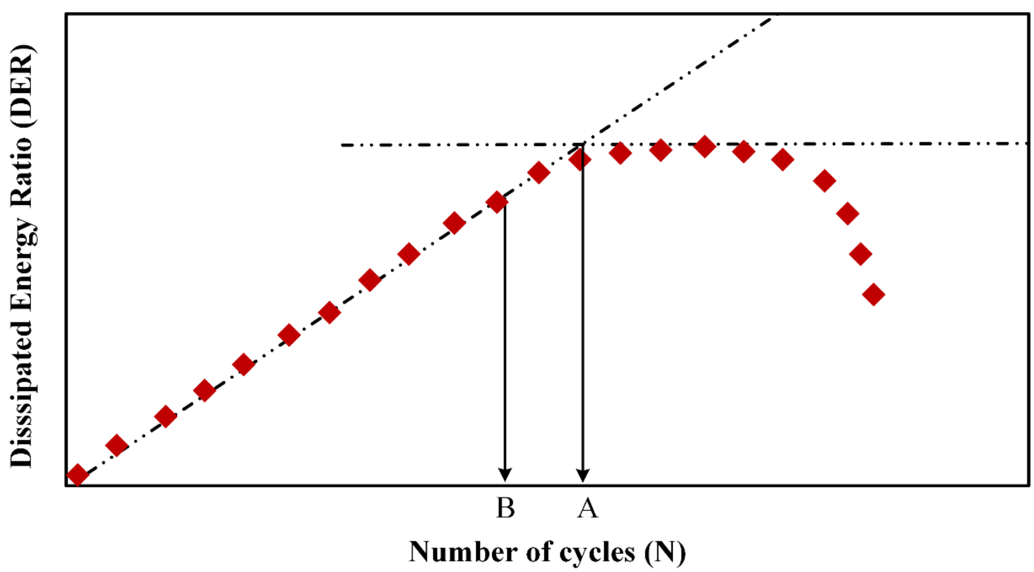

Figure 6-12. Dissipated energy failure Criterion 2: Failure point is where the relationship becomes nonlinear for the dissipated energy ratio in controlled stress mode.

Figure 6-13 describes the general concept of the dissipated energy ratio during NBFTs for the CS and five geosynthetic-reinforced specimens tested in this study. The dissipated energy ratio plots are bilinear in nature; the initial linear region shows the crack activity in the bottom layer. However, the second linear region appears once dominant cracks appear in the top layer. A noticeable increase in the slope occurs and approaches a second asymptote. This asymptote is not well defined, and determining a definite failure point is not possible and remains subjective. Fitting straight lines through these data points and selecting offsets to represent failure (as reported in the literature) were deemed undesirable approaches in this study due to the arbitrary nature of fitting the lines and selecting offset values. Hence, a fitting method similar to that used for the R^2 criterion was used here by applying the piecewise linear function with two segments to the dissipated energy ratio plots, as shown in Equation (6-10). The failure points identified by this method are marked as red stars in the Figure 6-13 plots.

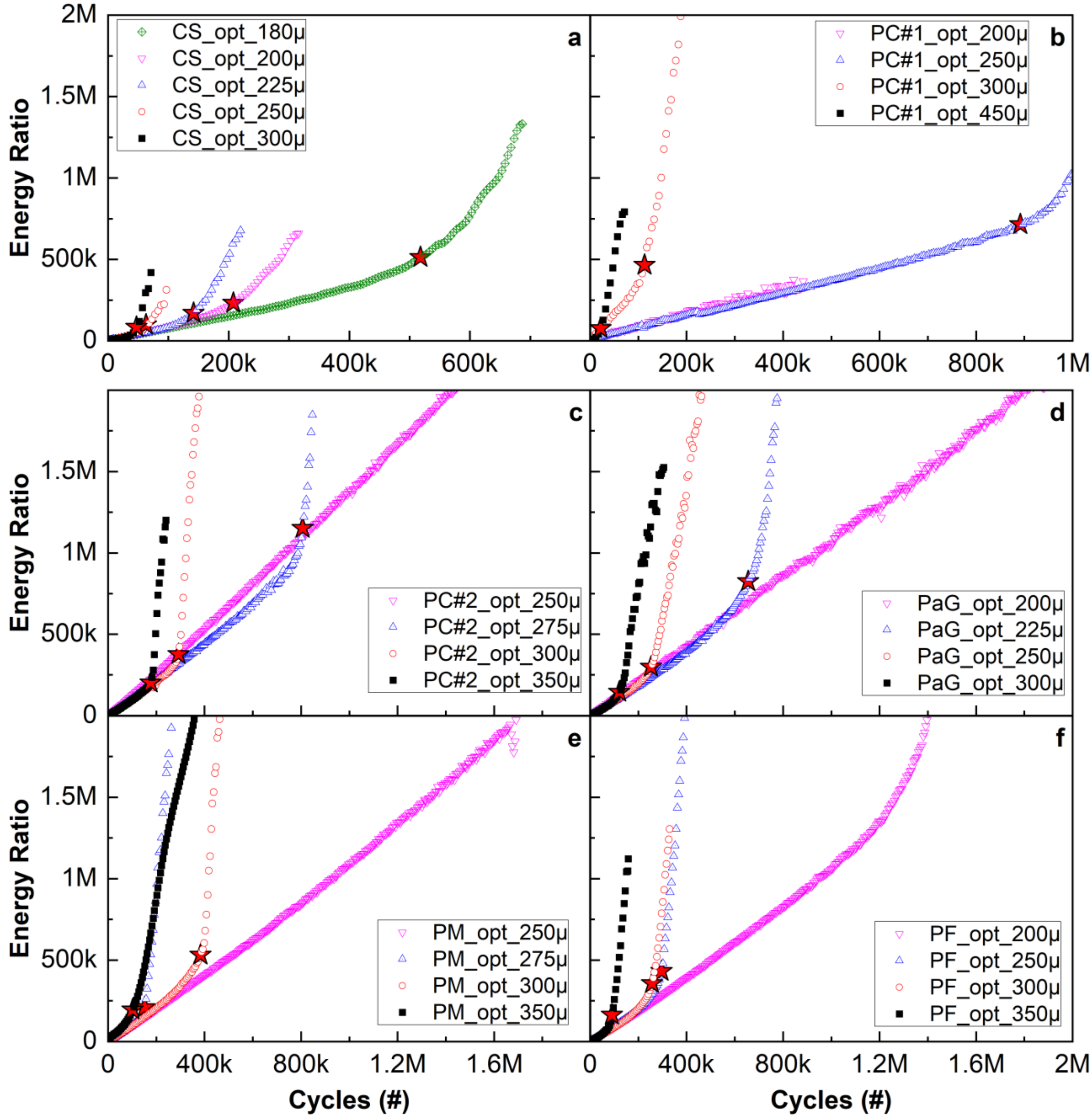

Figure 6-13. Dissipated energy ratios with load cycles during fatigue tests: (a) CS, (b) PC#1, (c) PC#2, (d) PaG, (e) PM, and (f) PF.

Stiffness Degradation Ratio Criterion

Rowe and Bouldin (2000) improved the energy ratio concept by multiplying the material's stiffness value at a particular cycle by the load cycle number, as shown in Equations (6-13) and (6-14) for constant stress tests and constant strain tests, respectively. The new function produces a peak value when plotting the relationship between the reduced dissipated energy ratio and the load cycle number. The fatigue life of the material is defined as this peak value for both constant stress and constant strain (Rowe and Bouldin 2000).

$$\left(R_E^{\sigma}\right)_i = N_i S_i \text{ (constant stress test)} \tag{6-13}$$

$$\left(R_E^{\varepsilon}\right)_i = \frac{N_i}{S_i} \text{ (constant strain test)} \tag{6-14}$$

where

N_i = cycle number, and

S_i = stiffness at the i^{th} cycle.

The main advantage of the Rowe and Bouldin (2000) method is that the peak value N_iS_i can easily be determined by fitting a high-order polynomial function to the data and differentiating. Zeiada (2012) further modified the Rowe and Bouldin (2000) stiffness ratio (N_iS_i) method by normalizing the energy ratio by dividing it by the initial stiffness (S_0) of the material, resulting in a new stiffness ratio shown in Equation (6-15).

$$\text{Stiffness degradation ratio} = \frac{N_i \times S_i}{S_0} \tag{6-15}$$

where

N_i = cycle number,

S_i = stiffness at the i^{th} cycle, and

S_o = initial stiffness measured at the 50^{th} load cycle.

Figure 6-14 depicts the stiffness degradation ratio versus load cycle for controlled strain and controlled stress modes of loading. The peak value obtained is considered the failure point of the material. The degradation of the material's stiffness during the initial cycles is minimal (S_i and S_0 are comparable). Hence, the stiffness degradation ratio increases with the increase in the number of cycles, N_i, until the peak. After reaching the peak, a sudden reduction in the material's stiffness occurs with the increase in the load cycle, N_i, resulting in the sudden decrease in the stiffness degradation ratio. The number of cycles required for the stiffness degradation ratio to reach its peak is considered the material's fatigue failure criterion in either constant stress or constant strain mode.

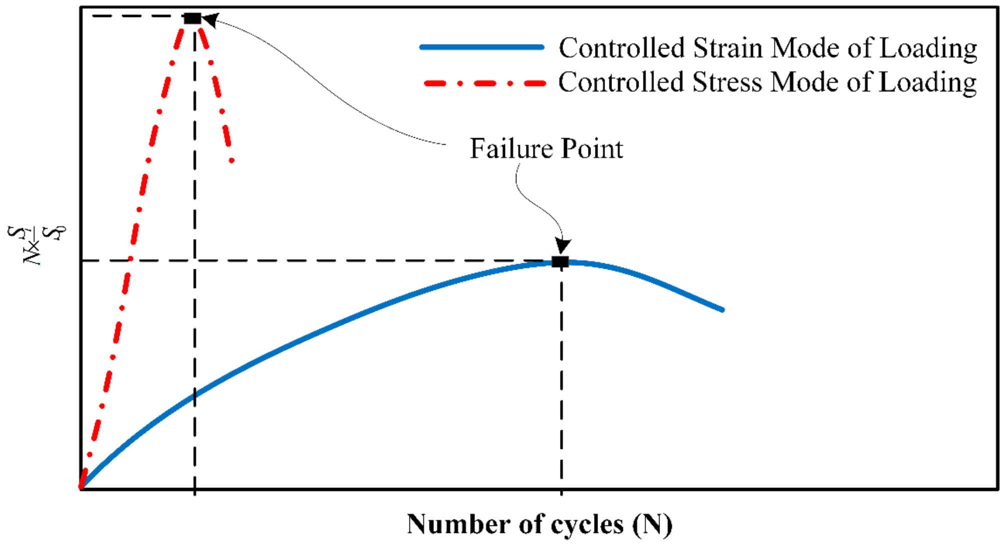

Figure 6-14. Stiffness degradation ratio.

Figure 6-15 shows the change in the stiffness degradation ratio as the fatigue loading continues for different strain levels for Control and five geosynthetic-reinforced specimens. The control specimens show clear failure points for different strain levels, whereas failure points are difficult to identify due to the distorted stiffness degradation ratio pattern or due to the non-existent peak points.

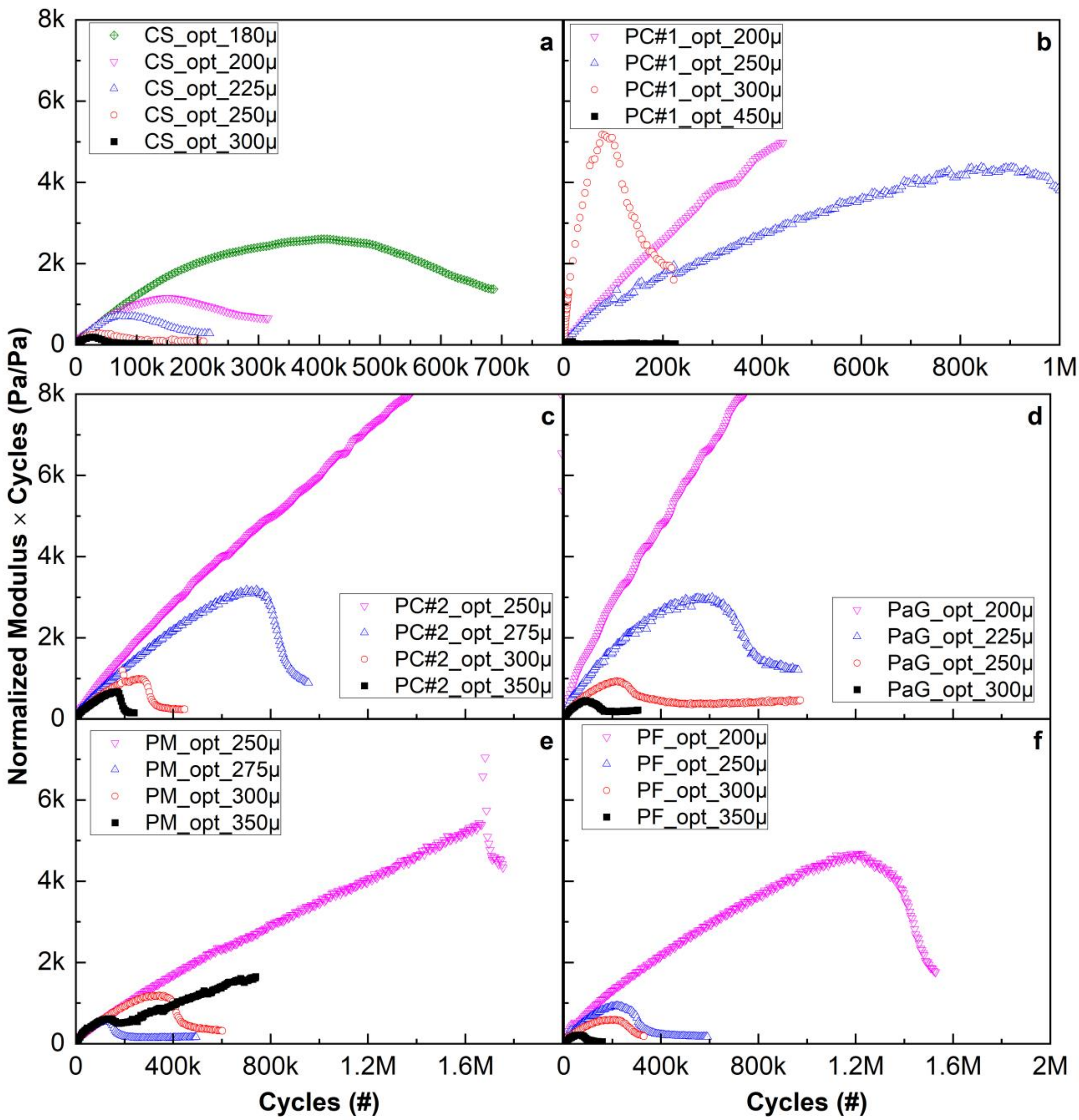

Figure 6-15. Normalized modulus × load cycles during fatigue tests: (a) CS, (b) PC#1, (c) PC#2, (d) PaG, (e) PM, and (f) PF.

Stress × N Failure Criterion

The stiffness degradation ratio provides a quick and reasonable alternative for finding the failure point. Following this approach, a refined failure definition is proposed for cyclic fatigue testinhg, where cyclic fatigue failure is the cycle at which the product of the stress amplitude and cycle number reaches a peak value. Figure 6-16 shows the product of the stress and cycle number versus cycle number for a typical uniaxial cyclic fatigue test. The use of stress amplitude instead of stiffness eliminates the need for any on-specimen LVDT measurements and allows the failure cycle to be defined accurately even in cases where the specimen fails outside the LVDT gauge points. Lee (2020) analyzed the effect of changing the failure definition by applying both the phase angle criterion and the product of the stress and cycle number approach during a uniaxial cyclic fatigue test. The peak of the stress times the number of cycles yields approximately 6% shorter fatigue life than the phase angle criterion.

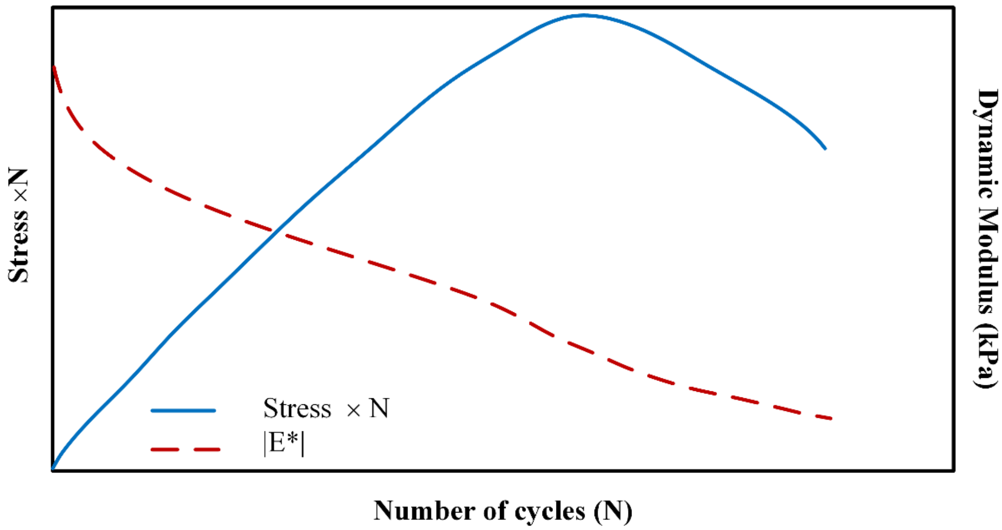

Figure 6-16. Stress × N versus number of loading cycles.

Figure 6-17 shows the change in the stress × N versus load cycles at different strain levels for the Control and five geosynthetic-reinforced specimens. Similar in regard to the stiffness degradation ratio, the control specimens show clear failure points at different strain levels, whereas the failure points are difficult to identify for the geosynthetic-reinforced specimens at certain strain levels due to the distorted stress × N versus N pattern or due to non-existent peak points.

Note that two different mechanisms develop as the notched beam is subjected to cyclic loading, i.e., vertical cracking and horizontal debonding at the interface of the geosynthetic interlayer and asphalt layer. The cyclic loading in NBFTs causes a crack to start at the tip of the notch and propagate to the interface. Then, the energy input that is due to the cyclic loading causes the vertical crack to turn in the horizontal direction if the bond strength between the geosynthetic and the bottom asphalt layer is low. If the bond strength is high, then the crack stalls at the interface of the geosynthetic layer and overlay. When the energy input that is due to cyclic loading exceeds the resistance from the interlayer, the crack starts to propagate upwards, causing reflective cracking. Therefore, the bond strength between the geosynthetic interlayer and the asphalt overlay is an extremely important factor and must be sufficient in order to fully capture the benefits of geosynthetic interlayers. The evolution of these mechanisms is captured via DIC and discussed in detail in Chapter 7.

Also note that the ‘failure’ detected by the stress × N failure criterion is caused by a combination of both the vertical cracking and horizontal debonding mechanisms. Therefore, the number of loading cycles at failure (N_f) should not be interpreted as the conventional fatigue life that is due to fatigue cracking, but rather as the life of the asphalt overlay that is due to the combined effects of vertical cracking and horizontal debonding on the geosynthetic-reinforced asphalt beam’s resistance to loading.

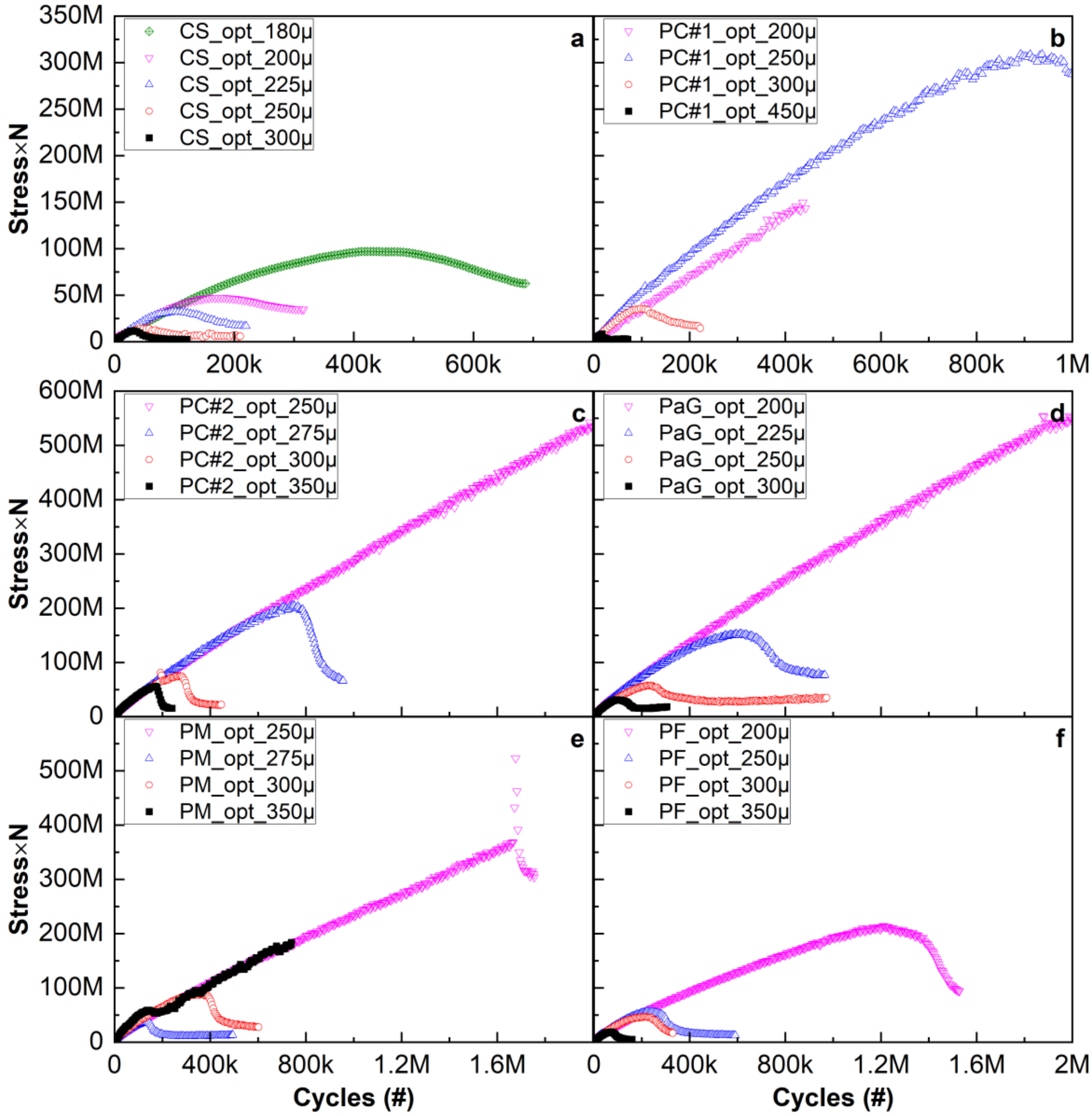

Figure 6-17. Stress × N (cycles) versus load cycles during fatigue tests: (a) CS, (b) PC#1, (c) PC#2, (d) PaG, (e) PM, and (f) PF.

Crack Resistance Capacity of Geosynthetic-Reinforced Beam Specimens

The results for the NBFTs carried out using all the test specimens were analyzed via all the failure criterion determination methods described in Section 6.1.2. The different failure criteria were applied to find the fatigue life in terms of crack resistance capacity of the various geosynthetic products. Table 6-2 presents a summary of the failure cycle/life outcomes based on the various failure criteria. Note that the failure cycle numbers measured for the 50% reduction in stiffness criterion are considered as the base values for comparison in the table, and the other failure cycles that are based on the other criteria are represented as multiplying factors to the failure cycles at 50% reduction in initial stiffness.

Table 6-2 shows that, compared to the 50% reduction in stiffness criterion, all the other five failure criteria result in longer fatigue life. Hence, the 50% reduction in stiffness criterion underestimates the fatigue life of beam specimens. However, this underestimation might be considered as support for a conservative design but it is not encouraged when estimating the fatigue life of reinforced AC. The outcomes from the five other failure criteria show that reinforced products can amplify the life prediction by two to 25 times, depending on the geosynthetic product and the testing strain level. In other words, the geosynthetic product's resistance to cracking is triggered after the 50% reduction in stiffness in many cases. The DIC images also justify this finding. Furthermore, crack propagation to the top layer typically occurs after the failure is measured when using the non-conventional criteria. Hence, the conventional criterion, i.e., the 50% reduction in stiffness criterion, is not recommended, especially to measure the crack resistance capacity of geosynthetic products. One of the major difficulties when applying the non-conventional failure criteria in this study was that, at lower strain levels, a definite failure point could not be identified for most of geosynthetic-reinforced beam specimens even after two million load cycles. Hence, in such cases, the three-stage Weibull model was used to identify failure. The fatigue lives of the cells in Table 6-2 tagged as 'Not Failed' were later identified using the three-stage Weibull survivor function.

Table 6-2. Failure Life Based on Different Failure Criteria for Control and Geosynthetic-Reinforced Beam Specimens

Nomenclature		ε_{act} (μ)	ε_{os} (μ)	N_f @ $S_{50\%}$	Multiplying Factor				
					Phase angle	R^2	ER	NM × Cycles	Stress × N
Control Specimen	CS_opt_300μ	300	215	16,001	2.0	2.3	2.9	1.7	2.0
	CS_opt_250μ	250	174	27,001	2.3	2.0	2.3	1.5	1.8
	CS_opt_225μ	225	156	73,001	1.7	1.8	2.0	1.2	1.4
	CS_opt_200μ	200	135	105,001	2.1	1.6	2.0	1.5	1.7
	CS_opt_180μ	180	138	227,001	2.5	2.3	2.3	1.7	2.0
Paving Composite #1	PC#1_opt_450μ	450	295	6,101	0.9	1.9	3.5	2.2	2.7
	PC#1_opt_300μ	300	169	33,001	2.8	4.1	3.5	2.6	2.9
	PC#1_opt_250μ	250	127	110,001	8.4	8.1	8.1	7.8	8.3
	PC#1_opt_200μ	200	106	NF	NF	NF	NF	NF	NF*
Paving Grid	PaG_opt_300μ	300	192	19,001	4.9	6.4	6.3	4.4	5.4
	PaG_opt_250μ	250	175	27,001	7.4	9.1	9.4	7.9	8.5
	PaG_opt_225μ	225	144	110,001	5.7	6.2	6.0	5.2	5.4
	PaG_opt_200μ	200	117	1,220,000	NF	NF	NF	NF	NF*
Paving Mat	PM_opt_350μ	350	203	31,001	1.9	3.7	3.3	6.3	4.6
	PM_opt_300μ	300	208	17,001	20.5	22.7	22.5	20.6	20.1
	PM_opt_275μ	275	174	21,001	5.7	7.0	7.3	5.6	6.1
	PM_opt_250μ	250	167	25,001	NF	NF	NF	65	66
Paving Fabric	PF_opt_350μ	350	243	5,901	19.0	13.9	15.4	9.0	11.2
	PF_opt_300μ	300	197	18,001	15.1	14.7	14.3	10.7	11.1
	PF_opt_250μ	250	172	35,001	8.7	8.4	8.4	6.1	6.7
	PF_opt_200μ	200	148	53,001	NF	26.5	25.8	22.2	22.7
Paving Composite #2	PC#2_opt_350μ	350	223	13,001	11.3	13.6	13.7	11.8	12.2
	PC#2_opt_300μ	300	179	11,001	23.4	26.7	25.8	21.9	22.9
	PC#2_opt_275μ	275	180	31,001	24.4	26.0	26.1	22.4	23.0
	PC#2_opt_250μ	250	154	43,001	NF	NF	NF	NF	NF*

Note: ε_{act} = tensile strain at the bottom of a beam calculated from the actuator displacement, ε_{os} = on-specimen tensile strain at the bottom of a beam calculated from the displacement measured by the LVDT mounted on the beam, NF = not failed, * = failure cycles were predicted using Weibull Survivor Function, ER = dissipated energy ratio, NM = normalized modulus.

Among all the failure criteria considered in this study, the stress × N failure criterion was selected to evaluate the failure cycle because it offers many advantages over the other methods. For example, the stress × N failure criterion (1) does not demand on-specimen deflection, which is often difficult to achieve in a typical four-point beam test set-up, (2) can clearly define the failure point by indicating the peak value followed by a drop in the numeric value, and (3) is applicable for geosynthetic-reinforced as well as unreinforced beam specimens. Note that the multiplying factor for the stress × N failure criterion is between the minimum and maximum multiplying factor values for all the failure criteria, indicating that the stress × N failure criterion yields the fatigue life that balances the fatigue lives determined by all the failure criteria.

Extrapolating a Failure Point Based on Three-Stage Weibull Survivor Function

ASTM D7460 (ASTM 2010) proposes a one-stage Weibull equation that does not appear to represent the damage process when the fatigue test has a prolonged initial phase and is conducted beyond a certain stiffness ratio threshold at which fatigue cracks start to propagate. Therefore, an alternative function is necessary to describe the stiffness deterioration process. Tsai et al. (2005) used a three-stage Weibull model to define the fatigue failure of asphalt mixtures, as illustrated in Figure 6-18. The three stages are defined as the initial stage (warm-up), crack initiation, and crack propagation. The three-stage Weibull model consists of three equations that are based on the stiffness ratio (SR = S_i/S_0). By plotting the ln(-ln (SR) versus ln(loading cycle, n), three curves can be distinguished that can be fitted using the three different equations of the Weibull model.

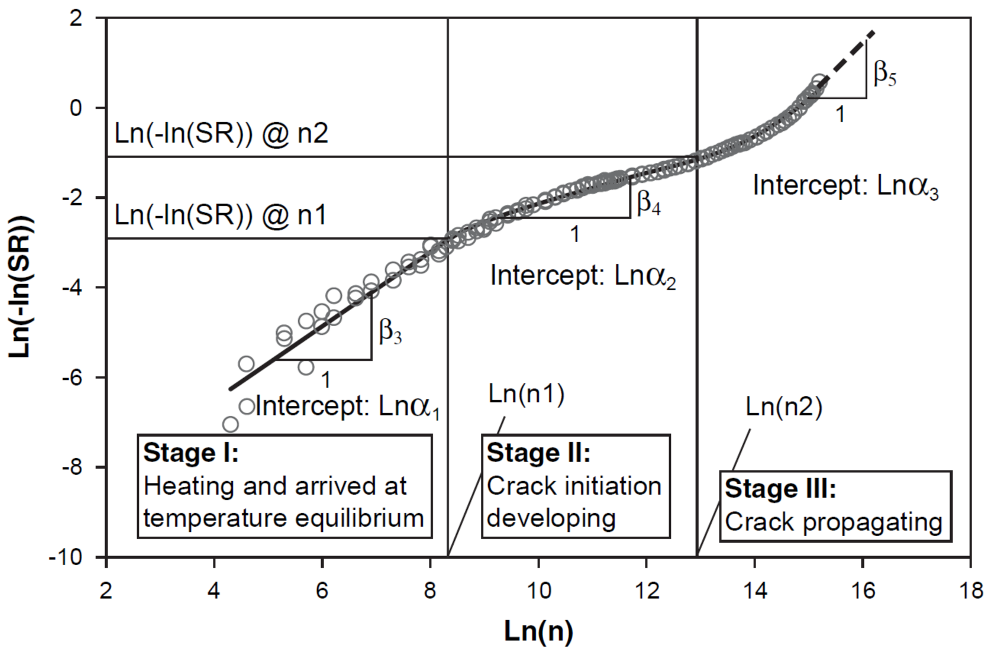

Figure 6-18. Failure curve defined in three stages of Weibull model (Tsai et al. 2005).

Once the data are fitted, ASTM D7460 assumes the failure point to have a stiffness ratio of 0.5. However, analysis of the current data set to find the unknown Weibull parameters for tests with known failure points (stress × N) revealed that, for CS, failure usually occurs at SR = 0.3, whereas for the geosynthetic-reinforced beam specimens, the stiffness ratio is around 0.24. The stiffness ratio specified is the point at which the crack propagation stage begins. In the case of CS, failure occurred whenever the crack propagated rapidly whereas for the geosynthetic-reinforced beam specimens, the crack had to reach the top layer. Figure 6-19 shows the validation of the proposed stiffness ratio criterion by comparing the measured failure point against the predicted failure cycles based on the Weibull survivor function.

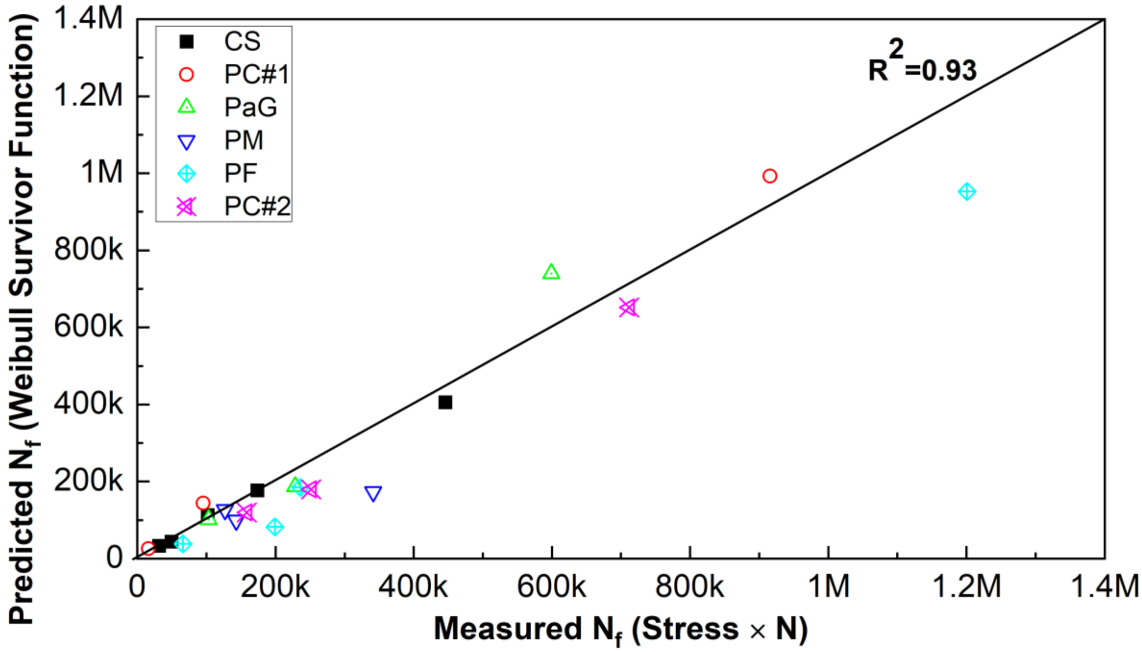

Figure 6-19. Validation of measured and predicted failure points using Weibull three-stage survivor function.

After finding the stiffness ratio that could predict the failure point effectively, the selected stiffness ratio criterion was used to predict the failure point for the non-failed specimens after prolonged testing (over 2 million cycles). The second stage of the Weibull curve is fitted with a linear function shown in Equation (6-16).

$$\ln(-\ln(SR)) = \ln\alpha + \beta \ln N \tag{6-16}$$

where

SR	=	flexural beam stiffness ratio, beam stiffness at the cycle of interest divided by initial beam stiffness,
N	=	number of cycles,
β	=	slope of the linear regression in the second stage, β_4, and
ln (α)	=	intercept of the linear regression of the second stage, α_2.

The failure point is estimated by solving Equation (6-16) for the value of *N* where the stiffness ratio is equal to 0.3 for the unreinforced beam specimens (CS) and is around 0.24 for the geosynthetic-reinforced beam specimens. If the user has more than three data sets with definite failure in different constant strain tests for a specific type of product, then, with the help of the stress × N failure criterion, a more reliable stiffness ratio could be found for that specific product, thus leading to a better prediction of the number of cycles to failure for tests where the decreasing trend of stress × N versus N cannot be found within the duration of the test.

Table 6-3 provides a summary of the N_f values of the different interlayer types and strain levels based on the stress × N failure criterion. The life of the geosynthetic-reinforced specimens is clearly longer than that of the Control specimens (CS). Table 6-4 shows the life extension ratio values of the different geosynthetic-reinforced specimens compared to CS. The magnitude of the life extension that is due to the use of geosynthetic interlayers ranges from two-fold to over 60-fold. Note that these numbers are based on laboratory tests in a controlled environment. The actual magnitude of the life extension due to geosynthetic interlayers under field conditions should be determined based on a field study. Also, a well-designed field study would allow for the development of transfer functions that are necessary to predict the fatigue life of asphalt overlays reinforced by geosynthetic interlayers in the field using laboratory NBFTs.

Table 6-3. Failure Life Based on Stress × N Failure Criterion for Control and Geosynthetic-Reinforced Beam Specimens

ε_{act}		**450 µ**	**350 µ**	**300 µ**	**275 µ**	**250 µ**	**225 µ**	**200 µ**	**180 µ**
CS	ε_{os} (ε_{int})			215 µ (72 µ)		174 µ (58 µ)	156 µ (52 µ)	135 µ (45 µ)	138 µ (46 µ)
	N_f			31,634		49,645	101,858	173,938	445,615
PC#1	ε_{os} (ε_{int})	295 µ (98 µ)		169 µ (56 µ)		127 µ (42 µ)		106 µ (35 µ)	
	N_f	16,376		95,523		916,086		10,292,161	
PC#2	ε_{os} (ε_{int})		223 µ (74 µ)	179 µ (60 µ)	180 µ (60 µ)	154 µ (51µ)			
	N_f		158,518	251,437	712,071	2,066,647			
PaG	ε_{os} (ε_{int})			192 µ (64 µ)		175 µ (58 µ)	144 µ (48 µ)	117 µ (39 µ)	
	N_f			103,302		228,283	598,842	6,079,324	
PF	ε_{os} (ε_{int})		243 µ (81 µ)	197 µ (66 µ)		172 µ (57 µ)		148 µ (49 µ)	
	N_f		66,062	198,975		236,163		1,200,735	
PM	ε_{os} (ε_{int})		203 µ (68 µ)	208 µ (69 µ)	174 µ (58 µ)	170 µ (57 µ)/ 167 µ (56 µ)			
	N_f		142,941	341,311	127,114	384,046/ 1,641,352			

Table 6-4. Life Extension Ratios of Geosynthetic-Reinforced Beam Specimens Compared to Control Specimens

$\varepsilon_{t\text{-}act}$	350 μ	300 μ	275 μ	250 μ	225 μ	200 μ
CS		1.0		1.0	1.0	1.0
PC#1		3.0		18.5		59.2
PC#2	2.4	7.9	5.6	41.6		
PaG		3.3		4.6	5.9	35.0
PF	1.0	6.3		4.8		6.9
PM	2.2	10.8	1.0	7.7/33		

Figure 6-20 and Figure 6-21 respectively present the actuator and on-specimen tensile strain levels versus number of cycles to failure (N_f) plots for CS and the five geosynthetic-reinforced beam specimens used in this study. The stress × N failure criterion was applied to the NBFT results to determine the number of cycles to failure (N_f). The results of lengthy tests for PC#1, PC#2, and PaG that require the prediction of N_f values using Equation (6-16) are not included in these figures to be consistent with other interlayer cases. The data in Figure 6-20 and Figure 6-21 were used to determine the fatigue coefficients k_1 and k_2 in Equation (6-17) for the five geosynthetic-reinforced products and the 'no interlayer' unreinforced scenario (CS). Table 6-5 and Table 6-6 present the fatigue coefficients obtained after fitting the data shown in Figure 6-20 and Figure 6-21, respectively, as well as the R^2 values obtained from regression analysis.

$$N_f = k_1 \left(\frac{1}{\varepsilon_t} \right)^{k_2} \tag{6-17}$$

where

N_f = number of cycles to failure, representing crack resistance,

k_1, k_2 = regression coefficients, and

ε_t = tensile strain in microns.

Both visual observations of the figures and the R^2 values suggest that the actuator tensile strain yields a better correlation (i.e., less scatter) with N_f than the on-specimen tensile strain. The reason for this finding is that on-specimen strain is determined from the on-specimen displacement at the 50th cycle. As mentioned in Section 3.2.3, the on-specimen displacement changes during the NBFT, which is in actuator displacement control mode. Changes in the on-specimen displacement during the NBFT may be different for different beam specimens for the same interlayer type and therefore may cause variation in the on-specimen strain at the 50th cycle.

The data shown in Figure 6-20 and Figure 6-21 clearly show the benefits of using a geosynthetic interlayer. Also, the slopes of the different geosynthetic interlayers are similar in Figure 6-20. Table 6-5 and Table 6-6 show that the range of k_2 values (i.e., the slopes of the tensile strain versus N_f relationship) for the actuator tensile strain is smaller than for the on-specimen tensile strain, confirming the visual observations from Figure 6-20 and Figure 6-21.

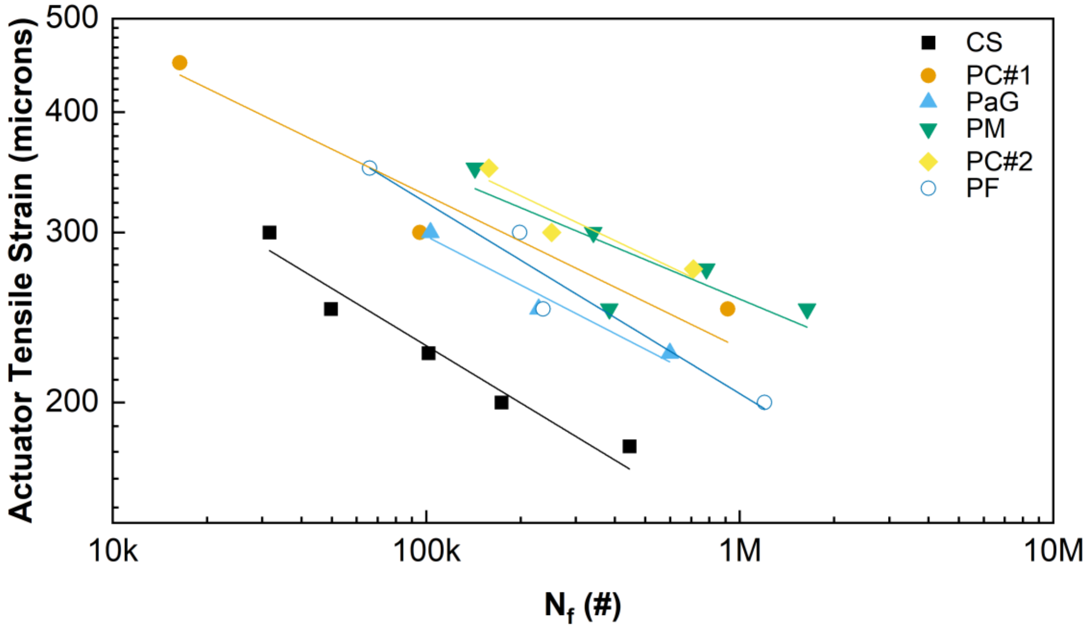

Figure 6-20. Actuator tensile strain versus fatigue life for reinforced and unreinforced (CS) beam specimens.

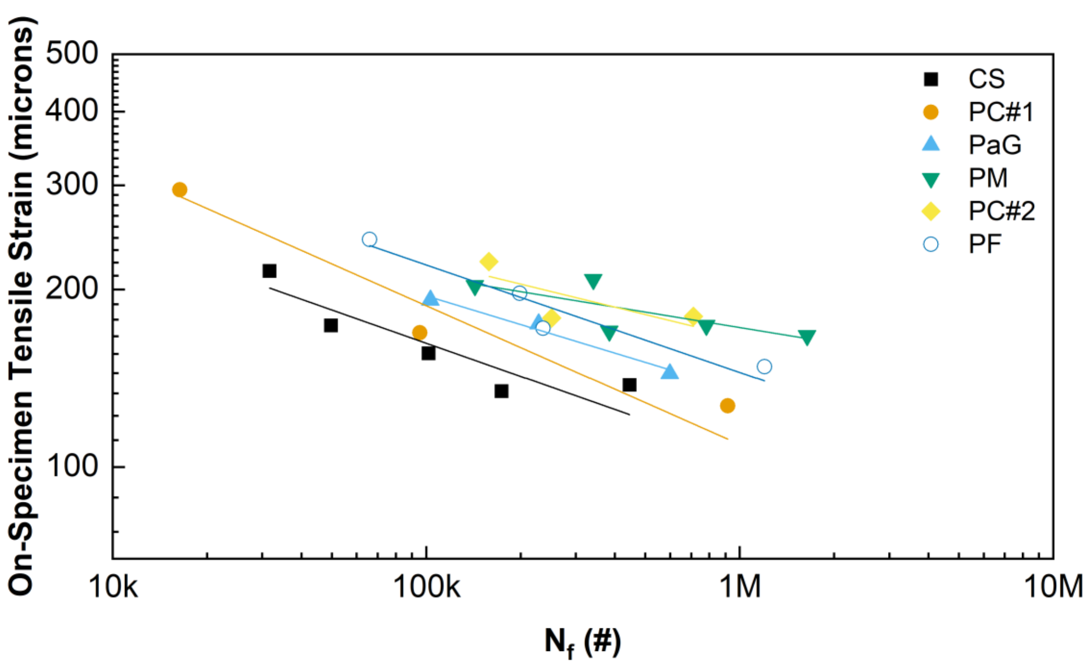

Figure 6-21. On-specimen tensile strain versus fatigue life for reinforced and unreinforced (CS) beam specimens.

Table 6-5. Fatigue Coefficients of Actuator Tensile Strain versus N_f for Unreinforced and Reinforced Specimens

Interlayer Type	**CS**	**PC#1**	**PaG**	**PM**	**PC#2**	**PF**
k_1	3.52×10^{-14}	1.08×10^{-17}	9.15×10^{-17}	3.30×10^{-21}	5.81×10^{-18}	2.35×10^{-13}
k_2	5.07	6.31	5.97	7.37	6.47	5.05
R^2	0.93	0.87	0.92	0.57	0.72	0.9

Table 6-6. Fatigue Coefficients of On-Specimen Tensile Strain versus N_f for Unreinforced and Reinforced Specimens

Interlayer Type	**CS**	**PC#1**	**PaG**	**PM**	**PC#2**	**PF**
k_1	5.15×10^{-16}	1.42×10^{-11}	8.82×10^{-19}	5.09×10^{-38}	6.38×10^{-24}	8.03×10^{-16}
k_2	5.35	4.25	6.21	11.50	7.72	5.49
R^2	0.78	0.90	0.95	0.42	0.1	0.89

Note again that the major fracture modes that drive reflective cracking are Mode I and Mode II. Both thermal effects and vehicular loading cause Mode I fracture, whereas vehicular loading alone primarily causes Mode II fracture. The Mode I fracture that is caused by thermal effects can be mimicked using an overlay tester and the Mode I fracture that is caused by vehicular loading is represented by a bending test. The Mode II fracture of AC that is caused by vehicular loading on the edge of cracked pavements. Mode II fracture in the field is significant and yet is a relatively unexplored research topic. Moreover, available test protocols for Mode II are lacking. Hence, in this study, NBFTs were performed to capture Mode I fracture under vehicular loading, which can be mitigated by geosynthetic product application.

6.2 Effect of Tack Coat Application Rate on Crack Resistance Capacity

One of the initial goals of this study was to verify the performance of geosynthetic reinforcement installed at the tack coat application rate recommended by the manufacturer and compare that performance against that achieved at other tack coat rates. Three tack coat application rates were selected for this purpose. The manufacturer's recommended rate serves as the optimal rate, and the rates for dry and wet tack coats were later defined by reducing and increasing the optimal rate by 0.02 gal/yd^2. The 0.02 gal/yd^2 difference from the optimal rate was selected based on other study results (Al-Qadi et al. 2009, Mohammad et al. 2012) and by comparing the target application rate set on the tack coat sprayer truck to the earlier studies' resultant application rates measured in the field. Figure 6-22 shows that scatter of 0.02 gal/yd^2 from the target typically is observed in the field.

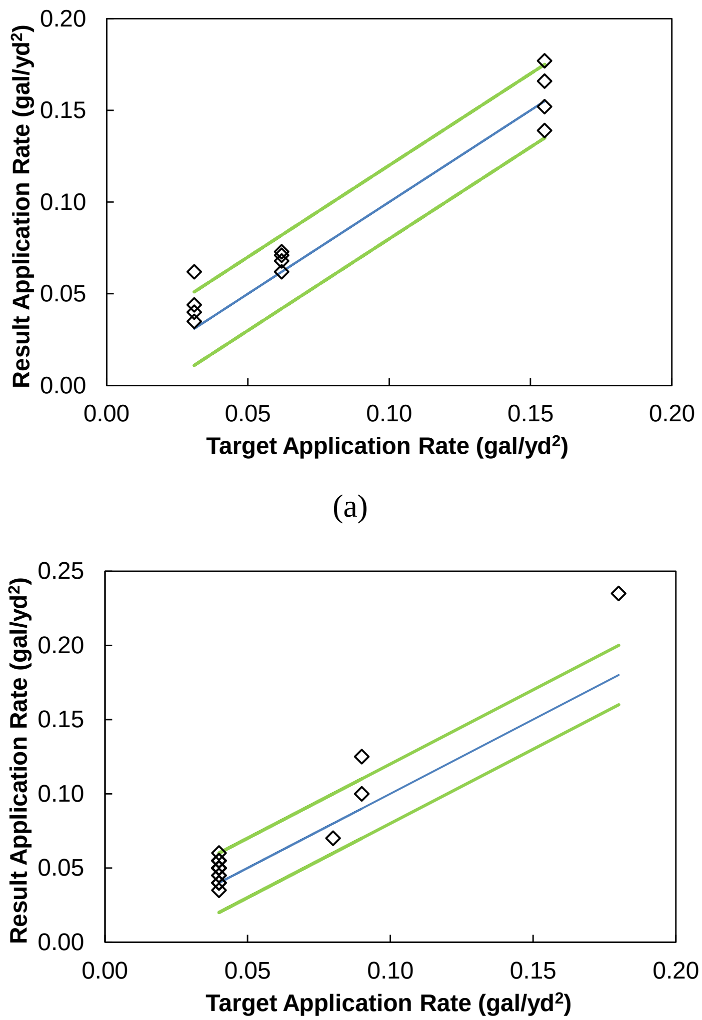

(a)

(b)

Figure 6-22. Comparison of target application rates and application rates measured in the field in other research efforts: (a) NCHRP 712-2012 (Mohammad et al. 2012) and (b) FHWA-ICT-09-035 (Al-Qadi et al. 2009).

CS and PC#1 were selected for the initial study. The three tack coat rates used for CS are 0.01 gal/yd^2 (dry), 0.03 gal/yd^2 (optimal), and 0.05 gal/yd^2 (wet) and those used for PC#1 are 0.12 gal/yd^2 (dry), 0.14 gal/yd^2 (optimal), and 0.16 gal/yd^2 (wet). The NBFTs were carried out at a constant actuator strain of 250 µ. Figure 6-23 and Figure 6-24 respectively present the stress × N test results for CS and PC#1 and illustrate that, with an increase in the tack coat application rate, the crack resistance capacity of the beam specimens also increases. Note that, for the PC#1 wet specimen, definite failure was not found; hence, its failure was predicted using the method described in the subsection of Section 6.2 called *Extrapolating a Failure Point Based on Three-Stage Weibull Survivor Function.* Figure 6-25 presents a comparison chart for the crack resistance capacity of CS and PC#1.

The results shown in Figure 6-25 indicate that the reinforcement action of PC#1 causes the crack resistance to increase more in comparison to CS. However, weather the reinforcement is used or not, an increase in the tack coat application rate leads to an increase in the failure cycle. Also noteworthy is that the difference in the initial on-specimen tensile strain of PC#1 among the various tack coat application rates is significant. An increase in the composite modulus of the specimen with an increase in the tack coat rate, which in turn affects machine compliance, can be attributed to such a response. Even though the wet PC#1 specimen's failure cycle could not be measured and is predicted, it will fail only after the optimal PC#1 specimen fails, based on the measured data presented in Figure 6-24. The response expected prior to testing is that an increase in the tack coat rate would improve the specimen's performance until it reaches a peak and then would drop after the 'optimal' (not necessarily the manufacturer's recommended rate) tack coat rate is reached. However, for the tack coat rates considered for this study, such a phenomenon was not found and the increase in the tack coat rate that is needed for the performance to drop is unknown. Further testing to identify the optimal rate was not carried out in this study due to time limitations and the priority to meet other project objectives.

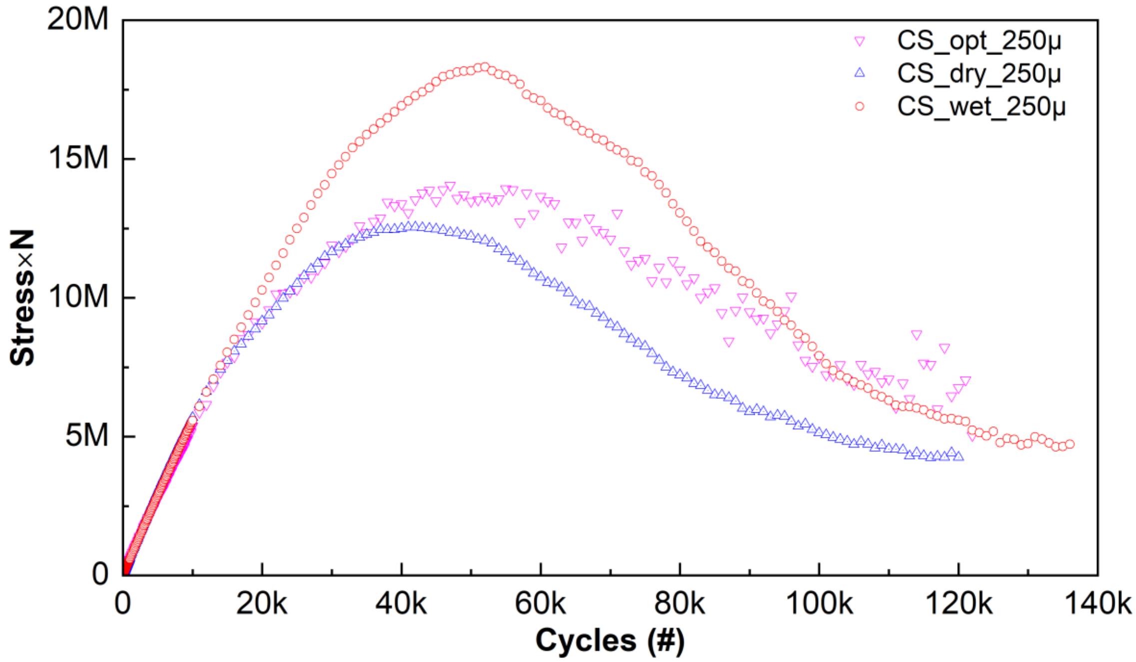

Figure 6-23.Change in 'stress × N' with number of cycles for CS.

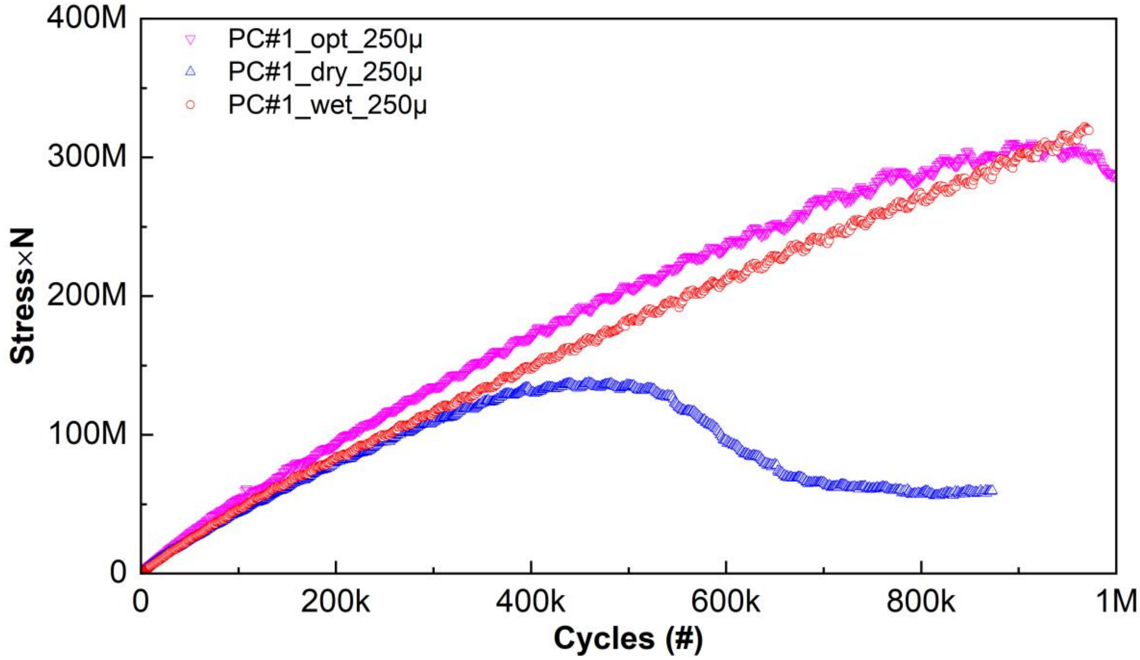

Figure 6-24.Change in 'stress × N' with number of cycles for PC#1.

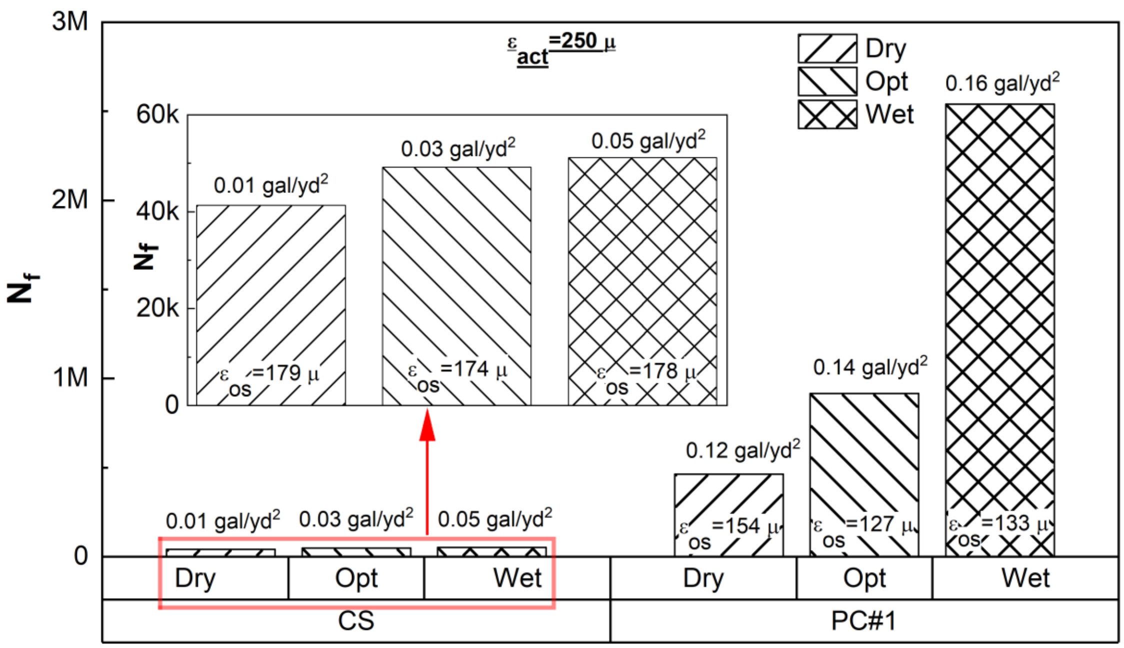

Figure 6-25. Comparison of crack resistance capacity of CS and PC#1.

Chapter 7. Digital Image Correlation Test Results and Discussion

7.1 Background

Reflective cracking is a complex phenomenon and understanding its mechanism using only strain/displacement measurements at the beam specimen's center is inadequate. A reasonable alternative is to obtain full-field displacements and strain at the surface of the specimen using DIC technology. The DIC method works by taking a reference image of the sample before loading and subsequently taking multiple images throughout the test. Next, image correlation software is used to compare each test image to the reference image. Any differences between the reference image and the test images are explained as deformations or movements of the sample that occurred when the test image was taken. In this way, full-field displacements and strain measurements of the sample can be monitored throughout the testing. The DIC system offers two crucial advantages for studying reflective cracking. First, it allows the differential movement observed throughout the interlayers of a layered AC sample to be tracked easily, which is a difficult task using traditional gauges. Second, the DIC system creates strain contour plots for easy visualization of the crack location(s) within the sample, as cracks on the surface show up as areas of extremely high strain. Although proprietary DIC software, VIC-2D, is used at the NCSU pavement laboratory, a basic understanding of the DIC method will help explain its overall usefulness and applicability for pavement engineering applications.

7.2 Digital Image Correlation System Terminology

The following terms are used when discussing DIC.

Digital image: A digital image is an image composed of picture elements, also known as pixels, each with finite, discrete quantities of numeric representation to indicate the intensity or grayscale level that is output from two-dimensional functions fed as input by spatial coordinates, denoted as x and y on the x-axis and y-axis, respectively (Gonzalez and Woods 2018). Figure 7-1 (a) shows a digital image of the face of Abraham Lincoln on a computer screen. The file is stored as a matrix of numeric values where each numeric value represents a grayscale pixel value (color) and the pixel location (x and y coordinates), as shown in Figure 7-1 (b).

Region of interest (ROI): The ROI represents an area of the picture chosen by the operator and is overlaid only on the object to be correlated. Therefore, between the reference and the deformed images, the ROI represents the analysis mask in which the correlation algorithm operates. Figure 7-1 (b) provides an example of a ROI.

Subset: DIC is a subset-based image correlation technique. The subset is a collection of pixels that carry unique grayscale value information for deformation measurements within the ROI. Figure 7-1 (b) provides an example of a subset.

Step size: The distance between the subset centers is the step size. A coarser step size (higher value) results in faster computation, while a finer step size improves the spatial resolution. A step size in terms of subset size helps identify the surrounding subsets' contribution to measuring each subset. For instance, a step size of half the subset size indicates that eight surrounding subsets $(1/2)^3$ contribute to measuring the deformation of the subset in question. A greater number of subsets contributing to measurements leads to better accuracy. Figure 7-1 (b) provides an example of the concept of step size. Figure 7-2 illustrates the concept of step size in terms of subset size.

Speckle pattern: A DIC system tracks features on the sample's surface that collectively form a speckle pattern that is used to match the reference and deformed images. The pattern/speckle should be be random in location but uniform in size and have good grayscale contrast, which reduces error. Ideally, the pattern should have a speckle density of about 50% for accuracy.

Subset shape functions: Subset shape functions are applied to the subsets of the reference image to approximate the deformation of the subset in the deformed (target) image. These functions essentially represent a transformation from the pixel coordinates of the subset in the reference image to the coordinates of the deformed image.

Correlation function: A correlation function is used for matching the subset in the deformed and undeformed images. The common correlation algorithms used are sum squared differences, normalized sum square differences, and zero-normalized square differences.

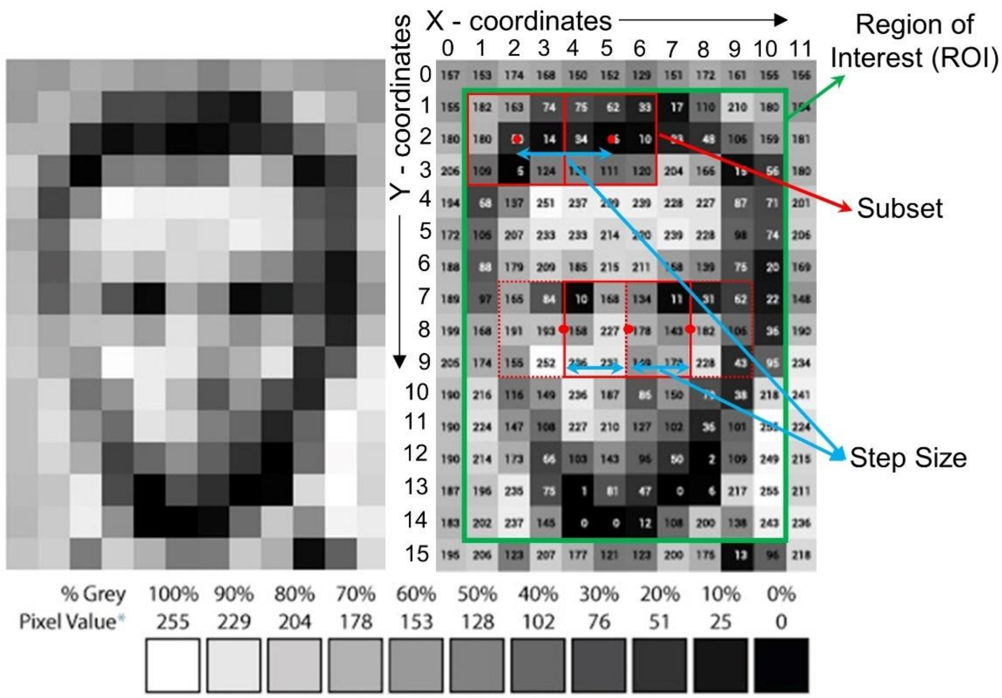

Figure 7-1. DIC image: (a) shown on a computer screen and (b) stored in the computer's memory.

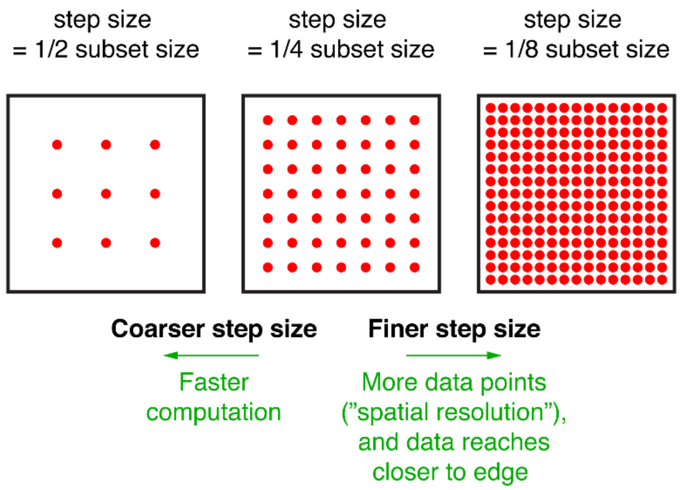

Figure 7-2. Step size in terms of subset size.

7.3 Principle Behind Digital Image Correlation

Image processing was performed in this study by tracking the displacements and deformations of the reference subsets on the surface of deformed specimens. A subset from the intact reference image was tracked in the deformed images to find the best match. This matching process was accomplished by matching the grayscale pattern of the original subset, as illustrated in Figure 7-3. The size of the subset plays an important role in the accuracy as well as matching error. The subset that is described by an intensity function (grayscale pattern) $f(x,y)$ in the reference image is deformed during the test, and the intensity function of the same subset in the subsequent image becomes $f'(x',y')$. The variables x' and y' are related to x and y through displacements u and v. These displacements, u and v, can be described as functions of x and y known as shape functions (ξ, η) (Pan 2018, Schreier et al. 2009, Yates et al. 2010). A standard representation of the shape function is given in Equation (7-1).

$$\begin{aligned} \xi(x_i, y_j) &= x_i' - x_i \\ \eta(x_i, y_j) &= y_j' - y_j \end{aligned} \tag{7-1}$$

where

$i, j = -M{:}M$ and the subset size is represented by $(2M+1)\ (2M+1)$ pixels.

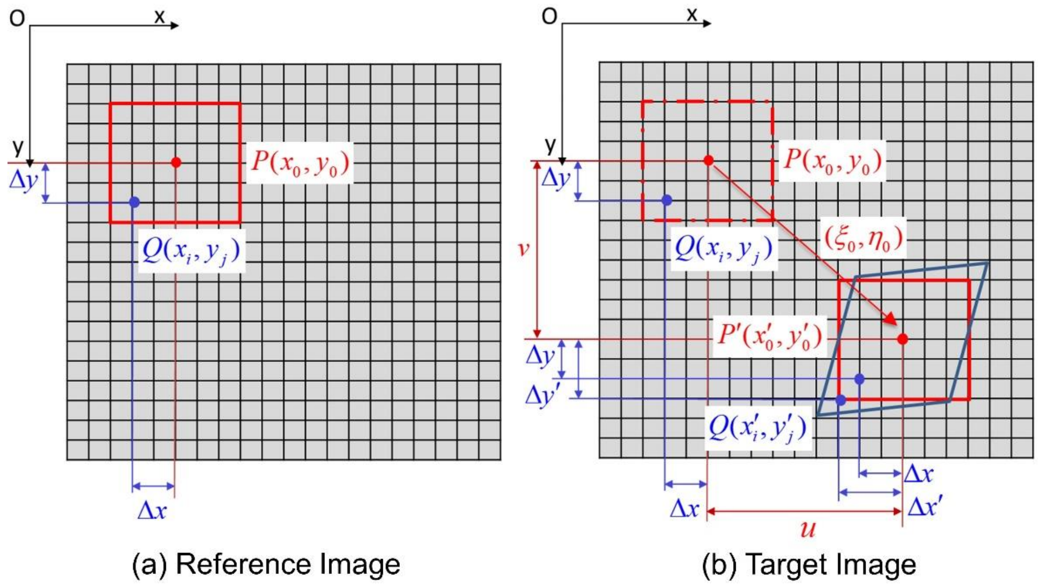

Figure 7-3. Schematic of basic underlying principle of digital image correlation.

Defining the order of the shape function decides the accuracy of the DIC measurements. Zero-order and first-order shape functions are relatively simple and can predict only displacement and velocity. However, the second-order function predicts displacement, velocity, and acceleration. Equation (7-2) shows the form of the second-order shape function.

$$\begin{aligned} \xi_1(x_i, y_j) &= u + u_x \Delta x + u_y \Delta y + \frac{1}{2} u_{xx} \Delta x^2 + \frac{1}{2} u_{yy} \Delta y^2 + u_{xy} \Delta x \Delta y \\ \eta_1(x_i, y_j) &= v + v_x \Delta x + v_y \Delta y + \frac{1}{2} v_{xx} \Delta x^2 + \frac{1}{2} v_{yy} \Delta y^2 + v_{xy} \Delta x \Delta y \end{aligned} \tag{7-2}$$

where

u and v = displacements,

$$u_x = \frac{\delta u}{\delta x}, u_y = \frac{\delta u}{\delta y}, v_x = \frac{\delta v}{\delta x}, v_y = \frac{\delta v}{\delta y},$$

$$u_{xx} = \frac{\delta^2 u}{\delta x^2}, u_{yy} = \frac{\delta^2 u}{\delta y^2}, v_{xx} = \frac{\delta^2 v}{\delta x^2}, v_{yy} = \frac{\delta^2 v}{\delta y^2},$$

$$u_{xy} = \frac{\delta^2 u}{\delta x \delta y}, v_{xy} = \frac{\delta^2 v}{\delta x \delta y}$$

$\Delta x = x_0 - x_i$,

$\Delta y = y_j - y_0$,

(x_0,y_0) = subset center, and

(x_i,y_j) = arbitrary pixel point within a subset.

Next, the DIC algorithm assumes trial functions for u and υ and attempts to minimize the error of the correlation coefficient, C, to find the best trial displacement functions, as presented in Equation (7-3).

$$C = \frac{\sum[f(x,y) - f'(x',y')]^2}{\sum f^2(x,y)} \tag{7-3}$$

The unknown parameters u, v, u_x, u_y, v_x, v_y, u_{xx}, u_{yy}, v_{xx}, v_{yy}, u_{xy}, and v_{xy} are determined by minimizing the correlation function using the Newton-Raphson method. This process is then repeated for all the image subsets, thereby allowing the construction of contour plots of both displacements and strain levels.

The matching error depends on the subset size and speckle pattern. A coarse speckle pattern relative to the subset size will increase the matching error, and a large subset size can reduce the accuracy if high displacement and strain gradients exist. In this study, relatively fine speckle patterns were created to obtain good accuracy and decrease the matching error as much as possible when a relatively small subset size was used. Also, other factors, such as the distance of the camera from the specimen surface, image resolution, distortion of the camera lens, and lighting conditions, can affect the accuracy and matching error. A detailed description of the effect of such factors on DIC measurement accuracy is presented by Safavizadeh et al. (2017).

The fundamental assumption of this simple DIC algorithm is that the grayscale values of the featured images stay the same. However, this assumption is rarely the case due to the discrete nature of pixels in a digital image. In fact, due to the stretching of the features, and the features moving only distances that correspond to fractions of the distance between pixels, changes in the intensities of the features between $f(x,y)$ and $f'(x',y')$ are almost always seen. Therefore, more advanced DIC algorithms that use interpolation functions to account for these changes in grayscale values will significantly increase the accuracy of DIC algorithms and allow for sub-pixel precision in displacement measurements (Wargo 2015).

7.4 Strain Tensors and Associated Criteria

A strain tensor is used to define the state of strain at a particular point. Many tensors are available for VIC-2D, such as Lagrange, engineering, Henchy (logarithmic), and Euler-Almansi. The strain tensor that best matches the anticipated values must be selected. Many of these tensors will give similar results at low strain levels, but at higher strain levels, the results can differ. Therefore, selecting the wrong tensor can lead to unexpected results. Lagrange is the default tensor in VIC-2D and was used for the current study. The Lagrangian finite strain tensor, also known as the Green-Lagrangian strain tensor, is a finite strain measure that includes higher-order displacement terms and defines gradients in the original configuration. This measure is commonly used for materials that undergo large strain, such as elastomers. Note that Lagrangian strain can become much greater than the extension or engineering state of strain at high strain levels due to the higher-order term. The form of the tensors is given in terms of ε_{xx} (the strain along the x-axis), ε_{yy} (the strain along the y-axis), ε_{xy} (the shear strain tensor, which is equal to half the engineering shear strain), as well as e_1 (major strain), e_2 (minor strain), and gamma (the major strain angle, which is the angle, in radians, between the +x-axis (positive side) and the major strain axis). The Lagrangian strain formulations are shown in Equations (7-4) through (7-7).

$$\varepsilon_{xx} = u_x + \frac{u_x^2 + v_x^2}{2} \tag{7-4}$$

$$\varepsilon_{yy} = v_y + \frac{u_y^2 + v_y^2}{2} \tag{7-5}$$

$$\varepsilon_{xy} = \frac{u_y + v_x + u_x u_y + v_x v_y}{2} \tag{7-6}$$

$$\varepsilon_{1,2} = \frac{\varepsilon_{xx} + \varepsilon_{yy}}{2} \pm \sqrt{\left(\frac{\varepsilon_{xx} - \varepsilon_{yy}}{2}\right)^2 + \varepsilon_{xy}^2} \tag{7-7}$$

where

u and v = displacements,

$$u_x = \frac{\delta u}{\delta x}, u_y = \frac{\delta u}{\delta y}, v_x = \frac{\delta v}{\delta x}, v_y = \frac{\delta v}{\delta y},$$

ε_{xx} = the strain along the x-axis,

ε_{yy} = the strain along the y-axis, and

ε_{xy} = the shear strain tensor, which is equal to half the engineering shear strain.

Von Mises Strain Analysis

Von Mises strain is an equivalent strain and is used as a yield criterion. This type of strain provides the equivalent uniaxial strain of the existing strain state from the yield point of view. Von Mises strain is frequently used as a yield criterion for metal. However, VIC-2D calculates the surface strain, and the built-in Von Mises calculation uses the principal plane strain formulation shown in Equation (7-8).

$$\varepsilon^v = \frac{2}{3}\sqrt{\varepsilon_1^2 - \varepsilon_1\varepsilon_2 + \varepsilon_2^2} \tag{7-8}$$

where

ε_1 and ε_2 are the principal strains at an element, and

ε^v = Von Mises strain.

7.5 Tracking Crack Propagation Using Digital Image Correlation

Wargo (2015) and Sudarsanan et al. (2019a) found that strain field contour plots could be used to identify cracks in NBFT specimens. In particular, contour plots of Von Mises strain, which provides an estimate of the total strain given by Equation (7-8), allow the areas of high strain caused by cracking to be tracked easily. As such, the Von Mises strain was the first strain field observed in any of the tests performed in this study. Although many iterations of the DIC analysis parameters and strain criteria were used to identify cracks in this investigation, all final analyses of the NBFT results were performed with a DIC window size (subset size) of 19 pixels × 19 pixels and a step size of 1. The Von Mises strain threshold of 3% was found to identify macrocrack locations consistently for all DIC analyses performed using these parameters. The images at the peak displacement only were collected and analyzed to reduce the number of large analysis files produced by the post-processing DIC software.

As previously discussed, stiffness curves do not provide enough information to study the damage mechanisms in NBFTs. DIC was utilized in this study to identify the failure mechanisms and failure mode of the beam specimens. Then, Von Mises strain contours were used to identify the damage mechanisms and track the crack propagation within the beam specimen and at the interface. Figure 7-4 through Figure 7-10 present color maps with a limited number of fire shades (dark red to light yellow) that gradually change from black (representing the low strain areas) to white (representing the high strain areas) that were used to facilitate comparisons among the conditions. Black indicates 0% Von Mises strain and white indicates 10% Von Mises strain. Each shade within these strain contours represents a specific range of strain.

As an example of the primary use of DIC information, Figure 7-4 shows the Von Mises strain (which serves as an estimate of the total strain) for samples of different interlayers tested at 23°C and 250 μ actuator tensile strain. By presenting the DIC images under the same test conditions, general descriptions of the damage evolution within the samples could be developed for different geosynthetic-reinforced beams. For CS, cracking proceeded through the bottom AC layer with minimal interfacial movement. The crack spent little to no time trapped in the interlayer and rapidly propagated through the top layer. For the geosynthetic-reinforced specimens, cracks began to propagate in the bottom AC layer and then interfacial movement started to occur. Once the vertical cracks reached the interlayer, the interfacial movement increased significantly. This interfacial movement helped to stall the crack at the interface before cracking (both top-down and bottom-up cracking) in the top layer caused a full-depth crack to develop.

Figure 7-5 shows the Von Mises strain contour plots for CS tested at five different constant tensile strain levels. In most cases, no interfacial damage is evident except for subtle damage at the lower tensile strain of 180 μ. All the specimens failed quickly as the vertical crack moved upward, eventually causing complete rupture.

Figure 7-6, Figure 7-7, Figure 7-8, Figure 7-9, and Figure 7-10 show the Von Mises strain contour plots for PC#1, PC#2, PaG, PF, and PM, respectively. In order to investigate the failure modes for different geosynthetic types and strain levels, the Von Mises strain contour plots at the failure cycles are presented in Figure 7-11.

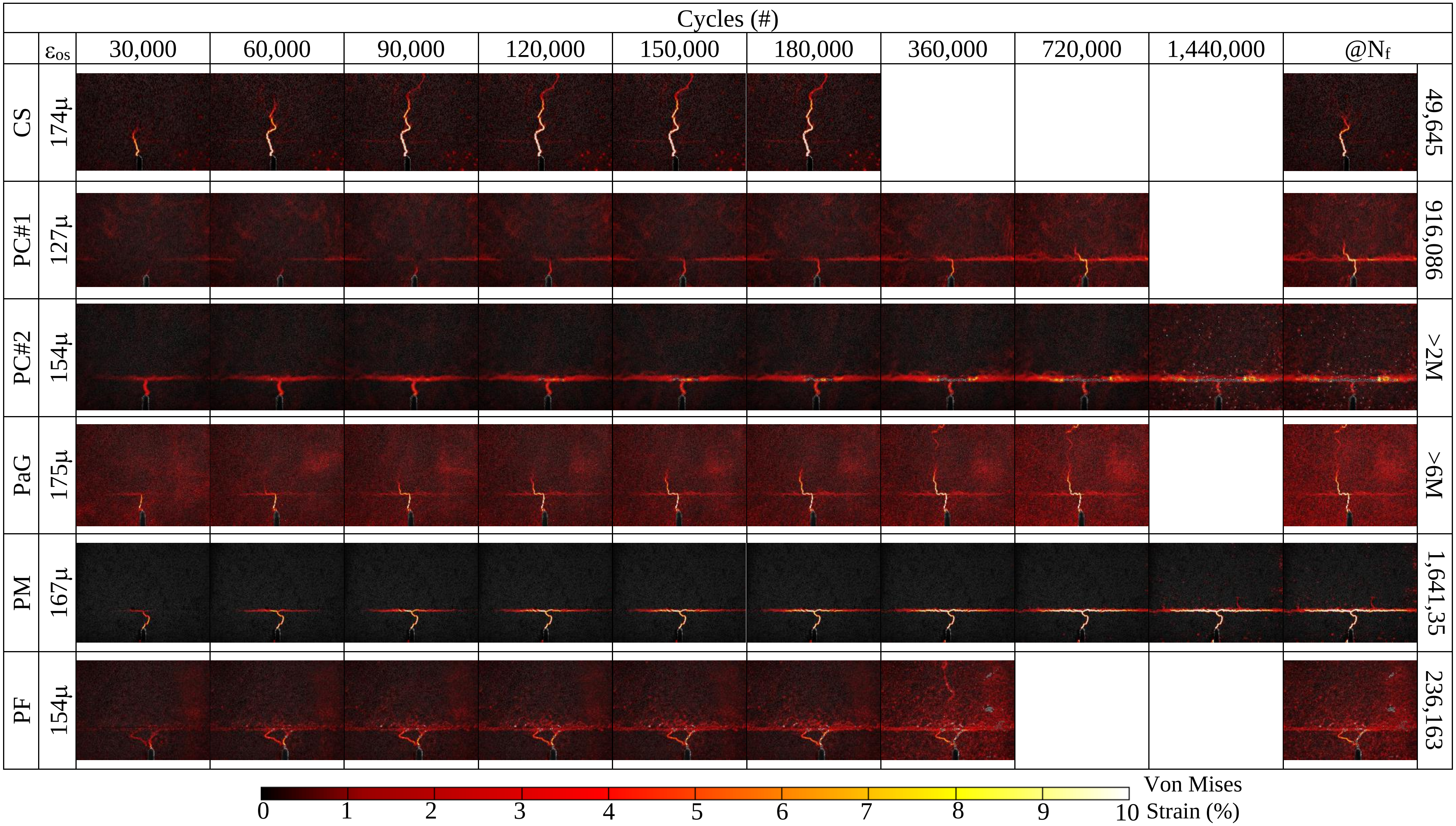

Figure 7-4. Von Mises strain measured for CS and all types of geosynthetic-reinforced beam specimens tested at 250 μ strain.

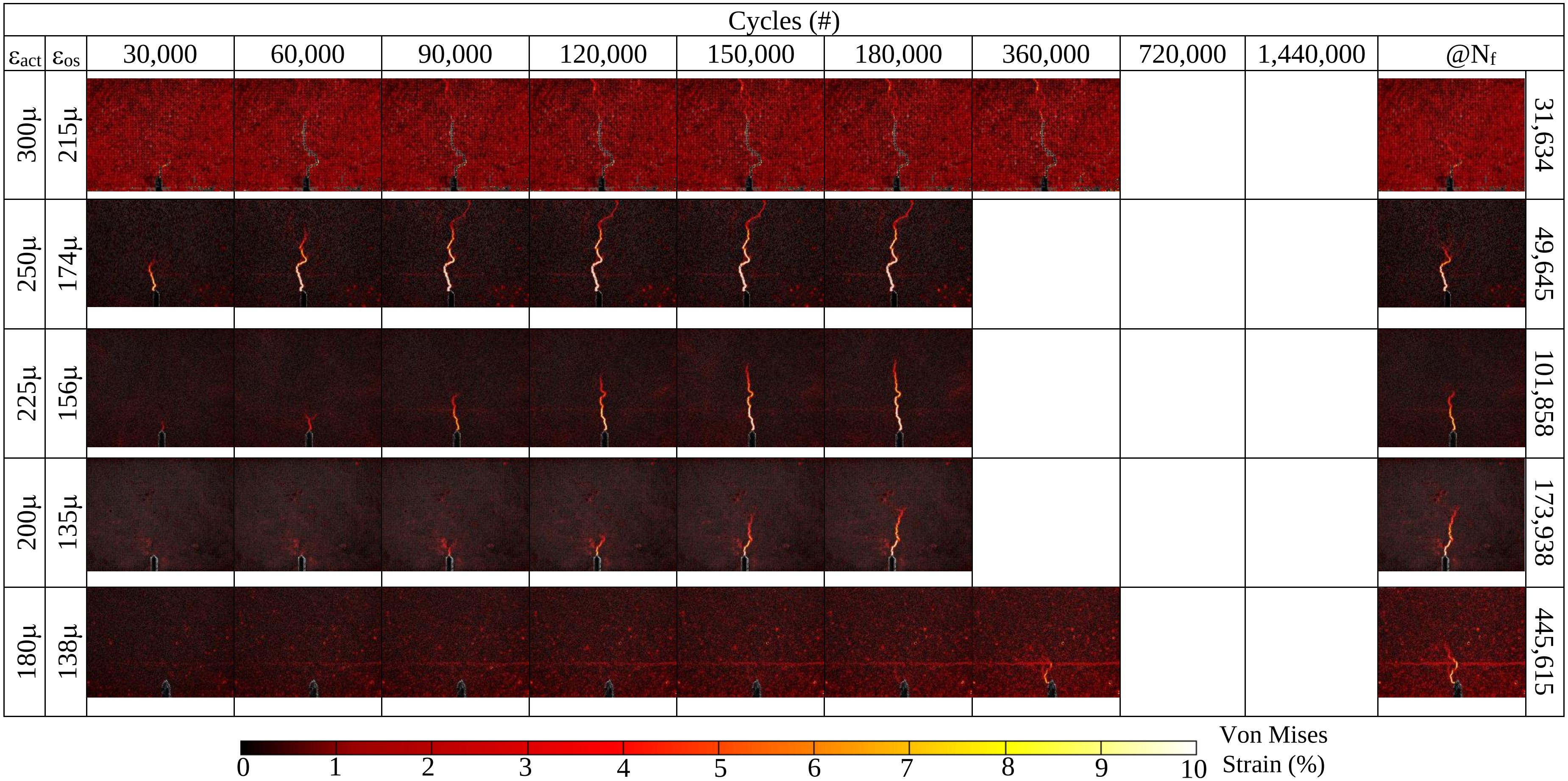

Figure 7-5. Von Mises strain measured for control specimen (CS) tested at different strain levels.

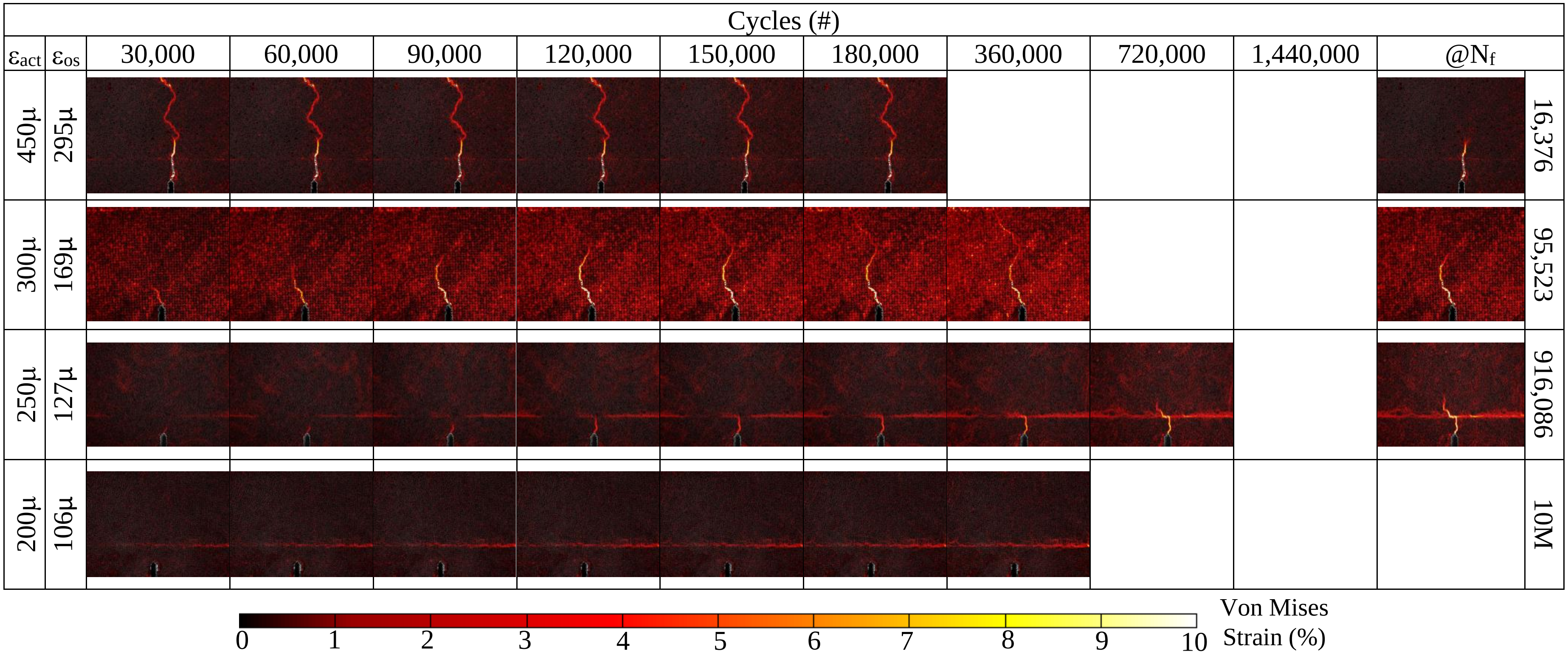

Figure 7-6. Von Mises strain measured for PC#1-reinforced beams tested at different strain levels.

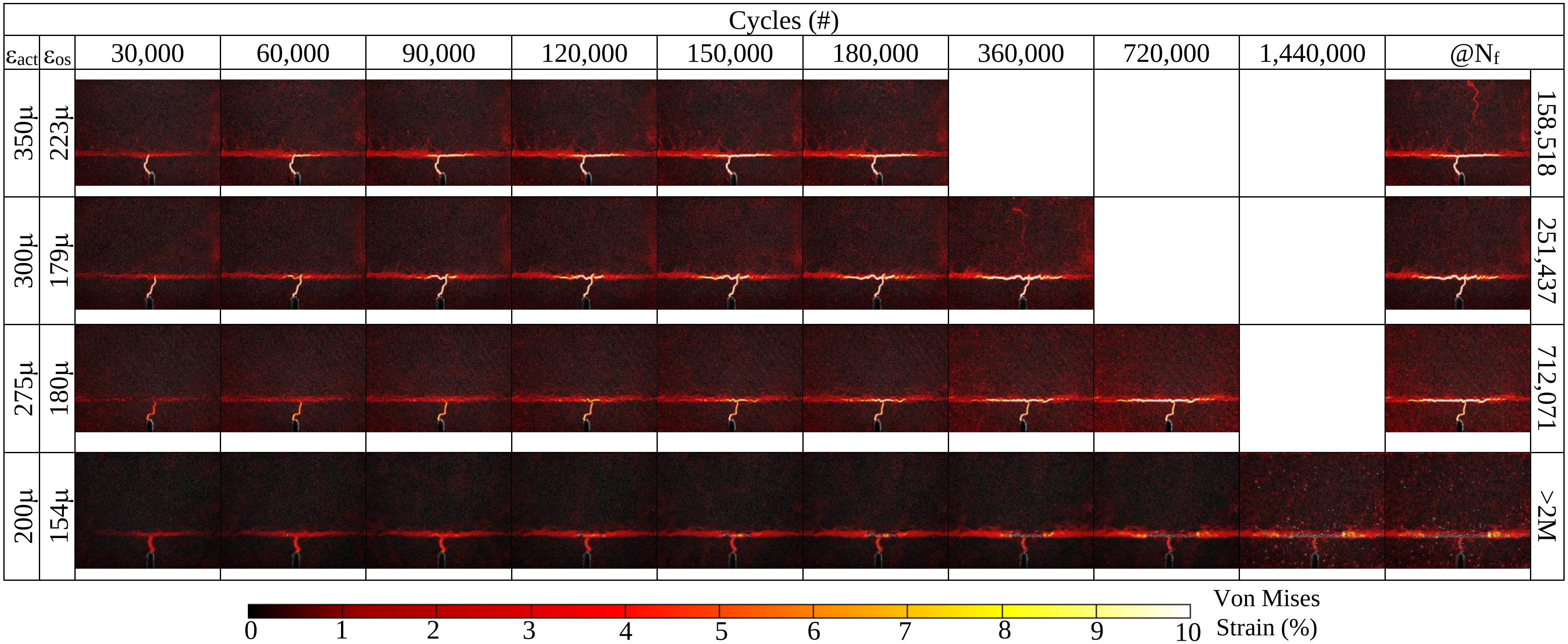

Figure 7-7. Von Mises strain measured for PC#2-reinforced beams tested at different strain levels.

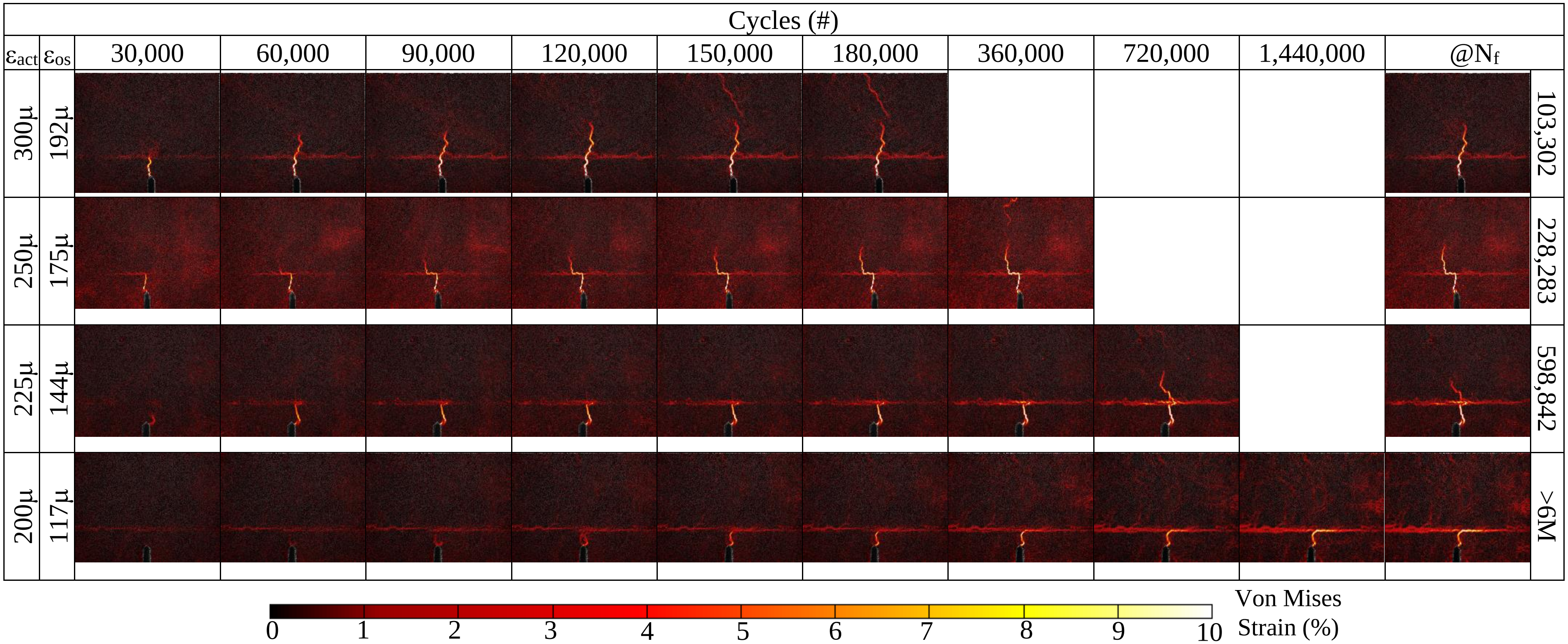

Figure 7-8. Von Mises strain measured for PaG-reinforced beams tested at different strain levels.

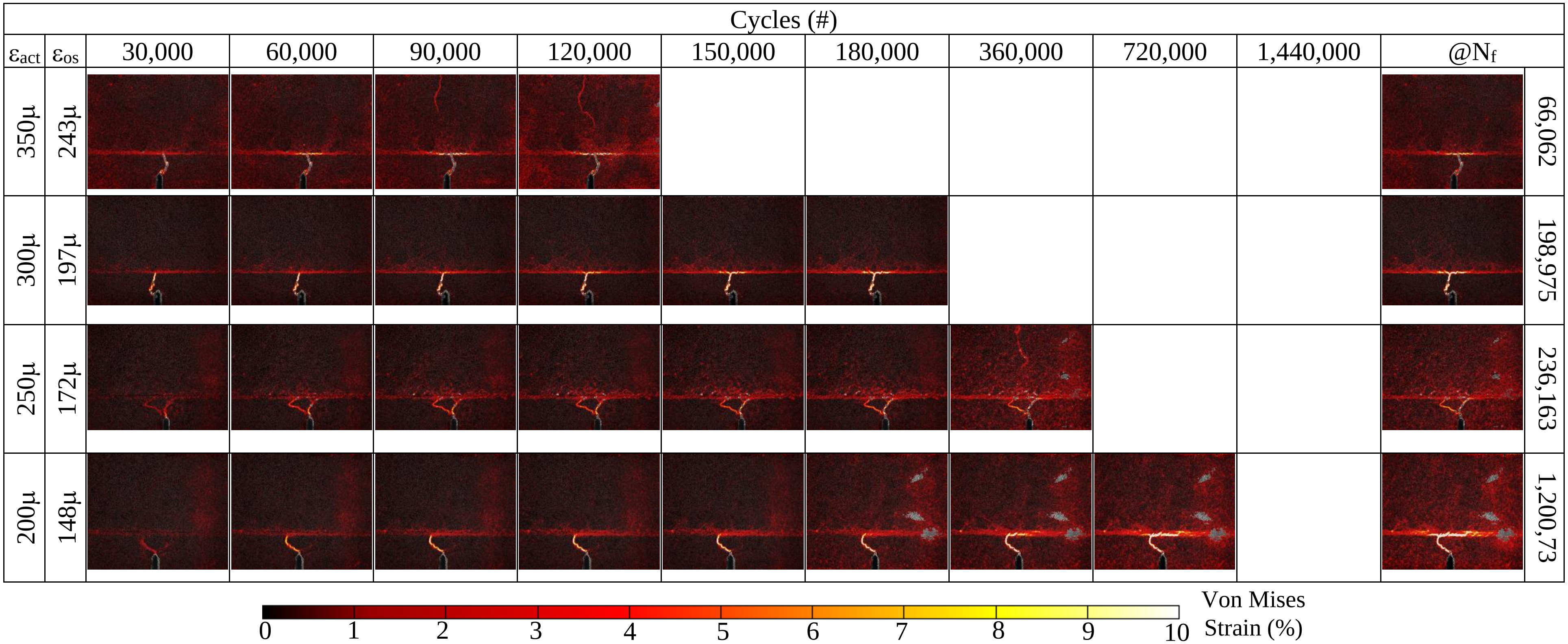

Figure 7-9. Von Mises strain measured for PF-reinforced beams tested at different strain levels.

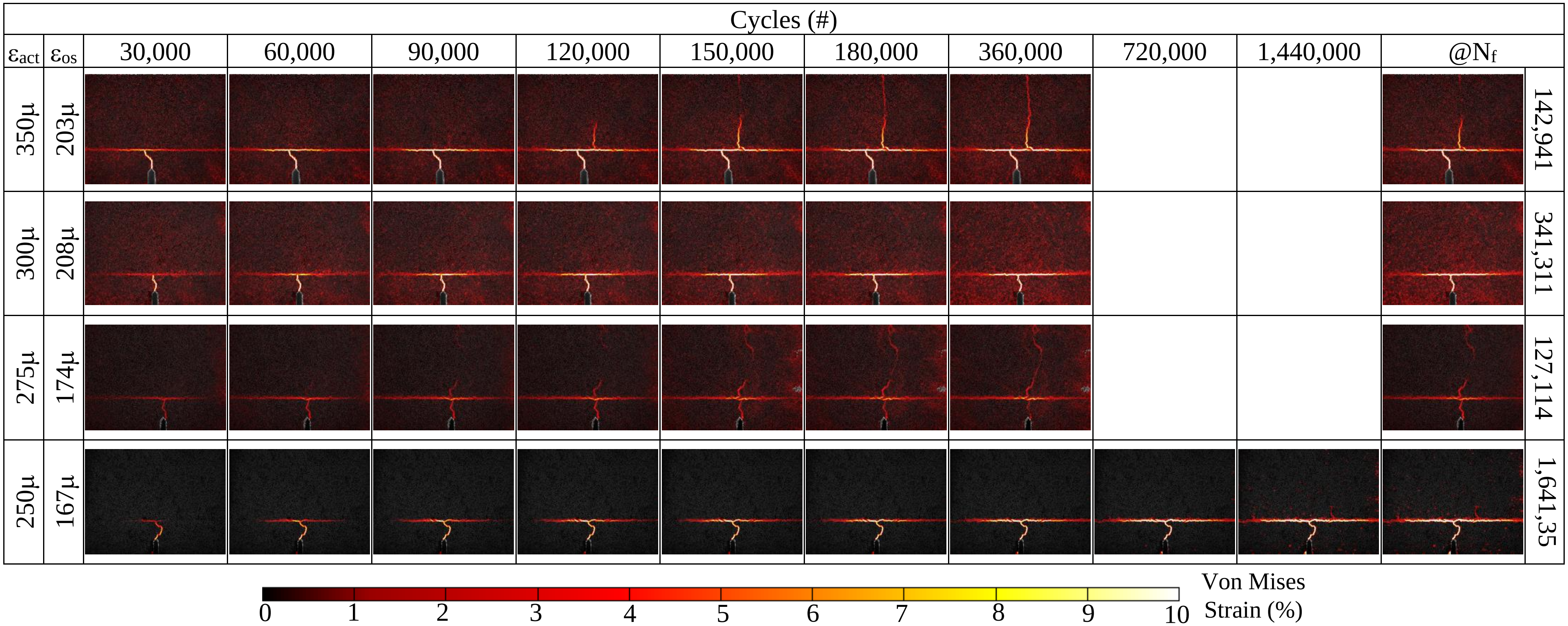

Figure 7-10. Von Mises strain measured for PM-reinforced beams tested at different strain levels.

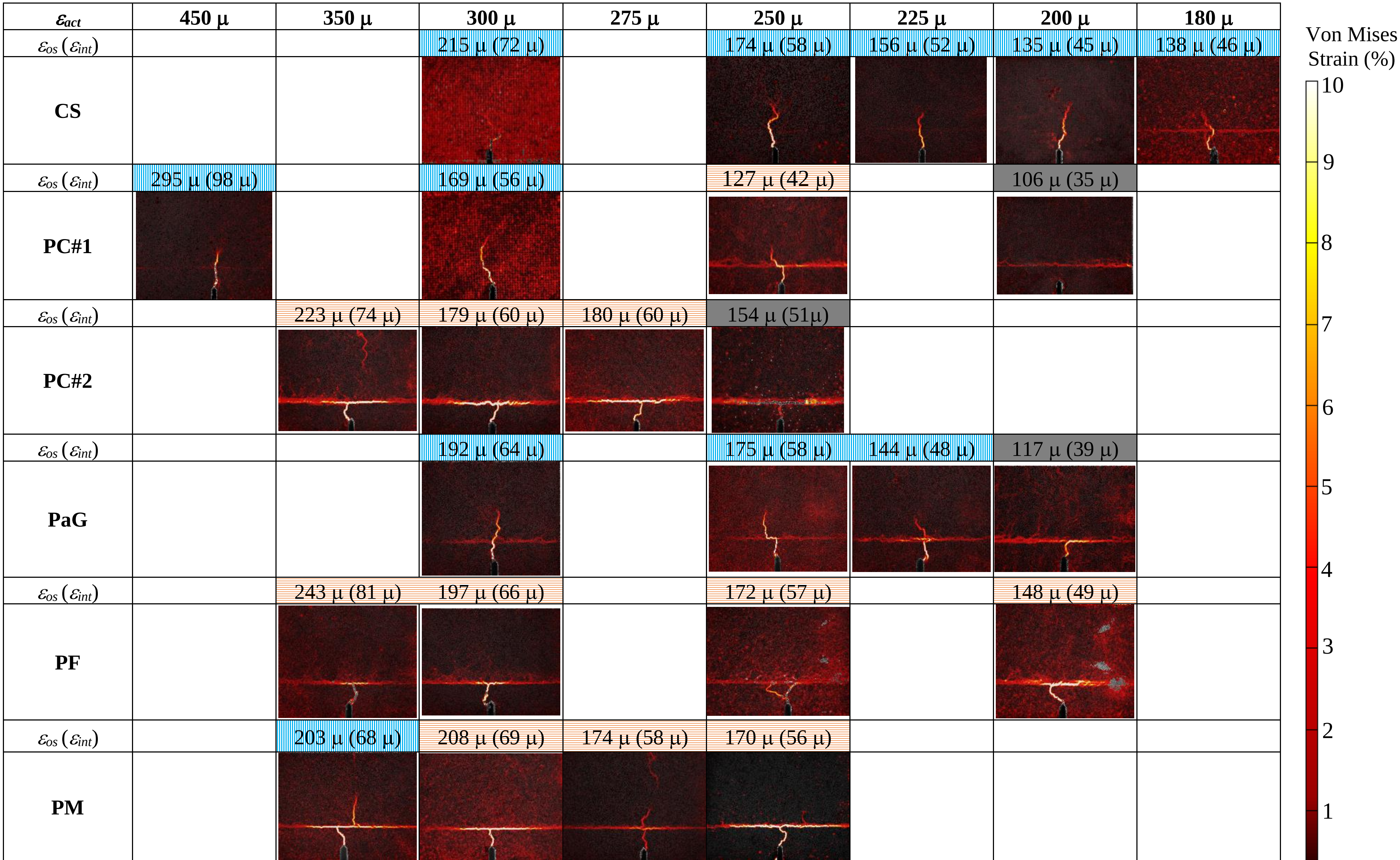

*Note: ε_{act} and ε_{os} are tensile strains calculated using actuator displacement and on-specimen displacement, respectively; and ε_{int} is tensile strain predicted at the interlayer based on on-specimen displacement ($\varepsilon_{int} = \varepsilon_{os}/3$). The failure mode of each test is identified by the shades in each cell with the following patterns:

Vertical Cracking | Debonding Cracking | Failure not recorded using *Stress* × *N*

Figure 7-11. Von Mises contours of NBFT results for interlayer beam specimens at failure points.

By comparing the DIC contours shown in Figure 7-6 through Figure 7-11, the following observations could be made.

1. All five geosynthetic-reinforced beam specimens exhibit improvement in their fatigue resistance. The composite structure of the geosynthetic-reinforced beam actively engages the geosynthetic reinforcement in transferring the load throughout the geosynthetic product, thereby reducing the stress concentration and dissipating the energy along the interface and preventing the crack tip from opening and further propagating upward.
2. A close investigation of the crack patterns shown in these contour figures reveals that the failure of geosynthetic-reinforced asphalt beam specimens can be classified into two failure modes, vertical cracking and debonding. The energy that is input by repeated loading is dissipated by the creation of new surfaces through vertical cracking and debonding. Therefore, the increase in interfacial damage effectively mitigates vertical cracking. However, this behavior is not necessarily beneficial to pavement life because the interlayer products that have a greater tendency for interfacial damage will cause debonding pavement failure.
3. The DIC contour results indicate that all five types of geosynthetic product delay vertical crack propagation but promote debonding.
4. A side-by-side comparison of the strain contours indicates that, even though these specimens have similar initial stiffness values, their failure modes differ depending on the geosynthetic type and strain level of testing.
5. The control specimens show the least amount of interfacial damage (therefore debonding), followed by PC#1 and PaG with limited interfacial damage (if any). PC#2, PF, and PM show the most extensive interfacial damage under all conditions among all the specimens. Note that these three products also have lower ISS values than the rest of the interlayer products (see Figure 5-3 and its discussion). The ISS test results explain the reason that the debonding mechanism is the major failure mode in the NBFTs for these products. The continuum nature and relatively thick PM, PC#2, and PF demand more asphalt for impregnation. Hence, these products tend to absorb more stress to mitigate vertical cracking while promoting interfacial damage via a softer interface. A higher quality tack coat may improve the debonding resistance of these products.
6. The interfacial damage (if any) initiates and starts to grow when the tip of the vertical crack reaches the vicinity of the interface. Once the vertical crack starts to propagate (bottom-up crack) within the top layer of the beam, the severity of the interfacial damage does not seem to change considerably.
7. For almost all the geosynthetic-reinforced specimens, an actuator strain level of 300 μ or higher indicates the initiation and propagation of a top-down crack and is one of the main reasons for specimen failure at higher strain levels.
8. The severity and extent of interfacial damage are affected by the strain level. In all the geosynthetic product cases, lower strain levels cause predominantly debonding failure whereas higher tensile strain levels lead to vertical cracking failure. During high tensile strain tests, debonding at the interface causes the top and bottom layers to serve as two

independent beams. Decoupled beam behavior occurs once the crack that is generated from the notch passes through the bottom layer and touches the top layer, causing crack initiation at the bottom of the top layer. For example, the DIC contours of the PM-reinforced beam at the actuator strain of 350 microstrain, presented in Figure 7-10, show that the bottom of the vertical crack in the top layer of the beam is not connected to the crack below the reinforcement. The extensive debonding that occurred under this condition separated the top and bottom layers of the beam, and the crack in the upper layer started from the weakest location at the bottom of the upper layer. Figure 7-8 shows a similar pattern in the DIC contours of the PaG-reinforced beam at the actuator strain of 250 microstrain. In these cases, the mode of failure at the failure cycle may seem to be vertical cracking, but the real cause of the failure is debonding. In fact, the predominantly vertical cracking failure at higher strain levels may be due to extensive debonding at these strain levels. This observation emphasizes the importance of sufficient bond strength at the interface of geosynthetic-reinforced asphalt overlays to mitigate reflective cracking.

9. The delay in crack initiation from the bottom of the top layer depends on the geosynthetic product type, interlayer bond strength, and test strain level. The strain level dependency indicates the existence of transition tensile strain, which is the tensile strain where the failure mode switches from debonding to vertical cracking.
10. Figure 7-11 shows that, in the cases of PC#1 and PaG, debonding failure can be observed only at an interlayer tensile strain that is less than 40 μ. The results for all the tests conducted above 40 μ interlayer tensile strain show vertical cracking failure. Therefore, the transition tensile strain is considered to be 40 μ. In the cases of PC#2 and PM, the transition tensile strain at the interlayer is approximately 70 μ. Note that PC#2 is thicker than the other products, and the tack coat application rate recommended by the manufacturer for PC#2 is higher than for the other geosynthetic products so that the product is completely impregnated. Note that, unfortunately, the data for PF are not sufficient to determine the transition tensile strain for PF. All the PF tests resulted in debonding failure. Further study using PF at higher tensile strain levels could help identify its transition tensile strain.

One of the major findings from the DIC study is that the failure mechanism in geosynthetic-reinforced overlays depends on the geosynthetic product type and the strain level at the bottom of the overlay. However, the selection of a suitable geosynthetic product should be made before the overlay is constructed, thus making it necessary to predict the tensile strain at the bottom of the overlay. Chapter 8 presents a methodology to predict the overlay tensile strain based on FWD deflections of existing pavements before the overlay is placed. Chapter 8 also presents the geosynthetic product selection guidelines that the research team developed based on the findings from this study.

7.6 Quantitative Analysis of DIC Images

One major drawback of using DIC contour plots to judge the relative interfacial movement of various NBFT specimens is the qualitative nature of constructing and interpreting such plots. Changing the number and range of the contour intervals can have a significant effect on the resultant plot and may make meaningful comparisons of the images somewhat subjective. In order to eliminate this subjectivity, a MATLAB code was written to count the number of pixels that satisfies the macrocrack criterion. These measurements helped to confirm the qualitative observations of interfacial movement and crack locations obtained from the DIC contour plots. Additionally, these results helped confirm that interfacial movement tended to increase significantly once the vertical crack reached the interlayer, which in turn helped to identify the failure mode of each test. A step-by-step procedure for identifying the failure mode is explained in this section.

The digital images captured using the DIC technique were analyzed using Vic-2D® to determine the Von Mises strain. The Von Mises strain for each pixel was stored as a matrix that corresponds to the *x* and *y* coordinates of the image. The Von Mises strain measured on the beam specimen surface between the loading points during the test was used to determine the macrocrack development and, thus, the failure mode. A comparison between visual observations of the DIC images and the Von Mises strain helped the research team to identify the macrocrack criterion, which is the point at which the Von Mises strain is greater than or equal to three percent. A MATLAB code was written to analyze the crack progression by counting the number of pixels that exceeds the Von Mises macrocrack criterion. Figure 7-12 presents the three steps involved in the DIC analysis and the following text describes the steps in detail.

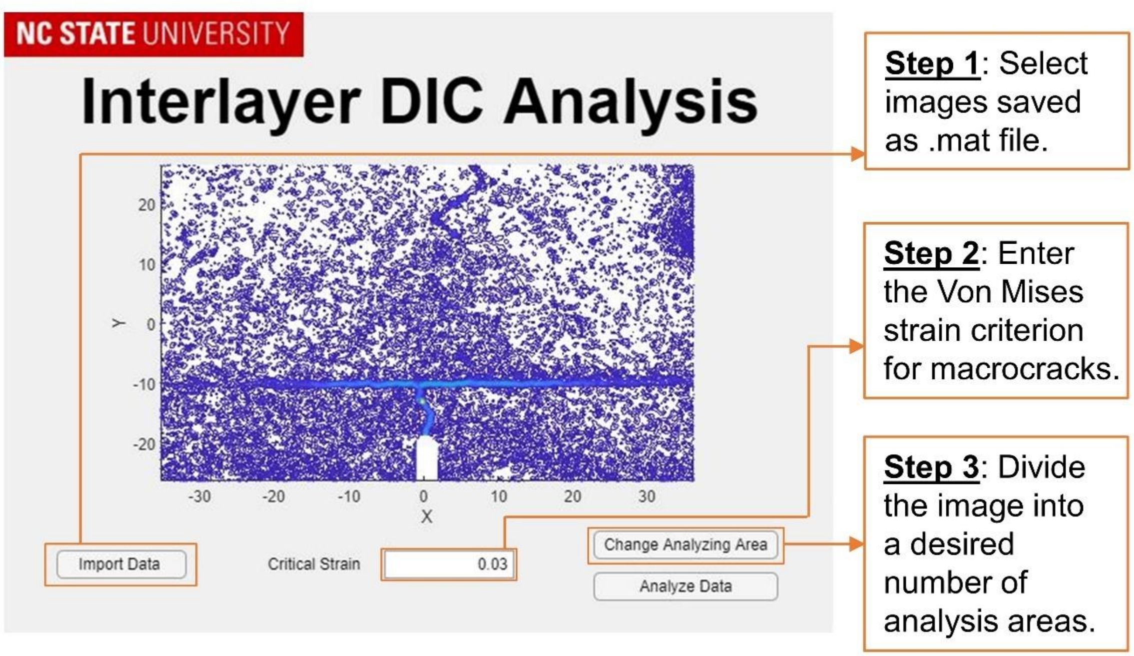

Figure 7-12. Graphic user interface for interlayer DIC analysis and steps involved in analysis.

Step 1: Prior to taking the analysis steps, export all the images at the peak displacement as MATLAB files that store the Von Mises strain data as a matrix. This step enables the software to count the pixels that exceed the macrocrack criterion Then, select the folder that contains all the image data set in .mat file format by clicking the 'Import Data' button.

Step 2: Enter the macrocrack criterion in the text box shown in Figure 7-12. The macrocrack criterion for the current study is three percent.

Step 3: Divide the region of interest selected during Vic-2D® post-processing into four areas, as shown in Figure 7-13. Determine the debonding area in terms of percentage around the interface by selecting a region of the constant area [Area 3 - 150 mm^2 (0.23 in.^{2})] with the dimensions of 60 mm × 2.5 mm (2.36 in. × 0.1 in.) and then counting the number of pixels that satisfies the Von Mises macrocrack criterion. Correspondingly, select the middle one-third of the beam with a constant area [340 mm^2 (0.53 in.^{2})] and dimensions of 20 mm × 17 mm (0.79 in. × 0.67 in.) to count the pixels that were used to determine the vertical macrocrack area. Similarly, select Areas 1 and 4 to see the whole crack activity within the beam specimen. Then, plot the vertical and debonding cracked areas against the number of load cycles. In this study, the percentages of the vertical and debonding cracked areas helped determine the failure mode for each test condition.

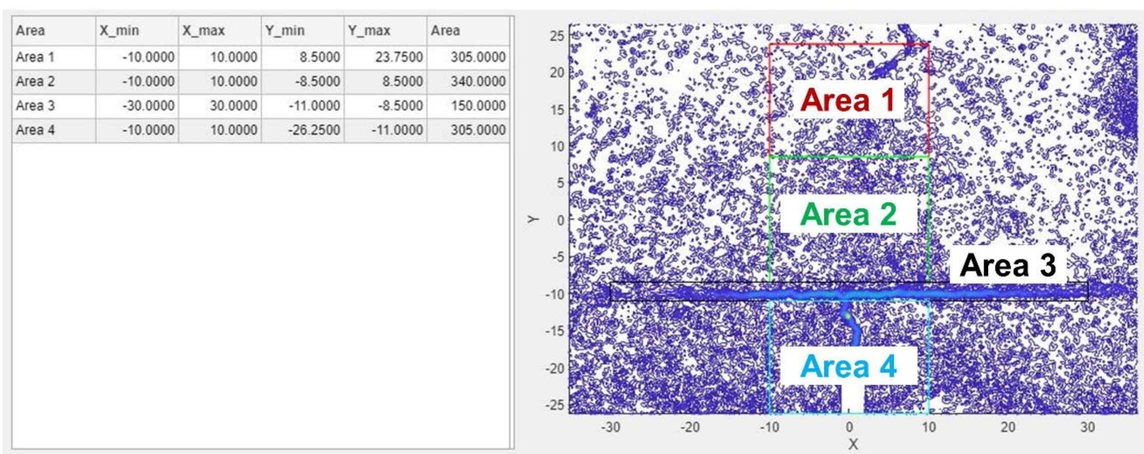

Area	X_min	X_max	Y_min	Y_max	Area
Area 1	-10.0000	10.0000	8.5000	23.7500	305.0000
Area 2	-10.0000	10.0000	-8.5000	8.5000	340.0000
Area 3	-30.0000	30.0000	-11.0000	-8.5000	150.0000
Area 4	-10.0000	10.0000	-26.2500	-11.0000	305.0000

Figure 7-13. Selecting analysis areas for interlayer DIC analysis.

A close investigation done in Section 7.5 on the crack patterns of the reinforced and unreinforced beams using DIC contour images revealed that each test failure could be classified into two failure modes, vertical cracking and debonding cracks. The results indicate that all five types of geosynthetic product delay vertical cracking propagation by promoting debonding cracks. Also, the likelihood of vertical cracking propagation was found to be higher at higher tensile strain levels. Therefore, depending on the type of geosynthetic product and testing tensile strain, the propensities of debonding and vertical cracking will vary. Hence, the failure mode of geosynthetic products depends on the tensile strain under service conditions and the product's ability to mitigate debonding.

The cracked area calculation findings support these observations. For the debonding crack failure mode, the debonding cracks in Area 3 are more numerous than vertical cracks in Areas 1 and 2 at failure. For the vertical cracking failure mode, the cracked area of the middle one-third (Area 2) shows a significant increase (numerically could be less than debonding cracks, however) in the cracked area.

Figure 7-14 to Figure 7-18 present the measured cracked areas for the unreinforced (CS) and geosynthetic-reinforced beam specimens. CS, irrespective of the tensile strain set during the NBFTs, shows vertical cracking at failure. However, at 180 μ actuator tensile strain, which is the lowest test strain level for the CS specimens, CS at failure shows signs of debonding. A close examination of Figure 7-5 at 180 μ actuator tensile strain clearly shows debonding strain at higher load cycles. The debonding strain becomes a debonding crack once it meets the macrocrack criterion. Hence, for CS, Figure 7-14 does not show any debonding cracks. For all the geosynthetic-reinforced specimens, lower strain levels correlate with predominantly debonding crack failure whereas vertical crack failure is observed at higher tensile strain levels.

In the cases of PC#1 and PaG, debonding crack failure is observed only at an interlayer tensile strain that is less than 40 μ. Figure 7-15 and Figure 7-17 show the vertical and debonding crack area growth of PC#1 and PaG, respectively. In both cases, the vertical crack above 40 μ interlayer tensile strain causes the crack in the middle one-third area to grow just before the measured failure cycle (N_f). Hence, the failure mode for all the tests conducted above 40 μ interlayer tensile strain can be categorized as vertical cracking failure. Therefore, the transition tensile strain is considered to be 40 μ for PC#1 and PaG, whereas for PC#2 and PM, shown respectively in Figure 7-16 and Figure 7-18, the transition tensile strain at the interlayer is approximately 70 μ. In Figure 7-16 and Figure 7-18, the vertical cracks (middle one-third) start to show up before the N_f is reached for tests above the transition tensile strain of 70 μ.

The concept of transient tensile strain was used for the development of the geosynthetic interlayer product selection guidelines in this work by defining the failure mechanism using the strain at the bottom of the asphalt overlay. If the product causes overlay strain above the transition tensile strain level, then the expected failure mechanism for that product is vertical cracking. In the opposite case, the expected failure mechanism for the product would be debonding. The geosynthetic interlayer product selection guidelines reported in Chapter 8 are based on this concept.

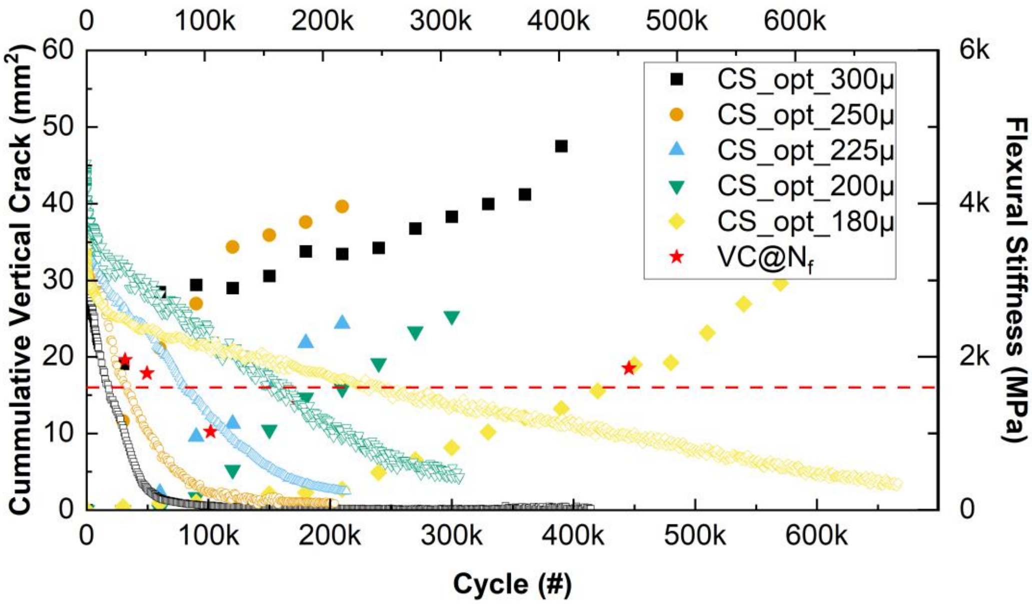

Figure 7-14. Cumulative vertical cracking area measured during NBFTs of CS.

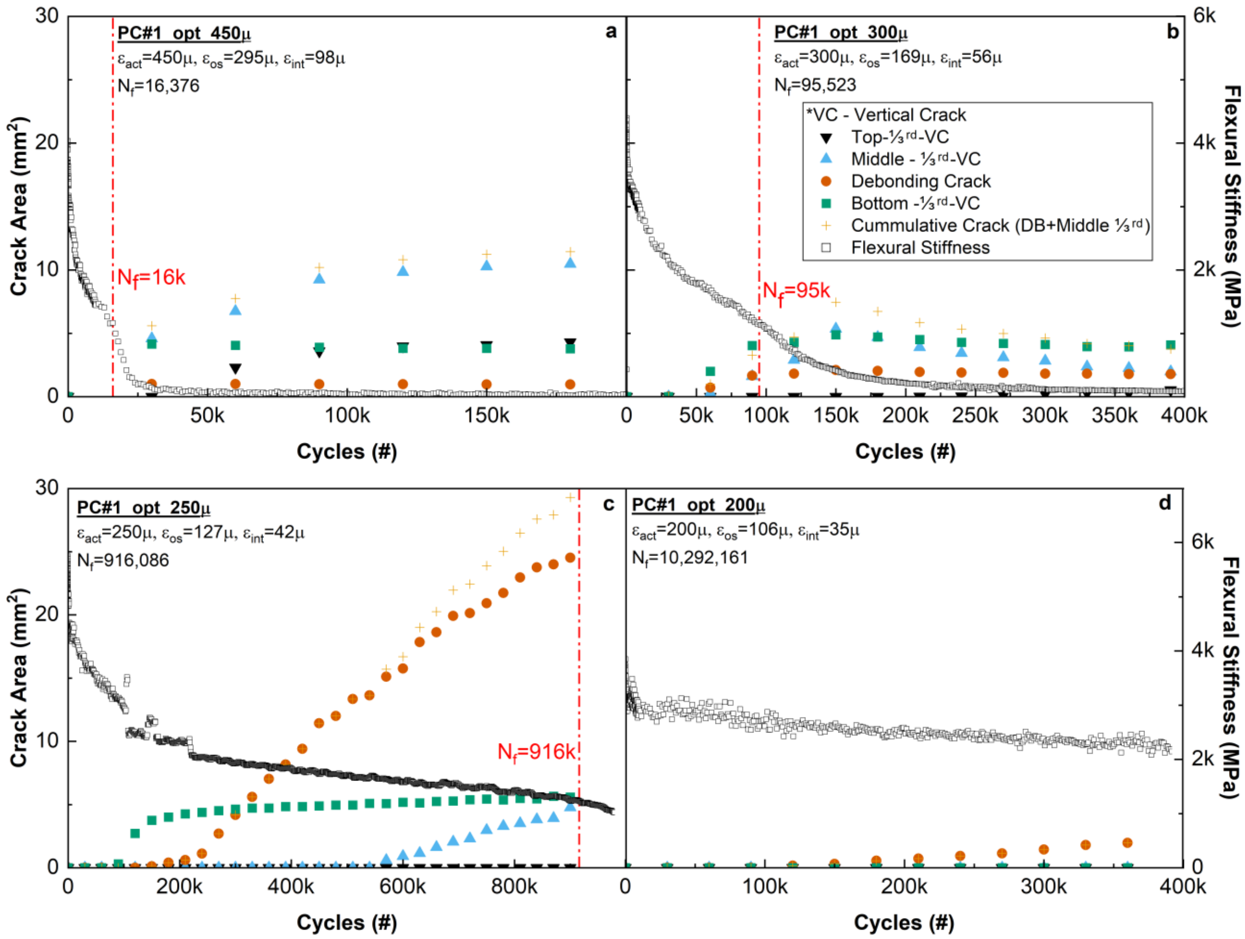

Figure 7-15. Cracked area measured during NBFTs of PC#1 specimens.

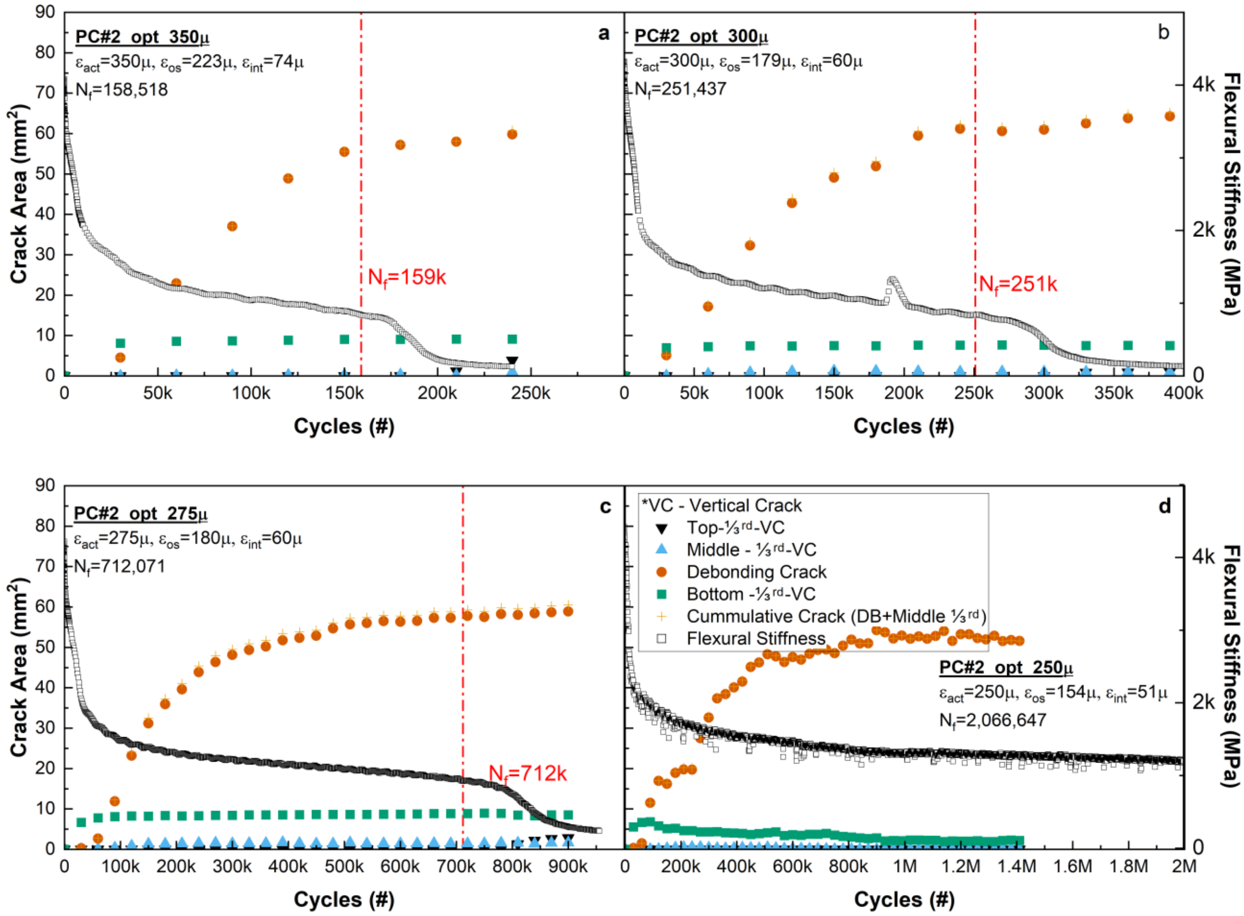

Figure 7-16. Cracked area measured during NBFTs of PC#2 specimens.

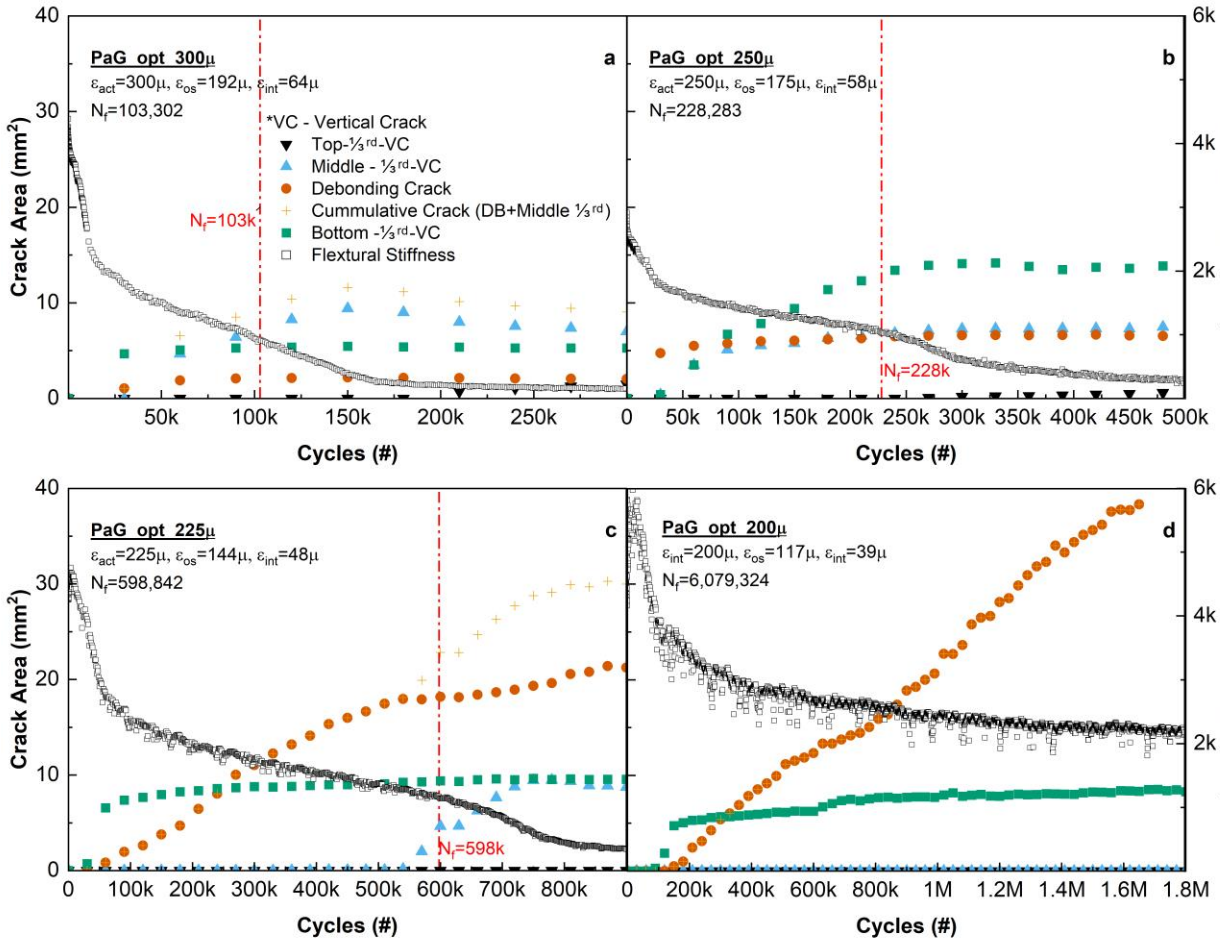

Figure 7-17. Cracked area measured during NBFTs of PaG specimens.

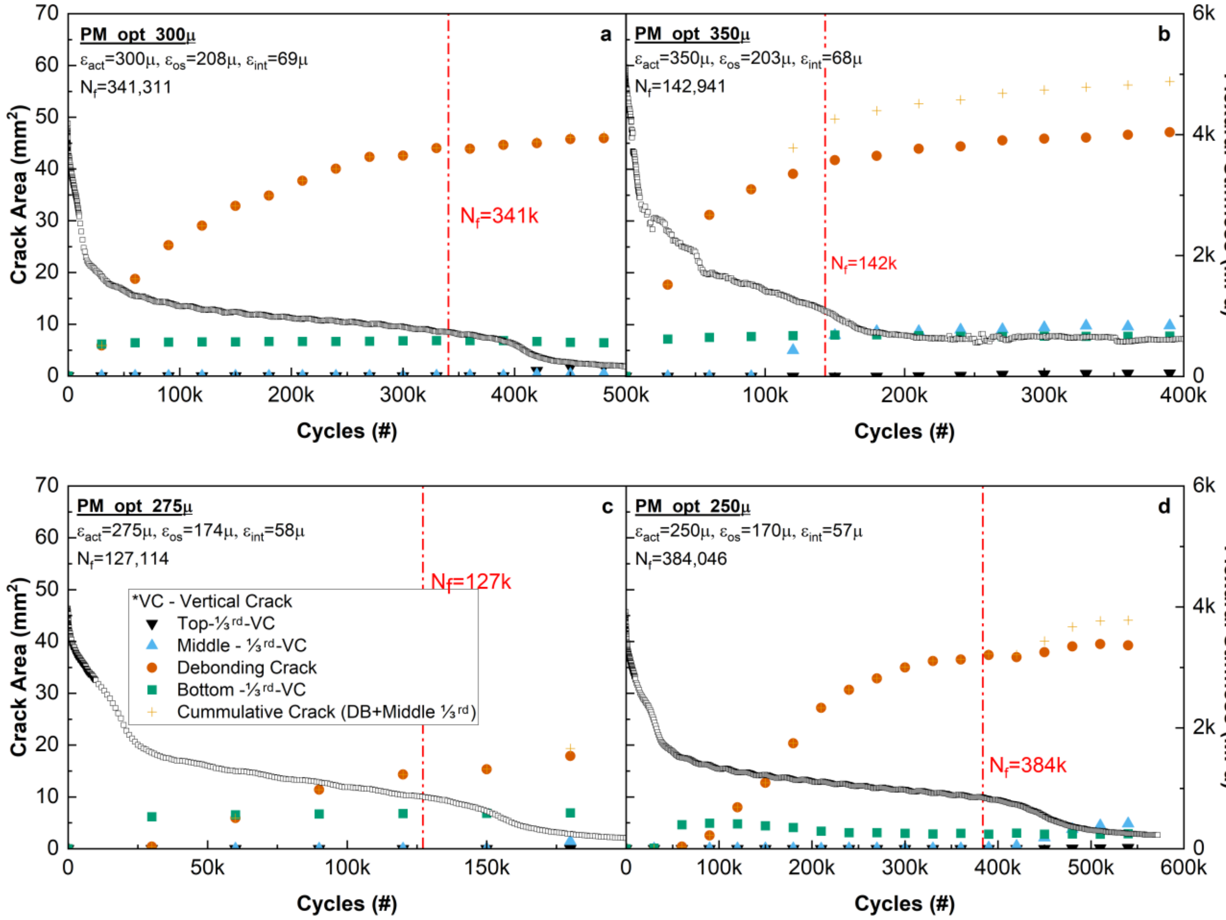

Figure 7-18. Cracked area measured during NBFTs of PM specimens.

Chapter 8. Development of Selection Criteria and Guidelines for Geosynthetic Products and Corresponding Tack Coats

This chapter discusses the research team's efforts to develop guidelines for both geosynthetic interlayer product selection and tack coat selection. The research elements required for the guidelines include:

- A predictive model to determine the crack resistance of different geosynthetic interlayer products. This model determines the fatigue life of an asphalt overlay that is reinforced with a geosynthetic interlayer using the tensile strain at the bottom of the overlay.
- A predictive model to determine the tensile strain at the bottom of asphalt overlay using the load-bearing capacity of the pavement layer under the overlay.
- A temperature correction model to predict FWD deflections at a reference temperature based on measured deflections at other temperatures.
- A predictive model to predict the ISS of geosynthetic-reinforced asphalt specimens as a function of temperature, shear strain rate, and confining pressure.
- A predictive model to predict the BBS as a function of temperature and loading rate.
- Determination of the shear stress in the asphalt layer using FlexPAVE™ whereby the shear stress at different temperatures, wheel loads, and pavement depths is calculated from moving load analysis using FlexPAVE™.
- The MSR failure envelope as a function of BBS and pavement depth. The ISS and BBS predictive models and the shear stress determined from FlexPAVE™ are used to develop the relationship between MSR and BBS as a function of pavement depth.
- Tack coat purchase criterion. Minimum allowable BBS values are developed for different geosynthetic products by applying the maximum MSR value of 0.7 to the MSR vs. BBS relationship.

The NCSU research team integrated these elements to develop guidelines for geosynthetic interlayer product selection and tack coat selection. The following sections discuss the research efforts undertaken to obtain each of these elements.

8.1 Development of Predictive Model for Crack Resistance Capacity

The crack resistance capacity of the different geosynthetic-reinforced beam specimens was measured using NBFTs carried out at different constant actuator tensile strain levels at 23°C (73°F). Typically, the crack resistance model is established between tensile strain and crack resistance. In NBFTs, tensile strain is measured at the underside of the beam specimen. However, in the field, the tensile strain of interest is at the interface/bottom of the overlay. Therefore, a relationship between interlayer tensile strain and crack resistance must be established for the beam crack resistance model. Knowing the location of the interlayer within the beam, the calculation of the interlayer tensile strain can be aided by the tensile strain at the bottom of the beam. For this study, the interlayer was installed at a depth that is one-third from the bottom of the beam. Assuming that linear elastic theory is valid for beam specimens during initial NBFT cycles, the initial interlayer tensile strain would be one-third of the initial tensile strain at the bottom of the beam. Analysis of the NBFT outcomes led to the relationship between interlayer tensile strain and crack resistance, presented here as Equation (8-1). Figure 8-1 shows the data points and the crack resistance model fit.

$$N_f = k_1 \left(\frac{1}{\varepsilon_t} \right)^{k_2} \qquad (8\text{-}1)$$

where

N_f = number of cycles to failure, representing crack resistance,
k_1, k_2 = regression coefficients, and
ε_t = tensile strain in microns.

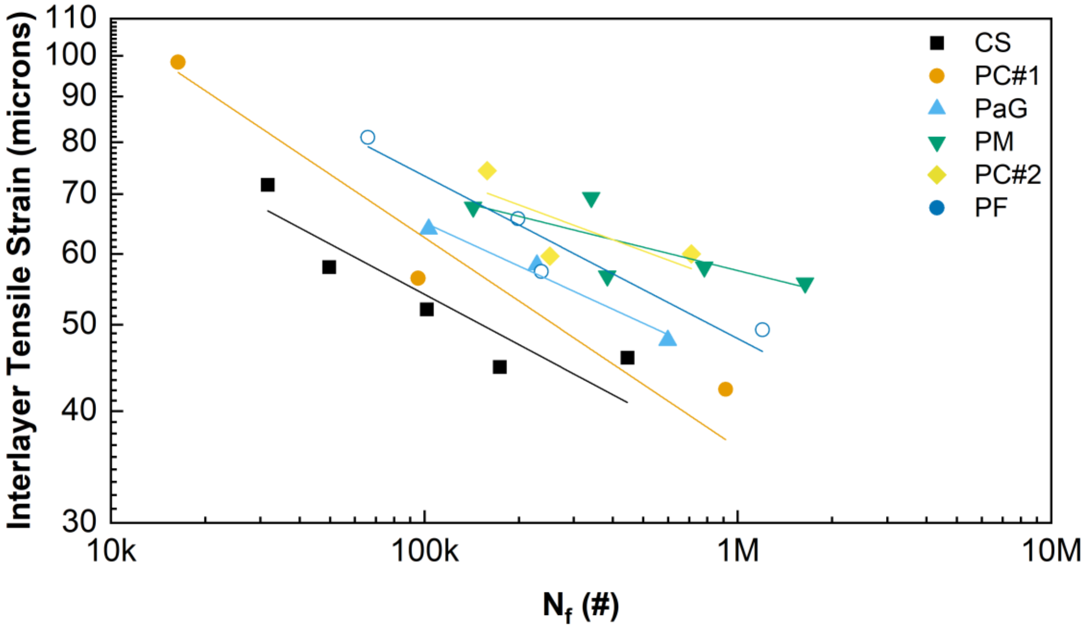

Figure 8-1. Crack resistance model showing relationship between tensile strain and NBFT failure cycle.

Table 8-1 presents the parameters k_1 and k_2 for the five geosynthetic products and the 'no interlayer' scenario (CS). Equation (8-1) and the k_1 and k_2 values in Table 8-1 are used to determine the crack resistance of asphalt overlays reinforced with different geosynthetic interlayer products. The results are used in developing the geosynthetic interlayer product selection guidelines, which is presented later in this chapter.

Table 8-1. Fatigue Coefficients of Interlayer Tensile Strain versus Number of Loading Cycles for Unreinforced and Reinforced Specimens

Interlayer Type	**CS**	**PC#1**	**PaG**	**PM**	**PC#2**	**PF**
k_1	1.47×10^{-18}	1.33×10^{-13}	9.83×10^{-22}	1.65×10^{-43}	1.32×10^{-27}	1.91×10^{-18}
k_2	5.35	4.25	6.21	11.50	7.72	5.49
R^2	0.78	0.90	0.95	0.42	0.1	0.89

8.2 Prediction of Tensile Strain at the Bottom of Asphalt Overlay

In Section 7.5, the DIC contours indicate that the failure mode (vertical cracking or debonding) depends on the type of geosynthetic interlayer and strain level. Also, the change in the failure mode of the beams that were reinforced with different geosynthetic interlayers that was observed as the strain level changed resulted in the transient tensile strain concept. This concept suggests that any overlay strain level above the transition tensile strain indicates vertical cracking and any overlay strain below the transition tensile strain indicates debonding.

In order to implement the transient tensile strain concept in the geosynthetic product selection guidelines, a predictive model for the tensile strain under the asphalt overlay is needed. This model must be based on the load-bearing capacity of the asphalt overlay and existing pavement and thus uses FWD deflections, the thickness and properties of the asphalt overlay, and the material type, thickness, and properties of the individual layers of the existing pavement as input parameters. The remainder of this section describes the research efforts that were undertaken to develop such a tensile strain predictive model.

Kim et al. (2000) demonstrated that the tensile strain at the bottom of an asphalt layer is closely related to the deflection basin parameters. Similarly, in this study, in order to develop the relationship between the tensile strain at the bottom of an overlay and the deflection basin parameters (SCI, BCI, and BDI), pavement response analysis using EverstressFE software for various thickness and modulus combinations (~1500 combinations) was carried out, as described in Section 4.4. The deflection basin parameters were calculated for sections without an overlay. Three overlay thicknesses were simulated for each section to measure the tensile strain underneath the overlay. Further, linear regression was carried out by selecting the overlay tensile strain as the 'Y-range' against the 'X-range' parameters of the $T_{overlay}$, SCI, BDI, BCI, and $E_{sg}{\times}T_{eq}$. The measured coefficients were used to develop.

$$\begin{aligned}\varepsilon_{t-overlay} = {} & 575\times\log\left(E_{sg}\times T_{eq}\right)+1034\times\log\left(\mathrm{SCI}\right)-1346\times\log\left(\mathrm{BDI}\right)+1136\times\log\left(\mathrm{BCI}\right)\\ & +115\times T_{overlay}-3539\end{aligned} \tag{8-2}$$

$$(E_{sg}\times T_{eq}) = 78683+7503965\times e^{\left(\frac{\mathrm{BCI}}{-0.3827}\right)}+698559\times e^{\left(\frac{\mathrm{BCI}}{-2.459}\right)} \tag{8-3}$$

where

SCI = $D_0 - D_{12}$, surface curvature index (mils),

BDI = $D_{12} - D_{24}$, base damage index (mils),

BCI = $D_{24} - D_{36}$, base curvature index (mils),

D_0, D_{12}, D_{24}, and D_{36} = deflections at distances of 0, 12, 24, and 36 inches from the center of the FWD loading plate, respectively,

$T_{overlay}$ = thickness of the overlay (in.),

T_{ac} = thickness of asphalt concrete layer (in.),

T_{abc} = thickness of aggregate base course (in.),

$T_{eq} = T_{(ac)eq} + T_{(abc)eq} = T_{ac}\sqrt[3]{\frac{E_{ac}}{E_{sg}}} + T_{abc}\sqrt[3]{\frac{E_{abc}}{E_{sg}}}$,

T_{eq} = equivalent thickness (in.) of pavement structure in terms of subgrade modulus,

E_{ac} = Young's modulus of asphalt concrete layer (psi),

E_{abc} = Young's modulus of aggregate base course (psi), and

E_{sg} = Young's modulus of subgrade (psi).

$E_{sg} \times T_{eq}$ was calculated with the help of Odemark's 'method of equivalent thickness'. In this method, all layer thicknesses of a pavement section are transformed into an equivalent thickness of a single layer that has the subgrade modulus. Figure 8-2 presents a schematic representation of this process, known as Odemark's method of thickness equivalency. Thus, the numerically simulated sections (without overlay) can be represented by a unique $E_{sg} \times T_{eq}$ that captures the damage condition of the pavement. Figure 8-3 shows a strong relationship between $E_{sg} \times T_{eq}$ and the BCI. The exponential function shown in Equation (8-3) fits the data well. Thus, the term $E_{sg} \times T_{eq}$ in Equation (8-2) is calculated using Equation (8-3).

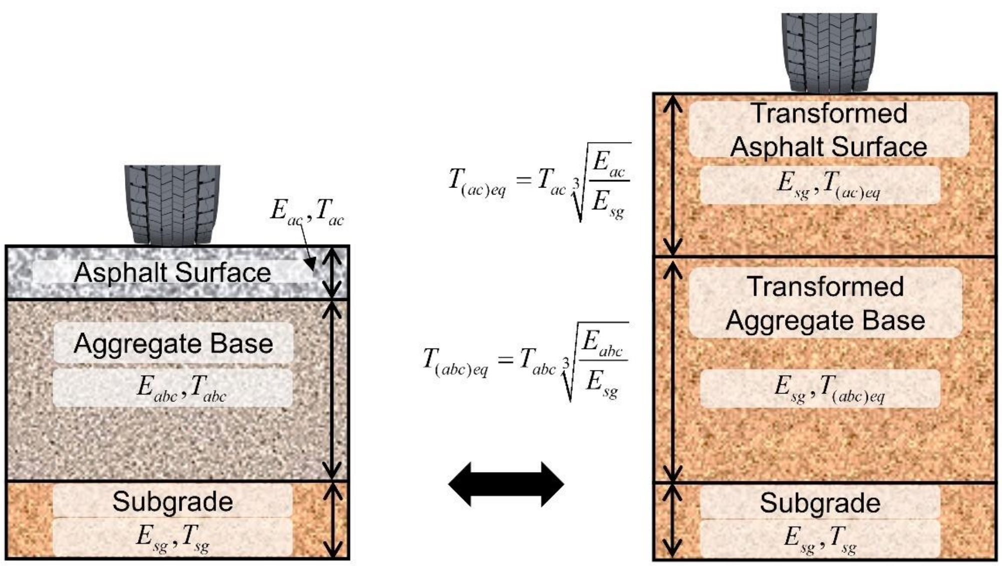

Figure 8-2. Odemark's concept of equivalent thickness calculation.

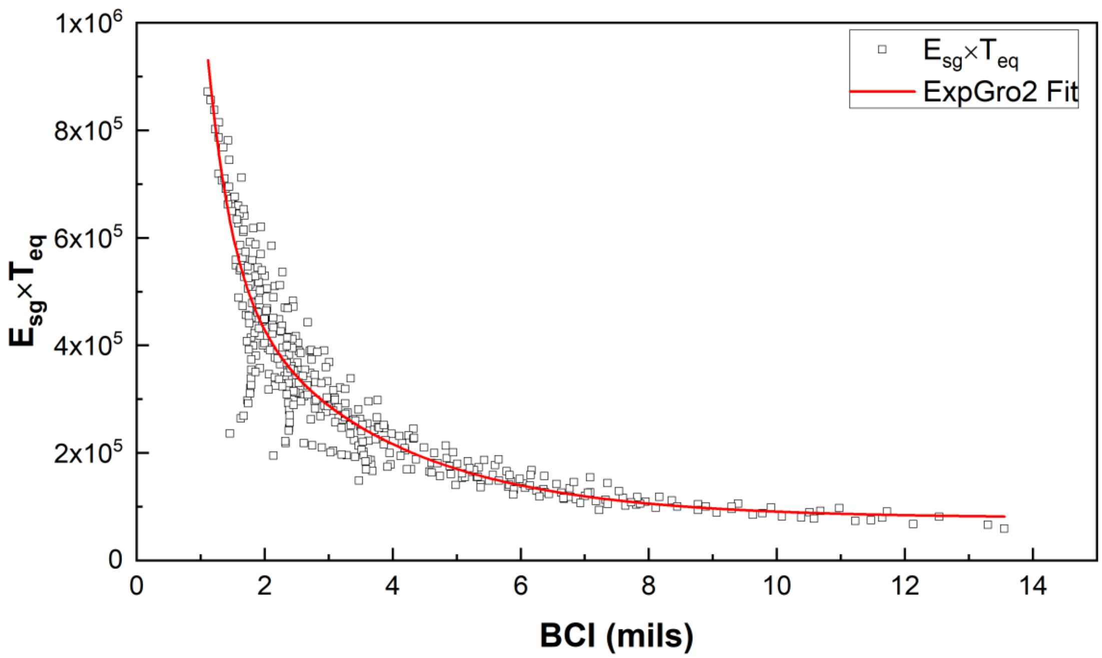

Figure 8-3. Relationship between $E_{sg} \times T_{eq}$ and BCI.

Equations (8-2) and (8-3) allow the prediction of the tensile strain at the bottom of the overlay ($\varepsilon_{t\text{-}overlay}$) using FWD deflections from the existing pavement and the thickness of the overlay ($T_{overlay}$). Figure 8-4 presents the predicted and measured overlay tensile values measured using Equation (8-2). Further investigation using measured values from the field is recommended to validate the accuracy of the predictive equation.

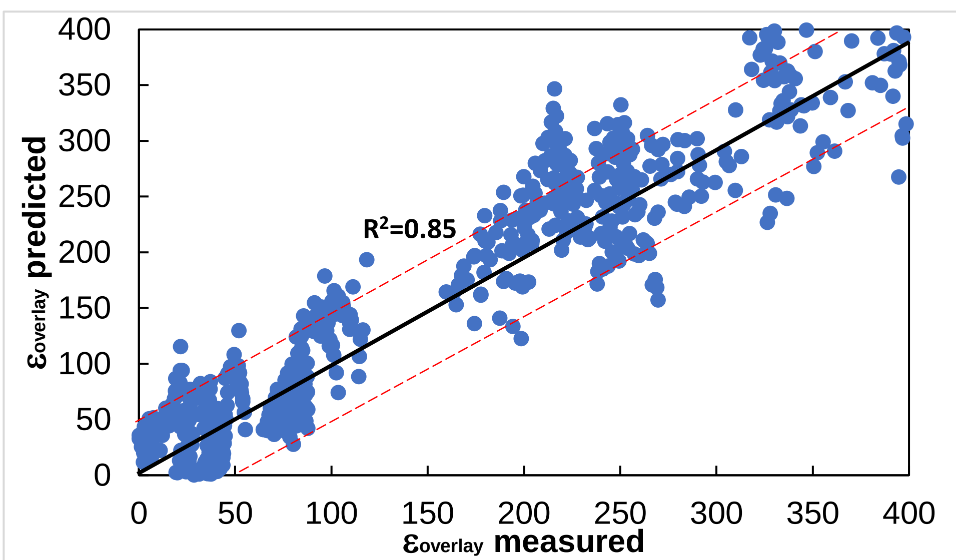

Figure 8-4. Predicted and measured overlay tensile strain using Equation (8-2).

8.3 Temperature Correction for Deflections at Radial Offset Distance

The FWD deflections measured at a specific temperature must be corrected to the reference temperature of 23°C (73.4°F), as the proposed prediction Equation (8-2) was developed assuming that the temperature is 23°C. The temperature correction factor is calculated as the ratio of the measured deflection at a specific temperature (*T*) to the deflection at a reference temperature, which in this case is 23°C (73.4°F).

Kim et al. (1997) proposed a deflection correction model shown in Equation (8-4) based on their statistical analyses of measured deflections and temperatures in North Carolina. The deflection correction factor (λ_w) for center deflections measured under a 9-kip FWD load can be expressed as Equation (8-5).

$$\lambda_w = \frac{w_{T_0}}{w_T} \tag{8-4}$$

where

w_{T_0} = deflection corrected to temperature T_0,

w_T = deflection at temperature T, and

λ_w = temperature correction factor.

$$\lambda_w = 10^{-C(H_{ac})(T-T_0)} \tag{8-5}$$

where

H_{ac} = asphalt concrete layer thickness (in.), and

C = regression constant.

To provide temperature correction factors at various offset distances, an empirical model was developed based on statistical analysis of the temperature deflection data. Because the degree of the temperature dependency of a deflection linearly decreases as the radial distance increases, the *C* value at a given offset distance may be determined using Equation (8-6).

$$C = -Ar + C_0 \tag{8-6}$$

where

r = radial distance from center of load plate (in.), and

C_0 and A = regression constants, which are different for three regions.

Table 8-2. C_0 and A Values for Each North Carolina Region and Statewide Values

Regions	C_0 values	Statewide C_0 value	A value	Statewide A value
East	3.61×10^{-5}	4.65×10^{-5}	-5.72×10^{-8}	-5.47×10^{-8}
Central	5.80×10^{-5}		-5.62×10^{-8}	
West	4.32×10^{-5}		-5.07×10^{-8}	

Kim et al. (1997) reported that the corrections appear to work well except for the last FWD sensor. At a radial distance of 60 in., the deflection at a low temperature is greater than at a high temperature. This phenomenon is thought to be due to the reduction in stiffness of the AC layer at high temperatures, which in turn reduces the lateral spread of the stress distribution.

8.4 Development of Geosynthetic Product Selection Guidelines Based on Performance

The findings discussed in Sections 8.1, 8.2, and 8.3 were used to develop geosynthetic product selection guidelines. Figure 8-5 presents a flow chart of the research approach that was taken to develop these guidelines based on the geosynthetic products' ability to resist reflective crack propagation. Sudarsanan et al. (2018, 2020a) reported a similar approach to measure geosynthetic reinforcement performance in terms of an improvement factor (IF) with reference to the no-interlayer condition. The outcomes of this research approach are the rankings of the various geosynthetic products in terms of the load-bearing capacity of the existing pavement for the overlay project and the expected mode of failure in the field, i.e., debonding or vertical reflective cracks.

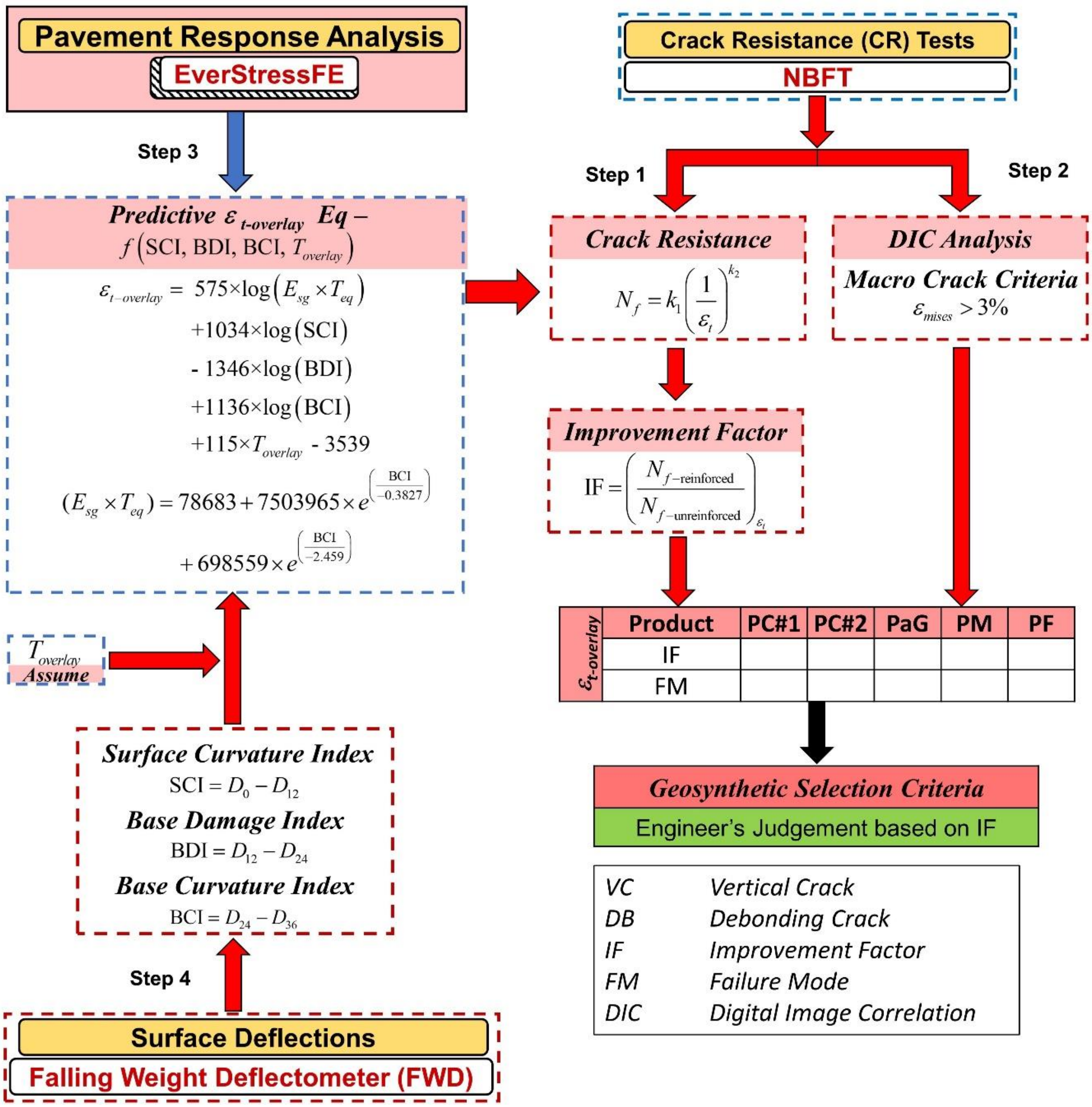

Figure 8-5. Flow chart of research approach to develop geosynthetic product selection guidelines.

8.5 Development of Predictive Model for Interface Shear Strength

The research team's efforts to develop a universal relationship between ISS and BBS for different tack coat materials are described as follows. In order to compare ISS and BBS, the initial step was to develop a prediction equation for ISS. The test parameters that govern the ISS prediction equation are the reduced strain rate (a combination of temperature and loading rate) and confining pressure. The prediction equation follows the same form proposed in the NCDOT HWY 2013-04 research project, presented here as Equation (8-7).

$$\tau_f = (a_I \times \dot{\gamma}_R^{b_I} + e_I) \times \sigma_c + c_I \times \dot{\gamma}_R^{d_I} \tag{8-7}$$

where

τ_f = ISS, kPa,

$\dot{\gamma}_R$ = reduced shear strain rate,

σ_c = normal confining stress, kPa, and

a_I, b_I, c_I, d_I, *and* e_I = material parameters.

The research team conducted fitting analysis of the data presented in Table 8-3 using MATLAB software. The corresponding coefficients a_I, b_I, c_I, d_I, and e_I of the prediction model presented in Equation (8-7) are shown in Table 8-3 for the different geosynthetic-reinforced interface conditions. Note that the two values for b_I in Table 8-3 have a minus sign, which indicates the opposite trend of a decrease in ISS as the reduced strain rate increases. However, the effect of the reduced strain rate on ISS is reflected through both b_I and d_I. The d_I value with a positive sign is much higher than the b_I value with a negative sign, and therefore, the overall effect of the reduced strain rate on ISS is correctly represented (i.e., an increase in the reduced strain rate results in an increase in ISS) according to the coefficient values shown in Table 8-3.

Table 8-3. Coefficients of Interface Shear Strength Prediction Equation for Different Asphalt Layer Interface Conditions at Reference Temperature of 35°C

Geosynthetic Type	Interface Shear Strength Model Coefficients					
	a_I	b_I	c_I	d_I	e_I	R^2
CS	4.679	12.72	1203	0.1112	1.24	0.95
PC#1	155.9	2.4	980.3	0.1372	0.5325	0.95
PC#2	18.35	15.73	787.8	0.1958	0.8114	0.90
PM	12.57	16.73	1152	0.2176	0.7194	0.82
PaG	7.659	20	1809	0.2811	1.294	0.93
PF	3.019	0.6974	453.2	0.07948	0.587	0.95

8.6 Development of Predictive Model for Binder Bond Strength

Based on PATTI test results, BBS mastercurve for the PG64-22 tack coat was constructed. Details regarding this procedure can be found in Sudarsanan et al. (2020b). In order to avoid extensive time and effort to test the tack coats at 13 different temperatures, a two-point analysis method was developed and applied in this study. For this method, PATTI tests are carried out at two temperatures, preferably both above 30°C (86°F) to avoid adhesive failure. The shift factors obtained from DSR test results are applied to the two calculated stress rates to measure the reduced stress rates that correspond to the test temperatures. Equation (8-8) expresses the typical power-form predictive equation for BBS. Table 8-4 presents the coefficients measured after fitting the BBS test data based on the two-point method.

$$\sigma_t = a_B \dot{\sigma}_R^{\,n_B} \tag{8-8}$$

where

σ_t	=	BBS,
$\dot{\sigma}_R$	=	reduced stress rates, and
a_B, n_B	=	material parameters.

Table 8-4. Coefficients of Binder Bond Strength Prediction Equation for PG 64-22 Tack Coat

Tack Coat	BBS Test Results		
	a_B	n_B	R^2
PG 64-22	155.7	0.268	0.88

8.7 Identification of Interface Debonding Potential for Tack Coats Based on Numerical Simulation

Field observations of interface debonding failure indicate that, in most cases, debonding occurs due to shearing. Therefore, the debonding potential at the interface is quantified by the shear ratio, which is defined as the ratio of shear stress (τ_{max}) to shear strength (τ_s). Shear stress is a function of the speed and weight of a vehicle, temperature, pavement structure, and depth of the layer interface. Equation (8-7) shows that shear strength is a function of the reduced strain rate (which is a combined parameter of temperature and strain rate) and confining pressure. Therefore, the shear strength at the interface can be determined from the laboratory-developed Equation (8-7) by inputting the temperature at the interface, the strain rate at the interface that can be determined from pavement response analysis, and the confining pressure, which is the normal stress at the interface that also can be determined from pavement response analysis. That is, by using Equation (8-7) and the shear stress and strain at the layer interface calculated from pavement response analysis, the shear ratio can be determined at various locations along the pavement interface under various conditions, e.g., vehicle weight and speed, and temperature. The location and magnitude of the maximum shear ratio, or MSR, then can be determined using a computed profile of the shear ratio under the tire at the AC layer interface. Theoretically, a higher MSR value indicates greater debonding potential. Figure 8-6 presents an example to determine the MSR for a pavement interface at a depth of 1.5 in. (3.81 cm) under the centerline of one tire (out of a dual tire configuration) in the longitudinal direction. The simulation condition is a dual tire, single-axle vehicular load of 80 kN under the braking condition while moving at a speed of 1 mph at an isothermal temperature of 50°C.

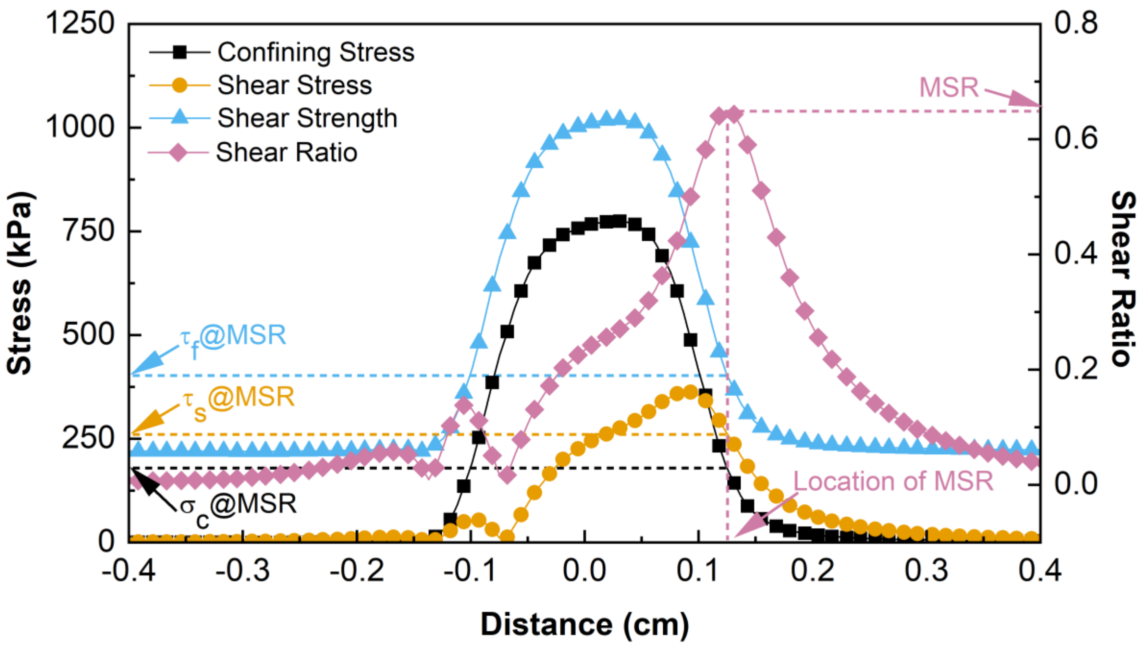

Figure 8-6. Shear ratio, shear strength (CRS-2 (Source1)), and shear and normal stress levels in longitudinal direction under the central axis of tire at layer interface to determine maximum shear ratio (MSR).

The ISS (τ_f) for each point on the layer interface under consideration was computed from the prediction model equation, Equation (8-7). The material coefficients for the various tack coats obtained by fitting Equation (8-7), reported in Table 8-3, enable the prediction of the ISS for an AC layer with a specific tack coat material at the layer interface. The ISS prediction model allows the ISS to be evaluated at any point on the layer interface for any shear strain rate and temperature combination as well as at any confining pressure (i.e., normal stress in the pavement analysis) level. The normal stress and shear strain rates required to determine the ISS at any point along the layer interface for a tack coat material were computed from the pavement response analysis carried out using FlexPAVE™. The normal stress (σ_{zz}) along the layer interface (each data point is the stress at a mesh node present at the interface), as shown in Figure 8-6, was determined for the worst field condition (1 mph, 50°C, 1.5 in.) considered for this study. The maximum shear stress and shear strain at each point of interest were computed using Equations (8-9) and (8-10), respectively.

$$\tau_{\max} = \tau_s = \sqrt{(\tau_{xz})^2 + (\tau_{yz})^2} \tag{8-9}$$

$$\gamma_{\max} = \gamma_s = \sqrt{(\gamma_{xz})^2 + (\gamma_{yz})^2} \tag{8-10}$$

where

τ_{xz} = shear stress in the transverse direction under the tire,

τ_{yz} = shear stress in the longitudinal direction under the tire,

γ_{xz} = shear strain in the transverse direction under the tire, and

γ_{yz} = shear strain in the longitudinal direction under the tire.

The shear stress and strain levels in the longitudinal (τ_{yz} and γ_{yz}) and transverse (τ_{xz} and γ_{xz}) directions were determined using FlexPAVE™. Further, the shear stress and strain were computed using Equations (8-9) and (8-10), respectively. The shear strain (γ_S) history as a function of time was then used to compute the shear strain rate, as presented in Figure 8-7. The difference in the maximum shear strain and strain at zero time is the strain amplitude (a). The slope of the linear fit over the data set, ranging from 0.4 times the strain amplitude to the maximum shear strain, gives the shear strain rate ($\dot{\gamma}_s$).

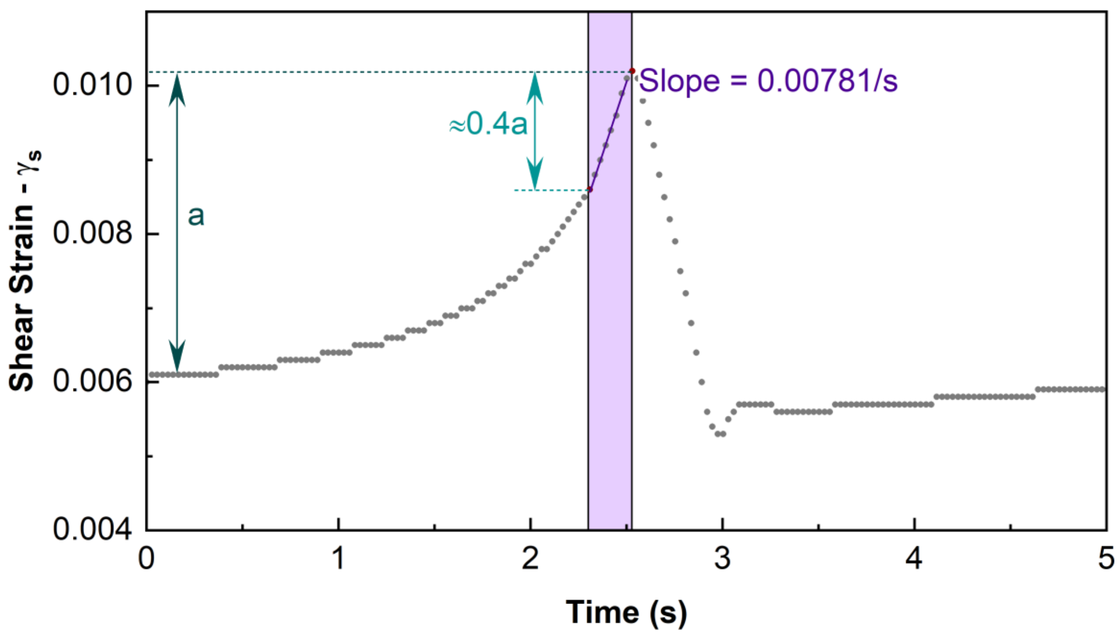

Figure 8-7. Typical interface layer shear strain history.

Once the shear strain rate and confining pressure at the layer interface are known, the shear strength can be computed. The shear stress over the computed shear strength at each mesh node gives a potential debonding factor (the shear ratio) along the layer interface. The point along the layer interface that has the greatest potential to debond is tagged as the MSR. Typically, this MSR point is found in front of the centerline of the tire in the longitudinal direction. The distance from the edge of the tire to the MSR point typically ranges from 0.1 cm to 0.14 cm depending on the simulation conditions and tack coat.

Similarly, the shear stress (τ_S) history as a function of time was used to compute the shear stress rates, as presented in Figure 8-8. The stress amplitude (a) is the difference between the maximum shear stress and the stress at zero time. The slope of the linear fit over the data set, ranging from 0.7 times the stress amplitude to the maximum shear stress, gives the shear stress rate ($\dot{\tau}_s$). This shear stress rate is used to predict the BBS at the layer interface. The confining pressure does not have any effect on the predicted BBS.

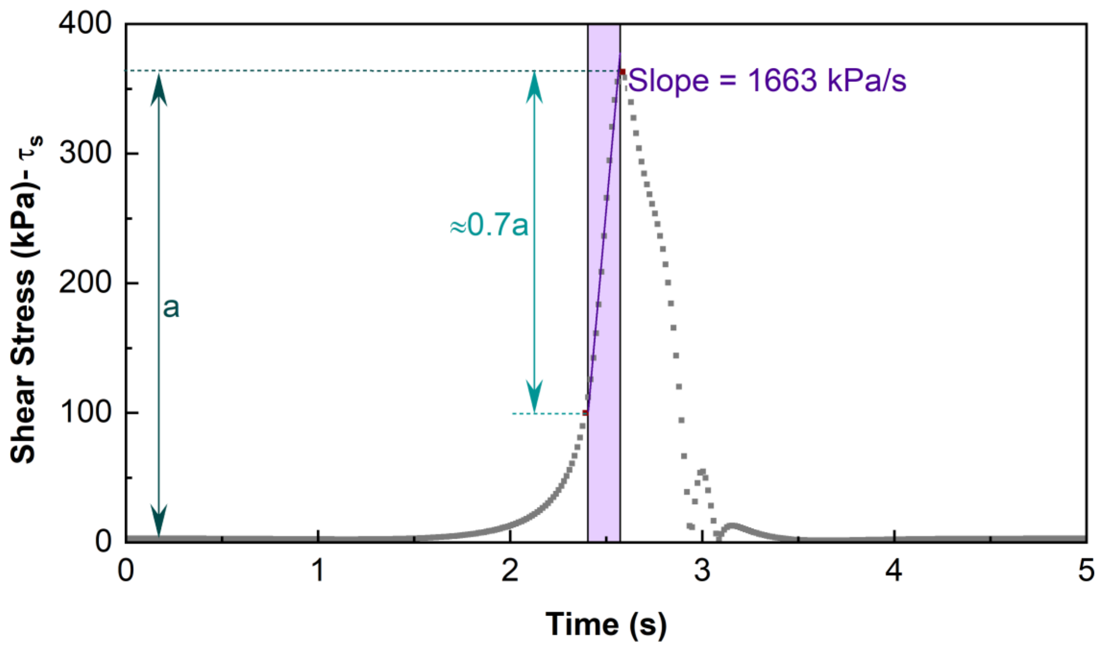

Figure 8-8. Typical interface layer shear stress history.

Figure 8-9 shows the shear ratio distribution under dual tires at the interface. For the specific conditions considered in this study, the MSR is located at a point in front of the tire along the center-line of the tire, as shown in Figure 8-9 (c) and (d). PM shows a higher MSR than PC#1-reinforced pavements, which indicates that PM-reinforced pavement is more likely to experience debonding failure.

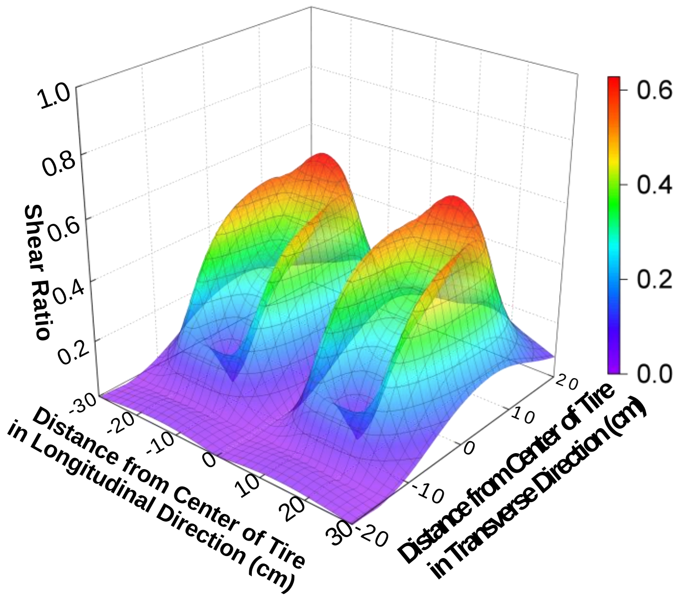
1.0
0.8
0.6
0.4
0.2
Shear Ratio
0.6
0.4
0.2
0.0
-30
-20
-10
0
10
20
30
Distance from Center of Tire
in Longitudinal Direction (cm)
-20
-10
0
10
20
Distance from Center of Tire
in Transverse Direction (cm)

(a)

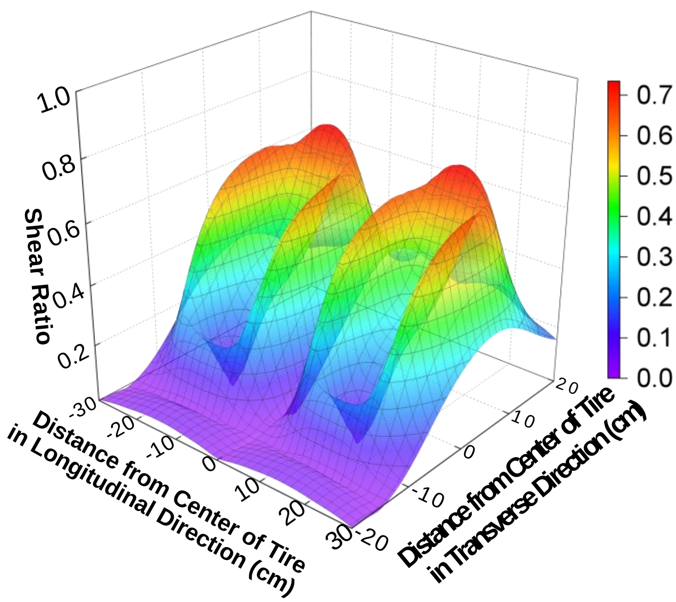
1.0
0.8
0.6
0.4
0.2
Shear Ratio
0.7
0.6
0.5
0.4
0.3
0.2
0.1
0.0
-30
-20
-10
0
10
20
30
Distance from Center of Tire
in Longitudinal Direction (cm)
-20
-10
0
10
20
Distance from Center of Tire
in Transverse Direction (cm)

(b)

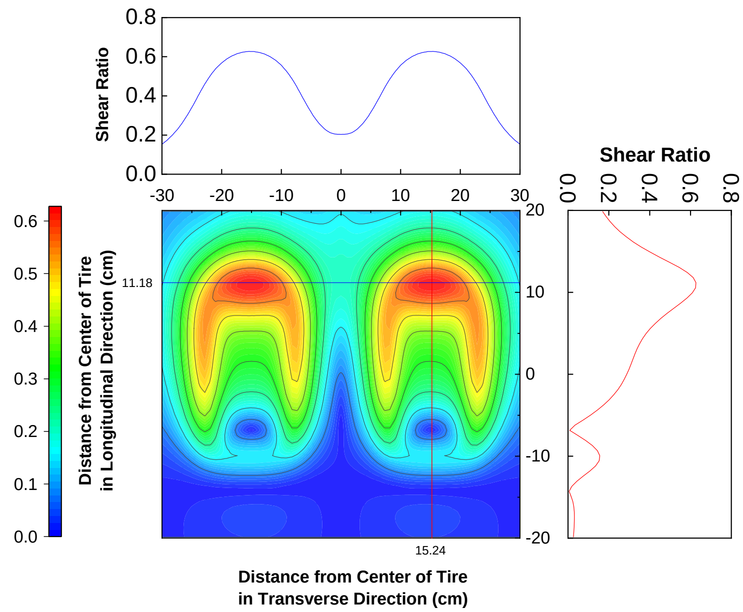

(c)

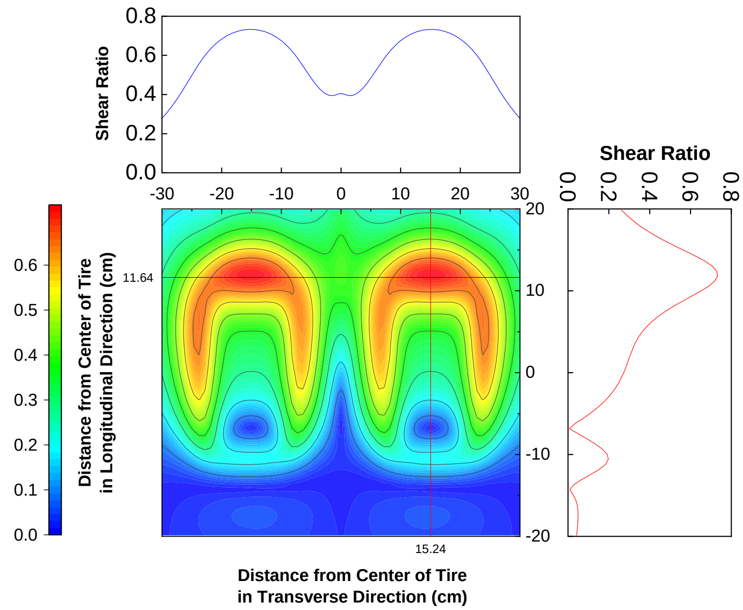

(d)

Figure 8-9. Shear ratio distribution under dual tires: (a) PC#1 results in 3-D, (b) PM results in 3-D, (c) PC#1 results in 2-D, and (d) PM results in 2-D.

8.8 Developing the Maximum Shear Ratio Failure Envelope

A universal relationship between ISS and BBS was found during the RP 2018-13 project, *Development of a Tack Coat Quality Control Program for Mitigating Delamination in Asphalt Pavement Layers*, which was undertaken to control the debonding distress (Kim et al. 2021). A similar approach was followed in the current study to determine the minimum tack coat BBS values for the different geosynthetic interlayer products. The end result of this approach is the minimum BBS value that serves as the criterion for acceptance of the tack coat that corresponds to a specific paving geosynthetic product. Figure 8-10 presents a flow chart of the research approach that was taken to develop the tack coat selection guidelines.

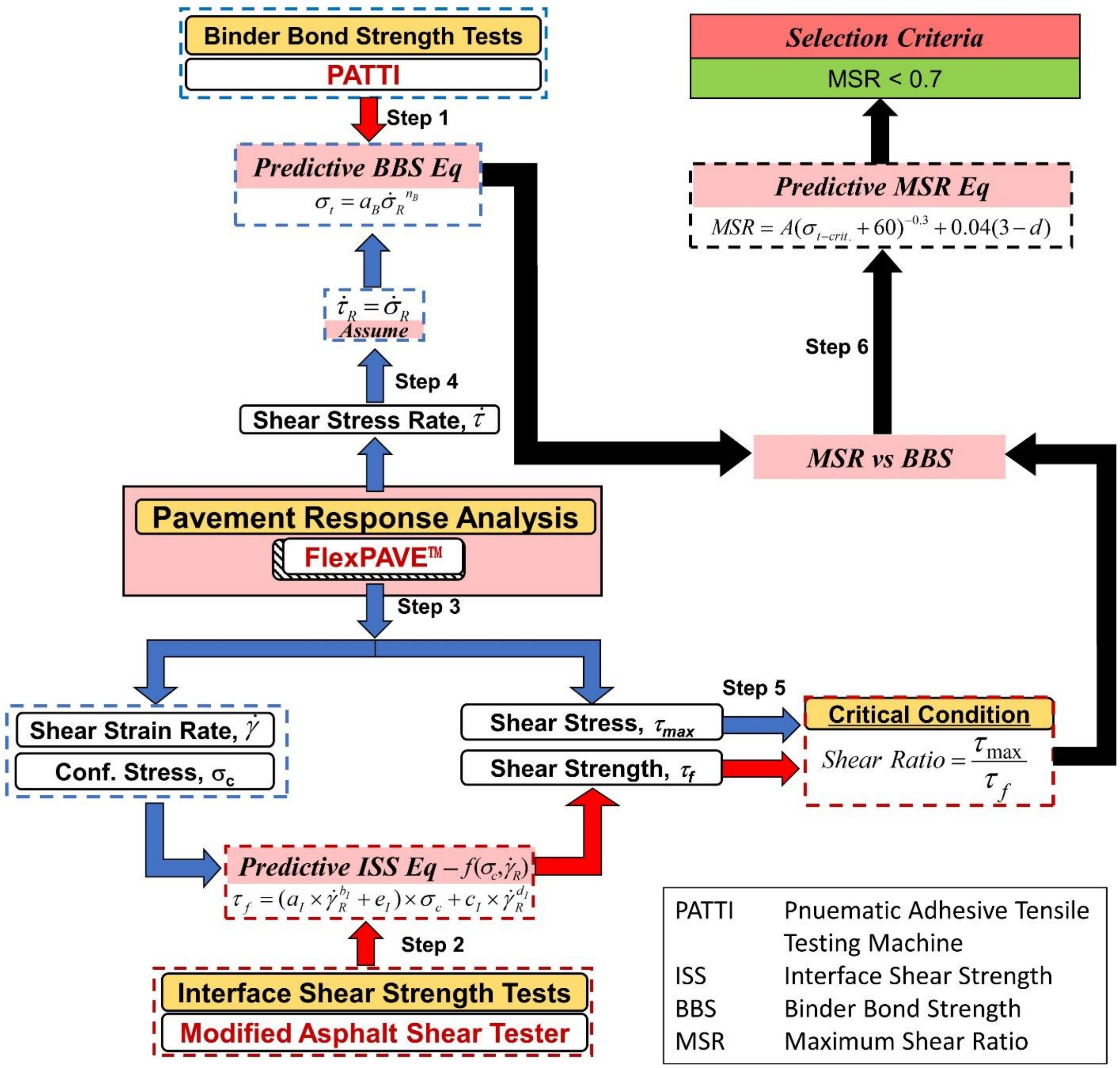

Figure 8-10. Flow chart of research approach taken to develop tack coat selection guidelines.

Further to establishing a universal relationship between ISS and BBS, the corresponding MSR and BBS for each specific numerical simulation condition were computed for the various geosynthetic-reinforced products. Figure 8-12 shows the computed MSRs and predicted BBS values for the layer interface at 3 in. depth during vehicle braking at a driving speed of 45 mph at the pavement temperature of 50°C. The multiple data points shown in Figure 8-12 for a specific tack coat or geosynthetic material at 3 in. depth represent the MSR and BBS values at different vehicle speeds during the vehicle's deceleration from 45 mph to a standstill (Figure 8-11). The speeds considered for the analysis during deceleration are 20 mph, 10 mph, 5 mph, 3 mph, and 1 mph. In Figure 8-12, the highest MSR corresponds to 1 mph, and the lowest MSR corresponds to 45 mph for a specific tack coat or geosynthetic material.

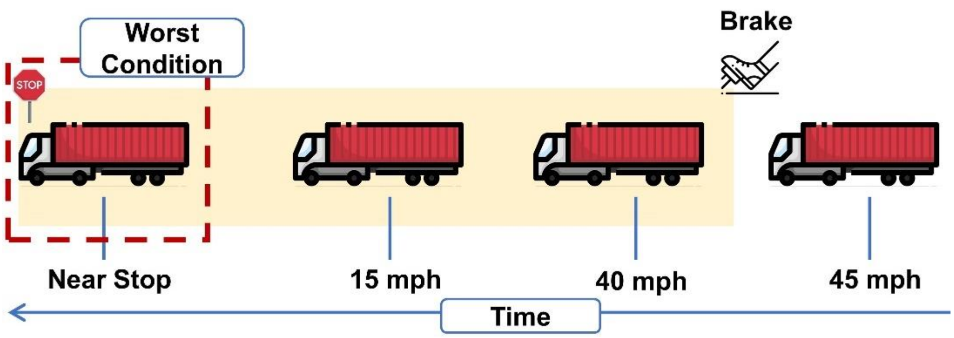

Figure 8-11. A schematic depicting the braking event that leads to the worst condition causing debonding.

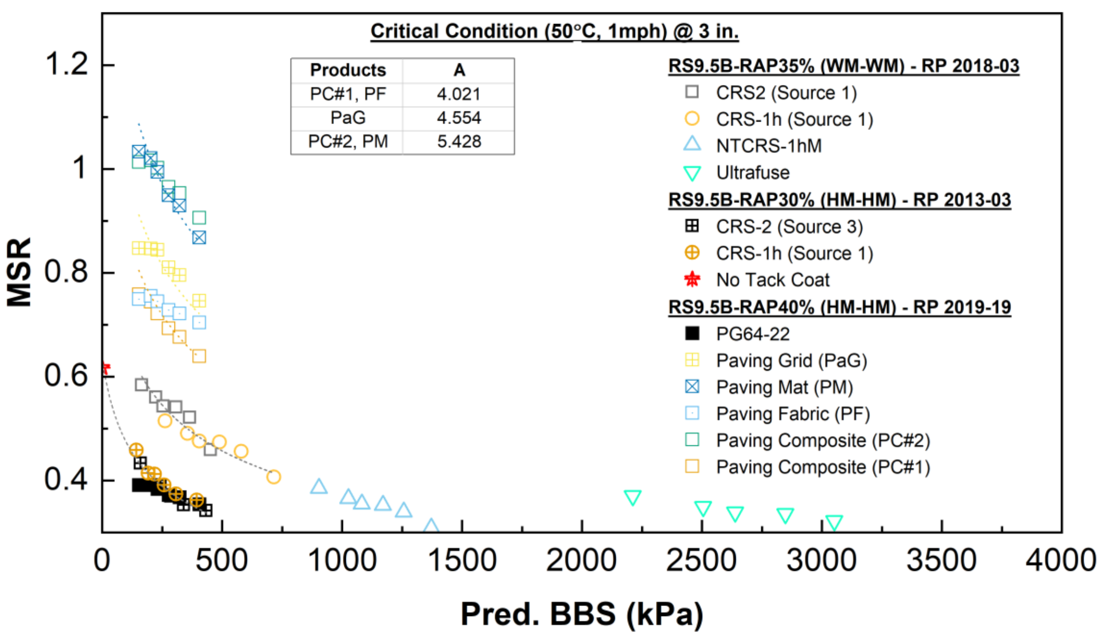

Figure 8-12. Maximum shear ratio (MSR) failure envelope for different mixtures.

The Belehradekit mathematical model was fitted over the available data to create the MSR failure envelope, as shown in Figure 8-12. The generic form of the Belehradekit mathematical model is shown here as Equation (8-11). However, in the case of the warm mix (WM in the figure), the fitting was carried out over the data sets for CRS-2 (Source 1) and CRS-1h only. The data computed for the tack coat, NTCRS-1hM, were left to verify the MSR predictive equation. While fitting the data sets, the material parameters *b* and *c* were fixed to -60 and -0.3, respectively, to create a universal relationship between the two tack coats. Even then, the fitted trend line shows an R^2 value that ranges from 0.9 to 0.97. This exercise helped to generalize the MSR predictive equation, and the independent material parameters that influence the MSR are coefficient *A* and the BBS. Note that the intercept of each trend line in Figure 8-12 at the 'no tack coat' condition (BBS = 1) depends on the mixture type, which indicates that the MSR is not only a function of the depth and BBS but also of mixture type. However, in the case of geosynthetic-reinforced AC mixes, the effect of the mix is negligible, as the interface response is much more dependent on the product and tack coat type than on the mixture type. The thickness of the geosynthetic products and the high tack coat application rate at the interface also contribute to the negligible effect of the mix type.

$$y = A(x-b)^c \tag{8-11}$$

Also, as the depth increases, the MSR value decreases for the same loading condition. The reduction in shear stress with an increase in depth is attributed to the reduction in the MSR. Figure 8-13 shows the effect of depth on the MSR of various tack coats. The MSR value changes by 0.04 per unit depth change (in.).

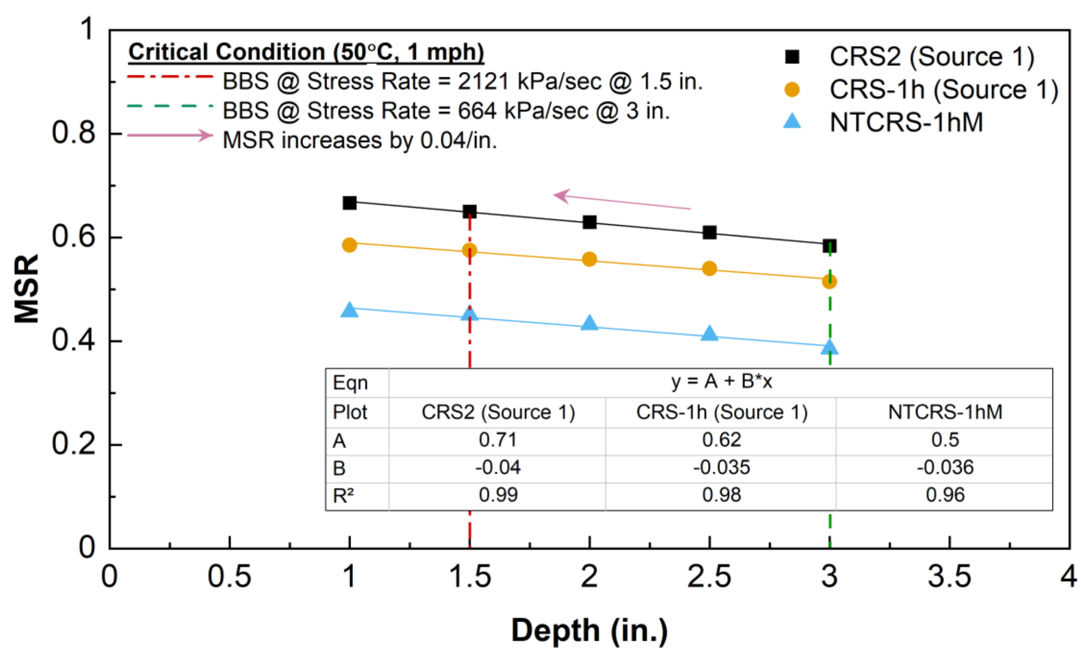

Figure 8-13. Change in maximum shear ratio (MSR) with depth (in.).

The BBS measured at the critical condition of 50°C and 1 mph corresponds to the stress rate of 2121 kPa/s at 1.5 in. and the stress rate of 664 kPa/s at 3 inches. A typical BBS test can be conducted between 620 kPa/s and 792 kPa/s with utmost care. In order to match the stress rate from a typical BBS test with that from the critical condition, an MSR predictive equation for 3-in. depth is used. Then, an additional term that represents the effect of depth on the MSR is used to predict the MSR at any depth. The resulting equation, shown here as Equation (8-12), expresses a universal relationship between BBS and the MSR, referred to as the MSR failure envelope.

$$MSR = A(\sigma_{t-crit.} + 60)^{-0.3} + 0.04(3 - d) \tag{8-12}$$

where

A	=	asphalt concrete mix parameter for tack coat only condition, or geosynthetic product parameter.
$\sigma_{t-crit.}$	=	BBS (kPa) at 50°C and stress rate of 690 kPa/s (100 psi/sec), and
d	=	depth of interface from the asphalt surface (in.).

8.8.1 Measuring Mix Parameter *A*

The material parameter *A* represents the MSR-BBS relationship for the mixture type in the pavement layer in question with any tack coat type. However, in the case of geosynthetic-reinforced AC, the effect of the mix type on the interface is negligible due to the thickness of geosynthetic products and the high tack coat application rate. Therefore, only two methods are recommended to measure mix parameter *A*. The first method is the rigorous experimental method that was followed during this study that requires more effort and time but provides high accuracy. However, this exercise is a single event and occurs only when a new product is launched; hence, the manufacturer or DOT could repeat the same procedure to evaluate the material parameter. The second method is to use the standard values that were obtained for the different types of geosynthetic products during this study. Table 8-5 presents the material parameter *A* values for the different geosynthetic products.

Table 8-5. Material Parameter *A* for Different Geosynthetic Products

Geosynthetic Products	*A* (at 3-in. depth)
PC#1, PF	4.021
PaG	4.554
PC#2, PM	5.428

8.8.2 Measuring Binder Bond Strength

The BBS is an important property of tack coat materials and is central to the proposed tack coat quality assurance method. Three levels of accuracy can be used to determine the BBS, with Level 3 being the simplest but least accurate method and Level 1 being the most accurate method.

Level 3: Single BBS test

A typical BBS test can be conducted between 620 kPa/s and 792 kPa/s. If the user carries out the test at 690 kPa/s (which is the average stress rate of four stub tests in a substrate) at 50°C, that test condition represents the typical stress rate in the field at 3-in. depth at 50°C. Therefore, the measured BBS can be used directly in Equation (8-12) to predict the MSR at any depth.

Level 2: Two-Point Method Using Generalized Shift Factor

If the user could not achieve the average stress rate of 690 kPa/s at 50°C, then an additional BBS test (four stubs per substrate) at any temperature above 30°C in addition to 50°C is recommended, with 35°C being the ideal test temperature. Once the BBS and stress rate of the tack coat are measured at both temperatures, the two-point method employed in the HWY 2018-13 project, *Development of a Tack Coat Quality Control Program for Mitigating Delamination in Asphalt Pavement Layers to Control the Debonding Distress*, should be used to measure the material parameters a_B and n_B of the BBS predictive equation, i.e., Equation (8-8). In order to do so, the reduced stress rate must be calculated, which requires the aid of a shift factor function. In order to simplify the calculation effort, a generalized shift factor is recommended. This generalized shift factor was developed by fitting the measured shift factors of various tack coats used for different projects at NCSU laboratories. The generalized shift factor at 50°C was found to be 0.001705. Thus, the material parameters a_B and n_B of the BBS predictive equation for the specific tack coat in question can be found. Subsequently, the BBS is predicted at the critical stress rate of 690 kPa/s and then is substituted in Equation (8-12) to determine the MSR.

Level 1: Two-Point Method Using DSR Shift Factor

Level 1 is the most rigorous and accurate way to carry out BBS predictions. Level 1 follows all the steps explained in Level 2; the only difference is that Level 1 uses a measured shift factor instead of a generalized shift factor. Level 1 requires the user to run DSR tests of the tack coat of interest as per AASHTO T 315-12 (AASHTO 2020e) to measure the shift factor coefficients. Even though Level 1 takes more effort and time, it provides the most reliable BBS predictions compared to the other levels.

In summary, predicting coefficient A for different interlayer systems made with different geosynthetic products is critical to finding the effect of the tack coat on the MSR. Selecting the most appropriate level of accuracy to measure the parameter depends on the user’s preference and requirements. In addition, adopting generalized binder and mixture shift factor coefficients reduces the amount of time and effort needed to determine the coefficients via DSR testing. Moreover, the resultant MSR failure envelope mimics the critical stress state in the field.

8.8.3 Quality Control Using Confined Interface Shear Strength Test

A threshold shear test protocol is proposed in this work to evaluate the geosynthetic products' potential to resist debonding. The confined ISS test should be conducted at 50°C (122°F), 5.08 mm/min (0.2 in./min) at the actuator deformation rate (on-specimen reduced shear strain rate of 2.6×10^{-4}/sec), and 275 kPa (40 psi) confining pressure. Based on the MSR information, the minimum required shear strength for acceptance of a geosynthetic-reinforced specimen is 470 kPa (68 psi). For quality control purposes in the field, the threshold shear test should be run using field cores. Once measured, the ISS value must be substituted in Equation (8-13) to verify the acceptance criteria.

$$MSR = \frac{210}{0.6 \times ISS} - 0.05 \leq 0.7 \tag{8-13}$$

where

ISS = interface shear strength (kPa).

8.9 Tack Coat Purchase Criteria

Figure 8-14 shows the failure envelopes for the different geosynthetic products. The MSR versus BBS curves are based on the steps described in Figure 8-14. The cut-off value for MSR acceptance is set at 0.7, which is the value proposed for tack coat selection alone (no interlayer). The results show that the MSR increases with different geosynthetic types, i.e., the shear strength reduces with the inclusion of different geosynthetic products in AC. This study's selection criteria will encourage pavement designers and engineers to consider the use of a tack coat, which provides greater bond strength than PG 64-22 (as provided in Table 8-6). The results show that a better tack coat should help geosynthetic products to perform as well as the no-interlayer condition (HM-HM) in terms of resisting debonding.

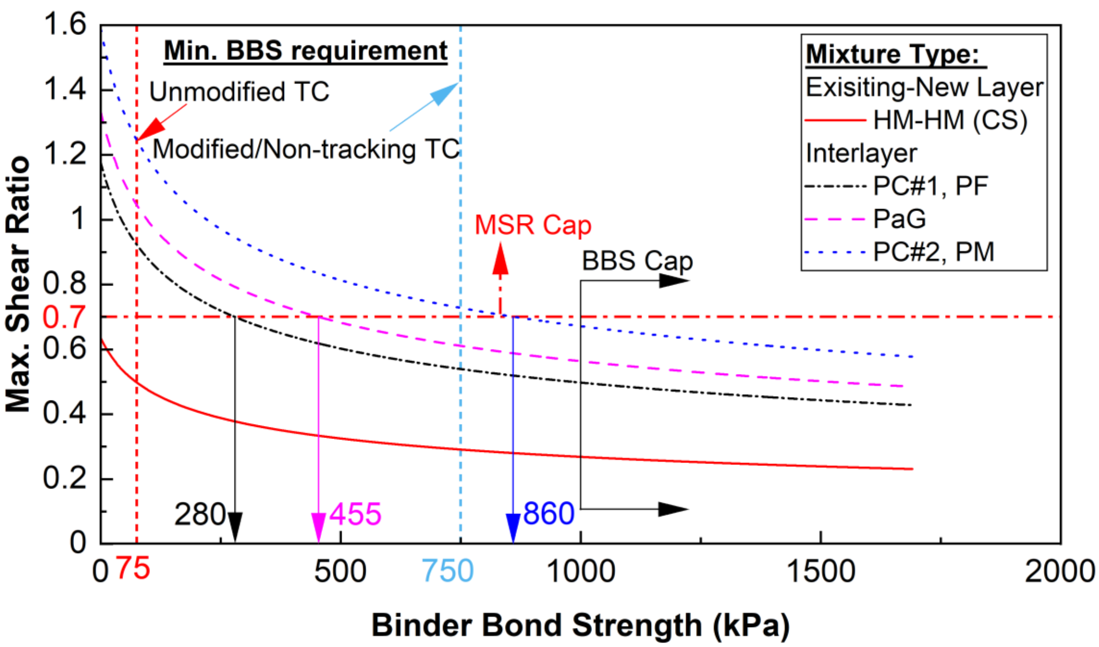

Figure 8-14. Failure envelopes showing minimum binder bond strength (BBS) required for tack coat selection.

Table 8-6. Minimum BBS Required for Tack Coat for Different Geosynthetic Products

Geosynthetic Products	Min. BBS (kPa)
PC#1, PF	280
PaG	455
PC#2, PM	860

Note also that, in certain cases, the MSR for the no tack coat condition is less than 0.7. Theoretically, any MSR that is less than 1.0 qualifies the product to resist debonding. However, the rate of damage that occurs at the interface is unknown. Thus, predicting the service life of the pavement before debonding occurs is a difficult task. Preliminary fatigue test results for interface bonding show that a tack coat applied at the interface is more resilient than the no tack coat condition. Hence, a tack coat should be used even if the mixture alone provides a sufficient MSR. Note also that, when the BBS value exceeds about 1000 kPa, only a small reduction in the MSR is caused by the large increase in BBS.

8.10 Geosynthetic and Tack Coat Selection Guidelines

This project's experimental and numerical research has resulted in geosynthetic interlayer selection guidelines and tack coat selection guidelines, presented in Figure 8-15.

Step 1: Measure surface deflections.

The existing pavement conditions must be evaluated using an FWD. The deflections must be measured at D_0, D_{12}, D_{24}, and D_{36}. D_r is the surface deflection, and r is the distance from the load center (in.). The measured deflections are used to determine the SCI, BDI, and BCI.

Step 2: Predict the tensile strain underneath the overlay.

The overlay tensile strain predictive equation shown in Equation (8-2) is a function of the SCI, BDI, BCI, and overlay thickness ($T_{overlay}$). The SCI, BDI, and BCI are measured in Step 1, so the only unknown factor is $T_{overlay}$. The designer must assume a minimum $T_{overlay}$ of 1.5 in. or more. Then, the parameters must be substituted in Equations (8-2) and (8-3) to predict the overlay tensile strain.

If the predicted overlay tensile strain is negative, then the interface is in the compressive stress state. This case indicates that the existing pavement under the overlay is in good condition. In this case, the selection of the geosynthetic product is at the engineer's discretion. The engineer needs to note that the initial compressive state of the interface would eventually transform to the tensile state as the damage progresses with time and traffic.

If the predicted overlay tensile strain is greater than 100 μ, then the pavement is severely damaged, in which case milling the surface layer followed by a leveling course is recommended before installing the geosynthetic product. Alternatively, increasing the overlay thickness also reduces the tensile strain. If increasing the overlay thickness reduces the interface tensile strain below 100 μ, then the geosynthetic product can be used after standard crack fill and patchwork.

These suggestions are based on laboratory test results; a thorough field study based on these recommendations would refine the findings.

Step 3: Select the geosynthetic product based on performance.

Determining the crack resistance of the various geosynthetic products helped the research team to develop the selection table shown in Step 3 of Figure 8-15. The improvement factor ('IF' in the table) reported in the table is the ratio of the crack resistance of a geosynthetic-reinforced AC beam at a specific strain level to that of an unreinforced AC beam. The DIC study helped identify the failure mode, i.e., either debonding cracks or vertical cracking. In general, the debonding type of crack failure is more common than vertical crack failure. The presence of vertical cracking accelerates damage by allowing moisture to infiltrate the pavement structure.

The strain range in Step 3 is based on the tensile strain at the bottom of the overlay that is predicted in Step 2. The improvement factor of each geosynthetic product for the selected strain range is provided, and the product then can be chosen based on the improvement factor for the predicted strain value for a given project. Note, however, that the improvement factor is insignificant for some products within a certain range of tensile strain. Hence, the engineer's judgment regarding product selection must be based on the cost-benefit ratio. The proposed selection table (Step 3 in Figure 8-15) is based on limited laboratory test results. Hence, relying on field improvement factors is unrealistic. Nonetheless, the table may offer a ranking pattern of the geosynthetic products' performance for different field conditions.

Step 4: Select the tack coat based on the geosynthetic product selected.

Once the geosynthetic product is selected, the tack coat is selected based on the minimum BBS of the geosynthetic product selected. PATTI is used to measure the BBS of the tack coat material at 50°C (122°F). The required stress rate during the test must be maintained at between 90 psi/sec and 115 psi/sec (620 kPa/sec and 792 kPa/sec, respectively). If the BBS value meets the minimum BBS reported in Step 4 of Figure 8-15, then the tack coat should be applied at the application rate recommended by the manufacturer. The minimum BBS value is based on the MSR of 0.7, which is the value used for tack coat selection (without a geosynthetic interlayer). Kim et al. (2015a) found from the laboratory study in a previous NCDOT research project that the crack resistance of geosynthetic-reinforced products increases with better quality tack coats (i.e., greater BBS). The crack resistance of all the geosynthetic products in the current study was evaluated using PG 64-22 binder as the tack. The typical BBS value of PG 64-22 binder is between 75 kPa (11 psi) and 90 kPa (13 psi). However, the recommended tack coat requires a BBS value that is at least three to eight times that of the PG 64-22 binder. Hence, the improvement factor proposed in Step 3 is expected to be observed in the field. Nonetheless, the superiority of one product over another with a better tack coat cannot be confirmed by the current study and remains a topic for future research.

Step 1: Measure the surface deflections.

Falling Weight Deflectometer (FWD)

Surface Curvature Index

$$\text{SCI} = D_0 - D_{12}$$

Base Damage Index

$$\text{BDI} = D_{12} - D_{24}$$

Base Curvature Index

$$\text{BCI} = D_{24} - D_{36}$$

SCI, BDI, BCI in mils

$T_{overlay}$ in inches

Ref. Temp is 23°C (73.4°F)

Step 2: Predict the tensile strain underneath the overlay.

Assume $T_{overlay}$ based on design

Predictive $\varepsilon_{t\text{-}overlay}$ Eq – $f\left(\text{SCI, BDI, BCI, } T_{overlay}\right)$

$$\varepsilon_{t-overlay} = 575\times\log\left(E_{sg}\times T_{eq}\right)+1034\times\log\left(\text{SCI}\right) - 1346\times\log\left(\text{BDI}\right) +1136\times\log\left(\text{BCI}\right)+115\times T_{overlay} - 3539$$

$$\left(E_{sg}\times T_{eq}\right) = 78683 + 7503965\times e^{\left(\frac{\text{BCI}}{-0.3827}\right)} + 698559\times e^{\left(\frac{\text{BCI}}{-2.459}\right)}$$

Step 3: Select the geosynthetic products based on performance.

Geosynthetic Selection Criteria						
$\varepsilon_{t\text{-}overlay}$	Products	PC#1	PaG	PM	PC#2	PF
40 μ- 60 μ	IF	1.7	3.4	32.6	14.2	5.4
	FM	VC	VC	DB	DB	DB
60 μ- 80 μ	IF	2.5	2.5	4.1	6.4	5.1
	FM	VC	VC	DB	DB	DB
>80 μ	IF	3.3	2.0	1.0	3.5	5.0
	FM	VC	VC	VC	VC	DB/VC

Note: VC-Vertical Crack, DB-Debonding, IF-Improvement Factor, FM-Expected Failure Mode

Step 4: Select the tack coat based on geosynthetic product in use.

Tack Coat Selection Criteria						
Product		PC#1	PC#2	PaG	PM	PF
Min. BBS	kPa	280	860	455	860	280
	psi	41	125	66	125	41

Figure 8-15. Step-by-step selection guidelines for geosynthetic products and tack coats.

Chapter 9. Conclusions and Recommendations for Future Work

Past studies that involved geosynthetic installations in surface AC layers certainly have led to improvements in controlling reflective cracking. However, no standard guidelines have been developed to help the designer select the best-fit geosynthetic product. The current study proposes a framework that practitioners can follow to identify the improvement factors for various geosynthetic products as well as the products' failure modes. The results from this study's laboratory tests were linked to field-measured deflections, aided by a regression equation that was developed based on numerical simulations of pavement responses. The findings of this study will help engineers to select the best-fit geosynthetic product based on existing pavement conditions. The study also proposes a minimum BBS requirement for the tack coat that best corresponds to the selected geosynthetic product.

The following sections present the conclusions that can be drawn based on the experimental work and computational analyses conducted in this research.

9.1 Experimental Work Based on Test Results

9.1.1 Interface Shear Strength Tests

The use of the t-T superposition principle to establish ISS and BBS mastercurves was verified in this study. The t-T shift factors determined from DSR measurements of the asphalt binder (PG 64-22 in this study) were used successfully to develop ISS and BBS mastercurves.

- The predictive model equation for ISS developed by Cho (2016) was fitted to obtain coefficients for the double-layered AC specimens with five different geosynthetic types and one unreinforced (CS) condition used in this study. This predictive model can predict the shear strength at a specific pavement depth of interest, which then can be compared against the shear stress at that depth predicted from FlexPAVE™.
- In comparison to the unreinforced specimen (CS), the presence of any geosynthetic product under any test conditions reduced the ISS and increased the chance of interfacial debonding.
- The ISS decreased with an increase in test temperature and a decrease in strain rate. This finding applies to all the tested MAST specimens, independent of geosynthetic product type.
- The shear strength reduced 40% to 65% with a change in temperature from 23°C (73°F) to 54°C (129°F). The difference in the shear strength of the different geosynthetic-reinforced specimens decreased with an increase in the testing temperature.
- Three different confining pressures were applied to determine the effects of confinement on the ISS. The results clearly indicate that ISS is proportional to the applied confinement pressure. The mobilization of aggregate interlocking resulted in increased frictional resistance to the applied shear stress. Therefore, the shear strength increased with an increase in confining pressure. However, the rate of the ISS increase with confining pressure is a function of the geosynthetic product type.
- No effect of the tack coat application rate on the ISS of the geosynthetic-reinforced specimens was readily apparent. Statistical analysis of the ISS data generated in this study also supports the visual observations.

- The bond at the interface will deteriorate with environmental impacts and traffic loading. Hence, a safety factor should be considered to take into account field conditions. The acceptance MSR was set at 0.7 based on findings from this study and NCDOT RP2018-13.
- According to the MSR analysis results, threshold shear strength tests for the evaluation of geosynthetic-reinforced products should be conducted at 50°C (122°F), 5.08 mm/min (0.2 in./min) actuator deformation rate (on-specimen reduced shear strain rate of 2.6×10^{-4}/sec), and 275.8 kPa (40 psi) confining pressure. Based on the MSR information, the minimum required shear strength for geosynthetic-reinforced specimens under these conditions is 470 kPa (68 psi).

9.1.2 Notched Beam Fatigue Tests

- All the geosynthetic products studied can improve crack resistance (in terms of reducing the number of cycles to failure) under in-service conditions (typical tensile strain expected in the field).
- The tack coat application rate affects the pavement's crack resistance whereby an increase in the tack coat rate extends the fatigue life. However, this conclusion is based on three application rates that were applied only to CS and PC#1. Further study is required to confirm the observed results.
- Several failure criteria were applied to the outcome of each NBFT to identify the failure cycle number. However, the stress × N failure criterion eventually was selected for determining failure due to its ease of application and non-dependency on on-specimen deformation measurements. Moreover, the N_f values from the stress × N failure criterion are comparable to those determined by other available failure criteria.
- Full-field displacement and strain contours obtained through the NBFTs using the DIC technique revealed that the failure of geosynthetic-reinforced asphalt beam specimens can be classified into two failure modes, vertical cracking and debonding. The energy that is input by repeated loading is dissipated by the creation of new surfaces through vertical cracking and debonding. Therefore, the increase in interfacial damage effectively mitigates vertical cracking. However, this behavior is not necessarily beneficial to pavement life because the interlayer products that have a greater tendency for interfacial damage will cause debonding pavement failure.
- Strong bonds between geosynthetic interlayers and surrounding asphalt layers that can be provided by high quality tack coat not only prevent the debonding but also allow the full use of the strength of the geosynthetic interlayers in mitigating the reflective cracking.
- DIC analysis revealed that interlayer movement can be significant depending on the geosynthetic product type. Typically, thick and continuous geosynthetic products exhibited greater interlayer movement than thinner and grid-type products.
- When the tip of a vertical crack in the bottom layer nearly reached the interface, the interface damage (if any) started to grow. However, when the vertical crack propagation reached the top layer, i.e., the crack initiated from bottom of top layer, the energy input by the repeated loading was mostly used to propagate the vertical crack and therefore the severity of the interfacial damage did not change significantly.

- During the NBFTs, the failure modes for the PC#1- and PaG-reinforced beam specimens were observed to change from debonding cracking at a low strain level to vertical cracking at a high strain level. Hence, depending on the strain level chosen for testing, the failure mode could change.
- For all the geosynthetic product cases, lower strain levels led to predominantly debonding failure whereas higher tensile strain levels led to vertical cracking failure. During the high tensile strain tests, both the top and bottom layers served as two independent beams due to local debonding at the crack tip. Therefore, vertical cracking at high tensile strain levels could be mitigated if debonding is minimized. This observation emphasizes the importance of sufficient bond strength at the interface of geosynthetic-reinforced asphalt overlays, which is needed to capture the full benefits of geosynthetic products and mitigate reflective cracking.
- The areas of debonding cracking and vertical cracking that were measured on the geosynthetic-reinforced beam specimens corresponded closely to the stress degradation rate that can be measured from load responses without the DIC technique. However, insufficient data led to the inability to establish a relationship. Hence, future research is recommended that could help identify the failure mode without the aid of the DIC technique.

9.2 Experimental Work Based on Numerical Simulations

9.2.1 FlexPAVE™ Analysis

The FlexPAVE™ analysis of various overlay pavement structures, traffic speeds, temperatures, and overlay thicknesses suggest the following conclusions.

- In this research, 'shear ratio' is defined as the ratio between the shear stress at the interface under vehicular loading and the ISS. The MSR is determined by comparing the shear ratios at various locations in a pavement structure that are determined using the shear stress calculated from FlexPAVE™ and the shear strength calculated from the ISS predictive model. A higher MSR implies greater potential for interface debonding that is due to repeated vehicular braking. An MSR that is greater than one indicates that debonding failure would occur due to the single braking of a dual tire at 80 kN (18 kips). The tack coat considered in this study (PG64-22 binder) generated sufficient shear strength to resist shear stress in the field, based on the numerical simulations. Hence, the potential for interface debonding using this tack coat is minimal.
- The MSR typically is found at the center of the longitudinal axis of the tire at 10 cm (3.9 in.) to 14 cm (5.5 in.) in front of the tire. The MSR location depends on the depth of the interface and the tack coat type.
- The worst field conditions expected in North Carolina for an interface to resist debonding during its service life are as follows: a thick pavement with a dual tire at 80 kN (18 kips) under the braking condition at a speed of 1 mph (1.61 km/hour) at 50°C.
- The difference in the MSR values among different structures typically is between 2.5% and 3.5 percent. The pavement structures considered for the current study did not significantly affect the MSR because shear debonding is a near-the-surface phenomenon.

9.2.2 EverstressFE Linear Elastic Model Analysis

- The batch analysis of 1500 combinations of pavement structures with various elastic modulus values and thicknesses was undertaken to predict the overlay tensile strain based on FWD measurements of the existing pavement.
- All the analyses were carried out assuming the temperature of 23°C (73°F). Hence, the deflection measurements had to be corrected for temperature using BELLS equation and the NCDOT deflection correction method.
- The predictive equation for overlay tensile strain is a function of the SCI, BDI, BCI, and $T_{overlay}$. Hence, this approach is not dependent on any back-calculation software to identify the elastic modulus and then analyze simulated responses of an overlay pavement.

9.3 Minimum Required Binder Bond Strength

- Rigorous numerical simulations for different field conditions helped to develop a universal relationship between the ISS and BBS, followed by the MSR versus BBS relationship. The MSR-BBS relationship is presented as a function of interface depth and was used to determine the BBS threshold values for different interface depths.
- A methodology that was developed under the NCDOT RP 2018-13 project as part of a tack coat quality control program is used in this study to ensure the appropriate bonding of tack coat and provide acceptable field performance. This methodology uses PATTI to measure the BBS of the tack coat material tested at 50°C (122°F). The required stress rate during the test must be maintained at between 90 psi/sec and 115 psi/sec (620 kPa/sec and 792 kPa/sec, respectively).
- Based on the MSR-BBS relationship, the BBS value at 50°C (122°F) that corresponds to the MSR value of 0.7 can be found, as presented in Figure I-7. Therefore, if the BBS of a tack coat at 50°C (122°F) is above that shown in Figure I-7, then the tack coat can be accepted for application with the corresponding geosynthetic product at the manufacturer's recommended rate.
- Employing the selected tack coat that corresponds to a specific geosynthetic product will improve overall pavement performance. Safavizadeh (2015) also reported that a better-performing tack coat will help geosynthetic-reinforced beam specimens exhibit superior performance.

9.4 Step-by-Step Guidelines for Geosynthetic and Tack Coat Selection

The geosynthetic product selection guidelines developed in this study (see Section 8.4) provide both the improvement factor and failure mode for a specific geosynthetic product so the designer can make the proper selection. Engineers should follow the developed step-by-step process presented in Figure I-5 to select a best-fit geosynthetic product based on expected pavement performance. The appropriate tack coat can then be selected based on the minimum BBS required for the geosynthetic product selected.

9.5 Recommendations for Further Research

The following topics are recommended to be investigated in future research:

- Notched beam fatigue tests of geosynthetic-reinforced beam specimens for a wide range of strain levels with more replicates to identify the failure mechanism(s) and to improve the reliability of improvement factors.
- Overlay tests of geosynthetic-reinforced AC specimens to evaluate the Mode I fracture due to thermal loading.
- Mode II fracture performance tests.
- Effect of types and application rates of tack coat on the cracking and debonding resistance of geosynthetic-reinforced beam specimens.
- Effect of fatigue on the ISS of geosynthetic-reinforced specimens.
- Field investigation of the performance of geosynthetic-reinforced pavements.
- Development of a quality control test procedure for field installation acceptance of geosynthetic products for paving applications.

REFERENCES

AASHTO. (2017a). *Bulk Specific Gravity (Gmb) and Density of Compacted Hot Mix Asphalt (HMA) Using Automatic Vacuum Sealing Method*. Standard, AASHTO T331, American Association of State and Highway Transportation Officials, Washington DC, USA.

AASHTO. (2017b). *Standard Method of Test for Determining the Fatigue Life of Compacted Asphalt Mixtures Subjected to Repeated Flexural Bending*. Standard, AASHTO T321, American Association of State and Highway Transportation Officials, Washington DC, USA.

AASHTO. (2017c). *Standard Method of Test for Determining the Fatigue Life of Compacted Asphalt Mixtures Subjected to Repeated Flexural Bending*. Standard, AASHTO T321, American Association of State and Highway Transportation Officials, Washington DC, USA.

AASHTO. (2019). *Provisional Standard Method of Test for Determining the Dynamic Modulus for Asphalt Mixtures Using Small Specimens in the Asphalt Mixture Performance Tester (AMPT)*. Standard, AASHTO TP132, American Association of State and Highway Transportation Officials, Washington DC, USA.

AASHTO. (2020a). *Standard Method of Test for Theoretical Maximum Specific Gravity (Gmm) and Density of Asphalt Mixtures*. Standard, AASHTO T209, American Association of State and Highway Transportation Officials, Washington DC, USA.

AASHTO. (2020b). *Standard Practice for Recovering Residue from Emulsified Asphalt Using Low-Temperature Evaporative Techniques*. Standard, AASHTO R78, American Association of State and Highway Transportation Officials, Washington DC, USA.

AASHTO. (2020c). *Standard Method of Test for Determining the Rheological Properties of Asphalt Binder Using a Dynamic Shear Rheometer (DSR)*. Standard, AASHTO T315, American Association of State and Highway Transportation Officials, Washington DC, USA.

AASHTO. (2020d). *Standard Method of Test for Determining Asphalt Binder Bond Strength by Means of the Asphalt Bond Strength (ABS) Test*. Standard, AASHTO T 361, American Association of State and Highway Transportation Officials, Washington DC, USA.

AASHTO. (2020e). *Standard Method of Test for Determining the Rheological Properties of Asphalt Binder Using a Dynamic Shear Rheometer (DSR)*. Standard, AASHTO T 315, American Association of State and Highway Transportation Officials, Washington DC, USA.

AASHTO. (2021). *Standard Practice for Preparation of Cylindrical Performance Test Specimens Using the Superpave Gyratory Compactor (SGC)*. Standard, AASHTO R83, American Association of State and Highway Transportation Officials, Washington DC, USA.

Airey, G. D., Rahimzadeh, B., and Collop, A. C. (2002). "Linear and nonlinear rheological properties of asphalt mixture." *Performance of Bituminous and Hydraulic Materials in Pavements*, Taylor & Francis, Nottingham, UK.

Al-Khateeb, G., and Shenoy, A. (2004). “A distinctive fatigue failure criterion.” *Journal of the association of asphalt paving technologists*, 73, 585–622.

Al-Khateeb, G., and Shenoy, A. (2011). “A simple quantitative method for identification of failure due to fatigue damage.” *International Journal of Damage Mechanics*, 20, 3–21.

Al-Qadi, I. L., Carpenter, S. H., Leng, Z., Ozer, H., and Trepanier, J. (2008). *Tack Coat Optimization for HMA Overlays: Laboratory Testing*. Technical Report, FHWA-ICT-08-023, Illinois Center for Transportation, Rantoul, IL, USA.

Al-Qadi, I. L., Carpenter, S. H., Leng, Z., Ozer, H., and Trepanier, J. (2009). *Tack Coat Optimization for HMA Overlays: Accelerated Pavement Test Report*. Technical Report, FHWA-ICT-09-035, Illinois Center for Transportation (ICT), Urbana-Champaign, IL, USA, 56.

Amini, F. (2005). *Potential Applications of Paving Fabrics to Reduce Reflective Cracking.* Technical Report, FHWA/MS-DOT-RF-05-174, Jackson State University, Jackson, MS, USA, 45.

Asphalt Institute (Ed.). (1991). *Thickness Design-Full depth Asphalt Pavement Structures for Highways and Streets*. Manual Series, The Asphalt Institute, College Park, MD, USA.

ASTM. (2010). *Test Method for Determining Fatigue Failure of Compacted Asphalt Concrete Subjected to Repeated Flexural Bending*. Standard, ASTM D7460, American Standards for Testing Materials International, West Conshohocken, PA, USA.

ASTM. (2017). *Standard Test Method for Pull-Off Strength of Coatings Using Portable Adhesion Testers*. Standard, ASTM D4541, American Standards for Testing Materials International, West Conshohocken, PA, USA.

ASTM. (2019). *Standard Specification for Steel, Sheet, Carbon, Structural, and High-Strength, Low-Alloy, Hot-Rolled and Cold-Rolled, General Requirements for*. Standard, ASTM A568 / A568M-19a, American Standards for Testing Materials International, West Conshohocken, PA, USA.

Bae, A., Mohammad, L. N., Elseifi, M. A., Button, J., and Patel, N. (2010). “Effects of temperature on interface shear strength of emulsified tack coats and its relationship to rheological properties.” *Transportation Research Record*, SAGE Publications Inc, 2180(1), 102–109.

Baek, J. (2010). “Modeling reflective cracking development in hot-mix asphalt overlays and quantification of control techniques.” *ProQuest Dissertations and Theses,* Ph.D., University of Illinois at Urbana-Champaign, Urbana-Champaign, IL, USA.

Benedetto, H. D., Roche, C. de L., Baaj, H., Pronk, A., and Lundström, R. (2004). “Fatigue of bituminous mixtures.” *Materials and Structures*, 37(3), 202–216.

Blankenship, P., Iker, N., and Drbohlav, J. (2004). “Interlayer and design considerations to retard reflective cracking.” *Transportation Research Record*, SAGE Publications Inc, 1896(1), 177–186.

Bognacki, C. J., Frisvold, A., and Bennert, T. (2007). “Investigation of asphalt pavement slippage failures on runway 4R-22L, Newark International Airport.” *New Directions in Airport Technology*, Federal Aviation Administration, Atlantic City, NJ, USA, 14.

Boulangé, L., and Sterczynskia, F. (2012). “Study of interfacial interactions between bitumen and various aggregates used in road construction.” *Journal of Adhesion Science and Technology*, Taylor & Francis, 26(1–3), 163–173.

BS EN. (2019). *Specimen Prepared by Roller Compactor*. Bituminous Mixtures. Test Methods. Standard No. EN 12697-33, EN 12697-33, British Standards Institution, London, UK, 22.

Button, J. W., and Lytton, R. L. (1987). “Evaluation of fabrics, fibers and grids in overlays.” *Structural Design of Asphalt Pavements 1*, Ann Arbor, MI, USA, 925–934.

Button, J. W., and Lytton, R. L. (2007). “Guidelines for using geosynthetics with hot-mix asphalt overlays to reduce reflective cracking.” *Transportation Research Record*, SAGE Publications Inc, 2004(1), 111–119.

Canestrani, F., Grilli, A., Santagata, F., and Virgili, A. (2006). “Interlayer Shear Effects of Geosynthetic Reinforcements.” Quebec City, Canada.

Canestrari, F., Ferrotti, G., Abuaddous, M., and Pasquini, E. (2016a). “Geocomposite-Reinforcement of Polymer-Modified Asphalt Systems.” Springer, 383–395.

Canestrari, F., Ferrotti, G., Abuaddous, M., and Pasquini, E. (2016b). “Geocomposite-Reinforcement of Polymer-Modified Asphalt Systems.” *8th RILEM International Symposium on Testing and Characterization of Sustainable and Innovative Bituminous Materials*, F. Canestrari and M. N. Partl, eds., Springer Netherlands, Dordrecht, 383–395.

Chakroborty, P., and Das, A. (2017). *Principles of Transportation Engineering*. Prentice Hall India Pvt., Limited, Delhi, India.

Chehab, G. R., Kim, Y. R., Schapery, R., Witczak, M. W., and Bonaquist, R. (2002). “Time-temperature superposition principle for asphalt concrete with growing damage in tension state.” *Technical Sessions 71*, Association of Asphalt Paving Technologists, Lino Lakes, MN, 559–593.

Chehab, G. R., O’Quinn, E., and Kim, Y. R. (2000). “Specimen geometry study for direct tension test based on mechanical tests and air void variation in asphalt concrete specimens compacted by Superpave gyratory compactor.” *Transportation Research Record*, 1, SAGE Publications Inc, 1723(1), 125–132.

Cho, S. H. (2016). “Evaluation of interfacial stress distribution and bond strength between asphalt pavement layers.” Ph.D. dissertation, North Carolina State University, Raleigh, NC, USA.

Cho, S. H., Karshenas, A., Tayebali, A. A., Guddati, M. N., and Kim, Y. R. (2017a). “A mechanistic approach to evaluate the potential of the debonding distress in asphalt pavements.” *International Journal of Pavement Engineering*, 12, Taylor & Francis, 18(12), 1098–1110.

Cho, S. H., Safavizadeh, S. A., and Kim, Y. R. (2017b). “Verification of the applicability of the time–temperature superposition principle to interface shear stiffness and strength of GlasGrid-reinforced asphalt mixtures.” *Road Materials and Pavement Design*, 4, Taylor & Francis, 18(4), 766–784.

Cho, S.-H. and Kim, Y. R. (2016). “Verification of time–temperature superposition principle for shear bond failure of interlayers in asphalt pavements.” *Transportation Research Record*, SAGE Publications Inc, 2590(1), 18–27.

Christensen, D. W. and Anderson, D. A. (1992). “Interpretation of dynamic mechanical test data for paving grade asphalt cements (with discussion).” *Journal of the Association of Asphalt Paving Technologists,* Association of Asphalt Paving Technologists (AAPT), 61, 67–116.

Collop, A. C., Sutanto, M. H., Airey, G. D., and Elliott, R. C. (2011). “Development of an automatic torque test to measure the shear bond strength between asphalt.” *Construction and Building Materials*, *Composite Materials and Adhesive Bonding Technology*, 25(2), 623–629.

De Beer, M., Fisher, C., and Kannemeyer, L. (2004). “Towards the application of stress-in-motion (SIM) results in pavement design and infrastructure protection.” *8th International Symposium on Heavy Vehicle Weights and Dimensions*, Document Transformation Technologies, Johannesburg, South Africa.

Ferrotti, G., Canestrari, F., Pasquini, E., and Virgili, A. (2012). “Experimental evaluation of the influence of surface coating on fiberglass geogrid performance in asphalt pavements.” *Geotextiles and Geomembranes*, 34, 11–18.

Ferrotti, G., Canestrari, F., Virgili, A., and Grilli, A. (2011). “A strategic laboratory approach for the performance investigation of geogrids in flexible pavements.” *Construction and Building Materials*, 25(5), 2343–2348.

FHWA. (2016). *Tack Coat Best Practices*. Technical Bulletin, FHWA-HIF-16-017, Federal Highway Administration, Washington DC, USA, 17.

Findley, W. N., and Davis, F. A. (2013). *Creep and Relaxation of Nonlinear Viscoelastic Materials*. Dover Civil and Mechanical Engineering, Courier Corporation, Chelmsford, MA, USA.

Gonzalez, R. C., and Woods, R. E. (2018). *Digital Image Processing*. Pearson Education.

Hachiya, Y., Umeno, S., and Sato, K. (1997). "Effect of tack coat on bonding characteristics at interface between asphalt concrete layers." *Doboku Gakkai Ronbunshu*, 571, Japan Society of Civil Engineers, 1997(571), 199–209.

Huesker. (2015). "HaTelit® Asphalt Reinforcement Grid Installation Guideline." <<https://www.huesker.com.au/fileadmin/Media/Brochures/AUS/HaTelit_C_Installation_Guidelines_AUS.pdf>>.

Joel Sprague, C., Allen, S., and Tribbett, W. (1998). "Tensile properties of asphalt overlay geosynthetic reinforcement." *Transportation Research Record*, SAGE Publications Inc, 1611(1), 65–69.

Karshenas, A. (2015). "Tack coat bond strength evaluation methods and mechanistic design of the interface for multilayer asphalt pavement." Ph.D. dissertation, North Carolina State University, Raleigh, NC, USA.

Khodaei, A., and Falah, SH. (2009). "Effects of geosynthetic reinforcement on the propagation of reflection cracking in asphalt overlays." *International Journal of Civil Engineering*, 7(2), 131–140.

Khweir, K., and Fordyce, D. (2003). "Influence of layer bonding on the prediction of pavement life." *Proceedings of the Institution of Civil Engineers - Transport*, 156(2), 73–83.

Kim, Y. R., Gabr, M. A., Wargo, A. D., and Islam, S. (2015a). *Performance of Cracking Mitigation Strategies on Cracked Flexible Pavements*. Technical Report, HWY-2012-02, North Carolina State University, Raleigh, NC, USA, 286.

Kim, Y. R., Park, S., and Shao, L. (1997). *Statewide Calibration of Asphalt Temperature Study from 1992 and 1993: Appendices*. Center for Transportation Engineering Studies, Department of Civil Engineering, North Carolina State University, Raleigh, NC, USA.

Kim, Y. R., Ranjithan, S. R., Troxler, J. D., and Xu, B. (2000). *Assessing Pavement Layer Condition Using Deflection Data*. Technical Report, NCHRP 10-48, North Carolina State University, Raleigh, NC, USA, 198.

Kim, Y. R., Sudarsanan, N., Fonte, B., and Xue, L. G. (2021). *Development of a Tack Coat Quality Control Program for Mitigating Delamination in Asphalt Pavement Layers*. Technical Report, RP 2018-13, North Carolina State University, Raleigh, NC, USA, 245.

Kim, Y. R., Tayebali, A. A., Murthy, G. N., Karshenas, A., and Cho, S.-H. (2015b). *Surface Layer Bond Stress and Strength*. Technical Report, HWY 2013-04, North Carolina State University, Raleigh, NC, USA, 289.

Kruntcheva Mariana R., Collop Andrew C., and Thom Nicholas H. (2005). "Effect of bond condition on flexible pavement performance." *Journal of Transportation Engineering*, American Society of Civil Engineers, 131(11), 880–888.

Kuai, H. D., Lee, H. J., Lee, J. H., and Mun, S. (2010). “Fatigue crack propagation model of asphalt concrete based on viscoelastic fracture mechanics.” *Transportation Research Record: Journal of the Transportation Research Board*, 2181(1), 11–18.

Luo, X., Luo, R., and Lytton, R. L. (2013). “Modified Paris’s law to predict entire crack growth in asphalt mixtures.” *Transportation Research Record: Journal of the Transportation Research Board*, 2373(1), 54–62.

Lytton, R. L. (1989). “Use of geotextiles for reinforcement and strain relief in asphalt concrete.” *Special Issue on Geotextiles and Geogrids in Pavements*, 8(3), 217–237.

Makowski, L., Bischoff, D. L., Blankenship, P., Sobczak, D., and Haulter, F. (2005). “Wisconsin experiences with reflective crack relief projects.” *Transportation Research Record*, SAGE Publications Inc, 1905(1), 44–55.

Mohammad, L. N., Elseifi, M. A., Bae, A., and Patel, N. (2012). *Optimization of Tack Coat for HMA Placement*. NCHRP 9-40, Technical Report, 712, The National Academies Press, Washington, D.C., USA, 146.

Mohammad, L. N., Elseifi, M. A., Das, R., and Cao, W. (2018). *Validation of the Louisiana Interlayer Shear Strength Test for Tack Coat*. Technical Report, NCHRP 09-40, Transportation Research Board, Washington, D.C., USA, 25458.

Mohammad, L. N., Hassan, M., and Patel, N. (2011). “Effects of shear bond characteristics of tack coats on pavement performance at the interface.” *Transportation Research Record: Journal of the Transportation Research Board*, 1, 2209(1), 1–8.

Mohammad, L. N., Raqib, M., and Huang, B. (2002). “Influence of asphalt tack coat materials on interface shear strength.” *Transportation Research Record: Journal of the Transportation Research Board*, 1789(1), 56–65.

Monismith, C. L., Epps, J. A., and Finn, F. N. (1985). “Improved asphalt mix design (with discussion).” *Association of Asphalt Paving Technologists Proc*, Minnesota, USA, 340–406.

Mukhtar, M. T., and Dempsey, B. J. (1996). *Interlayer Stress Absorbing Composite (ISAC) for Mitigating Reflection Cracking in Asphalt Concrete Overlays*. Technical Report, UILU-ENG-96-2006, University of Illinois at Urbana-Champaign, Urbana-Champaign, IL, USA.

NCDOT. (2018). *Asphalt Quality Management System*. Guide, North Carolina Department of Transportation, NC, USA, 364.

Pan, B. (2018). “Digital image correlation for surface deformation measurement: Historical developments, recent advances and future goals.” *Measurement Science and Technology*, IOP Publishing, 29(8), 082001.

Park, S. W., Richard Kim, Y., and Schapery, R. A. (1996). "A viscoelastic continuum damage model and its application to uniaxial behavior of asphalt concrete." *Mechanics of Materials*, Elsevier, 24(4), 241–255.

Partl, M. N., Porot, L., Benedetto, H. D., Canestrari, F., Marsac, P., and Tebaldi, G. (Eds.). (2018). *Testing and Characterization of Sustainable Innovative Bituminous Materials and Systems: State-of-the-Art Report of the RILEM Technical Committee 237-SIB*. RILEM State-of-the-Art Reports, Springer International Publishing.

Pasquini, E., Bocci, M., Ferrotti, G., and Canestrari, F. (2013). "Laboratory characterisation and field validation of geogrid-reinforced asphalt pavements." *Road Materials and Pavement Design*, Taylor & Francis, 14(1), 17–35.

Pasquini, E., Giacomello, G., Pasetto, M., and Canestrari, F. (2015). "Laboratory evaluation of the effect of low-temperature application of warm-mix asphalts on interface shear strength." *Construction and Building Materials*, 88(Complete), 56–63.

Peattie, K. R. (1980). "The incidence and investigation of slippage failures." *The Performance of Rolled Asphalt Road Surfacings*, The Institution of Civil Engineers.

Petersen, D., Link, R., Wagoner, M., Buttlar, W., and Paulino, G. (2005). "Development of a single-edge notched beam test for asphalt concrete mixtures." *Journal of Testing and Evaluation*, 33(6), 12579.

Pronk, A., and Hopman, P. (1991). "Energy dissipation: The leading factor of fatigue." *Highway Research: Sharing the Benefits*, Thomas Telford Publishing, 255–267.

Raab, C., and Partl, M. N. (2004). "Interlayer shear performance: Experience with different pavement structures." *Proceedings of the 3rd Eurasphalt and Eurobitume Congress*, Vienna, Austria.

Ragni, D., Sudarsanan, N., Canestrari, F., and Kim, Y. R. (2021). "Investigation into fatigue life of interface bond between asphalt concrete layers." *International Journal of Pavement Engineering*, Taylor & Francis, 1–15.

Raposeiras, A. C., Castro-Fresno, D., Vega-Zamanillo, A., and Rodriguez-Hernandez, J. (2013). "Test methods and influential factors for analysis of bonding between bituminous pavement layers." *Construction and Building Materials*, 43, 372–381.

Reese, R. (1997). "Properties of aged asphalt binder related to asphalt concrete fatigue life." *Journal of the Association of Asphalt Paving Technologists*, 66.

Rigo, J.-M., Degeimbre, R., and Francken, L. (2014). *Reflective Cracking in Pavements: State of the Art and Design Recommendations*. CRC Press.

Rowe, G. M., and Bouldin, M. G. (2000). “Improved techniques to evaluate the fatigue resistance of asphaltic mixtures.” *2nd Eurasphalt & Eurobitume Congress*, Breukelen, The Netherlands : Foundation Eurasphalt, Barcelona, Spain, 754–763.

Safavizadeh, S. A. (2015). “Fatigue and fracture characterization of GlasGrid® reinforced asphalt concrete pavement.” Ph.D. dissertation, North Carolina State University, Raleigh, NC, USA.

Safavizadeh, S. A., and Kim, Y. R. (2017). “DIC technique to investigate crack propagation in grid-reinforced asphalt specimens.” *Journal of Materials in Civil Engineering*, American Society of Civil Engineers, 29(6), 04017011.

Safavizadeh, S. A., Wargo, A., and Kim, Y. R. (2017). “Utilizing digital image correlation (DIC) in asphalt pavement testing.” *Journal of Testing and Evaluation*, ASTM International, 46(3), 984–998.

Schapery, R. A. (1962). *A Simple Collocation Method for Fitting Viscoelastic Models to Experimental Data*. GALCIT, Technical Report, SM 61-23A, California Institute of Technology, Pasadena, CA, USA, 15.

Schreier, H., Orteu, J.-J., and Sutton, M. A. (2009). *Image Correlation for Shape, Motion and Deformation Measurements*. Springer US, Boston, MA, USA.

Seo, Y., Kim, Y., Witczak, M. W., and Bonaquist, R. (2002). “Application of digital image correlation method to mechanical testing of asphalt-aggregate mixtures.” *Transportation Research Record*, SAGE Publications Inc, 1789(1), 162–172.

Shell International Petroleum Company. (1978). *Shell Pavement Design Manual: Asphalt Pavements and Overlays for Road Traffic*. Shell International Petroleum Company, London, UK.

Si, Z., Little D. N., and Lytton R. L. (2002). “Characterization of microdamage and healing of asphalt concrete mixtures.” *Journal of Materials in Civil Engineering*, American Society of Civil Engineers, 14(6), 461–470.

Su, K., Sun, L., Hachiya, Y., and Maekawa, R. (2008). “Analysis of shear stress in asphalt pavements under actual measured tire-pavement contact pressure.” *Proceedings of the 6th ICPT, Sapporo, Japan*, 11–18.

Sudarsanan, N. (2018). “Investigations on the control of reflective cracking in flexible pavements using geosynthetics.” Ph.D. dissertation, Indian Institute of Technology Madras & Swinburne Univeristy of Technology, Chennai, India.

Sudarsanan, N., Arulrajah, A., Karpurapu, R., and Amrithalingam, V. (2019a). “Digital image correlation technique for measurement of surface strains in reinforced asphalt concrete beams under fatigue loading.” *Journal of Materials in Civil Engineering*, American Society of Civil Engineers, 31(8), 04019135.

Sudarsanan, N., Arulrajah, A., Karpurapu, R., and Amrithalingam, V. (2020a). “Fatigue performance of geosynthetic-reinforced asphalt concrete beams.” *Journal of Materials in Civil Engineering*, American Society of Civil Engineers, 32(8), 04020206.

Sudarsanan, N., Fonte, B. R., and Kim, Y. R. (2020b). “Application of time-temperature superposition principle to pull-off tensile strength of asphalt tack coats.” *Construction and Building Materials*, 262, 120798.

Sudarsanan, N., Karpurapu, R., and Amirthalingam, V. (2019b). “Investigations on fracture characteristics of geosynthetic reinforced asphalt concrete beams using single edge notch beam tests.” *Geotextiles and Geomembranes*, 47(5), 642–652.

Sudarsanan, N., Karpurapu, R., and Amrithalingam, V. (2015). “State-of-the art summary of geosynthetic interlayer systems for retarding the reflective cracking.” *Indian Geotechnical Journal*, 45(4), 472–487.

Sudarsanan, N., Karpurapu, R., and Amrithalingam, V. (2016). “Critical review on the bond strength of geosynthetic interlayer systems in asphalt overlays.” *Japanese Geotechnical Society Special Publication*, 2(67), 2296–2301.

Sudarsanan, N., Karpurapu, R., and Amrithalingam, V. (2018a). “An investigation on the interface bond strength of geosynthetic-reinforced asphalt concrete using Leutner shear test.” *Construction and Building Materials*, 186, 423–437.

Sudarsanan, N., Mohapatra, S. R., Karpurapu, R., and Amirthalingam, V. (2018b). “Use of natural geotextiles to retard reflection cracking in highway pavements.” *Journal of Materials in Civil Engineering*, American Society of Civil Engineers, 30(4), 04018036.

Sutanto, M. H. (2009). “Assessment of bond between asphalt layers.” Ph.D. dissertation, University of Nottingham, Nottingham, UK.

Tashman, L., Nam, K., and Papagiannakis, A. T. (2006). *Evaluation of the Influence of Tack Coat Construction Factors on the Bond Strength Between Pavement Layers*. Technical Report, WA-RD 645.1, Washington State Department of Transportation Olympia, Pullman, WA, USA, 91.

Tayebali, A. A., Rowe, G. M., and Sousa, J. B. (1994). *Fatigue Response of Asphalt-Aggregate Mixtures*. Technical Report, SHRP A-404, National Research Council, Washington DC, USA.

Tencate. (2019). “Installation Guidelines for Tencate Mirafi® MPG Composite Paving Grids.” <<https://www.tencategeo.us/media/4feb9b04-41fe-4e4b-a78a-0656ab1318f7/3NVyZw/TenCate%20Geosynthetics/Documents%20AMER/Installation%20Guidelines/Pavement%20Solutions/IG_MPG010720>>.

Tozzo, C., Fiore, N., and D’Andrea, A. (2014). “Dynamic shear tests for the evaluation of the effect of the normal load on the interface fatigue resistance.” *Construction and Building Materials*, 61, 200–205.

Tsai, B.-W., Harvey, J. T., and Monismith, C. L. (2005). "Using the three-stage Weibull equation and tree-based model to characterize the mix fatigue damage process." *Transportation Research Record*, SAGE Publications Inc, 1929(1), 227–237.

Tschoegl, N. W. (2012). *The Phenomenological Theory of Linear Viscoelastic Behavior: An Introduction*. Springer Berlin Heidelberg.

Uzan, J., Livneh, M., and Eshed, Y. (1978). "Investigation of adhesion properties between asphaltic-concrete layers." *Association of Asphalt Paving Technologists Proc*, Lake Buena Vista, FL, USA, 495–521.

Van Dijk, W. (1975). "Practical fatigue characterization of bituminous mixes." *Journal of the Association of Asphalt Paving Technologists*, 44, 38–72.

Vanelstraete, A., and De Bondt, A. (2004). "Crack prevention and use of overlay systems." *Prevention of Reflective Cracking in Pavements*, CRC Press, 53–67.

Vismara, S., Molenaar, A. A. A., Crispino, M., and Poot, M. R. (2012). "Toward a better understanding of benefits of geosynthetics embedded in asphalt pavements." *Transportation Research Record,* SAGE Publications Inc, 2310(1), 72–80.

Wargo, A. D. (2015). "Laboratory and field investigation of reflective crack mitigation in layered asphalt concrete pavements." Ph.D. dissertation, North Carolina State University, Raleigh, NC, USA.

Wilkins, E. W. C. (1956). "Cumulative damage in fatigue." *Colloquium on Fatigue / Colloque de Fatigue / Kolloquium über Ermüdungsfestigkeit*, Springer, Berlin, Heidelberg, 321–332.

Wilson, B., Chowdhury, A., Hu, S., Kim, S.-S., Nazzal, M., and Abbas, A. R. (2017). *Tack Coat Performance and Materials Study*. Technical Report, FHWA/OH-2017-33, Texas Transportation Institute, Texas A&M University System, College Station, TX, USA.

Witczak, M. A., Mamlouk, M. W., Kaloush, M. S., and Kaloush, K. E. (2007). "Validation of initial and failure stiffness definitions in flexure fatigue test for hot mix asphalt." *Journal of Testing and Evaluation*, ASTM International, 35(1), 95–102.

Yates, J. R., Zanganeh, M., and Tai, Y. H. (2010). "Quantifying crack tip displacement fields with DIC." *International Conference on Crack Paths 2009*, 77(11), 2063–2076.

Zeiada, W. (2012). "Endurance limit for HMA based on healing phenomenon using viscoelastic continuum damage analysis." Ph.D. dissertation, Arizona State University, Tempe, AZ, USA.

Zhiming, T. (1997). "Mechanistic analysis for reflective cracking in asphalt overlay." *Journal of Tongji University Natural Science*, 25(6).

Zhou, F., and Sun, L. (2000). "Mechanistic analysis of reflective cracking and validation of field test." *Fourth International RILEM Conference on Reflective Cracking in Pavements-Research in Practice*, RILEM Publications SARL, 81–91.

Zofka, A., Maliszewski, M., Bernier, A., Josen, R., Vaitkus, A., and Kleizienė, R. (2015). "Advanced shear tester for evaluation of asphalt concrete under constant normal stiffness conditions." *Road Materials and Pavement Design,* Taylor & Francis, 16(sup1), 187–210.

Appendix A. Literature Review

A.1. Reflective Cracking

Reflective cracking is the most common type of distress that occurs after an overlay is placed over old, cracked Portland concrete cement or hot mix asphalt pavement. Existing cracks in the old underlying pavement cause cracks to form at the bottom of the overlay and propagate upward. Such reflective cracking breaks the continuity of the overlay and allows water to enter the pavement, which reduces the pavement's load-bearing capacity and causes the entire pavement structure to deteriorate. Reflective cracking also has a significant negative impact on travel safety, ride comfort, and the service life of the pavement (Rigo et al. 2014). Figure A-1 illustrates the mechanism of reflective cracking. Temperature variations and repeated traffic loading can induce the stress concentration that is adjacent to the tip of the crack in the existing pavement. An initial crack forms and propagates through the overlay due to the effects of bending, shear, and thermal contraction (Lytton 1989).

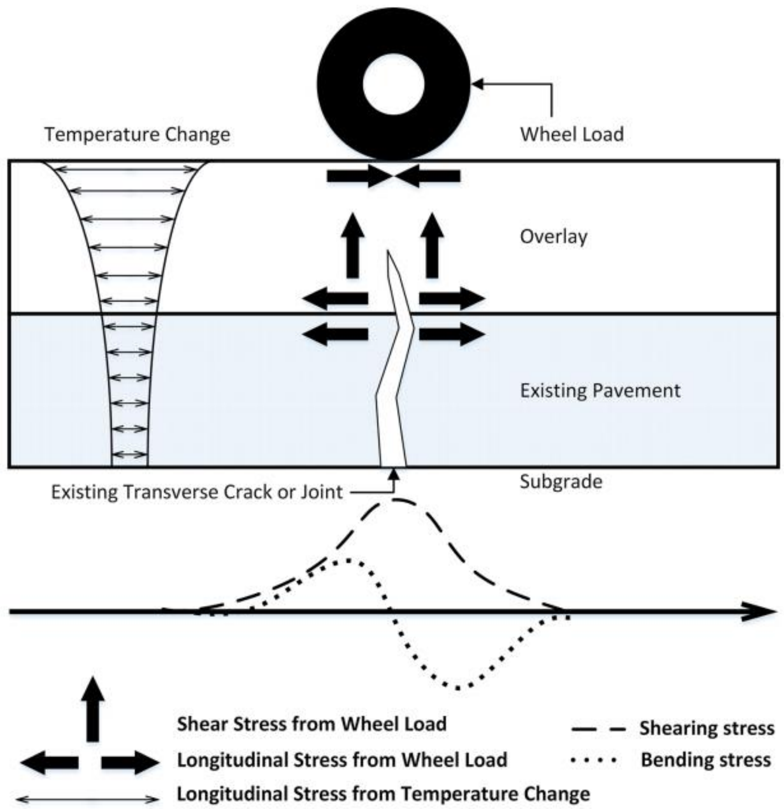

Figure A-1. Mechanism of reflective cracking (Sudarsanan et al. 2015).

Methods to mitigate reflective cracking include rubblization, milling, placing a chip seal, sealing, increasing the overlay thickness, and installing a stress-absorbing membrane interlayer (SAMI) (Blankenship et al. 2004, Makowski et al. 2005, Zhiming 1997, Zhou and Sun 2000). However, a properly selected and constructed geosynthetic interlayer is one of the most promising ways to mitigate or control reflective cracking (Baek 2010, Khodaei and Falah 2009, Mukhtar and Dempsey 1996).

A.2. Functions of Geosynthetics

The three primary functions of geosynthetic materials are to reinforce the interlayer, relieve stress in the interlayer, and to provide a moisture barrier. The reinforcing function of geosynthetic products, such as paving fabrics and paving grids, requires the product to have a significantly higher modulus value (more than five times) at the interface than the AC layer in which it is embedded (Lytton 1989). Sprague et al. (1998) also found that geosynthetic products with stiffness values higher than 200 kN/m at a strain between 2% to 5% are able to provide sufficient reinforcement for overlays. When a reflective crack reaches the reinforced interlayer, the original perpendicular crack propagation will change and move in the horizontal direction below the reinforced interlayer. A properly installed reinforcing geosynthetic interlayer thus can indefinitely delay reflective cracking (Button and Lytton 1987). The reinforcing function of geosynthetic products also requires a sufficient overlay thickness. The common thickness that is recommended by geosynthetic product manufacturers is at least 3.81 cm (1.5 in.) (Huesker 2015, Tencate 2019).

Stress-relieving geosynthetic products have low stiffness values and are able to stall reflective cracking at the interlayer, although cracks still may form at the top of the interlayer system and propagate through the overlay. A stress-relieving geosynthetic product can store strain at a low stress level and mitigate reflective cracking (Sprague et al. 1998, Lytton 1989).

When a crack penetrates the overlay, the geosynthetic product acts as a barrier to prevent water infiltration and protect the underlying structure (Lytton 1989). A fully impregnated geosynthetic system can significantly reduce water permeability. However, extra care should be taken when compacting the overlay as a permeable overlay can allow water to be trapped at the reinforced layer, which will cause the rapid failure of the overlay due to moisture damage (Bognacki et al. 2007).

A.3. Debonding

The interlayer bond between the AC surface and underlying course significantly influences the performance of asphalt pavement (Khweir and Fordyce 2003, Kruntcheva et al. 2005, Sudarsanan et al. 2016). The different pavement layers act together as a monolithic structure that efficiently transfers the stress and strain that are caused by temperature changes and repeated traffic loading. This efficient transfer of stress and strain requires an adequate interlayer bond. An insufficient interlayer bond leads to the concentration of stress and may result in debonding (Su et al. 2008). Debonding causes the slippage or delamination of the surface course, and such premature distress significantly decreases the service life of the pavement (Hachiya et al. 1997, Peattie 1980, Sutanto 2009). Figure A-2 illustrates the stress at the interlayer that is caused by moving traffic. Raab and Partl (2004) found that the tension mode, shear mode, or a combination of tension and shear modes could characterize debonding in fracture mechanics.

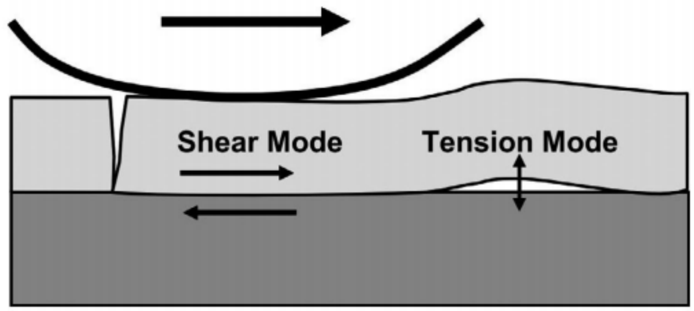

Figure A-2. Stress at interlayer caused by moving traffic (Raab and Partl 2004).

A.4. Factors that Influence Bonding

A.4.1 Tack Coat Type

Asphalt emulsion is widely used in tack coat applications in the field. Based on the emulsion curing time, emulsions can be categorized into rapid-setting (e.g., CRS-2), medium-setting, and slow-setting (e.g., SS-1, CSS-1) emulsions. A survey conducted by Mohammad et al. (2012) indicates that slow-setting emulsions are widely used worldwide because they are easy to spray and are not too costly. The selection of the asphalt emulsion type depends on the construction window, traffic conditions, and environmental temperature. If the emulsion fails to meet the construction conditions, then the interlayer bond strength cannot be guaranteed and premature distress may occur. Asphalt emulsions are not commonly used in geosynthetic-reinforced interlayer installations for several reasons. For example, Button and Lytton (2007) found that most emulsions have less viscosity than asphalt binder and thus may not provide a sufficient bond. Also, a geosynthetic-reinforced interlayer requires a high application rate for emulsion, depending on the emulsion's binder content. This high application rate will lengthen the curing time and can lead to difficulties in construction.

Asphalt binder is a tack coat material that can generate greater interlayer bond strength compared to most asphalt emulsions. Also, the application of asphalt binder does not require a curing time, so it is recommended for geosynthetic-reinforced interlayer construction (Button and Lytton 2007). However, due to asphalt binder's high viscosity compared to asphalt emulsion, it must be heated to a high temperature to ensure an even spray.

Cutback asphalt should not be used for polymer types of geosynthetic products because the solvent will remain in the geosynthetic layer and further deteriorate the polymer (Button and Lytton 2007).

A.4.2 Tack Coat Application Rate

The tack coat application rate impacts the interlayer bond performance. An excessive amount of tack coat or too little tack coat can induce premature distress in the pavement. However, researchers debate whether an optimum tack coat application rate is even possible (Al-Qadi et al. 2008, Bae et al. 2010, Mohammad et al. 2002, Raposeiras et al. 2013). Table A-1 and Table A-2 list the tack coat application rates for different surface conditions recommended in National

Cooperative Highway Research Program (NCHRP) Report 712 and the 2016 Federal Highway Administration (FHWA) Tech Brief, respectively (Mohammad et al. 2012).

Table A-1. NCHRP Report 712 Recommended Tack Coat Application Rates (Mohammad et al. 2012)

Surface type	Residual application rate (gal/yd^2)
New asphalt mixture	0.035
Old asphalt mixture	0.055
Milled asphalt mixture	0.055
Portland concrete cement	0.045

Table A-2. FHWA Tech Brief Recommended Tack Coat Application Rates (FHWA 2016)

Surface type	Residual application rate (gal/yd^2)
New asphalt mixture	0.02-0.05
Old asphalt mixture	0.04-0.07
Milled asphalt mixture	0.04-0.08
Portland concrete cement	0.03-0.05

The asphalt retention rate of geosynthetic material also should be taken into consideration when applying tack coats for geosynthetic-reinforced interlayers. Amini (2005) suggested that the tack coat application rate for geosynthetic products is the same as the tack coat application rate for a particular pavement surface type plus the asphalt retention rate. However, an excessive tack coat application may cause difficulties during the installation of the geosynthetic-reinforced interlayer (Button and Lytton 2007).

A.4.3 Curing Time

Discrepancies are evident regarding the effect of curing time. The Washington State Department of Transportation (WDOT) found that the curing time is not a significant factor in influencing shear strength (Tashman et al. 2006). However, uncured asphalt emulsion that fails to achieve the design tack coat application rate in the field is commonly reported to be lifted/tracked by the wheels of haul trucks. Trackless tack coats can solve this problem of tracking. The setting time for trackless tack coats is between 5 and 15 minutes and provides sufficient bond strength (Bae et al. 2010, Mohammad et al. 2011).

A.4.4 Surface Texture

Wilson et al. (2017) found that milled pavements provide high interlayer bond strength. However, in their study, the shear strength of milled specimens cored from the field did not differ from that of unmilled specimens. Wilson et al. (2017) claimed that this discrepancy might be due to moisture damage to the milled specimens. WDOT researchers extracted field cores from both unmilled and milled surfaces and found that the milled surface texture provides better shear resistance than the unmilled surface (Tashman et al. 2006).

A.5. Test Methods

Various assessment methods used in the field or laboratory can shed light on interface shear properties. For laboratory conditions, various tests can be performed using either field-cored or laboratory-prepared specimens. Such laboratory tests allow the experimental setting to be controlled more accurately and can obtain better repeatability and reproducibility than field tests.

Fracture mechanics interlayer bonding assessment tests typically are categorized as the Mode I tension opening test, Mode II in-plane shear test, and Mode III out-of-plane shear test (Collop et al. 2011), as shown in Figure A-3. These tests cover a wide range of methods and conditions to capture interface shear properties. The different test protocols require various respective test devices. Due to the multiple factors that contribute to interface shear properties, the selection of the test method is closely related to the mode of loading, failure mode, and testing accuracy. The Mode II in-plane shear test is commonly used to characterize interface shear properties because it is easy to perform and closely mimics *in situ* conditions, which are helpful in better understanding the mechanisms of interface shear properties. The Mode II in-plane shear test can be categorized further into the direct shear test and simple shear test. The interface shear property is controlled by various factors, such as test temperature, loading rate, material type, tack coat application rate, and interaction among those factors (Boulangé and Sterczynskia 2012).

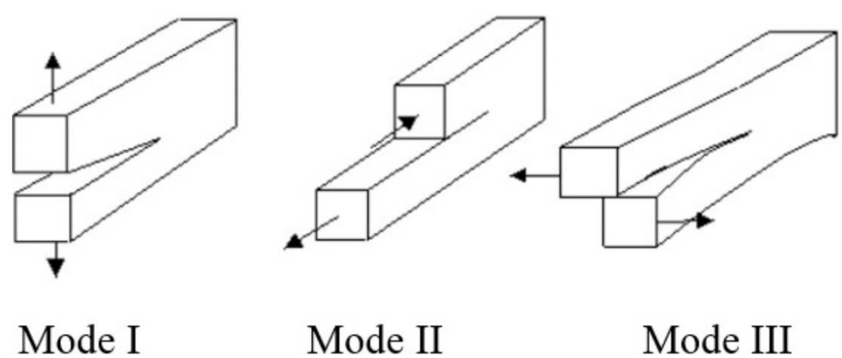

Figure A-3. Crack modes of fracture mechanics.

The Leutner test was developed in Germany based on soil mechanics principles, and its counterpart shear test was developed in the United States by Uzan (1978). The Mode II plane shear test can be categorized into the 'guillotine' type of direct shear test or a shear box simple shear test. Figure A-4 shows the stress distribution for the direct shear test and simple shear test.

Note that the direct shear test has a significant shear stress concentration and the simple shear test has a parabolic shear stress distribution.

(a) 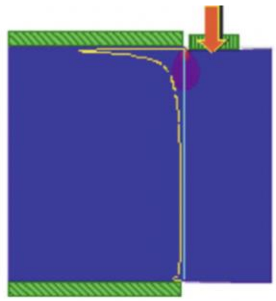 (b) 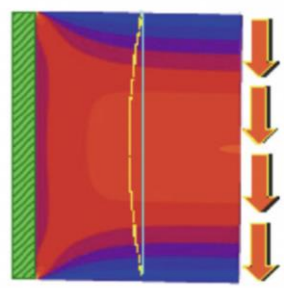

Figure A-4. Shear stress distribution: (a) direct shear test and (b) simple shear test (Raab et al. 2009).

Generally, the direct shear test does not require a confining pressure apparatus. Normal stress plays a critical role in dictating the interface asphalt mixture interlock and friction behavior. Therefore, some researchers use an extra load cell or an actuator to induce normal stress. The shear test device typically is installed in a servo-hydraulic loading system (e.g., the Material Testing System/MTS) that controls the mode of loading, with an extra environmental chamber to maintain the testing temperature. The typical laboratory-prepared specimen is double-layered with a cylindrical or cubical shape. In order to address interface alignment issues, a gap is introduced between the shear device's two shearing rings.

A.5.1 Ancona Shear Testing Research and Analysis (ASTRA) Device

Figure A-5 presents an illustration of the Ancona Shear Testing Research and Analysis (ASTRA) device that was developed in Italy in 2005 by researchers at the Universita Politecnica delle Marche in Ancona. ASTRA is a simple shear tester that is used to perform shear tests of double-layered specimens. The shear box holds the 95-mm diameter cylindrical specimen. During the test, a constant vertical normal load is maintained on the specimen. Also, a linear variable displacement transducer (LVDT) is used in the ASTRA system to record the specimen's deformation. ASTRA's measuring system records the interface shear stress and vertical displacement. Conducting ASTRA tests at different deformation rates and temperatures can yield adhesion and friction parameters for constructing a Mohr-Coulomb type envelope (Pasquini et al. 2015).

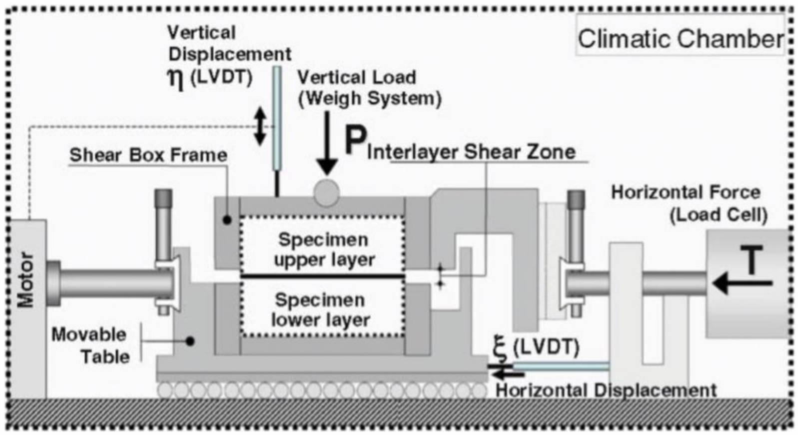

Figure A-5. Ancona Shear Testing Research and Analysis (ASTRA) device (Pasquini et al. 2015).

A.5.2 Louisiana Interlayer Shear Strength Tester (LISST)

Figure A-6 presents an illustration of the Louisiana Interlayer Shear Strength Tester (LISST), developed by researchers at Louisiana State University. The LISST is used for 100-mm or 150-mm diameter double-layered test specimens. It is composed of a shearing frame and reaction frame. During the test, the shearing frame is connected to the loading system while the reaction frame remains stationary. This test employs the displacement rate of 2.54 mm/min and test temperature of 25°C ± 1°C. The normal confining pressure is applied at up to 206.84 kPa (30 psi) (Mohammad et al. 2018).

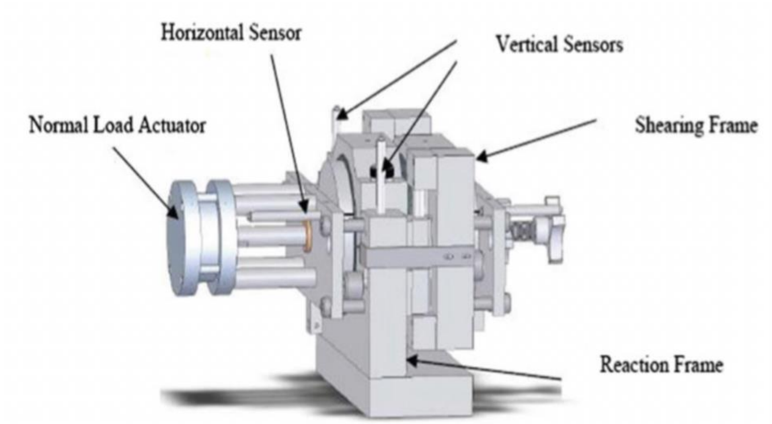

Figure A-6. Louisiana Interlayer Shear Strength Tester (LISST) (Mohammad et al. 2018).

A.5.3 Sapienza Direct Shear Testing Machine

Figure A-7 presents a schematic illustration of the Sapienza direct shear testing machine, developed by researchers at the Sapienza University of Rome (Tozzo et al. 2014). The tests are performed using 100-mm diameter double-layered specimens. The gap between the two molds is 10 mm. This test controls the load with the frequency of 5 Hz, and the test temperature is 21°C ±

1°C. The Tozzo et al. (2014) study found that normal pressure significantly affects interface fatigue properties. Monotonic shear tests exhibit the same trend as cyclic fatigue shear tests with regard to the effects of normal pressure.

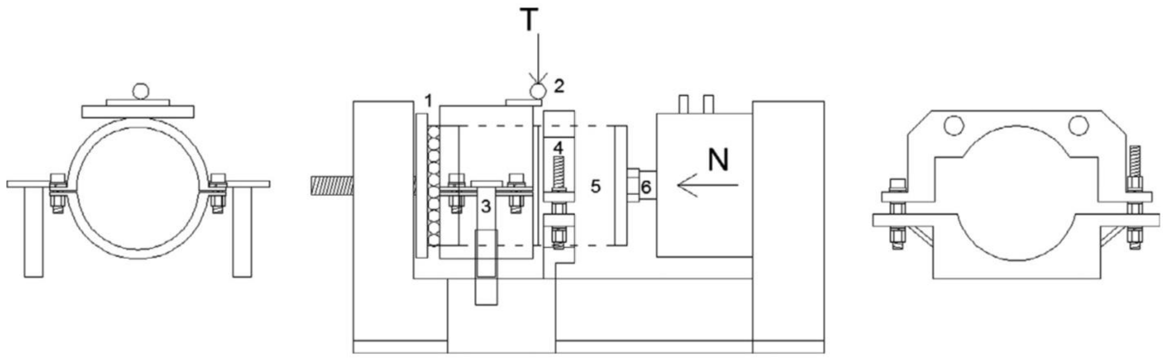

Figure A-7. Sapienza direct shear testing machine (Tozzo et al. 2014).

A.5.4 Advanced Shear Tester

Figure A-8 shows the Advanced Shear Tester designed in 2015 by Zofka et al. (2015). This shear test device can be installed in a servo-hydraulic loading system with an extra environmental chamber. The laboratory-prepared specimen used in this device is a double-layered 150-mm diameter cylindrical specimen.

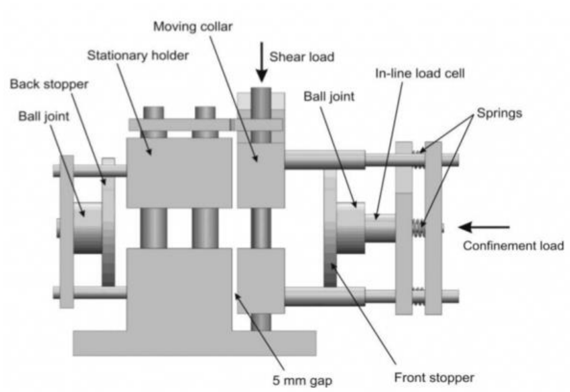

Figure A-8. Advanced Shear Tester (Zofka et al. 2015).

Zofka et al. (2015) stated that the boundary conditions for the shear test can be divided into constant normal load, constant normal stiffness, and constant volume. Although the constant normal load condition is used for most shear devices, Zofka et al. (2015) proposed that the constant normal stiffness condition is preferable because it mimics a low-speed heavy truck for the thin layer condition. Also, the dilation property at the interlayer cannot be explained comprehensively by the constant normal load condition. Therefore, constant normal stiffness could be a suitable candidate for the constant normal load condition to be used for the shear device. Also, when using a constant normal load, a vertical actuator should be installed to maintain the load. However, a constant normal stiffness shear device uses die springs to maintain the confining pressure, which significantly lowers the cost of the device.

A.5.5 Modified Asphalt Shear Tester (MAST)

By modifying Zofka et al.'s Asphalt Shear Tester, a North Carolina State University research team developed the Modified Asphalt Shear Tester (MAST), shown in Figure A-9 (Cho 2016). The MAST is capable of conducting shear tests in both monotonic and fatigue modes of loading under confining pressure. A cylindrical specimen with a diameter of 101.6 mm (4 in.) extracted from a 152.4-mm (6-in.) gyratory-compacted sample or a square specimen, either 152.4-mm (6-in.) square or 101.6-mm (4-in.) square, trimmed from a slab sample can be used for MAST shear tests. The original Asphalt Shear Tester allows only cylindrical gyratory-compacted specimens 150 mm (6 in.) in diameter to be tested. As is well known, an air void gradient exists along the periphery of gyratory-compacted specimens (Chehab et al. 2000). Therefore, using a 101.6-mm (4-in.) specimen cored from a 150-mm (6-in.) gyratory-compacted sample in the MAST nullifies the uncertainties of the air void effect on the test outcomes.

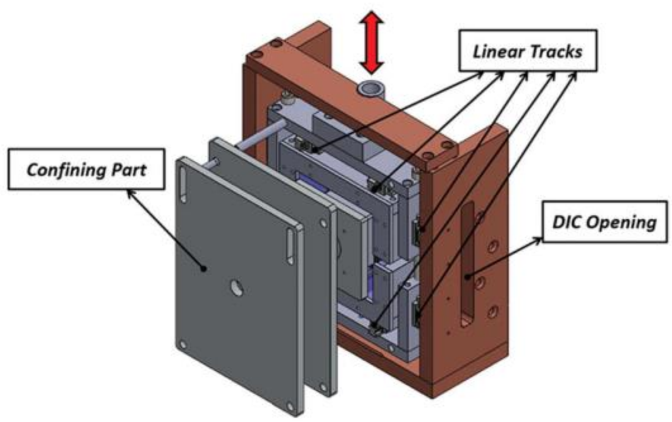

Figure A-9. Modified Asphalt Shear Tester (MAST) (Cho et al. 2017b).

The initial confining pressure is controlled by an in-line load cell and by tightening the bolts on the side panel. The technique employed to apply confining pressure is the same for both the Asphalt Shear Tester and the MAST. However, the methods used to fasten the specimen to the test device vary vastly. For the Asphalt Shear Tester, the user connects the specimen directly to the device's upper jaw and lower jaw of the moving and stationary collars by tightening the threaded bolt and nut arrangement. The specimen typically expands during shear tests due to the aggregate rearrangement along the interface. Therefore, the frictional forces between the collar walls and the specimen cannot hold the specimen in place, which leads to slippage. This slippage affects the shear and confining load cell readings during the test. The MAST addresses this problem via gluing the specimen firmly to a four-set 'shoe' arrangement. The shoe is fastened to a stationary portion of the MAST jig that is free to move horizontally (along the confining pressure load cell) with the aid of linear tracks. Thus, the MAST allows the free expansion of the specimen during testing without any slippage along the walls of the shoe.

The gap between the fixed and movable side platens of MAST is 8 mm. Even though the specimen is fastened to the jig firmly using shoes, the large bending moment that is generated during the test causes a rocking motion. The MAST includes the provision to monitor the on-specimen displacements during such events with the aid of the non-contact digital image correlation (DIC) technique. The MAST is designed to have an opening on one side, which allows the DIC system to track on-specimen displacements. All the aforementioned factors make the MAST a superior device over the original Asphalt Shear Tester.

Figure A-10 shows the typical confining pressure during a MAST monotonic shear test. The confining pressure recorded by the in-line load cell varies from the initial stress by 5% and stabilizes after reaching peak shear.

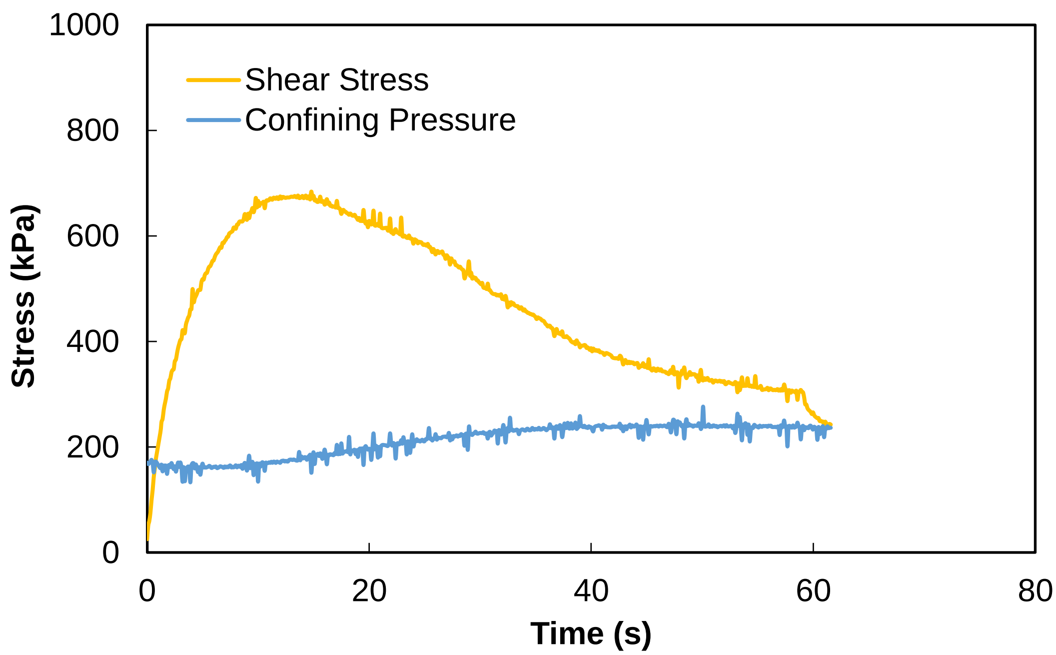

Figure A-10. Typical MAST test results.

Cho and Kim (2016) verified the time-temperature superposition principle with regard to the shear failure of double-layered asphalt concrete specimens with different tack coats and a GlasGrid interlayer. They proposed a shear strength prediction model to predict the shear strength at various confining pressures, temperatures, and shear strain rates. Cho and Kim (2016) also conducted FlexPAVE™ analysis to determine the potential debonding state. Figure A- 11 describes the shear ratio concept whereby the shear ratio is the FlexPAVE™-computed shear stress to the model-predicted shear bond strength. The maximum shear ratio (MSR) is presented as an index parameter to determine the pavement's debonding potential (Cho et al. 2017a).

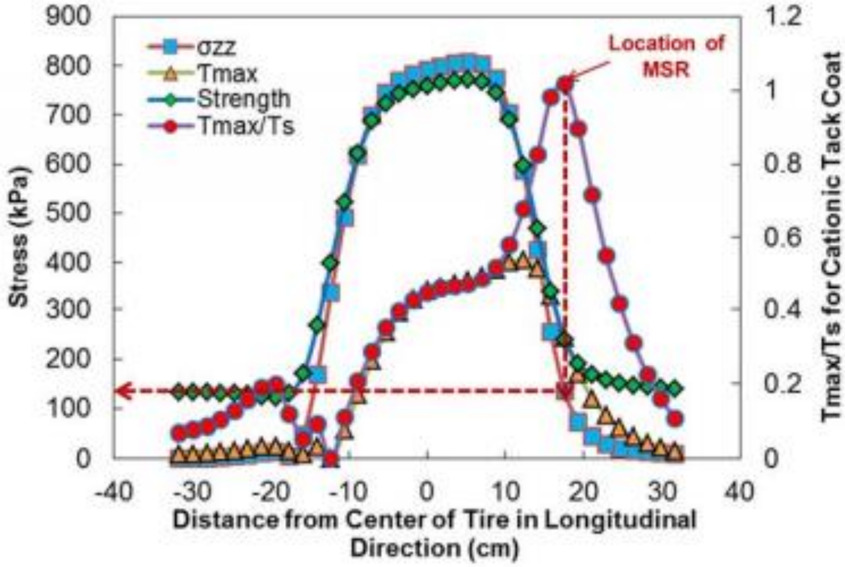

Figure A- 11. Shear ratio concept.

A.6. Bonding of Geosynthetic-Reinforced Interlayer

Baek (2010) found that the shear bond strength at the interface is a good indicator of the potential for reflective cracking; i.e., low interface bond strength could increase the possibility of reflective cracking. A geosynthetic reinforcement at the interlayer can compromise the bond strength of the interlayer (Canestrari et al. 2016b, Pasquini et al. 2013). However, an adequate bond will sufficiently distribute the stress and guarantee the functionality of the geosynthetic-reinforced interlayer. In addition, the improper installation of a geosynthetic-reinforced system can compromise the geosynthetic interlayer's ability to mitigate reflective cracking propagation, which in turn negatively affects the durability of the pavement (Ferrotti et al. 2012, Vanelstraete and De Bondt 2004).

Canestrari et al. (2006) used ASTRA to conduct shear tests of specimens reinforced with two types of glass geogrid, polyester geogrid, and geomembrane. The top layer of the reinforced double-layered system was a dense-graded mix, and the bottom layer was either a dense-graded mix or open-graded mix. The Canestrari et al. (2006) study results show that the larger mesh dimensions (25×25 mm^2) of the paving grid provide better shear resistance than the smaller mesh dimensions (12.5×12.5 mm^2). With a smaller mesh size, the residual friction angle from the friction envelope also is smaller. The Canestrari et al. (2006) research shows also that the bottom layer surface condition does not have any impact on the shear strength of geomembrane-reinforced specimens. In another paper, Canestrari et al. (2016b) found that thicker geosynthetic products could significantly decrease the shear strength of the interlayer.

Vismara et al. (2012) conducted monotonic shear tests to investigate the performance of geosynthetic-reinforced interlayers. Polypropylene nonwoven and fiberglass grid composite reinforced slab specimens were subjected to Leutner shear tests at 5°C and 25°C with a constant deformation rate of 0.85 mm/s (2 in./min). Vismara et al. (2012) found an average 70% reduction in shear strength in the geosynthetic-reinforced specimens compared to the control specimen.

Ferrotti et al. (2011) performed monotonic shear tests of both paving grid-reinforced specimens and unreinforced specimens at 20°C. The tests were performed at three confining pressures (0 MPa, 0.2 MPa, and 0.4 MPa) at the constant displacement rate of 2.5 mm/min (0.1 in./min) to obtain shear strength and friction envelopes. Under unconfined conditions, the shear strength of the paving grid-reinforced specimens was lower than that of the unreinforced specimens; however, this trend reversed with confining pressure. Among the grid-reinforced specimens tested, the polymer-modified emulsion specimen exhibited greater shear resistance than the conventional emulsion type specimen under all three confining pressures. Ferrotti et al. (2011) found a similar residual friction angle for both the grid-reinforced and unreinforced specimens. They reported that, due to the poor interlayer bond, one double-layered specimen was separated during the specimen coring process. This specimen did not have any tack coat applied to it. The researchers claimed that this problem is attributed to poor quality of asphalt loose mix that was produced in a mix plant. They claimed also that, for the same reason, unreinforced specimens show greater variability in monotonic shear tests.

Sudarsanan et al. (2018a) conducted Leutner shear tests of three different geosynthetic materials (Jute, Coir, and Synthetic GlasGrid). They found that, with the inclusion of a geosynthetic product, the interlayer's shear strength exhibits a certain reduction that takes place in conjunction with the tensile modulus of corresponding geosynthetic products whereby the geosynthetic products with higher modulus values experience less shear strength reduction. The shear tests are reported to have more variability at lower temperatures and higher deformation rates. When the temperature is increased from 10°C to 30°C, the shear strength decreases by nearly 80 percent.

A.7. Critical Summary

Many methods can be used to mitigate reflective cracking, including rubblization, milling, placing chip seals, sealing, increasing the overlay thickness, and installing a SAMI. Placing a geosynthetic interlayer is one of the most promising ways to mitigate or control reflective cracking.

The three primary functions of geosynthetic products are to reinforce the interlayer, relieve stress, and provide waterproofing. The reinforcing function requires the geosynthetic material to have a significantly greater modulus than the surrounding asphalt layer. The reinforcement redirects any crack propagation at the interlayer, which can indefinitely delay or mitigate reflective cracking. Stress-relieving geosynthetic products have lower stiffness values and can store strain at a low stress level. A fully impregnated geosynthetic system can significantly reduce water permeability. Proper installation, adequate overlay thickness, and compaction quality also are required to achieve these primary functions of geosynthetic interlayers.

A tack coat is required for geosynthetic-reinforced interlayer construction. Cutback asphalt should not be used for polymeric types of geosynthetics because the solvent will remain in the geosynthetic layer and further deteriorate the polymer. Geosynthetic-reinforced interlayers require a high application rate for emulsions, depending on the binder content. However, this high application rate will lengthen the curing time and may lead to difficulties in construction. By contrast, the application of asphalt binder does not require a curing time and the application rate is satisfactory for construction. Therefore, asphalt binder is recommended as the tack coat in geosynthetic-reinforced interlayer systems. Some researchers suggest that the tack coat application rate for geosynthetics in practice is the tack coat application rate for a pavement surface type plus the asphalt retention rate. However, an excessive tack coat application may cause difficulty during geosynthetic product installation.

The direct shear test is helpful in understanding the mechanism of interface shear properties. Geosynthetic material installed at the interlayer decreases the interlayer's shear bond strength, and low interface bond strength increases the possibility of reflective cracking. Also, improper installation of the geosynthetic material will compromise the geosynthetic product's ability to stall or mitigate reflective cracking propagation. In addition, thicker geosynthetic products significantly decrease the interlayer's shear strength.

Appendix B. Beam Bending Theory and Four-Point Beam Bending Stress/Strain

Classical beam bending theory is an essential consideration for nearly all structural designs and analyses. To evaluate the bending stress or strain in a four-point bending beam test, consider a small element cut from the middle one-third of the beam, as shown in Figure B- 1 (a). Due to the bending action, the element will be deformed, as shown in Figure B- 1 (b). The amount by which a layer increases or decreases in length depends upon the position of the layer with respect to the neutral axis (N-N). The layers above the N-N axis will reduce the layer length when subjected to compressive stress whereas the layer length will increase for layers below the N-N axis under tensile stress. This theory of bending is known as the theory of simple bending.

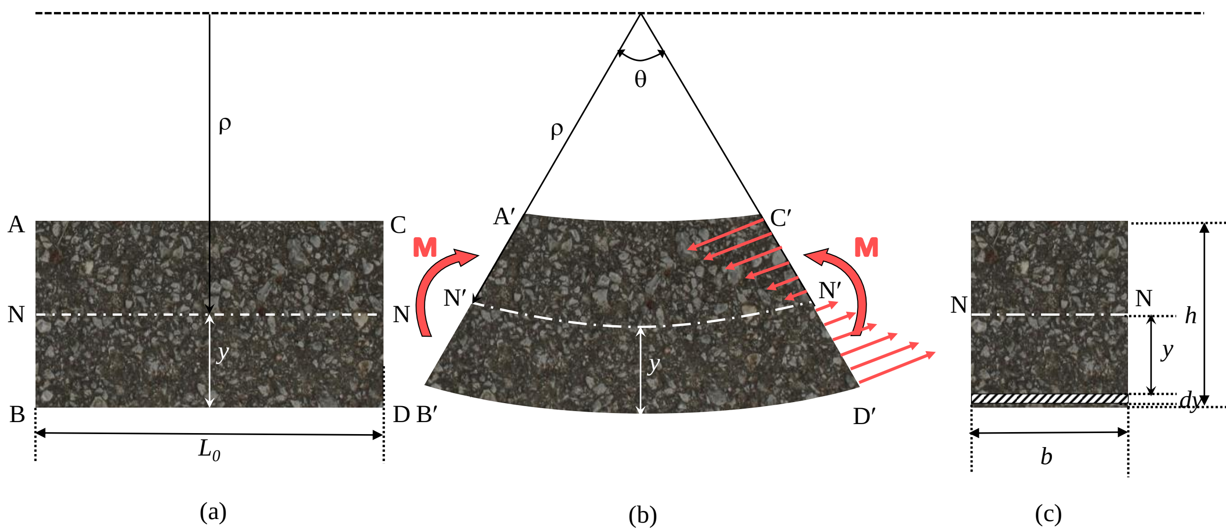

Figure B- 1. Beam bending of a small element: (a) before bending, (b) after bending, and (c) sectional view.

B.1. Bending strain

The arc length, L, is related to the radius of the curvature, ρ, through $L = \rho\theta$, where θ is the bending angle. In Figure B- 1, an object of initial length L_0 is bent as shown. Because the object has a finite thickness, different portions of it are stretched or compressed by different degrees. The outer portion of the beam is extended the most because it is farthest from the center. Mathematically, all portions are bent to the same angle, θ, but ρ varies throughout the thickness. Thus, the quantity $\rho\theta$ varies too, and therefore, L varies as well.

The next step is to avoid the confusion of having different radii of curvatures through the thickness of the bent object. This step is accomplished in two steps. First, find the one ρ that satisfies $\rho\theta = L_0$. Note that ρ is the computed result here, and θ and L_0 are the inputs. Note also that the length in the equation is L_0, which is the original undeformed length, not the deformed length. This step establishes one unique value of ρ for the cross-section rather than multiple values that could lead to much confusion. The second step is to introduce the variable y as the distance from the neutral axis to any other radius in the cross-section. Here, we consider the strain in the farthest layer, i.e., the tensile strain at the bottom of the beam.

The basic definition of normal strain is shown in Equation (B-1).

$$\varepsilon = \frac{\Delta L}{L} \quad \text{(B-1)}$$

Using the line segment, *BD*, the before bending [Figure B- 1 (a)] length and the after bending [Figure B- 1 (b)] length, $B'D'$, are used to measure the tensile strain, as shown in Equation (B-2).

$$\varepsilon = \frac{\overline{B'D'} - \overline{BD}}{\overline{BD}} \quad \text{(B-2)}$$

The line length *BD* is the same for all locations in the same element before bending. However, $B'D'$ lengthens as it is below the neutral axis for positive moment. The lines *BD* and $B'D'$ can be described using the radius of curvature ρ, and the bending angle θ, as shown in Equations (B-3) and (B-4), respectively.

$$\overline{BD} = \rho\theta \quad \text{(B-3)}$$

$$\overline{B'D'} = (\rho + y)\theta \quad \text{(B-4)}$$

Substituting Equations (B-3) and (B-4) into Equation (B-2) yields Equation (B-5).

$$\varepsilon = \frac{(\rho + y)\theta - \rho\theta}{\rho\theta} \Rightarrow \varepsilon = \frac{y}{\rho} \quad \text{(B-5)}$$

Equation (B-5) is a key result of the strain in the beam. It shows that the strain is zero at $y = 0$, the neutral axis, and varies linearly from it. If the object is thick, then y can take on large values, but for thin objects, it cannot. This phenomenon is the fundamental reason that thick objects have more bending stiffness (resistance to bending) than thin objects.

Also, the radius of the curvature in the denominator accounts for many effects of bending. When the object is not bent, then ρ is infinite and the strains are naturally zero. As the object bends, ρ decreases, and the equation shows that the strain values will increase.

Finally, note that the strain is normal strain and is, in fact, longitudinal along the length of the beam. It is common to align the x-axis along the beam's length, defining the strain, ϵ_x, as shown in Equation (B-6).

$$\varepsilon_x = \frac{y}{\rho} \tag{B-6}$$

B.2. Bending stress

Applying Hooke's Law, $\sigma_x = E \times \epsilon_x$, in Equation (B-6) to obtain stress, σ_x, yields Equation (B-7).

$$\sigma_x = \frac{Ey}{\rho} \tag{B-7}$$

Hooke's Law also states that each normal stress component is dependent on all three normal strain components. But here, the strain is multiplied by E to obtain the stress, assuming that no lateral loads/stresses are acting on the beam (like in uniaxial tension). This phenomenon occurs in most beams because they are thin relative to their length.

Measuring the radius of curvature is difficult and, hence, establishing a relationship with the bending moment would facilitate the measurements. Bending induces stress in the beam layers, thereby generating both compressive and tensile forces. These forces will have a moment about the neutral axis. The total moment of these forces about the neutral axis for a section is known as the moment of resistance of that section. Consider a cross-section of a beam, as shown in Figure B- 1 (c), where the thin layer at the bottom of the section has an area dA at distance y, as described by Equation (B-8).

$$\text{Force on layer} = \frac{E}{\rho} \times y \times dA \tag{B-8}$$

$$\begin{aligned} \text{Moment of this force about the neutral axis} &= \text{Force on layer} \times \text{y} \\ &= \frac{E}{\rho} \times y \times dA \times y \\ &= \frac{E}{\rho} \times y^2 \times dA \end{aligned}$$

The total moment of the forces on the section of the beam (or moment of resistance):

$$\therefore M = \int \frac{E}{\rho} \times y^2 \times dA = \frac{E}{\rho} \int y^2 \times dA$$

Note that the integral is the area moment of inertia, I_{zz}, or the second moment of the area.

$$\because I_{zz} = \int y^2 \times dA$$

Using the area moment of inertia gives Equation (B-9).

$$M_z = \frac{EI_{zz}}{\rho} \tag{B-9}$$

Substituting Equation (B-9) into Equation (B-7) gives Equation (B-10).

$$\sigma_x = \frac{M_z y}{I_{zz}} \tag{B-10}$$

Equation (B-10) gives the normal bending stress and is commonly called the flexure formula.

All these relationships, i.e., Equations (B-7) through (B-10), lead to the Euler-Bernoulli bending equation, shown here as Equation (B-11).

$$\frac{M}{I} = \frac{\sigma}{y} = \frac{E}{\rho} \tag{B-11}$$

The fatigue test involves the application of load or displacement in both the compression and tension direction. Consider compression loading in a four-point bending beam test with a deflection δ (negative for compression) generated by a load application of *P*, as shown

.

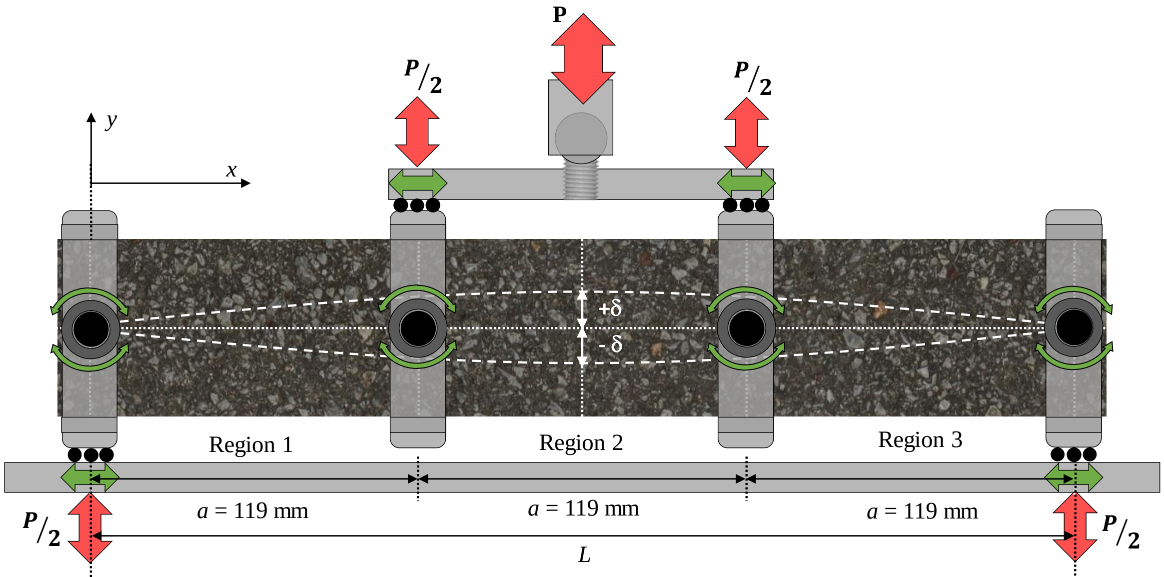

(a)

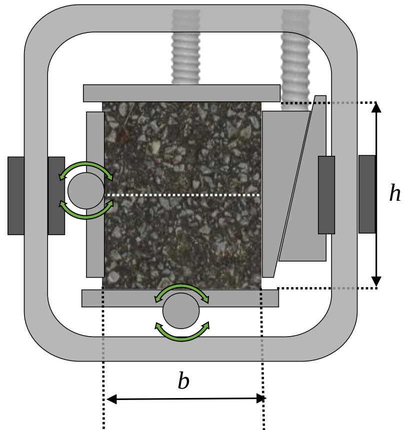

(b)

Figure B- 2. Four-pont bending beam fatigue test configuration: (a) front view and (b) sectional view.

From Equation (B-10), two factors, I_{zz} and M, should be represented in known terms, i.e., specimen dimensions and applied loads for the easy evaluation of tensile stress.

A rectangular cross-section of height h and width b has a moment of inertia shown in Equation (B-12).

$$I_{zz} = \frac{bh^3}{12} \tag{B-12}$$

The maximum moment is at the center of the beam, i.e., @ $x = L/2$, and is derived as Equation (B-13).

$$\begin{aligned} M_{z-\max} &= \frac{-P}{2}x + \frac{P}{2}(x-a) \\ \Rightarrow M_{z-\max} &= \frac{Pa}{2} \end{aligned} \tag{B-13}$$

Substituting Equations (B-12) and (B-13) into Equation (B-10) to calculate the maximum tensile stress at the extreme depths of beam sections gives Equation (B-14).

$$\sigma_{x-\max} = \frac{M_{z-\max} y_{bottom}}{I_{zz}} = \frac{{}^{Pa}\!/_{2} \times {}^{h}\!/_{2}}{{}^{bh^3}\!/_{12}}$$

$$\sigma_{x-\max} \text{ or } \sigma_t = \frac{3aP}{bh^2} \tag{B-14}$$

In order to derive the tensile strain at the bottom of the beam, the differential equations for the prismatic beams that establish the bending moment relationship, known as the bending moment equation, are as follows, i.e., Equations (B-15) through (B-31).

$$EI\frac{d^2y}{dx^2} = M \tag{B-15}$$

Region 1: x < a

$$M_1 = \frac{-Px}{2} \tag{B-16}$$

Substitute Equation (B-16) into Equation (B-15):

$$EI\frac{d^2y}{dx^2} = \frac{-Px}{2} \tag{B-17}$$

Integrate both sides of Equation (B-17):

$$EI\frac{dy}{dx} = \frac{-Px^2}{4} + C_1 \tag{B-18}$$

$$EI\theta_1 = \frac{-Px^2}{4} + C_1$$

$$\theta_1 = \frac{-Px^2}{4EI} + C_1 \tag{B-19}$$

Integrate both sides of Equation (B-18):

$$EI\delta_1 = \frac{-Px^3}{12} + C_1x + C_2$$

$$\delta_1 = \frac{-Px^3}{12EI} + C_1x + C_2 \tag{B-20}$$

Region 2: a < x < 2a

$$M_2 = \frac{-Px}{2} + \frac{-P(x-a)}{2} \Rightarrow M_2 = \frac{-Pa}{2} \quad \text{(B-21)}$$

Substitute Equation (B-21) into Equation (B-15):

$$EI\frac{d^2y}{dx^2} = \frac{-Pa}{2} \quad \text{(B-22)}$$

Integrate both sides of Equation (B-22):

$$EI\theta_2 = \frac{-Pax}{2} + C_3$$

$$\theta_2 = \frac{-Pax}{2EI} + C_3 \quad \text{(B-23)}$$

Integrate both sides of Equation (B-23):

$$\delta_2 = \frac{-Pax^2}{4EI} + C_3 x + C_4 \quad \text{(B-24)}$$

Boundary conditions

BC1	@x=0	$\delta_1=0$	BC3	@x=a	$\delta_1=\delta_2$
BC2	@x=L/2	$\theta_2=0$	BC4	@x=a	$\theta_1=\theta_2$

Applying the boundary conditions at different regions:

BC2 on Region 2, BC2: @x = L/2, θ_2 = 0 in Equation (B-23).

$$C_3 = \frac{PaL}{4EI} \quad \text{(B-25)}$$

BC4 in region 1 and 2, BC4: @x = a, $\theta_1 = \theta_2$, Equation (B-19) = Equation (B-23).

$$\frac{-Px^2}{4EI} + C_1 = \frac{-Pax}{2EI} + C_3 \Rightarrow \frac{-Px^2}{4EI} + C_1 = \frac{-Pax}{2EI} + \frac{PaL}{4EI}$$

$$\therefore C_1 = \frac{Pa}{4EI}(L-a) \quad \text{(B-26)}$$

BC1 in Region 1, BC1: @x = 0, δ_1 = 0 in Equation (B-20).

If δ_1 = 0, then C_2 should be zero:

$$\therefore C_2 = 0 \tag{B-27}$$

BC3 in Region 2, BC3: @x = a, $\delta_1 = \delta_2$, Equation (B-20) = Equation (B-24), substituting C_1, C_2, and C_3.

$$\frac{-Pax^2}{4EI} + \frac{PaL}{4EI}x + C_4 = \frac{-Px^3}{12EI} + \frac{Pa}{4EI}(L-a)x$$

$$C_4 = \frac{-Pa^3}{12EI} \tag{B-28}$$

After solving for all the constants, find the maximum tensile strain by finding the maximum deflection and moment @x = L/2 in Equation (B-24).

$$\delta_2 = \frac{-Pax^2}{4EI} + \frac{PaL}{4EI}x - \frac{Pa^3}{12EI} \Rightarrow \frac{Pa}{48EI}(3L^2 - 4a^2) \tag{B-29}$$

Consider Equation (B-10) and apply Hooke's law.

$$\varepsilon_{x-\max} = \frac{M_{\max} y_{bottom}}{EI_{zz}}$$

$$\text{where } M_{\max} = \frac{Pa}{2}, y = \frac{h}{2}$$

$$\therefore \varepsilon_{x-\max} = \frac{Pah}{4EI} \tag{B-30}$$

$$\delta_2 = \frac{Pa}{48EI}(3L^2 - 4a^2) = \frac{\varepsilon_{x-\max}}{12h}(3L^2 - 4a^2)$$

$$\varepsilon_{x-\max} \text{ or } \varepsilon_t = \frac{12\delta h}{(3L^2 - 4a^2)} \tag{B-31}$$

The maximum tensile stress (MPa) and maximum tensile strain in four-point bending beam fatigue tests were calculated using Equation (B-14) and Equation (B-31), respectively (ASTM D7460).

Appendix C. Sinusoidal fitting procedure

The procedure for analyzing the tensile strain utilizes a least-squares regression technique that first assumes that the stress and strain are represented by the functional form presented in Equation (C-1).

$$y(t) = A_0 + C_1 \cos(2\pi ft + \theta) \tag{C-1}$$

If the addition law for cosines is applied to Equation (C-1), then the function may be written as Equation (C-2).

$$y(t) = A_0 + A_1 \cos(2\pi ft) + B_1 \sin(2\pi ft) \tag{C-2}$$

where A_1 and B_1 are given by Equations (C-3) and (C-4), respectively.

$$A_1 = C_1 \cos(\theta) \tag{C-3}$$

$$B_1 = -C_1 \sin(\theta) \tag{C-4}$$

The angle, theta, can be calculated through Equations (C-3) and (C-4) as Equation (C-5).

$$\theta = \tan^{-1}\left(\frac{-B_1}{A_1}\right) \tag{C-5}$$

Note that, if θ is larger than π, then A_1 will be less than one, but from Equation (C-5), θ will be calculated as less than π. Therefore, presenting Equation (C-5) in a piecewise form, as shown in Equation (C-6), provides more accuracy.

$$\theta = \begin{Bmatrix} \tan^{-1}\left(\frac{-B_1}{A_1}\right), A_1 > 0 \\ \tan^{-1}\left(\frac{-B_1}{A_1}\right) + \pi, A_1 < 0 \end{Bmatrix} \tag{C-6}$$

The amplitude of the function, C_1, can similarly be calculated from Equations (C-3) and (C-4), from which Equation (C-7) is derived.

$$C_1 = \sqrt{A_1^2 + B_1^2} \tag{C-7}$$

Applying a least-squares model to Equation (C-2), the solution for coefficients A_0, A_1, and B_1 is given by Equation (C-8).

$$\begin{bmatrix} N & \sum\cos(2\pi ft) & \sum\sin(2\pi ft) \\ \sum\cos(2\pi ft) & \sum\cos^2(2\pi ft) & \sum\cos(2\pi ft)\sin(2\pi ft) \\ \sum\sin(2\pi ft) & \sum\cos(2\pi ft)\sin(2\pi ft) & \sum\sin^2(2\pi ft) \end{bmatrix} \begin{Bmatrix} A_0 \\ A_1 \\ B_1 \end{Bmatrix} = \begin{Bmatrix} \sum y \\ \sum y\cos(2\pi ft) \\ \sum y\sin(2\pi ft) \end{Bmatrix}$$
(C-8)

If the number of data points, *N*, is such that whole cycles can be analyzed, then Equation (C-8) may be written as Equation (C-9).

$$\begin{bmatrix} N & 0 & 0 \\ 0 & N/2 & 0 \\ 0 & 0 & N/2 \end{bmatrix} \begin{Bmatrix} A_0 \\ A_1 \\ B_1 \end{Bmatrix} = \begin{Bmatrix} \sum y \\ \sum y\cos(2\pi ft) \\ \sum y\sin(2\pi ft) \end{Bmatrix} \quad \text{(C-9)}$$

Then, coefficients A_0, A_1, and B_1 are easily given by Equations (C-10),(C-11), and (C-12) respectively.

$$A_0 = \frac{\sum y}{N} \quad \text{(C-10)}$$

$$A_1 = \frac{2}{N}\sum y\cos(2\pi ft) \quad \text{(C-11)}$$

$$B_1 = \frac{2}{N}\sum y\sin(2\pi ft) \quad \text{(C-12)}$$

Applying this methodology for tensile strain necessitates centering the stress (ε_t) so that the mean value is zero, as shown in Equation (C-13). Equations (C-6), (C-7), (C-10), (C-11), and (C-12) are then applied to the centered stress using Equations (C-13) through (C-18).

$$\sigma' = \sigma_i - \frac{\sum_{i=1}^{N}\sigma_i}{N} \quad \text{(C-13)}$$

$$A_{\sigma_0} = \frac{\sum_{i=1}^{N}\sigma'_i}{N} \quad \text{(C-14)}$$

$$A_{\sigma_1} = \frac{2}{N}\sum_{i=1}^{N}\sigma'_i\cos(2\pi ft_i) \quad \text{(C-15)}$$

$$B_{\sigma_1} = \frac{2}{N}\sum_{i=1}^{N}\sigma_i' \sin(2\pi f t_i) \tag{C-16}$$

$$\theta_\sigma = \begin{Bmatrix} \tan^{-1}\left(\dfrac{-B_{\sigma_1}}{A_{\sigma_1}}\right), A_{\sigma_1} > 0 \\ \tan^{-1}\left(\dfrac{-B_{\sigma_1}}{A_{\sigma_1}}\right) + \pi, A_{\sigma_1} < 0 \end{Bmatrix} \tag{C-17}$$

$$|\varepsilon_t| = \sqrt{A_{\sigma_1}^2 + B_{\sigma_1}^2} \tag{C-18}$$

The results of these equations then can be used with Equation (C-2) to verify the fitting procedure. The same methodology is used to measure the tensile stress $|\sigma_t|$.

The flexural or tensile stiffness of a beam specimen is measured as shown in Equation (C-19).

$$S = \frac{|\sigma_t|}{|\varepsilon_t|} \tag{C-19}$$

The phase angle (φ) is calculated using Equation (C-6) to yield Equation (C-20).

$$\phi = \theta_\sigma - \theta_\varepsilon \tag{C-20}$$

Appendix D. Laboratory Fabrication of MAST Test Specimens

Step 1. MAST test sample compaction using Superpave gyratory compactor

Figure D- 1. (a) shows the AFG2 Superpave gyratory compactor (Pine Test Equipment, Inc.) that was used to fabricate the double-layered MAST test samples for this study. The separated loose mix in cloth bags was heated to the compaction temperature of 145°C (293°F) for one hour. Then, the loose mix was batched in required quantities and placed into pans depending on whether the mix would be fabricated as a top or bottom layer. The pans containing the batched loose mix were placed in an oven at the compaction temperature of 145°C (293°F) for another hour. The molds and necessary test accessories (such as spatulas) also were heated in another oven for an hour to reach a temperature 10°C higher than the compaction temperature of 155°C (311°F). Subsequently, the bottom layer was compacted in a 150-mm (6-in.) diameter gyratory compaction mold to a height of 50.8 mm (2 in.) to create the bottom layer of the test specimen. Figure D- 1. (b) shows the compaction molds. Typically, a cooling period of 24 hours is required before applying the tack coat. The tack coat is applied uniformly using a hot spray gun to achieve a consistent thickness on the top of the bottom layer. Details regarding the tack coat application process using a hot spray gun are provided in the following section.

(a) (b)

Figure D- 1. (a) Superpave gyratory compactor (Pine Test Equipment, Inc.) and (b) compaction molds.

After the tack coat application process was completed, the bottom layer was placed back into the hot mold, and the top layer was compacted directly on top of it. No wait time was needed for the top layer compaction because hot binder was used as the tack coat. The same compaction process that was followed for the bottom layer was repeated for the top of the bottom layer to produce the upper AC layer with a thickness of 50.8 mm (2 in.). Thus, the total height of the MAST test sample becomes 101.6 mm (4 in.). Figure D- 2. presents the double-layered MAST test sample compaction procedure.

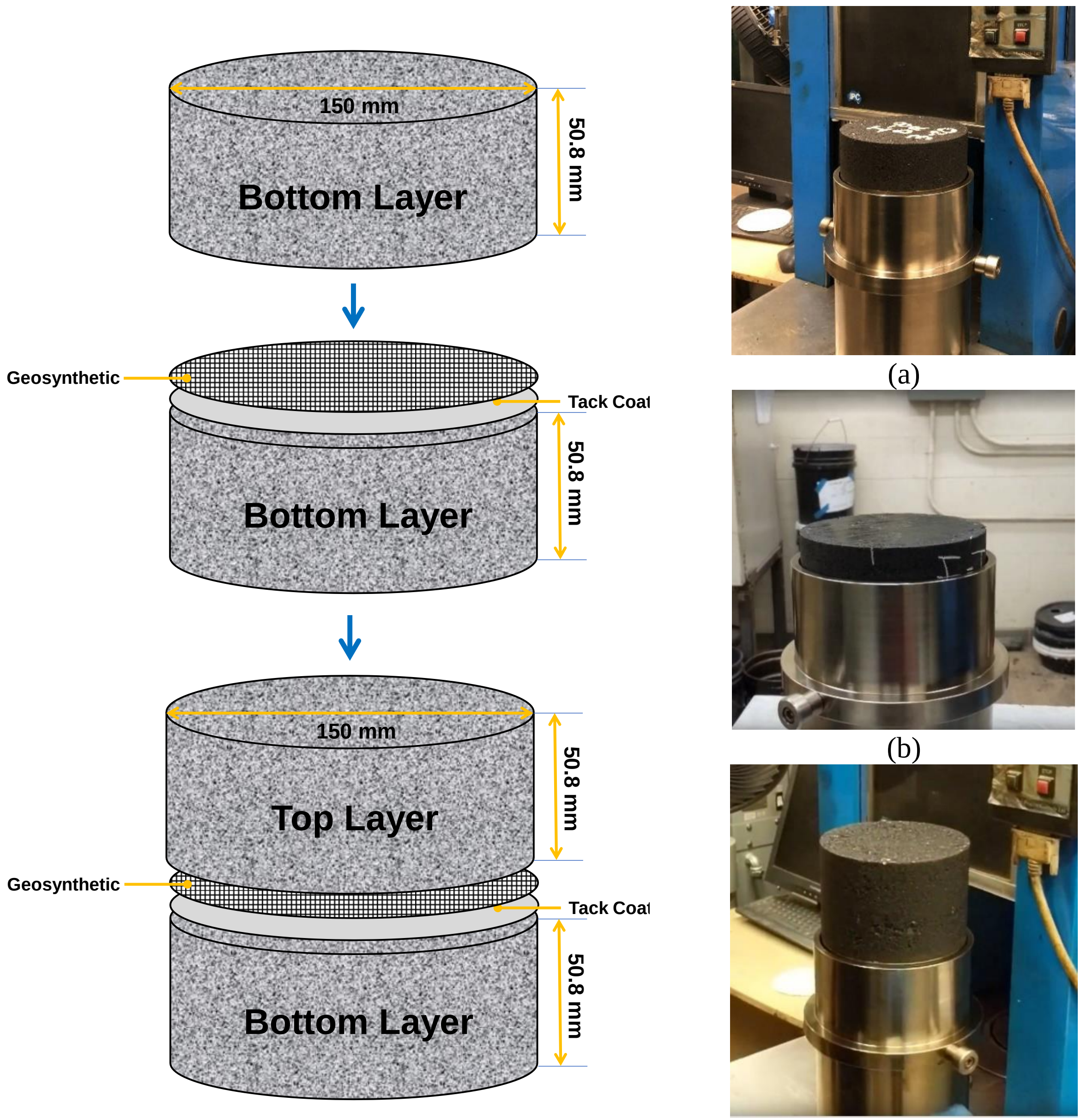

(c)

Figure D- 2. Compaction procedure for double-layered MAST test sample: (a) bottom layer fabrication, (b) bottom layer placement in hot mold with tack coat, and (c) completed MAST test sample.

Step 2. Geosynthetic material preparation for MAST samples

Geosynthetic circular samples, 140 mm (5.51 in.) in diameter, were cut from a roll of geosynthetic material to fabricate the geosynthetic-reinforced MAST test samples. Geosynthetic products typically are unrolled such that the machine direction (MD) aligns in the traffic direction, as shown in Figure D- 3. The geosynthetic samples were extracted diagonally to avoid replicating any manufacturing defects in the MD and cross-machine direction (xMD). Figure D-

4. (a) illustrates the template used for the trimming pattern. Figure D- 4. (b) and (c) show the template traced over PC#1 and PM, respectively.

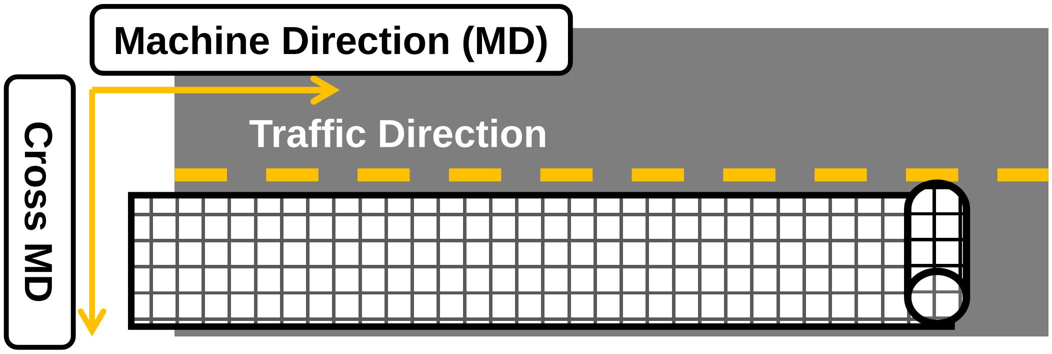

Figure D- 3. Alignment of placement of geosynthetic product in the field.

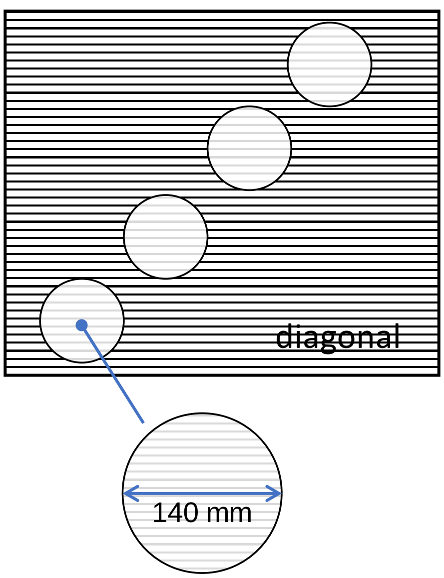

(a)

(b)

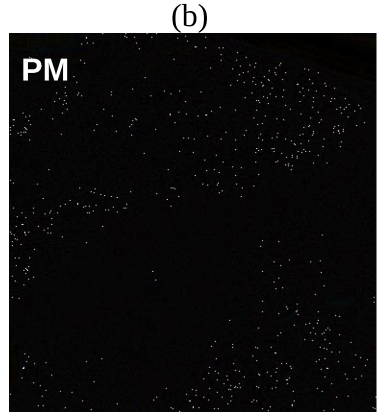

(c)

Figure D- 4. Geosynthetic interlayer sample cutting process.

The first step in trimming is to draw the outlines using the template and a peel-off marker, as shown in Figure D- 5 (a) and (b). A cloth cutter (Reliable 1500 FR) that can cut up to 2.54-mm (1-inch) thick fabric bundles was used to cut the geosynthetic sample shapes from the rolls. Figure D- 5 (c) shows the cutter being run through the trace marks to extract the geosynthetic samples.

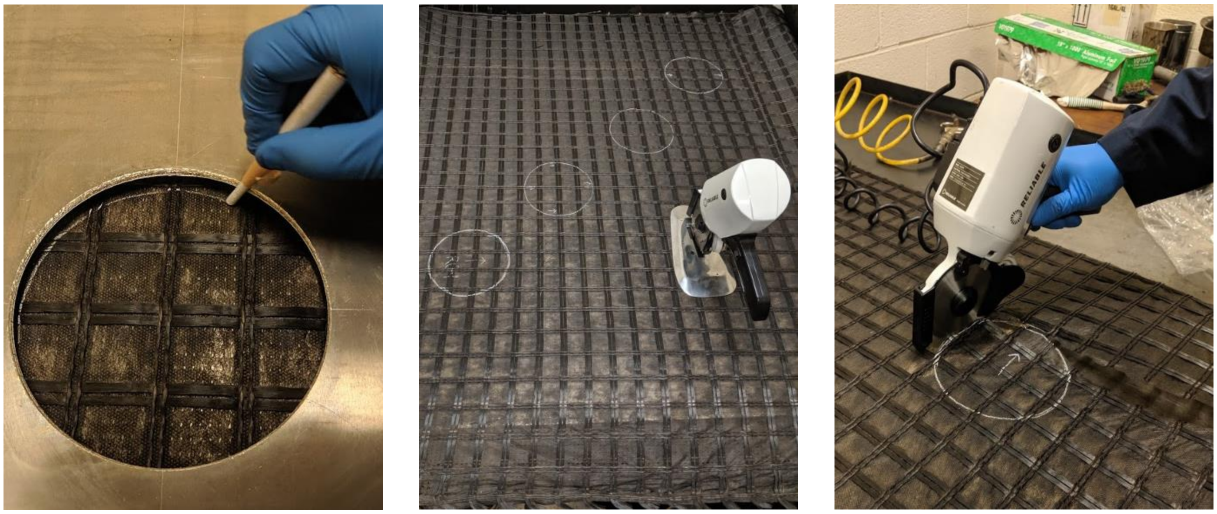

(a) (b) (c)

Figure D- 5. (a) Tracing the cutting pattern, (b) completed template pattern, and (c) cutting/extracting the geosynthetic sample using a cloth cutter.

Step 3. Tack coat application on MAST samples

The interface of the AC layers in this study was constructed as either a tack coat only (control specimen) or a tack coat-impregnated geosynthetic interlayer. A day-long cooling period was allowed for the freshly compacted bottom layer before applying the tack coat. In this study, the tack coat was hot binder, PG 64-22, applied on the sample to provide the desired interface bond. For application purposes, a metal canister with small holes in its cap was used to pour the hot binder to create a dense binder grid on top of the bottom layer, as shown in Figure D- 6 (a). Then, a heat gun and metal spatula were used to warm and then spread the binder evenly on the sample surface, as shown in Figure D- 6 (b). However, the optimal application rate stipulated by the NCDOT (0.04 gal/yd^2 for emulsified asphalt, Table 605-1) created challenges in applying the tack coat uniformly on the bottom layer. Figure D- 7 presents the specimen surfaces that were subjected to different tack coat application rates and shows the non-uniform application of the tack coat, especially at low application rates.

(a) (b)

Figure D- 6. Tack coat application process: (a) pouring hot binder from metal canister with perforated lid and (b) spreading binder uniformly using a heat gun and metal spatula.

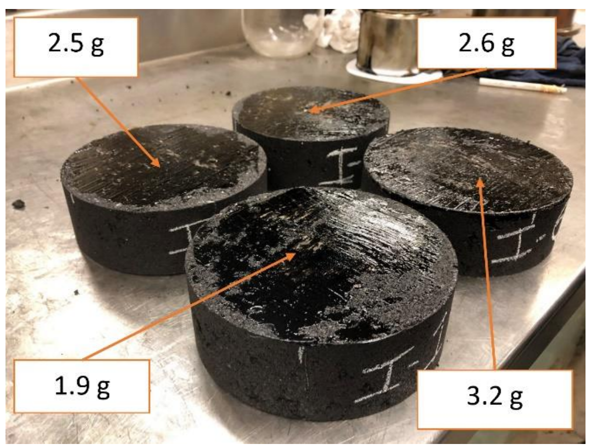

Figure D- 7. Non-uniform application of tack coat applied to bottom layer surface of MAST test samples.

Subsequently, the NCSU research team sought laboratory equipment that could be used to apply the tack coat in a uniform pattern on the AC surface. This search resulted in procuring a hot spray gun that dispenses hot liquic under pressure. Figure D- 8 (a) shows the test set-up for using the hot spray gun to apply the tack coat (hot asphalt in this study). Figure D- 8 (a) and (b) show that the system consists of a control panel with a stand that holds the spray gun when it is not in use. Compressed air control and manometer indication are integrated into the control panel. Figure D- 8 (c) shows the hot liquid applicator, i.e., the spray gun. Figure D- 9 (a), (b), and (c) show the components of the hot spray gun and cartridge, air spray nozzle, and liquid nozzle, respectively.

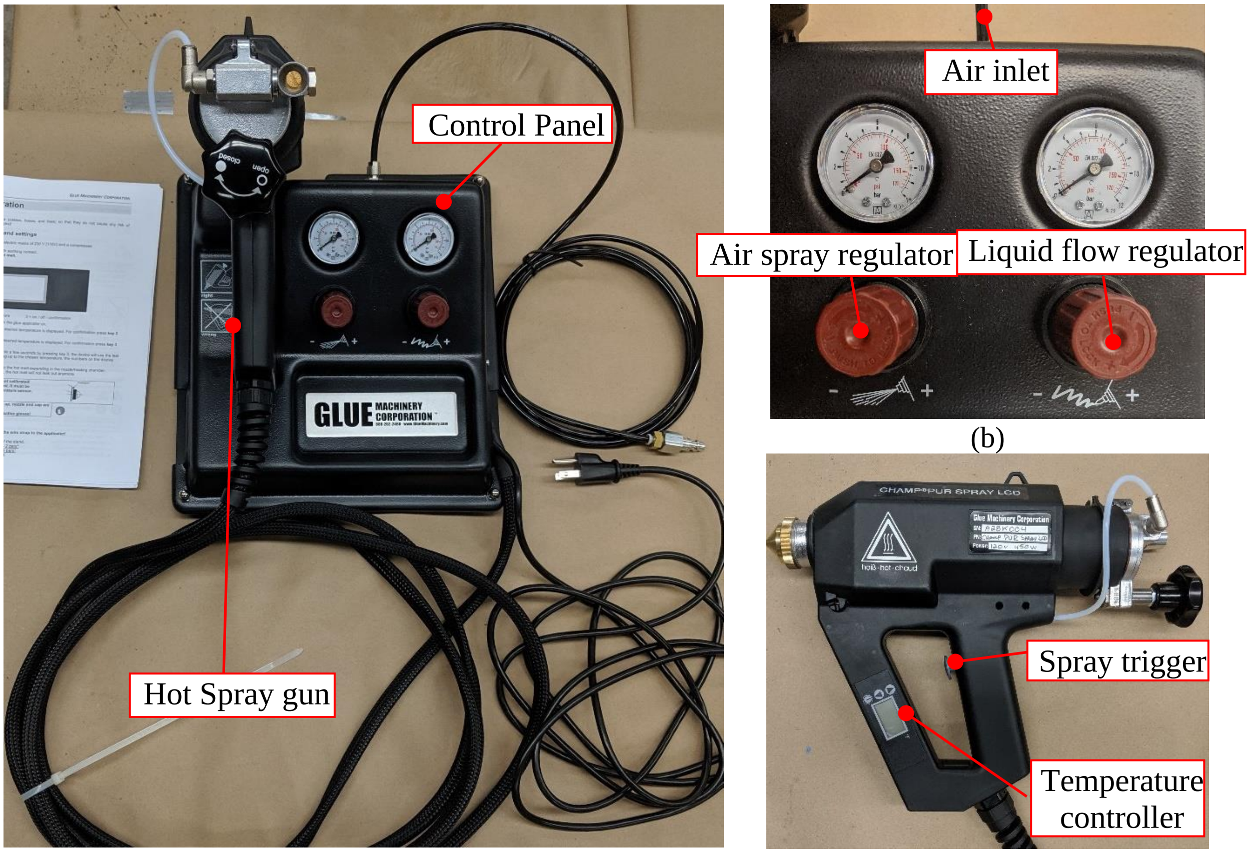

(a) (b) (c)

Figure D- 8. Hot spray gun test set-up for tack coat application: (a) test set-up, (b) control panel, and (c) hot spray gun.

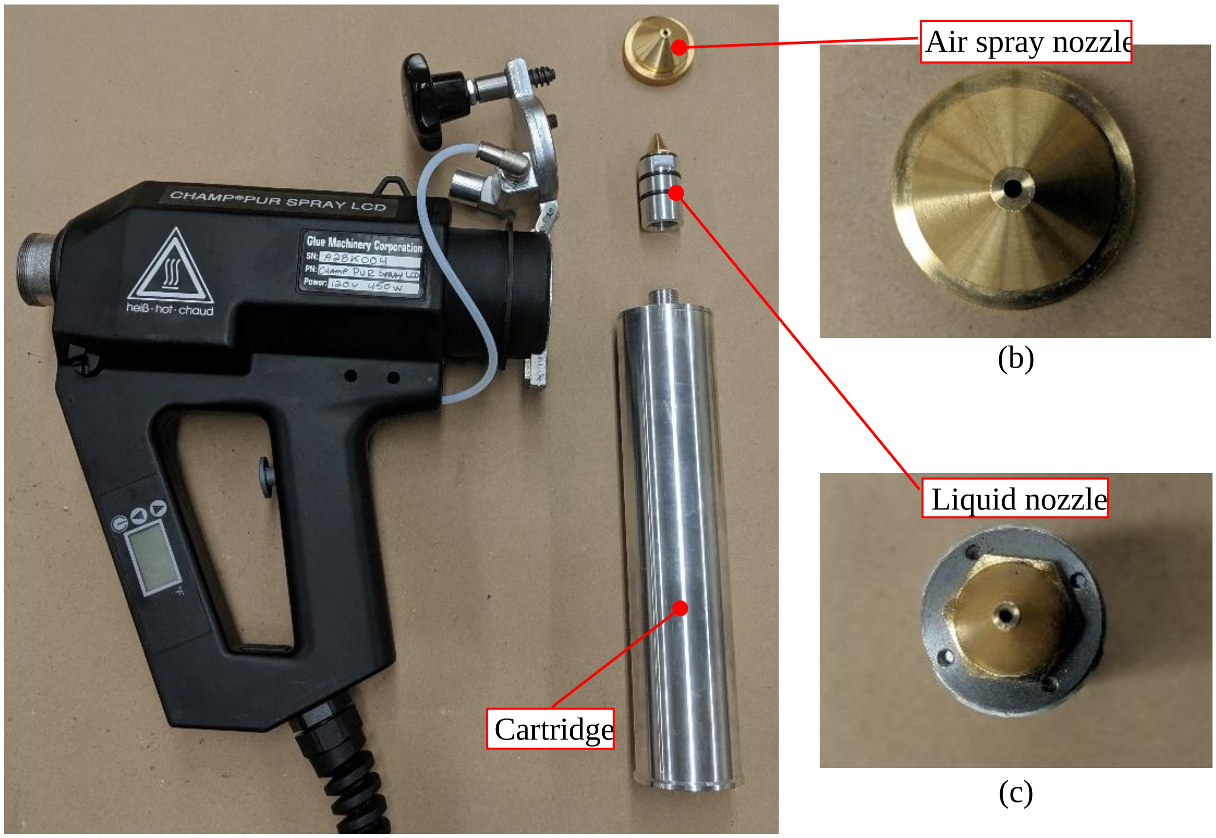

(a)

Figure D- 9.. Hot spray gun components: (a) gun, cartridge, and nozzles, (b) air spray nozzle, and (c) liquid nozzle.

The step-by-step procedure for using the spray gun is as follows and illustrated in Figure D- 10.

Step 1: Heat the asphalt binder can and cartridge (without nozzle) to 145°C for one hour in the oven. Meanwhile, set the temperature of the spray gun (without cartridge) for 20 minutes at 175°C (350°F) to preheat the heating chamber.
Step 2: Attach the nozzle to the cartridge after one hour; Figure D- 10 (a).
Step 3: Pour the asphalt into the cartridge to three-quarters capacity (roughly 250 ml); Figure D- 10 (b).
Step 4: Load the cartridge into the heating chamber; Figure D- 10 (c) and (d).
Step 5: Close the lid to pressurize the asphalt cartridge; Figure D- 10 (e).
Step 6: Measure the temperature at the nozzle tip shown in Figure D- 10 (f) for an accurate reading (because the temperature inside the heating chamber is not calibrated). Note that a trial study recommends that the set temperature be maintained at 175°C (350°F). Otherwise, for the set temperature of 145°C (293°F), the maximum achievable temperature is 120°C. An infrared thermal gun could be used to measure the temperature.
Step 7: Begin the spraying process once the spray applicator reaches the required temperature.
Step 8: Allow sufficient heating time between each spraying sequence and conduct a proper temperature check prior to application.

Step 9: Clean the spray applicator and control panel using a cloth moistened with a citrus solvent blended with hyper surfactants, commercially known as ‘orange cleaner’. The cartridge, liquid, and air nozzle must be cleaned using a kerosene-based solvent.

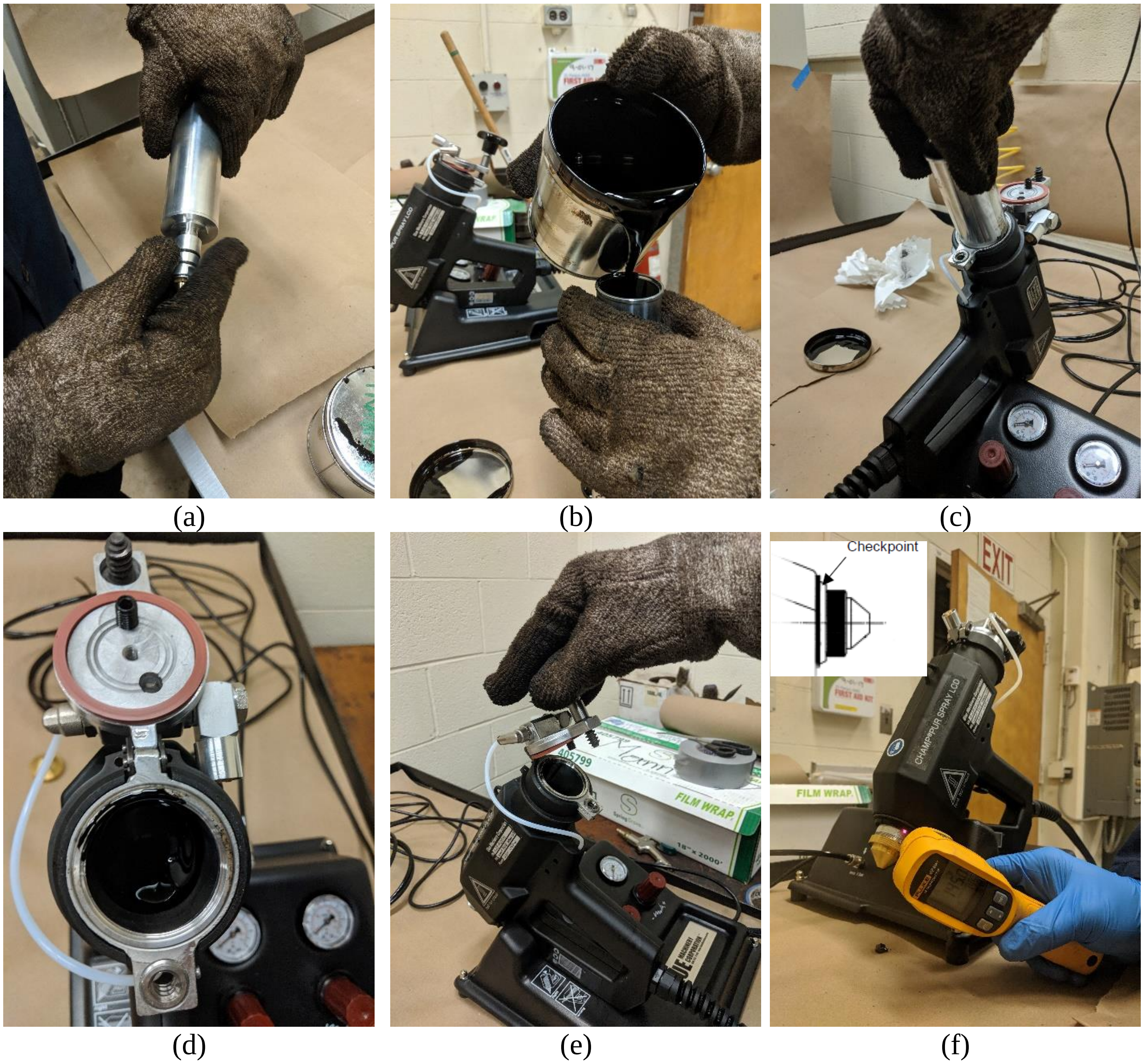

Figure D- 10. (a) Attaching nozzle to hot spray gun cartridge, (b) pouring liquid asphalt into cartridge, (c) loading cartridge into heating chamber of spray gun, (d) cartridge with asphalt inside spray gun, (e) closing spray gun mouth, and (f) measuring temperature at nozzle tip.

A few trial tests were carried out on white paper to measure the optimal air pressure and liquid flow for the hot binder PG 64-22. The results indicate that, as the air spray pressure is increased, the atomization of the asphalt becomes evident. However, increasing the liquid flow pressure above one bar could result in excessive flow. Therefore, based on this study, the air spray pressure should be maintained between four to five bars while the liquid flow pressure is below one bar. Also, sufficient heating time between applications (5 to 10 minutes) should be provided to allow proper atomization of the asphalt.

A metal cover sheet with standing legs was designed so that none of the excess tack coat spray could reach the sample side walls or scale. Figure D- 11 (a) shows this test set-up. The gyratory cover sheet diameter is 140 mm (5.5 in.). The metal sheet should not touch the sample because the weight measured by the scale should be only that of the tack coat applied above the 140-mm diameter circular area, as shown in Figure D- 11 (b). The application rate was recalculated for the metal cover sheet opening, i.e., 140 mm. Figure D- 11 (c) shows the hot asphalt being applied using the spray gun.

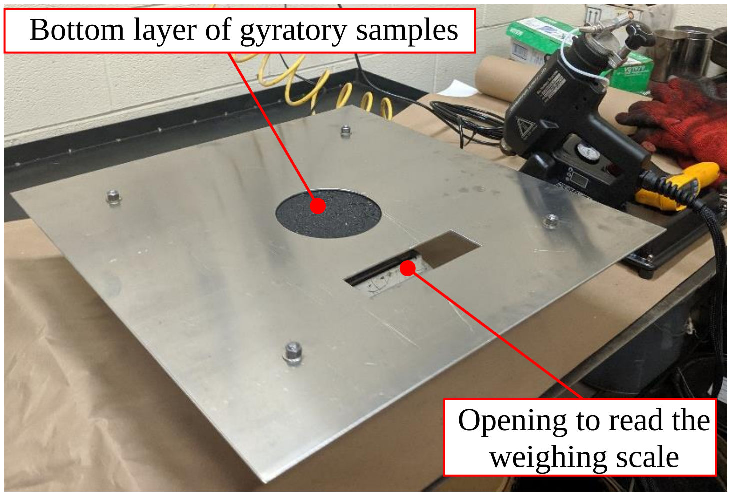

(a)

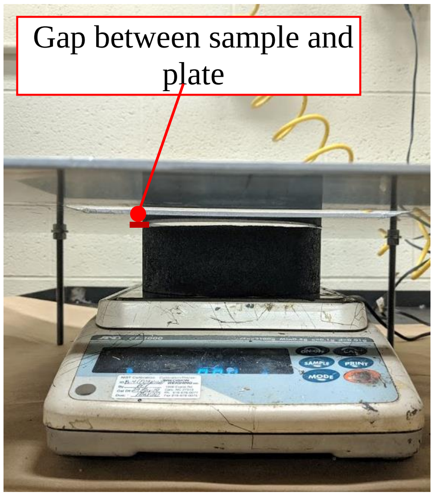

(b)

(c)

Figure D- 11. (a) Sheet cover above gyratory-compacted sample, (b) small gap between cover sheet and sample, and (c) application of hot asphalt using hot spray gun.

Figure D- 12 shows apparent differences between the surfaces where the tack coat was applied using the metal canister versus the hot spray gun. The expected sample-to-sample variation in the case of the hot spray gun is 0.3 g, but the tack coat is spread uniformly across the surface. The tack coat weight was checked at every application cycle. The definition of ‘application cycle’ is a single pass of the hot spray gun from left to right and vice versa continuously from top to bottom, then returning to the top where the application commenced. This process ensures uniformity above the surface.

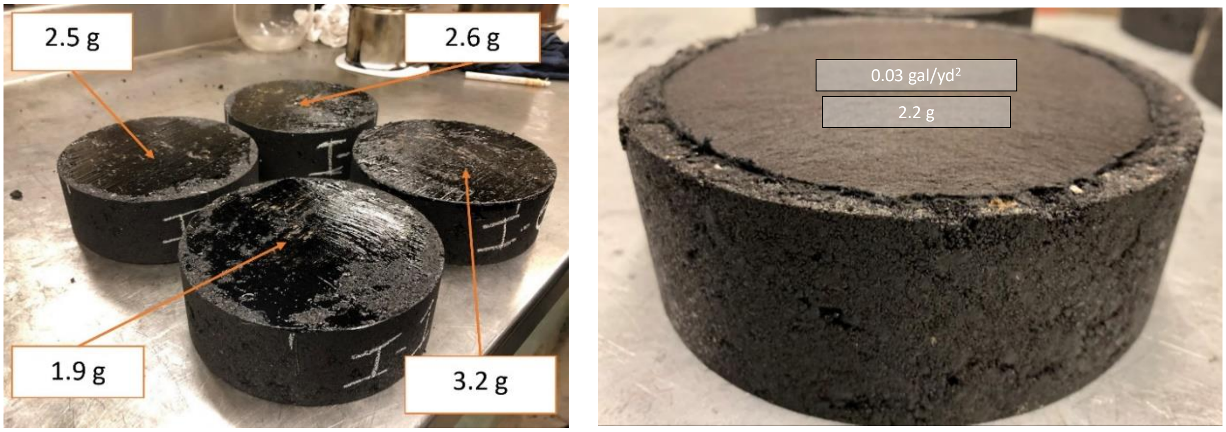

(a) (b)

Figure D- 12. Tack coat applied to the bottom layer surface of MAST test samples: (a) non-uniformity (metal canister) and (b) uniformity (hot spray gun).

Step 4. Geosynthetic interlayer installation on MAST samples

The placement technique that is used for each geosynthetic product is based on the manufacturer's guidelines. Figure D- 13 shows the placement of each of the five geosynthetic product types used in this study. For the installation of the two geosynthetic composites shown in Figure D- 13 (a) and (b), respectively, PC#1 should be placed with the grid side in contact with the top layer and PC#2 should be placed with the grid side facing the bottom layer. PaG, shown in Figure D- 13 (c), is made of glass fibers, with one side having self-adhesive properties. The manufacturer stipulates that the adhesive side of the grid facing the bottom layer must be placed first, and then the specified rate of tack coat is applied to the grid afterward. However, the other four geosynthetic products are installed after the tack coat application. PM, shown in Figure D- 13 (d) has two different colors on either side. A thin layer of asphalt applied to one side makes the side black, whereas the side without the tack coat is grey. After applying the optimal application rate onto the bottom layer, PM is placed with its grey side touching the tack coat. As PF is a fabric without either specific side precoated, placing either side on top of the bottom layer that already has been sprayed with the optimal tack rate is acceptable, as shown in Figure D- 13 (e).

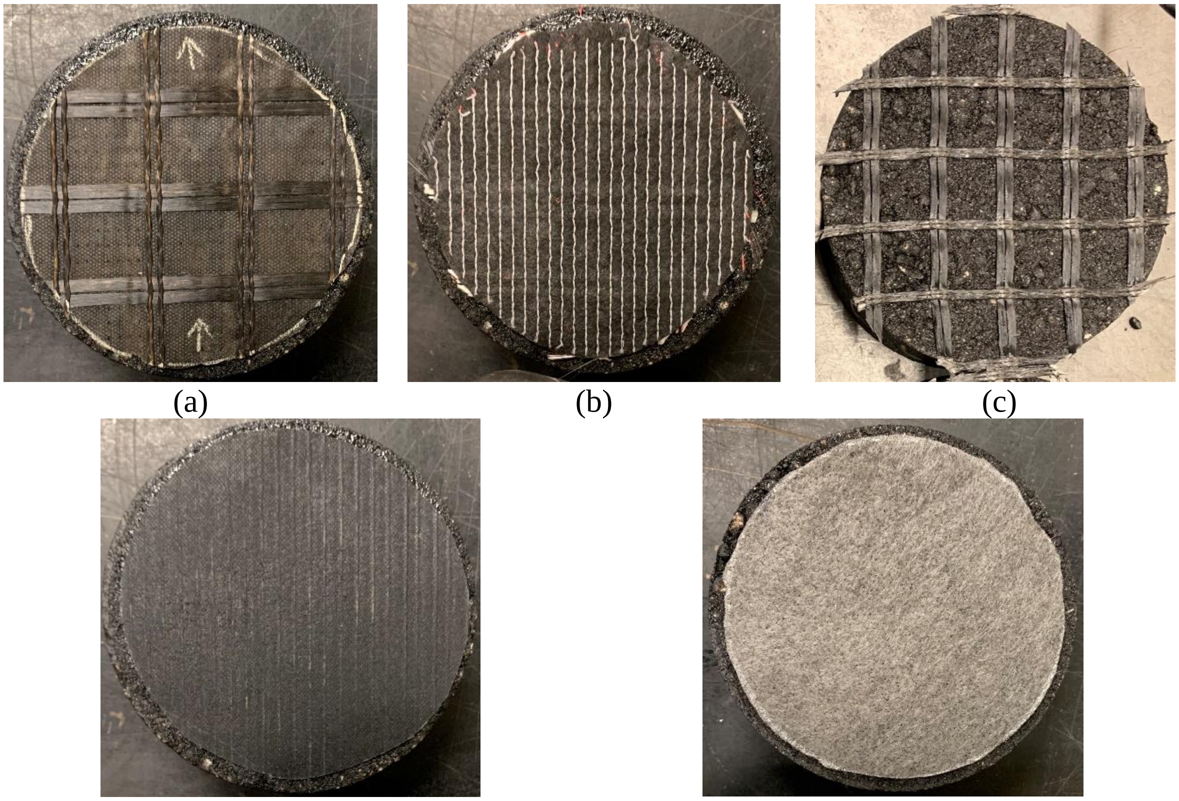

(a) (b) (c)

(d) (e)

Figure D- 13. Placement of geosynthetic interlayer products (view from top towards top of bottom layer): (a) PC#1, (b) PC#2, (c) PaG, (d) PM, and (e) PF.

Following the geosynthetic placement, a set pressure is applied to the specimen to ensure proper bonding throughout the contact area between the product and bottom layer, as shown in Figure D- 14 for PC#1. Note that, before placing the geosynthetic product, the bottom layer is heated to 145°C for two minutes to liquify the tack coat so that proper impregnation of the geosynthetic product and tack coat are achievable. Figure D- 14 (b) shows the liquified binder and Figure D- 14 (c) shows the metal rod being rolled over the specimen to set the application pressure.

(a)

(b)

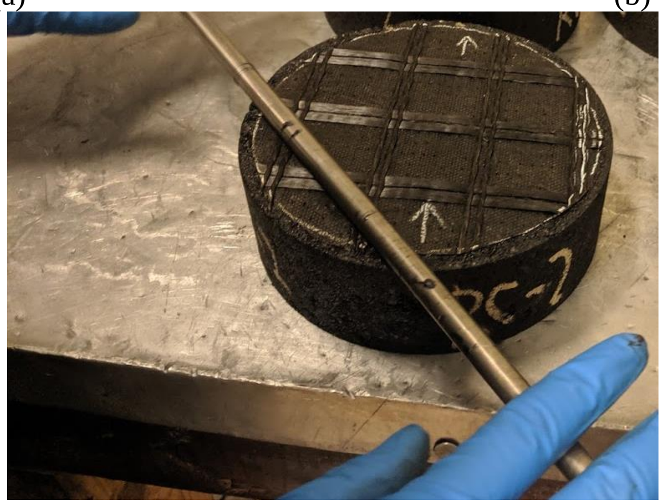

(c)

Figure D- 14. (a) Bottom layer after tack coat application, (b) liquified asphalt binder after placing the bottom layer with tack coat in the oven at 145°C for two minutes, and (c) setting pressure application by rolling metal rod over PC#1.

The direction of the geosynthetic installation is a critical factor in determining the specimen's shear performance. The MD of the geosynthetic is labeled on the samples/specimens throughout the sample fabrication process, as shown in Figure D- 15 (a) for a bottom-layer MAST test sample and Figure D- 15 (b) for the final MAST test specimens cored from the sample.

(a) (b)

Figure D- 15. Tracking the geosynthetic reinforcement placement direction: (a) bottom layer of MAST test sample and (b) final cored MAST test specimens.

Step 5. MAST test specimen extraction from MAST test samples

The presence of an air void gradient along the sample periphery that is in contact with the hot mold is well known (Chehab et al. 2000). Therefore, to maintain consistent air void distribution throughout the MAST test specimens, the MAST test samples were cored and cut to a height of 76.2 mm (3 in.) and a diameter of 101.6 mm (4 in.) before testing. Figure D- 16 presents the coring and cutting procedure.

Figure D- 17 illustrates that 100-mm diameter PVC pipe was used to protect the specimen during cutting. The pipe serves to hold the layers together and absorb the vibration and bending force imparted by the saw, thereby protecting the specimen from damaging the weak interfaces. In addition, the PVC pipe could be used as a guide scale to set the trimming location. First, as shown in Figure D- 17 (a), the sample is placed on a metal canister to keep the sample level. Figure D- 17 (b) shows that the PVC pipe with leveling marks is matched with the bottom of the specimen, i.e., at the top of the canister. Figure D- 17 (c) shows the completed geosynthetic-reinforced sample with PVC pipe protection. This procedure saves time and reduces human error by producing highly repeatable specimens (in terms of dimensions) compared to the typical pen-marking method. Figure D- 18 (a) through (e) respectively show side views of the five geosynthetic-reinforced specimens.

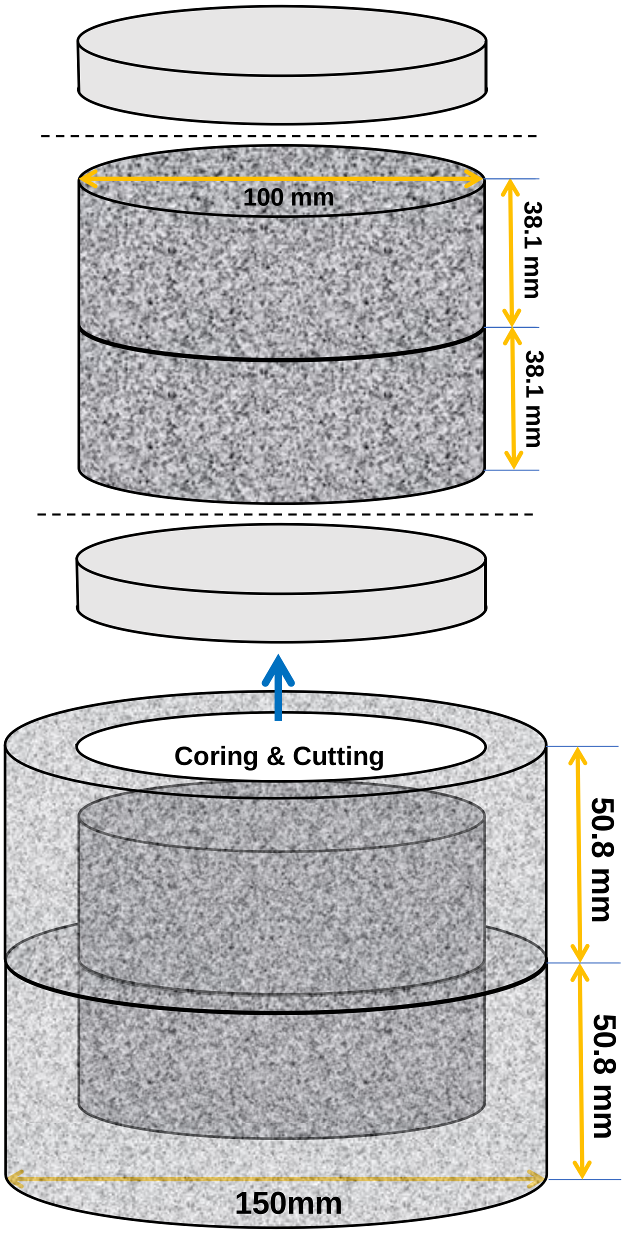

(a)

(b)

(c)

Figure D- 16. Procedure for coring and cutting cylindrical specimens: (a) cored MAST test sample, (b) trimming the top/bottom layer, and (c) finished specimens.

(a) (b) (c)

Figure D- 17. Process for protecting geosynthetic-reinforced sample with PVC pipe: (a) sample placed on canister, (b) the PVC pipe with leveling marks matched with the bottom of the specimen, and (c) completed sample with PVC pipe protection.

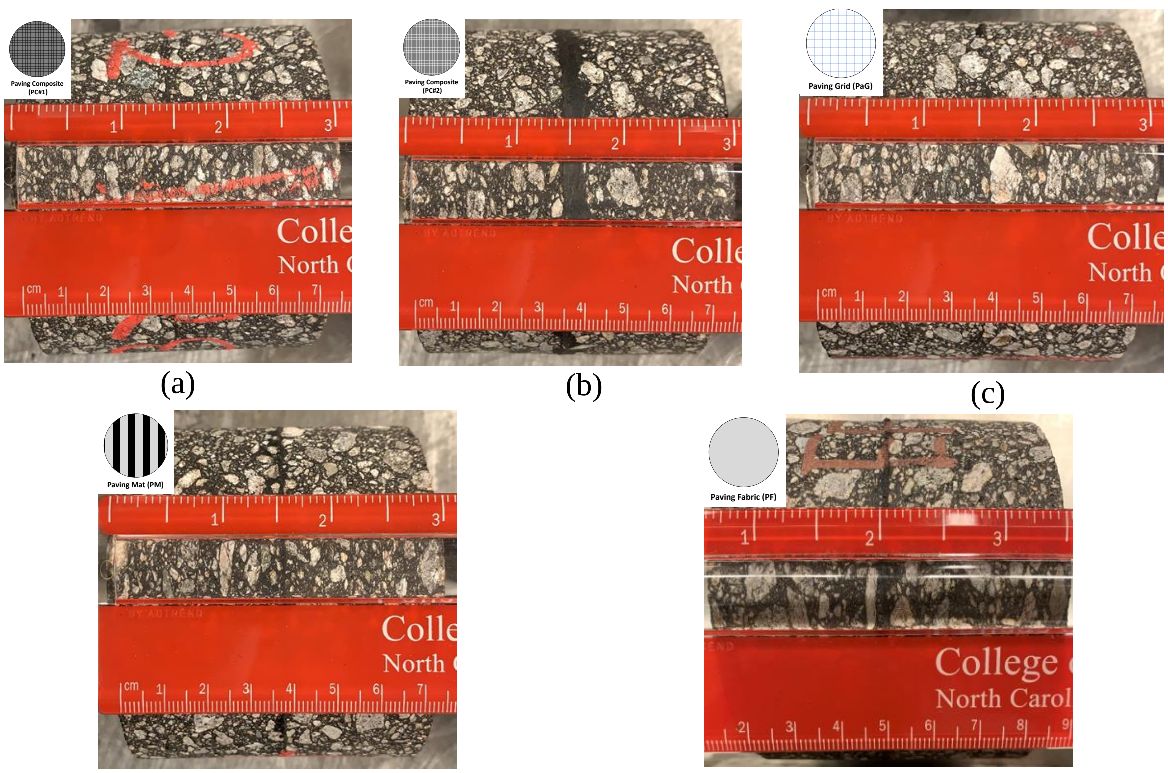

(a) (b) (c)

(d) (e)

Figure D- 18. Side views of geosynthetic-reinforced specimens made with (a) PC#1, (b) PC#2, (c) PaG, (d) PM, and (e) PF.

Appendix E. Laboratory Fabrication of Beam Specimens

Step 1. Compact the slab sample using a roller compactor.

A pneumatic steel roller compactor with a vibrator that complies with EN 12697-33 (BS EN 2019) was used to make beam specimens for this project. The slab compactor model CRT-RC2S, manufactured by James Cox and Sons and shown in Figure E- 1, was employed to perform the compaction. The compactor allows the user to select the number of passes and compaction load levels to reach the target height and thus the desired density. The metal mold provided with the compactor can make 400-mm (15.75-in.) long, 305-mm (12-in.) wide, and 100-mm (3.94-in.) tall slab samples.

Figure E- 1. Pneumatic roller compactor with vibrator (CRT-RC2S).

For this study, the CRT-RC2S compactor was used to make double-layered slabs, with each layer 50-mm (1.97-in.) thick. The compaction process was carried out in two stages. The first stage consists of bottom layer fabrication and the second stage consists of a hot asphalt tack coat application, geosynthetic placement, and top layer compaction. The two stages commence with measuring and placing the required weight of loose mix for the respective layer (top/bottom) along with batching spatulas in the oven at the compaction temperature of 145°C (293°F) for an hour. After completing the separation procedure (homogenization of the loose mix obtained from the hot mix plant), each cloth bag was found to weigh around 8.5 kg (18.7 lb). Each slab layer was estimated to require 13 kg (28.7 lb), which could vary depending upon the target air void content; hence, two cloth bags of loose mix were used. Figure E- 2 (a) shows weighing one of the cloth bags of loose mix and Figure E- 2 (b) shows two pans of loose mix in the oven.

(a) (b)

Figure E- 2. (a) Weighing loose mix in cloth bag and (2) two pans of loose mix obtained from two cloth bags in the oven at the compaction temperature (145°C).

After an hour in the oven at 145°C (293°F), the two bags of loose mix were separated into six equal parts, each around 2.1 kg (4.6 lb) spread evenly over each pan (three pans from each cloth bag are considered a set) for uniform heating. Then the six pans were placed in the oven at the mix temperature of 155°C (311°F) for an hour. The slab compaction mold, separation compartment, and necessary accessories (a spatula for spreading and plowing, the collar used during top layer compaction, etc.) were placed in the oven along with the pans. The reason to keep the batch pans at the mix temperature is that waiting to move the six pans to the compaction mold until the compaction process is completed takes nearly ten minutes. Hence, the mix temperature is selected for conditioning in order to prevent the material's temperature from cooling below the compaction temperature. Thermocouples inserted in the loose mix showed that, even though the oven was set at the mix temperature, the loose mix took around 55 minutes to reach the target temperature after batching. In essence, the loose mix should stay at the mix temperature for five minutes, thus mitigating the likelihood of aging. Figure E- 3 shows the batching procedure used for slab compaction.

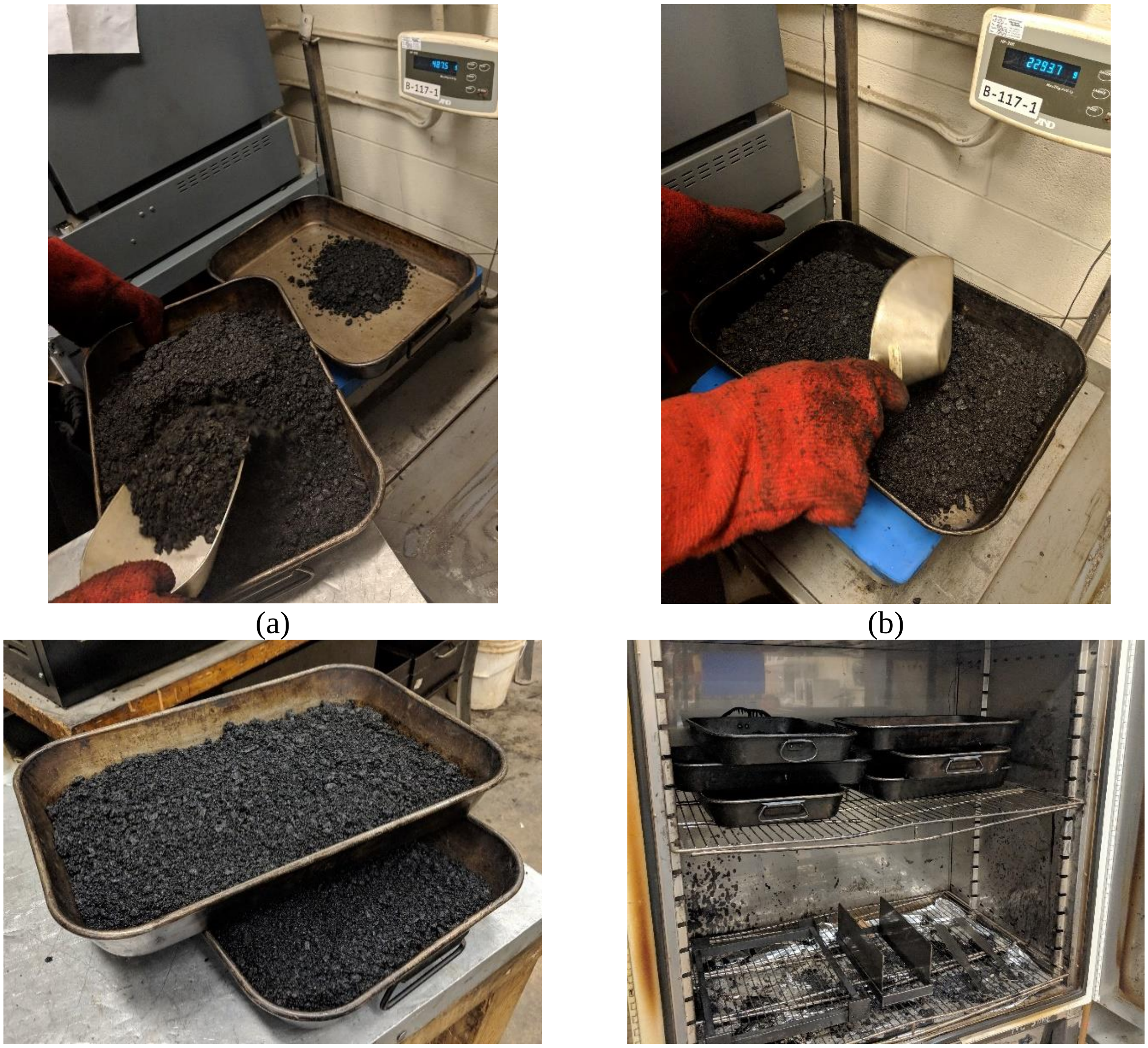

(a) (b)

(c) (d)

Figure E- 3. (a) Batching the necessary quantity of loose mix into pans, (b) spreading loose mix in the pans for uniform heating, (c) batched pans, and (d) batched pans, mold, and necessary accessories in the oven at mix temperature.

After one hour at the mixing temperature, the hot mold was moved near the compactor, and 'black magic' lubricant was applied to the mold. This lubricant causes the solvent to vaporize, which can irritate the eyes and throat. Therefore, proper masks and safety glasses should be worn during this process. Figure E- 4 (a) through (j) present the steps taken immediately prior to compaction. Once the lubricant is applied, the separation compartment is placed in the middle one-third of the mold, as shown in Figure E- 4 (a), so that the loose mix can be spread evenly within the slab. The first set of three pans is placed in each compartment, followed by the second set, as shown in Figure E- 4 (b). This procedure is recommended to be performed by two persons to reduce the delay for compaction and avoid cooling the loose mix. Figure E- 4 (c) shows the heaps of loose mix in each compartment after placing the AC in the mold. Figure E- 4 (d) shows the loose mix being evenly distributed with the help of a flexible spatula. Figure E- 4 (e) and (f) respectively show the separation compartment removed from the mold and the loose mix further leveled. Figure E- 4 (g) and (h) respectively show the mix being plowed at regular intervals (1.5-in. wide) along the slab length and width using the flexible spatula. Next, an infrared heat gun is used to verify the mix temperature, as shown in Figure E- 4 (i), and the slab mold is then pushed to the compacting platform to begin the compaction process. Figure E- 4 (j) shows the slab mold loaded onto the compaction platform.

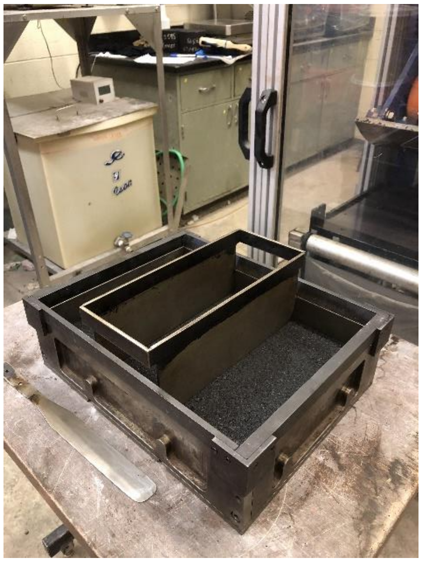

(a)

(b)

(c)

(d)

(e)

(f)

(g)

(h)

(i)

(j)

Figure E- 4. (a) Separation compartment in mold with collar, (b) pouring loose mix into each compartment, (c) heaps of loose mix in each compartment, (d) leveling the heaps in the compartment, (e) removing separation compartment, (f) leveling slab surface, (g) plowing contents of slab in length direction, (h) plowing contents of slab in width direction, (i) measuring surface temperature of loose mix before compaction using an infrared heat gun, and (j) loading mold onto compaction platform.

The initial task at the actual compaction stage is to set up the compactor, as described in Figure E- 5. This set-up is initiated immediately after the six batch pans are placed in the oven for conditioning. Figure E- 5 (a) shows the height adjustment scale in the compactor, which is set to the required height that corresponds to the thickness of the layer to be compacted. Even after setting the scale, the chances of visual errors in precision measurements are high, so relying solely on the compactor scale may lead to erroneous outcomes. Hence, as shown in Figure E- 5 (b), channel sections, 50.8 mm (1.97 in.) in height, were placed above an aluminum plate with the same thickness as that of the mold base, i.e., 10 mm (0.39 in.), with the compactor placed just above the channel. A small gap, less than a millimeter, is recommended to ensure that the compactor face is not set below the target height, which is accomplished by fine-tuning the scale lock. Figure E- 5 (c) shows the compactor face about to abut the channels.

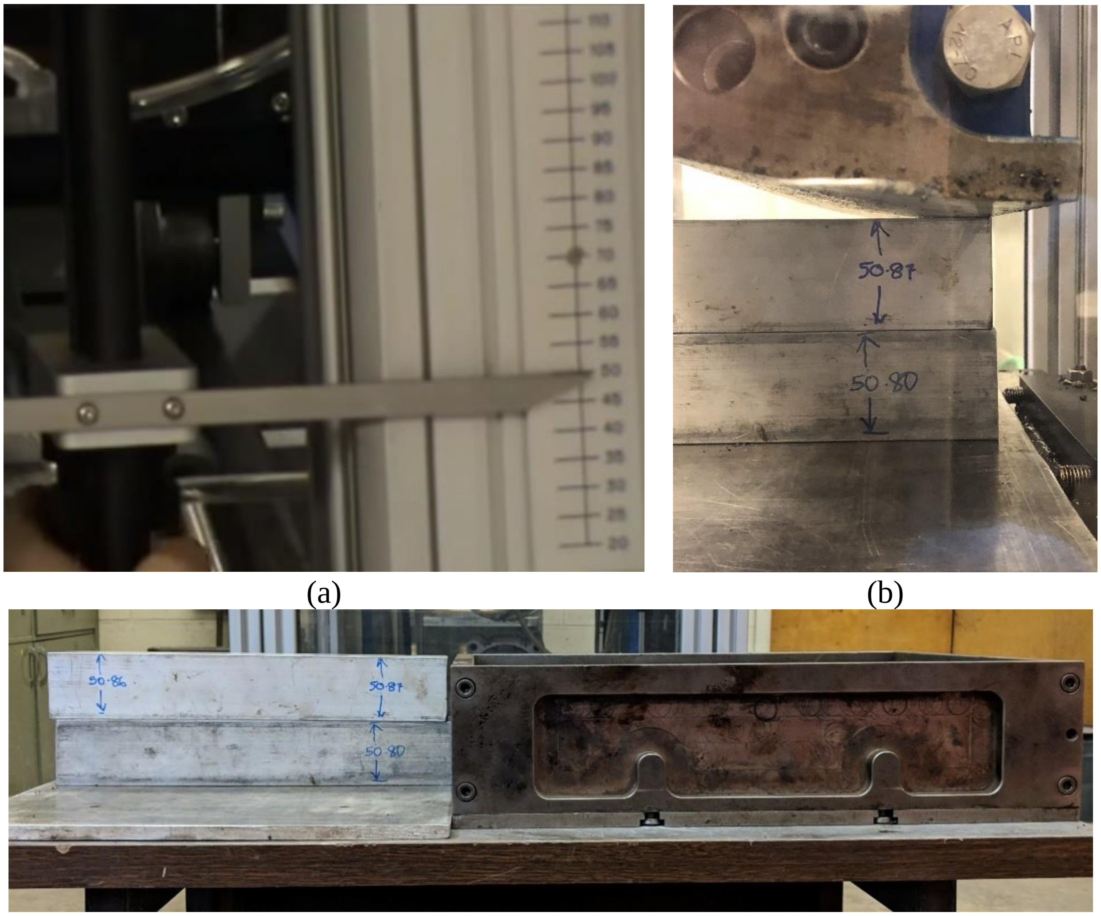

(a) (b)

(c)

Figure E- 5. (a) Height adjustment scale in compactor, (b) channel sections set above aluminum plate for precision measurements, and (c) compactor face about to abut channels.

Six compaction levels were set according to the numerous compaction iterations that were carried out on the slab samples. Each level consisted of a certain number of cycles and applied pressure on the material. As shown in Figure E- 6, the number of cycles and the applied pressure were increased gradually to compact the slab to the target height. All the compaction cycles were performed with vibration. Once the mold, filled and leveled with the loose mix, was loaded into the compactor, the preset compaction set-up was triggered for compaction. After the compaction was completed, the slab was left at ambient temperature to cool.

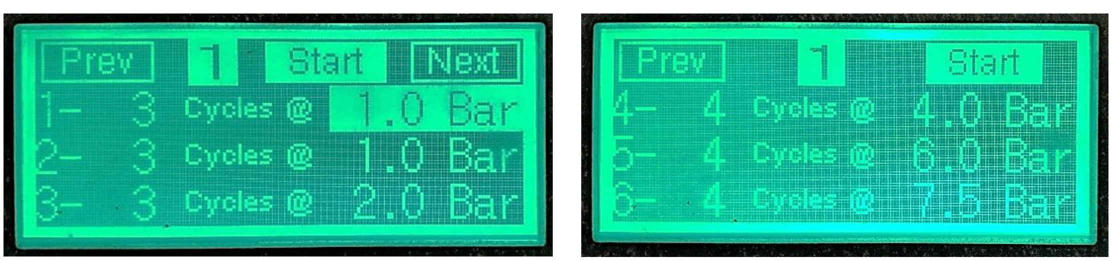

Figure E- 6. Details of each compaction level and number of cycles at respective applied pressure.

Step 2. Prepare the geosynthetic product for slab samples.

Geosynthetic products with the rectangular dimensions of 400 mm (15.7 in.) × 300 mm (11.8 in.) are required to fabricate geosynthetic-reinforced slab samples using a roller compactor. The geosynthetic products typically are unrolled in the traffic direction. Therefore, for this study, the products were cut into the rectangular dimensions such that the MD of the product matched the slab compaction direction. The geosynthetic samples were extracted diagonally within the rolled-out footprint to avoid manufacturing defects in the MD and xMD. Figure E- 7 (a) illustrates the diagonal pattern used for cutting the product. Figure E- 7 (b) shows the template tracing process over PC#2, where outlines were drawn using a template and china pencil. A cloth cutter (Reliable 1500 FR) that can cut up to 2.54-cm (1-in.) thick fabric bundles was then used to cut the geosynthetic sample shapes from the rolls. The cutter was run through the trace marks to extract the geosynthetic samples.

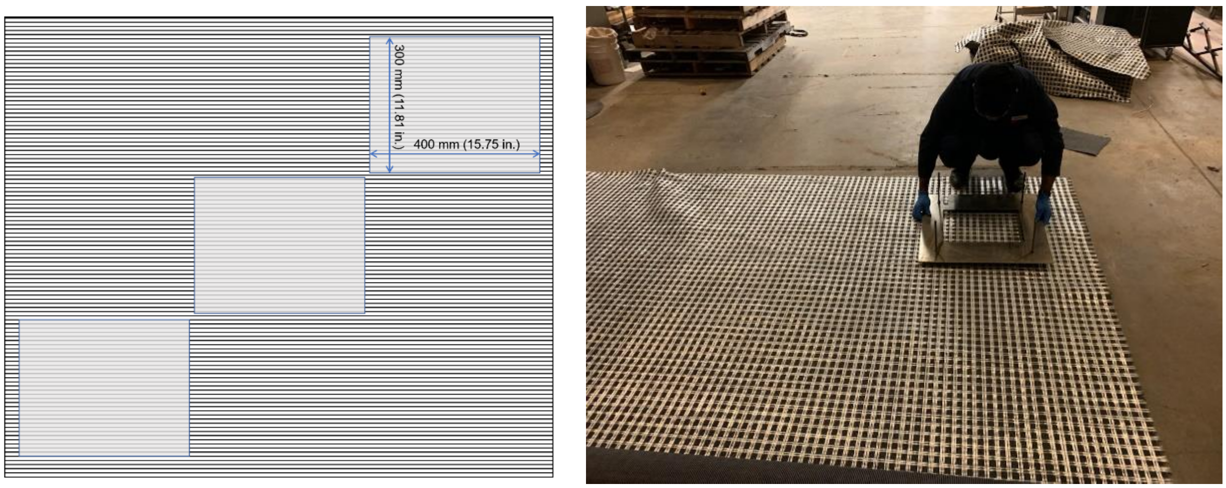

(a) (b)

Figure E- 7. (a) Template used for cutting pattern and (b) tracing the template over PC#2.

Step 3. Apply the tack coat using a hot spray gun.

Details regarding the tack coat application methodology and rates for the different geosynthetic product types are described in Step 3. Tack coat application on MAST samples under Section 3.1.1. The same method was followed here for applying the tack coat to the beam samples. Figure E- 8 depicts (a) the laboratory test set-up and (b) applying the tack coat to a beam sample.

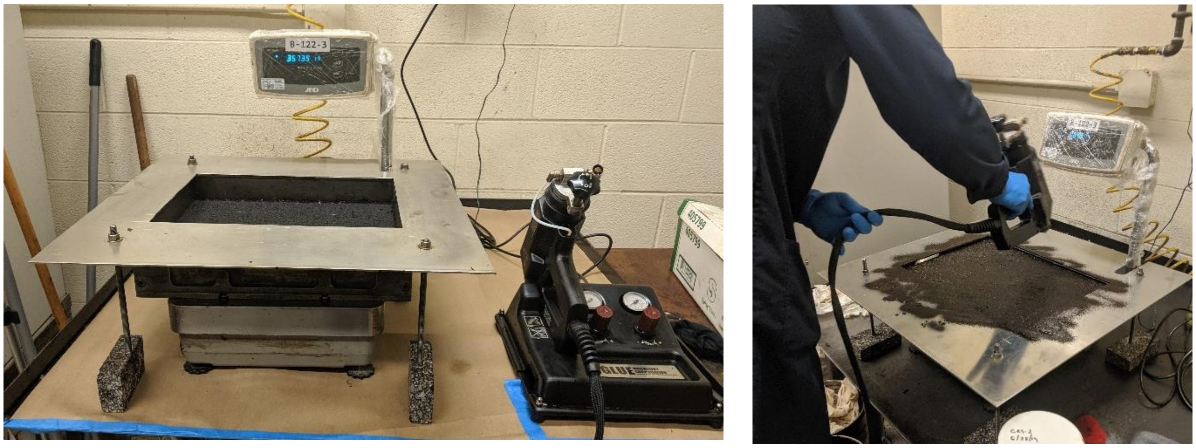

(a) (b)

Figure E- 8. (a) Tack coat application test set-up and (b) applying tack coat using hot spray gun.

Step 4. Place the geosynthetic product on the slab sample.

The procedure for the geosynthetic product installation is the same as that for the MAST test sample fabrication process and is described in Step 4. Geosynthetic interlayer installation on MAST samples under Section 3.1.1. After applying the optimal application rate, the geosynthetic product was placed as per the manufacturer’s guidelines. Note that, before placing the geosynthetic, the bottom layer was heated to 145°C (293°F) for two minutes to liquify the asphalt binder so that proper impregnation of the asphalt and glue were achievable. Following the geosynthetic placement, a set pressure was applied by rolling a metal rod over the sample to ensure adequate bonding throughout the contact area (interface) between the product and bottom layer, as shown in Figure E- 9 (a) and (b) before and after placement, respectively.

(a) (b)

Figure E- 9. Placement of geosynthetic product above bottom layer: (a) before and (b) after placement.

Care was taken to ensure the same footprint of the grids among the beam specimen replicates so that the effect of different footprint of the grids on the test results could be minimized. Figure E-10 (a), (b), and (c) show the footprints that are shared between each of the paving composites, PC#1, PC#2, and PaG, respectively, and the paving grid. Even though the grid layout is oriented symmetrically over the slab's bottom layer, the grid's footprint is asymmetric with reference to the beam’s plan view center. However, such an asymmetric layout is typical for replicates.

Modifying the cutting pattern to obtain a symmetric grid footprint in specimen replicates invites additional labor. Therefore, the DIC capture faces for the replicate specimens were chosen in a way that those faces have the same footprint of the grids. For example, in Figure E- 10(a), the cut through the beam's center divides the strip of PC#1 grid into two halves (square-shaped individual grids are divided into two halves). Thus, the two beam faces that face away from the beam's center [64-mm (2.52-in.)] are cut along the rib in the transverse direction. Hence, the DIC camera is set to capture the beam face from the sides that are marked by the red triangles such that the grid's footprint is identical among the replicates. In Figure E- 10, the capture faces are marked by triangular markers at the faces of the beam's middle one-third portion that will be oriented towards the DIC camera.

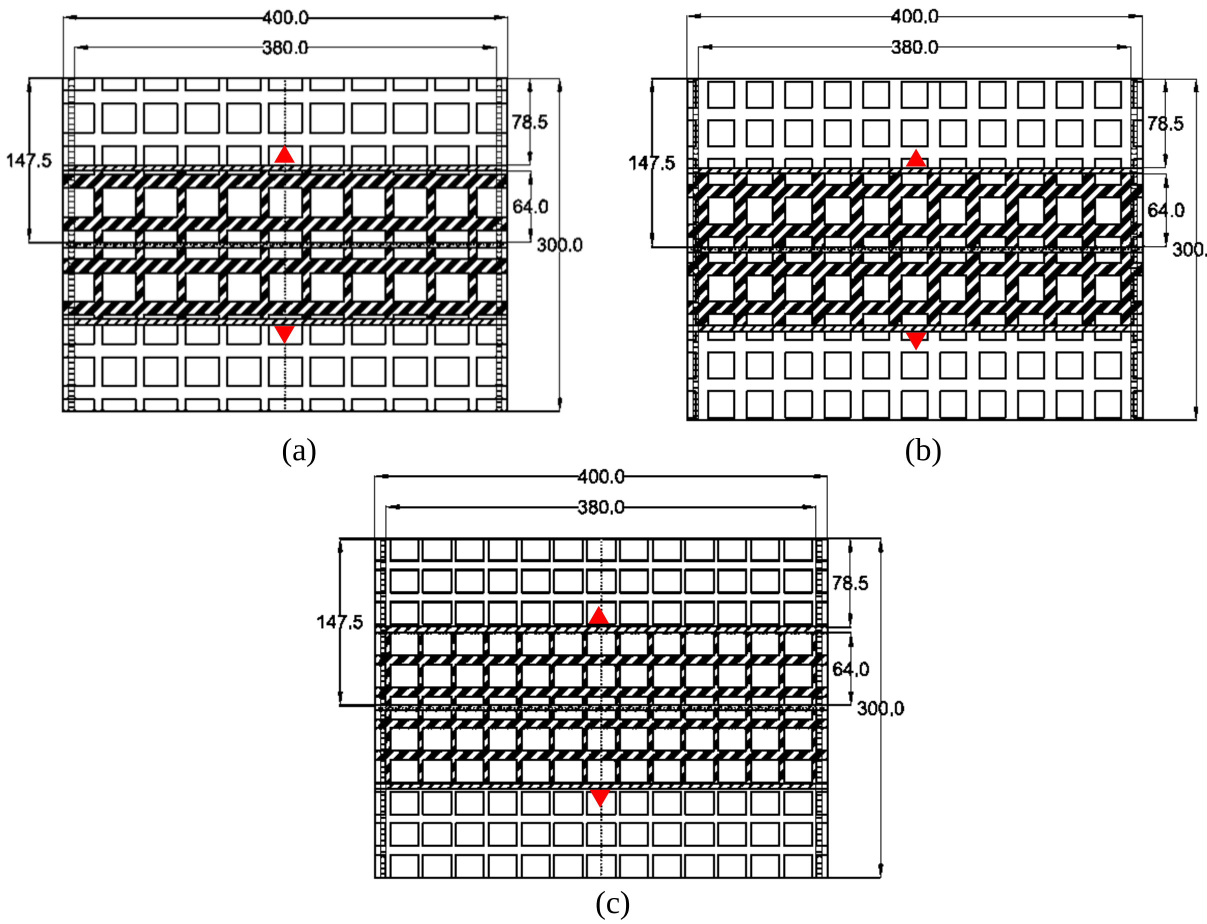

Figure E- 10. Layout pattern of grid for (a) PC#1, (b) PC#2, and (c) PaG.

Step 5. Prepare the beam specimens from slab samples.

In order to obtain beam specimens 400-mm (15.75-in.) long, 54-mm (2.12-in.) wide, and 64-mm (2.52-in.) in height, lab samples 400-mm (15.75-in.) wide to 305-mm (12-in.) long in the plan dimensions were cut into five pieces (four cuts) along the width. The outer two beam pieces were discarded to avoid the effect of the air void gradient. Figure E- 11 shows the slab-cutting process to create the beam specimens. Figure E- 11 (a) shows the slab-cutting dimensions and the slab just prior to being cut by the masonry saw. Three beam specimens were extracted from each slab and then cut from the slabs using the saw. First, beams 64-mm (2.52-in.) wide were cut out of the slab, and then the bottom and top layers of each beam were trimmed to retain thicknesses of 18 mm (0.71 in.) and 36 mm (1.42 in.), respectively, as illustrated in Figure E- 11 (b). That is, after cutting and trimming the specimens, the interlayer was located at one-third depth from the bottom of the beam.

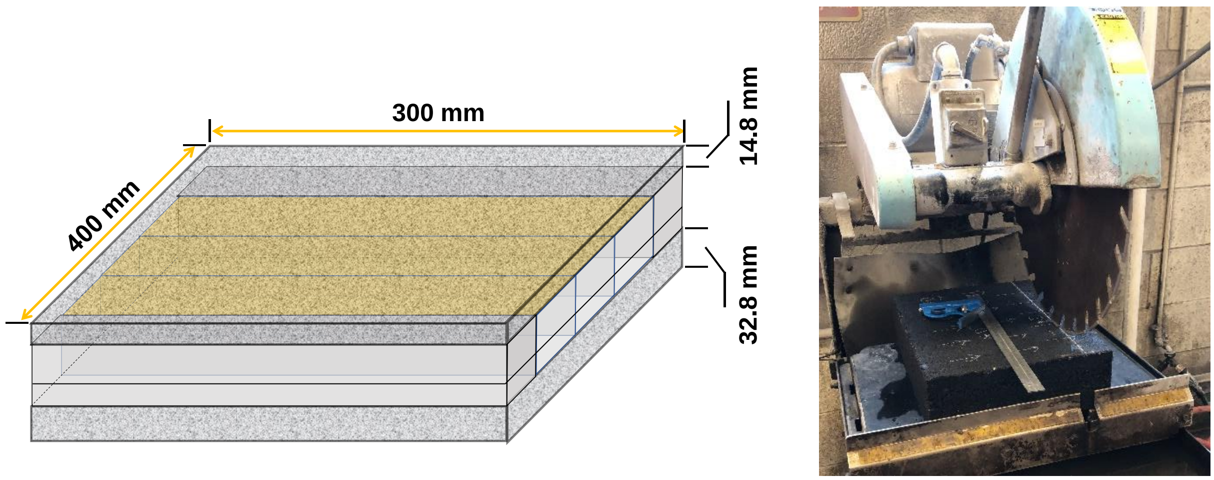

(a)

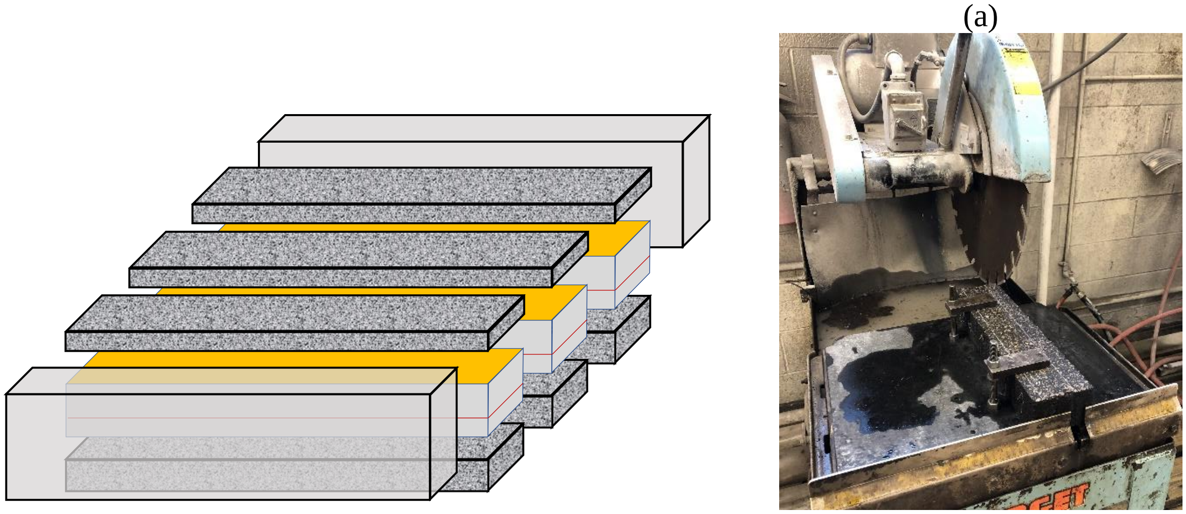

(b)

Figure E- 11. Procedure for cutting beam specimens: (a) slab dimensions and slab prior to sawing beam specimens and (b) before trimming top and bottom layers.

Step 6. Prepare the beam holding jig.

A jig to hold the beams can be used to store and transport the finished beam specimens to different laboratories and workshops. Placing a beam specimen on an uneven surface will cause creep deformation, especially if the beam has been stored for an extended period. Moreover, moving a finished beam specimen (just after cutting it from the slab) using bare hands within the different rooms in a laboratory also could cause creep deformation, and the chance of such deformation is high at elevated room temperatures (> 30°C). These uncertainties in sample handling need to be avoided and can be mitigated using the holding jig shown in Figure E- 12. The same jig can be easily mounted onto a milling machine so that no additional fasteners are required during the notch-cutting process. The research team strongly recommends using a holding jig after preparing the beam specimens until the beams are loaded into the NBFT apparatus.

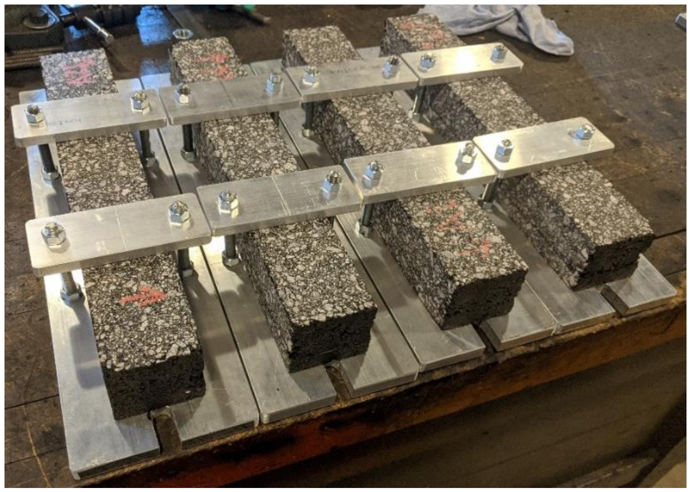

Figure E- 12. Beam specimens fastened in a holding jig.

Step 7. Cut a notch into the beam specimens.

Two methods typically are employed to make notches in AC beam specimens. The first method is to place a metal insert inside the compaction mold and the second method is to create a mechanical notch cut. The former method affects the mixture compaction effort by disturbing the aggregate alignment, thus leading to mixture segregation. The mechanical method results in a blunt notch compared to the sharper notch obtained using a metal insert. An alternative approach is to produce a well-defined pre-crack by applying a small cycle load. Previous studies of notched AC specimens (disk-shaped compacted specimens, single-edge notched beams) have led researchers to recommend a pre-crack or sharp notch on the specimen to eliminate the effects of different notch sizes for different specimens (Kuai et al. 2010, Petersen et al. 2005).

In the case of a single-edge notched beam, a mechanical notch to a depth ratio (a/W) of 0.19 is recommended over the standardized fracture test requirement of the a/W ratio between 0.45 and 0.55. However, using deep-notched specimens made with AC may produce undesirable test results, such as large statistical variations and crack initiation under self-weight (Petersen et al. 2005, Sudarsanan et al. 2019b). For notched disk-shaped compacted specimens, a notch length of 27.5 mm serves as a pre-crack and is preloaded until the initial crack length reaches 30 mm (Kuai et al. 2010). Wargo (2015) recommends the use of stiff notching saw to produce repeatable notches, as any flexibility of the saw could cause a variation in notch depth.

The recommended two steps needed to create a sharp notch make the procedure cumbersome. The first cut involves making a notch using a 5-mm wide blade to create a half-notch depth, followed by a 1-mm wide blade to make a full-notch depth. Inducing a well-defined pre-crack is possible for the current study but requires additional measurement gauges to develop an accurate crack. Therefore, a tapered notch could help the stress concentration and improve the likelihood that the crack will initiate from the same point. In order to make a consistent notch that could produce repeatable results, a drill was chosen as the tool in this study. Figure E- 13 shows two sizes of drill bits and Table E- 1 presents details regarding the drill bits that were used to make consistent notches.

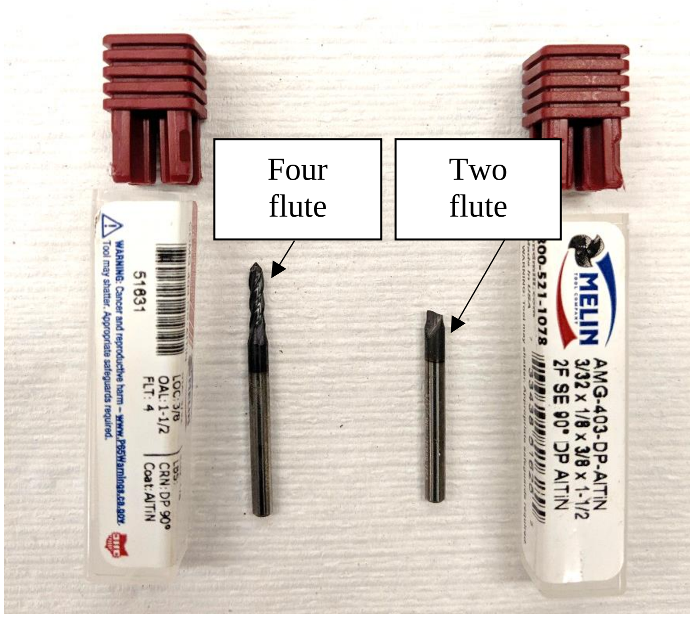

Figure E- 13. Drill bits used for making tapered notches.

Table E- 1. Material and Dimensions of Drill Bits Used for Current Study

Finish		Titanium aluminum nitride (TiAlN) -coated
Material		Carbide
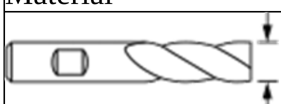	Mill diameter	2.381 – 23.8 mm (3/32 – 0.937 in.)
	Mill diameter tolerance	-0.003 in. to 0.000 in.
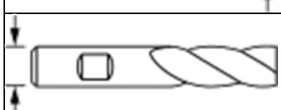	Shank type	Straight
	Shank diameter	3.175 mm (1/8 in.)
Length of Cut		9.525 mm (3/8 in.)
Overall Length		38.1 mm (1 1/2 in.)
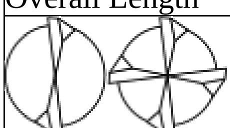	Flute Type	Spiral
	Number of Flutes	2 or 4
	Flute Spacing	Equal
Point Angle		90°
Helix Angle		30°

Figure E- 14 presents images of the tapered notches cut into the beam specimens used in the notch study. Three equidistant deep drilling steps achieved the desired notch depth of 5 mm.

Two approaches were followed for drilling. The first approach allowed the unidirectional movement of the drill along the width of the beam specimen during each depth step. Figure E- 14 (a) and (b) show that the aggregate chipped near the edge of the beam during the process. This outcome is common at the edges where the drill bit exits the beam. However, such chipping was not evident when the drill bit entered the beam specimen. Therefore, the second approach was adopted whereby the drill bit enters the beam from one edge, and drilling is stopped when the bit reaches the middle of the beam. The drill bit then is repositioned on the other edge, and drilling commences to reach the center of the beam to conclude each depth step. This method significantly reduced the problem of chipping the aggregate. However, the problem persisted when large aggregate particles were present at the edges. Nonetheless, a tapered notch was sustained throughout the width of the beam, and chipping was found only at the edges. In short, a careful procedure is needed to produce consistent tapered notches. This process is more time-consuming than saw cutting: 30 minutes using a drill versus 30 seconds using a saw.

(a) (b) (c)

Figure E- 14. Tapered notches made by drilling: (a) and (b) chipped edges under a unidirectional pass, and (c) non-chipped edge under a bidirectional pass.

Step 8. Speckle the beam specimen for DIC testing.

In order to track the crack propagation through a beam specimen using the DIC technique, the surface of the beam specimen should be speckled. The speckling procedure allows the surface to have sufficient contrast throughout the area of interest so that consistently sized speckle subsets may be tracked with certainty. Therefore, the certainty of the results is often defined by the quality of the speckle pattern.

A new speckle kit was procured for this study to obtain a consistent speckle pattern. Different sizes of speckle/dot sizes could be selected depending on the region of interest. Table E- 2 shows the different roller sizes that can be selected depending on the camera used and the region of interest. Based on Table E- 2, the dot sizes of 0.007 in. and 0.013 in. could work for the beam specimen's field-of-view. Typically, the smaller of the two provides better resolution. Figure E-15 shows the roller stamp used for speckling the beam specimens.

Table E- 2. Dot Size Selection Table for Speckling Process in DIC Testing.

	Field-of-View					
Camera / Dot size	0.007" (0.18 mm)	0.013 in. (0.33 mm)	0.026 in. (0.66 mm)	0.05 in. (1.27 mm)	0.10 in. (2.54 mm)	0.20 in. (5.08 mm)
1 MP camera 1024 pixels across	0.9 in. - 2.4 in. 2.3 - 6.1 cm	1.7 in. - 4.4 in. 4.2 - 11 cm	3.3 in. - 8.9 in. 8.4 - 23 cm	6.4 in. - 17.1 in. 16 - 43 cm	12.8 in. - 34.1 in. 33 - 87 cm	26.6 in. - 68.3 in. 65 - 173 cm
2.3 MP camera 1920 pixels across	1.7 in. - 4.5 in. 4.3 - 11 cm	3.1 in. - 8.3 in. 7.9 - 21 cm	6.2 in. - 16.6 in. 16 - 42 cm	12.0 in. - 32.0 in. 31 - 81 cm	24.0 in. - 64.0 in. 61 - 163 cm	48.0 in. - 128.0 in. 122 - 325 cm
5 MP camera 2448 pixels across	2.1 in. - 5.7 in. 5.4 - 15 cm	4.0 in. - 10.6 in. 10 - 27 cm	8.0 in. - 21.2 in. 20 - 54 cm	15.3 in. - 40.8 in. 39 - 103 cm	30.6 in. - 81.6 in. 78 - 207 cm	61.2 in. - 163.2 in. 155 - 415 cm
16 MP camera 4872 pixels across	4.3 in. - 11.4 in. 11 - 29 cm	7.9 in. - 21.1 in. 20 - 54 cm	15.8 in. - 42.2 in. 40 - 107 cm	30.5 in. - 81.2 in. 77 - 206 cm	60.9 in. - 162.4 in. 155 - 413 cm	121.8 in. - 324.8 in. 309 - 825 cm

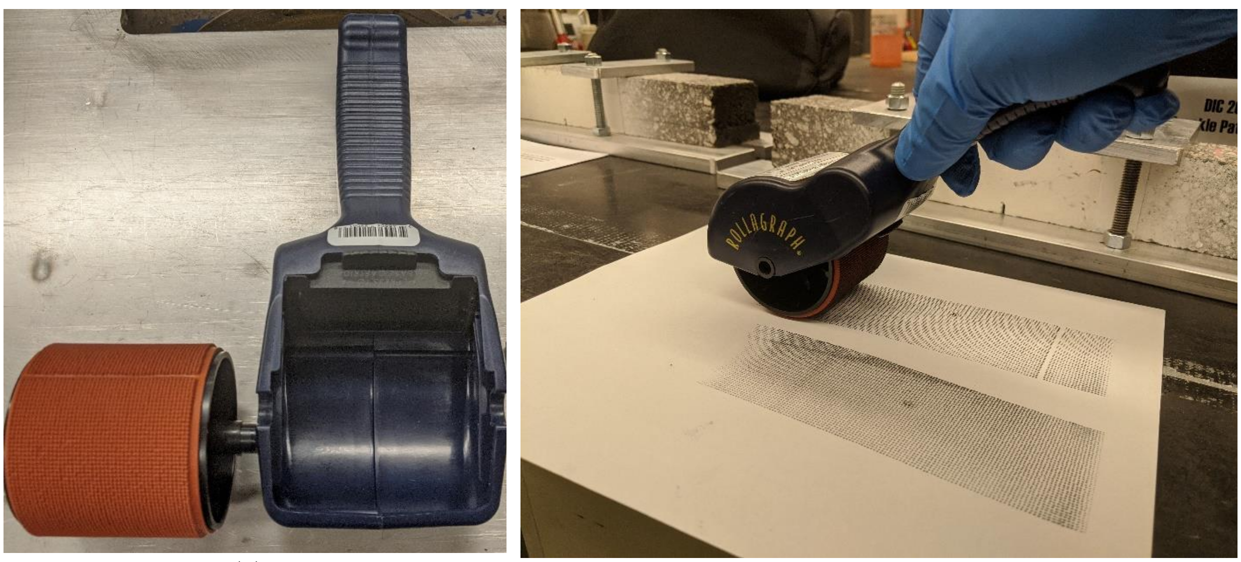

(a) (b)

Figure E- 15. (a) Components of roller stamp and (b) using roller stamp for speckling.

Figure E- 16 depicts the procedure for speckling the beam specimens. The first step is to apply a base coat of paint on the beam specimen, as shown in Figure E- 16 (a). The purpose of the base coat is to create as much contrast as possible. Speckle patterns may have a white base coat and black speckles. For the roller stamps, black ink is used, so the base coat must be white. When using stamps, the paint must be dry to the touch. Typically, about five to ten minutes is sufficient for drying to the touch. A Krylon chalky finish matte clear spray paint was used as the base coat in this study. Figure E- 16 (b) shows the different speckle patterns on beam specimens.

(a)

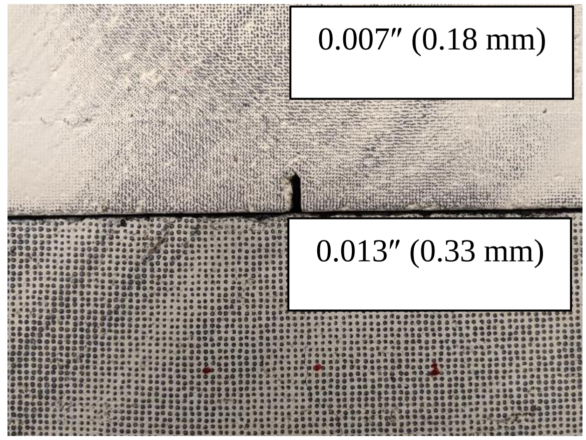

(b)

Figure E- 16. (a) Spraying the base coat on a beam specimen and (b) speckle patterns with different dot sizes on beam specimens.